LEVANI SKHIRTLADZE

SYNTHESIS AND STUDIES OF PROPERTIES OF ORGANIC SEMICONDUCTORS CONTAINING DONOR AND ACCEPTOR MOIETIES

DOCTORAL DISSERTATION

Kaunas
2024

KAUNAS UNIVERSITY OF TECHNOLOGY

LEVANI SKHIRTLADZE

SYNTHESIS AND STUDIES OF PROPERTIES OF ORGANIC SEMICONDUCTORS CONTAINING DONOR AND ACCEPTOR MOIETIES

Doctoral dissertation
Technological Sciences, Chemical Engineering (T 005)

2024, Kaunas

This doctoral dissertation was prepared at Kaunas University of Technology, Faculty of Chemical Technology, Department of Polymer Chemistry and Technology during the period of 2019–2023. The studies were supported by the Research Council of Lithuania.

Scientific Supervisor:
Prof. Dr. Hab. Juozas Vidas GRAŽULEVIČIUS (Kaunas University of Technology, Technological Sciences, Chemical Engineering, T 005).

Scientific Advisor:
Prof. Dr. Azhar Bin ARIFFIN (University of Malaya, Malaysia, Organic Chemical Synthesis, Organic Chemistry).

Edited by: English language editor Brigita Brasienė (Publishing House *Technologija*), Lithuanian language editor Aurelija Gražina Rukšaitė (Publishing House Technologija).

The public defense of the dissertation will be held at 10 a.m. on 5 April, 2024 at the public meeting of Dissertation Defense Board of Chemical Engineering Science Field in the Rectorate Hall at Kaunas University of Technology.

Address: K. Donelaičio 73-402, Kaunas, LT-44249, Lithuania
Phone: (+370) 608 28 527; e-mail doktorantura@ktu.lt

The doctoral dissertation was sent out on 5 March, 2024.
The doctoral dissertation is available on the internet at http://ktu.edu and at the library of Kaunas University of Technology (Gedimino 50, Kaunas, LT-44239, Lithuania).

KAUNO TECHNOLOGIJOS UNIVERSITETAS

LEVANI SKHIRTLADZE

ORGANINIŲ PUSLAIDININKIŲ, TURINČIŲ DONORINIUS IR AKCEPTORINIUS FRAGMENTUS SINTEZĖ IR TYRIMAI

Daktaro disertacija
Technologijos mokslai, chemijos inžinerija (T 005)

2024, Kaunas

Disertacija rengta 2019–2023 metais Kauno technologijos universiteto Cheminės technologijos fakultete, Polimerų chemijos ir technologijos katedroje. Mokslinius tyrimus rėmė Lietuvos mokslo taryba.

Mokslinis vadovas:
prof. habil. dr. Juozas Vidas GRAŽULEVIČIUS (Kauno technologijos universitetas, technologijos mokslai, chemijos inžinerija, T 005).

Mokslinis konsultantas:
prof. dr. Azhar Bin ARIFFIN (Malajos universitetas, Malaizija, organinė cheminė sintezė, organinė chemija).

Redagavo: anglų kalbos redaktorė Brigita Brasienė (leidykla „Technologija“), lietuvių kalbos redaktorė Aurelija Gražina Rukšaitė (leidykla „Technologija“).

Chemijos inžinerijos mokslo krypties disertacijos gynimo taryba:
prof. dr. Petras Rimantas VENSKUTONIS (Kauno technologijos universitetas, technologijos mokslai, chemijos inžinerija, T 005) – **pirmininkas**;
prof. habil. dr. Arūnas RAMANAVIČIUS (Vilniaus universitetas, gamtos mokslai, chemija, N 003);
prof. dr. Ramunė RUTKAITĖ (Kauno technologijos universitetas, technologijos mokslai, chemijos inžinerija, T 005);
Dr. Kaspars TRASKOVSKIS (Rygos technikos universitetas, Latvija, gamtos mokslai, chemija, N 003);
prof. dr. Virgilijus VALEIKA (Kauno technologijos universitetas, technologijos mokslai, chemijos inžinerija, T 005).

Disertacija bus ginama viešame chemijos inžinerijos mokslo krypties disertacijos gynimo tarybos posėdyje 2024 m. balandžio 5 d. 10 val. Kauno technologijos universiteto Rektorato salėje.

Adresas: K. Donelaičio g. 73-402, Kaunas, LT-44249, Lietuva
Tel. (+370) 608 28 527; el. paštas doktorantura@ktu.lt

Disertacija išsiųsta 2024 m. kovo 5 d.
Su disertacija galima susipažinti interneto svetainėje http://ktu.edu ir Kauno technologijos universiteto bibliotekoje (Gedimino g. 50, Kaunas, LT-44239, Lietuva).

TABLE OF CONTENTS

LIST OF TABLES

LIST OF FIGURES

LIST OF SCHEMES

LIST OF ABBREVIATIONS AND DEFINITIONS

AC	acridine
AIEE	aggregation-induced emission enhancement
CT	charge transfer
CV	cyclic voltamperometry
D–A	donor–acceptor
DF	delayed fluorescence
DFT	density functional theory
DMF	*N, N*-dimethylformamide
DPPA	(diphenylphosphino)ethyne
DPPB	1,2-bis(diphenylphosphino)benzene
DPPE	1,2-bis(diphenylphosphino)ethane
DSC	differential scanning calorimetry
EL	electroluminescence
EML	emissive layer
EQE	external quantum efficiency
ET	triplet energy
ETL	electron transporting layer
Fc	ferrocene
FWHM	full width at half maximum
HOMO	highest occupied molecular orbital
HONTO	highest occupied natural transition orbital
ICT	intramolecular charge transfer
IP	ionization potential
IP_{CV}	ionization potential estimated by cyclic voltamperometry
IQE	internal quantum efficiency
ISC	intersystem crossing
ITO	indium tin oxide
k_{ISC}	intersystem crossing rate constant
LED	light emitting diode
LiF	lithium fluoride
Lummax	maximum luminance
LUMO	lowest unoccupied molecular orbital
LUNTO	lowest unoccupied natural transition orbital
m.p.	melting point
mCBP	3,3′-d(9H-carbazol-9-yl)-1,1′-biphenyl
MCL	mechanoluminescent
NBS	N-bromosuccinimide
NMR	nuclear magnetic resonance
NTO	natural transition orbitals
OLED	organic light-emitting diode
ORTEP	Oak Ridge Thermal Ellipsoid Plot

$Pd_2(dba)_3$	tris(dibenzylideneacetone)dipalladium
PFBP-2a	2,7-di-tert-butyl-9,9-dimethyl-10-(perfluoro-[1,10 -
PL	photoluminescence
PLQY	photoluminescence quantum yield
PO	phenoxazine
PS	phenothiazine
RISC	reverse intersystem crossing
RTP	room temperature phosphorescence
S_0	ground state
S_1	lowest-lying singlet excited state
SimCP2	3,5-di(9H-carbazol-9-yl)tetraphenylsilane
T_1	lowest-lying triplet excited state
TADF	thermally activated delayed fluorescence
t-buONa	sodium *tert*-butoxide
TCTA	tris(4-carbazoyl-9-ylphenyl)amine
TD-DFT	time-dependent density functional theory
T_g	glass transition temperature
TGA	thermogravimetric analysis
TOF	time of flight
TPBi	2,2',2''-(1,3,5-benzinetriyl)-tris(1-phenyl-1-H-benzimi-
TSPO1	diphenyl-4-triphenylsilyl-phenylphosphineoxide
UV/Vis	ultraviolet/visible
XPhos	dicyclohexyl[2′,4′,6′-tris(propan-2-yl)[1,1′-biphenyl]-2-
ΔE_{ST}	energy gap between singlet and triplet excited states
$\lambda^{abs}max$	absorption maximum
λemmax	wavelength of emission maximum
λexc	excitation wavelength
Φ	photoluminescent quantum yield

1. INTRODUCTION

Organic semiconductors have drawn a great deal of attention because of their distinctive characteristics and potential uses. Some important areas where organic semiconductors are used are organic light-emitting diodes (OLEDs). One of the most popular uses for organic semiconductors is OLED technology[1,2]. They are used in displays and lighting panels in smartphones, TVs, wearable devices, and automotive displays[3]. High contrast, broad viewing angles, and low power consumption are just a few benefits that OLEDs can offer[4,5]. Organic semiconductors are used in organic solar cells as well. Flexible, lightweight, and cheap to produce organic and hybrid solar cells can convert sunlight into power[6,7]. Potential uses of these devices include portable electronics, as well as solar panels that are integrated into buildings, and other solar power systems[8,9]. One more potential application of organic semiconductors is organic field-effect transistors (OFETs)[10,11]. The advantages of these devices are the potential for large-area manufacture as well as low-cost fabrication and mechanical flexibility. OFETs can be used in radio frequency identification (RFID) tags, sensors, flexible displays, electrical circuits[12]. Organic thin-film transistors (OTFTs) are like OFETs; however, they use mostly thin films of organic semiconductors[13]. They have applications in active matrix displays, flexible electronics, and wearable devices[14,15]. OTFT technology enables the development of lightweight and bendable electronic products. Organic semiconductors are used in organic memory devices, such as organic random-access memory (ORAM) and organic flash memory (OFM) devices[16,17]. High-density data storage and low-cost manufacturing are two advantages of these memory devices[18,19]. Organic sensors represent the next field of application of organic semiconductors. The different sorts of sensors, including pressure sensors, biosensors, gas sensors, can be constructed using organic semiconductors[20]. These sensors can be used in a variety of products, including wearable technology[21], medical applications[22,23], environmental monitoring systems[24,25], etc. Organic lasers or organic semiconductor lasers have been developed using organic semiconductors[26]. The benefits of organic-semiconductor lasers include tunability[27], affordable production[28], and compatibility with flexible substrates[29]. They can be used in spectroscopy[30], biomedical imaging, and telecommunications[31]. With their ability to transform waste heat into power, organic semiconductors have demonstrated the potential use in thermoelectric applications[32]. Temperature sensors, wearable electronics[33,34], and energy harvesting[35] are potential uses for organic thermoelectric devices.

Due to their potential use in optoelectronic devices, sensors, and other fields, thermally activated delayed fluorescence (TADF) and room temperature phosphorescence (RTP) have attracted a great deal of attention lately[36,37]. Significant interest and research efforts have been put into the discovery and development of room-temperature phosphorescent materials. This is because RTP materials have the potential to improve the efficiency and performance of OLEDs and sensors. RTP can allow to enhance device lifetime[38,39], reduce power consumption, and enable different

applications in areas such as lighting[40], displays[41], and data communication[42]. The high efficiency of OLEDs is obtained by using phosphorescent materials[43]. However, rare and expensive metals such as platinum[44] and iridium[45] are used in phosphorescent OLED emitters[46,47]. TADF materials provide an alternative method by employing organic molecules that can achieve comparable effectiveness without the need of expensive metals[48,49]. TADF materials typically consist of two components, i.e., donor and acceptor moieties[50,51]. In the first-generation OLEDs, only singlet excitons (electron-hole pairs with parallel spins) can emit light efficiently, while triplet excitons (electron-hole pairs with antiparallel spins)[52] are typically non-emissive. As a result, singlet excitons are the primary source of light emission, while a significant amount of energy from triplet excitons is wasted as heat. However, TADF allows for the efficient harvesting of both singlet and triplet excitons, thereby enhancing the overall emission efficiency of the devices. TADF compounds can convert non-emissive triplet excitons into emissive singlet excitons, resulting in highly efficient fluorescence[53,54]. Organic compounds with a narrow energy gap between the lowest singlet and triplet excited states can accomplish this. This small energy gap allows for reverse intersystem crossing (RISC)[55,56], which enables the conversion of the non-emissive triplet excitons into emissive singlet excitons[57]. The TADF process involves three main steps: harvesting, up-conversion, and emission[58,59]. First, the TADF material harvests both singlet and triplet excitons generated by the electrical excitation. The harvested triplet excitons are then up-converted into singlet excitons through RISC[57]. This step involves efficient energy transfer and spin manipulation within the TADF molecule. Finally, the singlet excitons undergo radiative decay, resulting in the emission of light.

TADF materials come in a variety of forms, each having unique chemical characteristics and chemical structures[60,61]. Some commonly used TADF materials include carbazole derivatives[62,63]. Due to their high fluorescence efficiency and suitable energy levels, these compounds are widely researched as TADF materials. With their high emission efficiency and excellent color purity, triazine-based[64,65] materials have demonstrated intriguing TADF features. Acridine-based[66,67] TADF materials have been investigated for OLEDs due to their efficient blue and green emission. Spiroacridine[68,69] compounds exhibit efficient TADF properties and have been utilized in blue-emitting OLEDs.

TADF materials come in a variety of forms, each having unique chemical characteristics and chemical structures[60,61]. Carbazole derivatives represent commonly used TADF materials[62,63]. Due to their high fluorescence efficiency and suitable energy levels, these compounds are widely researched as TADF materials. With their high emission efficiency and excellent emission color purity, triazine-based[64,65] materials have demonstrated intriguing TADF features. Acridine-based[66,67] TADF materials have been investigated for OLEDs due to their efficient blue and green emission. Spiroacridine[68,69] compounds as well exhibit efficient TADF. They have been utilized in blue-emitting OLEDs.

RTP compounds can emit light at room temperature through phosphorescence, which is a process typically associated with metal complexes. This is achieved with organic molecules that have heavy-atom elements, such as phosphorus or heavy halogens[70], incorporated into their structure. These heavy atoms facilitate intersystem crossing (ISC) between singlet and triplet excited states, leading to phosphorescence. Normally, phosphorescence is related to materials that emit light even after an external energy source, such ultraviolet (UV) radiation, has been removed[71,72]. The emission occurs in the case of RTP without the requirement for cryogenic temperatures or other energy sources. In traditional organic materials, such as dyes and fluorescent compounds, the excited state energy is quickly lost by non-radiative processes, leading to prompt emission or fluorescence that lasts for just a very brief period (in the range of nanoseconds)[73,74]. However, phosphorescent materials exhibit a longer-lived excited state due to the presence of a triplet state. The triplet state can undergo intersystem crossing, where the energy is effectively stored and emitted as light over a longer timescale. In order to achieve RTP in organic materials, the researchers have been experimenting with a variety of methods. These methods include using, constructing rigid molecular frameworks[75,76], and including heavy elements in the molecular structure. In order to create effective RTP materials, the scientists have made great progress by carefully designing the molecular structure and optimizing their characteristics.

Aromatic and heteroaromatic compounds, containing trifluoromethyl (CF_3) group, have attracted significant attention in TADF and RTP research because of their special electronic and steric characteristics[77,78]. Due to the electron-withdrawing properties of the CF_3 group, there is a lower energy difference between the singlet and triplet excited states, which results in a lower energy of the lowest unoccupied molecular orbital (LUMO)[79,80]. The CF_3 group is relatively bulky. It may have an impact on the molecular packing and improve intersystem crossing and emission efficiency. The experimental studies have demonstrated that TADF compounds containing a trifluoromethyl group can exhibit high fluorescence quantum yields. OLEDs based on such compounds show low efficiency roll-off at high current densities[81]. Furthermore, the incorporation of a trifluoromethyl group has been shown to enhance the stability and durability of TADF materials, making them promising candidates for the use in the long-lasting lighting applications[82,83].

It has been shown that RTP compounds containing trifluoromethyl group can exhibit long-lived room temperature phosphorescence[84,85]. This makes them promising candidates for the use in a variety of applications, including imaging and sensing.

Donor–acceptor–donor (D–A–D) and donor–acceptor (D–A) type organic compounds are commonly used in organic electronics, such as organic solar cells, organic field-effect transistors, OLEDs. These materials have a specific molecular structure where a central electron-accepting unit is flanked by two electron-donating units. The D–A–D and D–A design strategies help in achieving desirable electronic and optical properties of organic materials. The energy levels, charge transport

characteristics, and light absorption properties of these materials can all be precisely controlled by carefully choosing the donor and acceptor units and fine-tuning their molecular structure.

Efficient TADF materials have several advantages in OLED technology. They enable the conversion of non-emissive triplet excitons into emissive singlet excitons, thereby enhancing the overall device efficiency. TADF OLEDs have shown great potential for achieving high external quantum efficiency (EQE) and low power consumption, making them desirable for various display and lighting applications.

Overall, TADF and RTP compounds, including those containing trifluoromethyl groups, have shown great potential for their use in a variety of optoelectronic applications, including organic light-emitting diodes (OLEDs) and biological imaging. However, the possibilities for the combination of different donor and acceptor moieties in the design of new potentially efficient TADF and/or RTP emitters are not fully explored yet. For this reason, the design, synthesis, and investigation of the properties of new D–A–D or D–σ–A type TADF and/or RTP emitters is an urgent problem.

The aim of the present work is the synthesis and investigation of the properties of new donor–acceptor–donor and donor–acceptor type derivatives containing trifluoromethyl benzene, difluorobenzene, pyridazine, sulfobenzimide as acceptor moieties and different donor units for the application in organic light emitting diodes and oxygen sensors.

In order to achieve the aim of the work, **the following objectives** have been outlined:

- Synthesis of new derivatives of trifluoromethyl benzene with the donor–acceptor–donor structures;
- Study of the thermal, photophysical, and photoelectrical properties of trifluoromethyl benzene-based materials;
- Synthesis of new compounds with the symmetrical donor–acceptor–donor structure containing pyridazine group and differently substituted phenoxazine or 9,9-dimethyl-9-10-dihydroacridine moieties;
- Investigation of the thermal, photophysical, photoelectrical, and electroluminescent properties of pyridazine derivatives;
- Synthesis and investigation of carbazole and sulfobenzimide derivative;
- Study of photophysical properties of the carbazole derivative, including absorption and emission spectra, fluorescence quantum yield, and fluorescence lifetime measurements.

Novelty of the work

- New donor–acceptor–donor type 2,5-bis(trifluomethyl)-1,4-phenylene derivatives were designed, synthesized, characterized, and applied in TADF OLEDs.

- New compounds with different donor moieties and 1,4-difluorobenzene unit as the acceptor were developed for the optical sensors of oxygen. It was established that phenothiazine containing derivative exhibits strong RTP.
- Two new compounds based on pyridazine as the acceptor core and different donor moieties were designed, synthesized, and characterized.
- New compound containing sulfobenzimide moiety as an acceptor unit was synthesized and characterized. The new type of D–σ–A emitter TADF was demonstrated.
- Two compounds consisting of electron-accepting trifluoromethylphenyl moiety and different electron-donating groups were designed and synthesized. 10,10'-(2-(Trifluoromethyl)-1,4-phenylene)bis(10H-phenothiazine) as efficient RTP emitter showed high oxygen sensitivity.

Contribution of the author

The author has designed, synthesized, and purified four series of the organic materials described in sub-chapters 2.1–2.4. The analysis of results were conducted by the author in collaboration with the colleagues/co-authors of the publications from Kaunas University of Technology, Vilnius University, University of Malaya, Silesian University of Technology, and Tbilisi State University. Charge mobility and ionization potential measurements were done in collaboration with Dr. Dmytro Volyniuk. Dr. Oleksandr Bezvikonnyi and Mr. Karolis Leitonas investigated the photophysical properties and studied the oxygen properties of the materials; Dr. Rasa Keruckienė has performed DFT calculations and analyzed the obtained data, performed cyclic voltammetry measurements; Dr. Audrius Bučinskas performed single crystal X-ray analysis. The measurements of the thermal properties by thermogravimetry (TG) and differential scanning calorimetry (DSC) were performed by Dr. Malek Mahmoudi. Mr. Lukas Dvylys assisted with the investigation and data curation. All of them are the representatives of the Department of Polymer Chemistry and Technology, KTU. Prof. Dr. Hab. Linas Labanauskas (Center for Physical Sciences & Technology, Department of Organic Chemistry, Vilnius, Lithuania) helped with the conceptualization and methodology. Prof. Dr. Mieczyslaw Lapkowski (Department of Physical Chemistry and Technology of Polymers, Silesian University of Technology) helped to analyze cyclic voltammetry data. Prof. Dr. Azhar Bin Ariffin (University of Malaya, Department of Chemistry) assisted with the synthesis and advised with the design of new materials. Assoc. Prof. Dr. Kai Lin Woon (Low Dimensional Materials, Department of Physics, University of Malaya) performed DFT calculation, analyzed and described the data. Dr. Omar Mukbaniani (Department of Chemistry, Faculty of Exact and Natural Sciences, Tbilisi State University, Tbilisi, Georgia) advised with the synthesis of new materials. Prof. Dr. Hab. Juozas Vidas Gražulevičius advised with the design of new light-emitting materials and the preparation of the manuscripts.

List of scientific publications on the topic of the dissertation

1. Skhirtladze Levani; Leitonas Karolis; Bucinskas Audrius; Volyniuk Dmytro; Mahmoudi Malek; Mukbaniani Omar; Woon Kai Lin; Ariffin Azhar; Grazulevicius Juozas Vidas. 1,4-Bis(trifluoromethyl)benzene as a new acceptor for the design and synthesis of emitters exhibiting efficient thermally activated delayed fluorescence and electroluminescence: experimental and computational guidance // Journal of Materials Chemistry C. ISSN 2050-7526 eISSN 2050-7534. 2022, vol. 10, iss. 12, p. 4929-4940. DOI: 10.1039/d1tc05420a. (Web of Science); [IF: 8,067; AIF: 6,018; IF/AIF: 1,340; Q1].

2. Skhirtladze Levani; Leitonas Karolis; Bucinskas Audrius; Woon Kai Lin; Volyniuk Dmytro; Keruckiene Rasa; Mahmoudi Malek; Lapkowski Mieczyslaw; Ariffin Azhar; Grazulevicius Juozas Vidas. Turn on of room temperature phosphorescence of donor-acceptor-donor type compounds via transformation of excited states by rigid hosts for oxygen sensing // Sensors and actuators B: Chemical. Lausanne: Elsevier. ISSN 0925- 4005. 2023, vol. 380, art. no. 133295, p. 1-10. DOI: 10.1016/j.snb.2023.133295. (Web of Science); [IF: 9,221; AIF: 5,220; IF/AIF: 1,766; Q1].

3. Skhirtladze Levani; Bezvikonnyi Oleksandr; Keruckienė Rasa; Dvylys Lukas; Mahmoudi Malek; Labanauskas Linas; Ariffin Azhar; Grazulevicius Juozas Vidas. Derivatives of pyridazine with phenoxazine and 9,9-dimethyl-9,10-dihydroacridine donor moieties exhibiting thermally activated delayed fluorescence // Materials. Basel: MDPI. ISSN 1996-1944. 2023, vol. 16, iss. 3, art. no. 1294, p. 1-10. DOI: 10.3390/ma16031294. (Web of Science); [IF: 3,748; AIF: 6,225; IF/AIF: 0,602; Q1].

4. Danyliv Yan; Ivaniuk Khrystyna; Danyliv Iryna; Bezvikonnyi Oleksandr; Volyniuk Dmytro; Galyna Sych; Lazauskas Algirdas; **Skhirtladze Levani**; Ågren Hans; Stakhira Pavlo; Karaush-Karmazin Nataliya; Ali Amjad; Baryshnikov Glib; Grazulevicius Juozas Vidas. Carbazole-σ-sulfobenzimide derivative exhibiting mechanochromic thermally activated delayed fluorescence as emitter for flexible OLEDs: theoretical and experimental insights // Dyes and pigments. Oxford: Elsevier. ISSN 0143-7208. eISSN 1873-3743. 2022, vol. 208, art. no. 110841, p. 1-11. DOI: 10.1016/j.dyepig.2022.110841 (Web of Science); Scopus; [IF: 5,122; AIF: 5,458; IF/AIF: 0,938; Q1].

2. REVIEW OF PUBLISHED ARTICLES

The chapter Review of Articles contains information from the articles of the author (see List of publications on the subject of the thesis).

2.1. Efficient thermally activated delayed fluorescence and electroluminescence from 1,4-bis(trifluoromethyl)benzene-based emitters (Scientific publication No. 1, Q1)

This chapter is based on the paper published in *Journal of Materials Chemistry C*, 2022, 10, 4929–4940. New emitters with symmetrical donor–acceptor–donor structures were designed and synthesized using 1,4-Bis(trifluoromethyl)benzene as an acceptor in combination with phenoxazine, phenothiazine, or 9,9-dimethyl-9-10-dihydroacridine as donor moieties. The method of synthesis of compounds 10,10'-(2,5-bis(trifluoromethyl)-1,4-phenylene)bis(10H-phenoxazine) (1), 10,10'-(2,5-bis(trifluoromethyl)-1,4-phenylene)bis(10H-phenothiazine) (2), and 10,10'-(2,5-bis (trifluoromethyl)-1,4-phenylene) bis(9,9-dimethyl-9,10 dihydroacridine) (3) is shown in Scheme 2.1. In order to obtain the target derivatives with the required donor–acceptor–donor structure, two step reactions were carried out. The chemical structures of synthesized compounds 1 and 2 were confirmed by using ^{1}H and ^{13}C NMR spectroscopies, mass spectrometry, and X-ray crystallography. The structure of compound 3 could not be confirmed by ^{1}H or ^{13}C NMR due to the low solubility in all of the available deuterated solvents; however, single crystal X-ray crystallography provided definitive evidence of the structure.

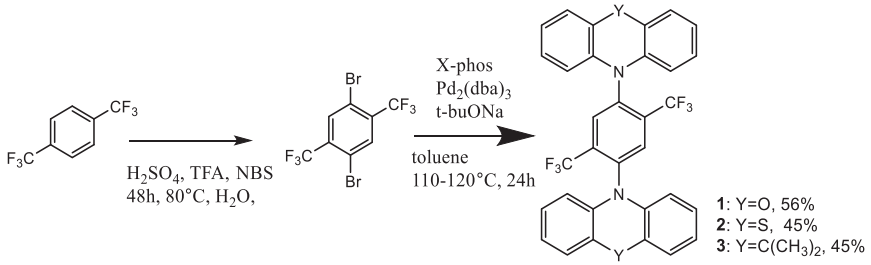

Scheme 2.1. Molecular structure and the synthetic route for compounds 1, 2, and 3

The techniques of thermogravimetric analysis (TGA) and differential scanning calorimetry (DSC) were utilized in order to investigate the thermal stability of compounds 1–3 as well as their morphological characteristics. Table 2.1 provides a summary of temperatures of 5% weight loss (T_{ID}), the melting point (T_m), and the crystallization points (T_{cr}).

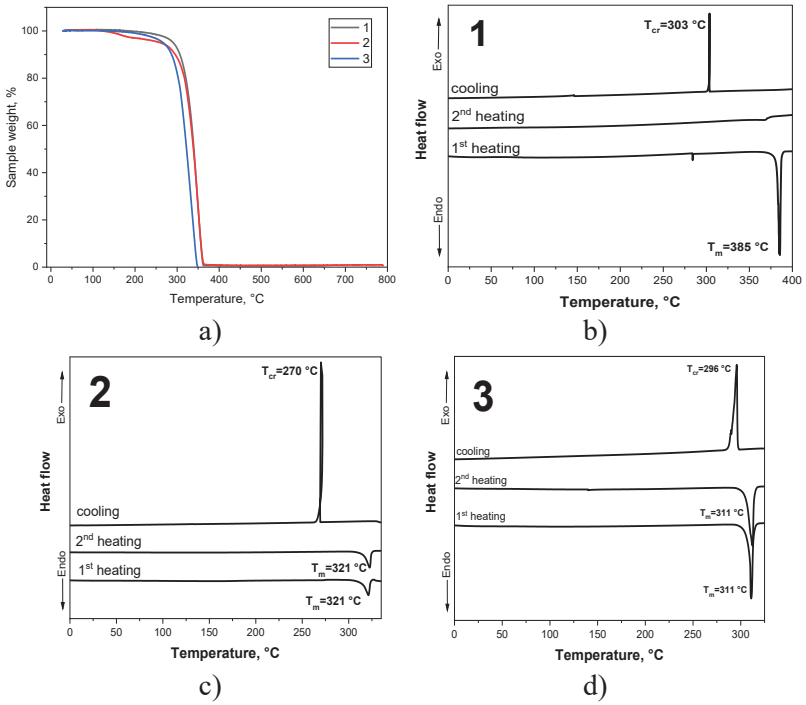

Fig. 2.1. TGA (a) and DSC (b, c, d) thermograms of compounds 1, 2, and 3

Table 2.1. Thermal characteristics of the compounds

Compound	T_{ID}, °C [1]	T_{cr}, °C [2]	T_m, °C [3]
1	290	303	385
2	260	270	321
3	267	296	311

[1] The temperature at which 5% of the mass of the sample was lost, as determined by the TGA, [2] crystallization temperatures determined by DSC, [3] melting points determined by DSC.

In addition, the structures of 1, 2, and 3 were confirmed and analyzed using single-crystal X-ray analysis. THF solution was used to grow single crystals of each of the compounds. The projections made using the Oak Ridge Thermal Ellipsoid Plot (ORTEP) show (Fig. 2.2 a–c) that all the target compounds are symmetrical. The X-ray examination of the packing pattern of the crystals revealed that the molecules are held together by very weak intermolecular Van der Waals bonds between the CF3 fluorine and the methyl hydrogen atoms or between the carbon and the hydrogen atoms of the phenyl ring. Concerning compound 3, the interactions C-H···F and C-H···C were observed. The distances between the atoms range from 2.61 to 2.85 Å (Fig.

2.2 d). In addition, the following weak intramolecular bonds can be found: C-H···F, C-F···N, C-H···H, and C-H···C. These bonds have a distance of less than 2.71 Å.

Electron-donating groups (phenoxazine, phenothiazine, and acridine) present in corresponding compounds (1, 2, and 3) are not flat: they have a twist of 15°, 30°, and 31°, respectively. The significant factor for TADF emitters is a large torsional angle between the donor fragments and the acceptor units[86]. It was discovered that the torsional angles between acceptor unite -1,4-bis(trifluoromethyl)benzene and donor fragments phenoxazine, phenothiazine, and acridine moieties were of 81.2°, 80.0°, 77.2° for compounds 1, 2, and 3, respectively.

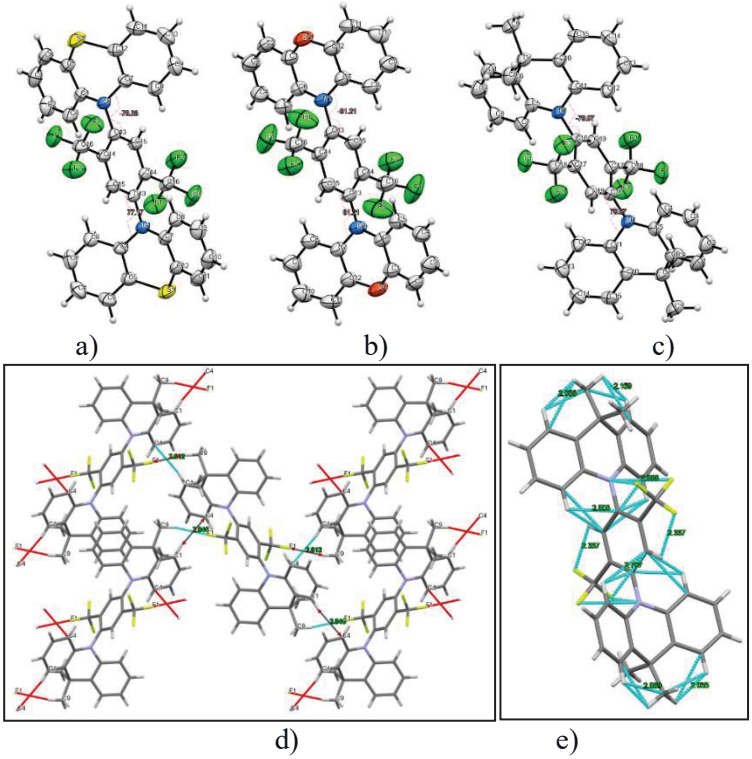

Fig. 2.2. X-ray structures of compounds 1 (a), 2 (b), and 3 (c); the torsion angles between the donor units and the acceptor units are shown in dashed purple lines; packing in the crystal structure of compound 3 viewed along the a-axis (d) and intramolecular bonding (e)

DFT simulations were carried out for the purpose of investigating the molecular structures. Fig. 2.3 illustrates their optimized configurations. Large dihedral angles of 81.3°, 84.8°, and 82.0° were displayed by the molecules between the donor and acceptor moieties for 1, 2, and 3, respectively. The values of the dihedral angles come close to matching the X-ray data that was obtained through the experimentation. Both 9,9-dimethyl-9-10-dihydroacridine and phenothiazine exhibited a saddle structure with the carbon and sulfur bending away from the planar structure at angles of 29.5° and 30.3°, respectively, whereas phenoxazine is relatively flat in comparison. This is

supported by the X-ray data with the exception of phenoxazine, which has a slightly saddled structure (15°), as opposed to being flat. As it can be seen in Fig. 2.3, the HOMOs are distributed in an equal manner across the two units of donors, while the LUMO is primarily located on the acceptor ($2CF_3Ph$). There is a slight overlap of electron clouds between the HOMOs and the LUMOs, which is essential for increasing the oscillatory strength of the emitters. The antinodes of the LUMO level are the nodes that are located at the acceptor on the HOMO level. The LUMO extends the electron clouds into the trifluoromethyl groups. A closer inspection reveals that the sigma-bond of C-F is hyperconjugated with the π bonds of the benzene rings. At the same time, the lone pairs of fluorine atoms interact with the hyperconjugated carbon, which results in resonance/electron delocalization that stretches from the benzene π-electrons to the fluorine lone pair of electrons[87,88].

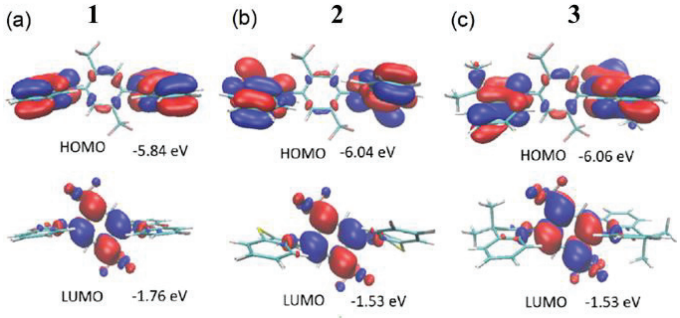

Fig. 2.3. HOMO and LUMO along with their energy levels of 1 (a), 2 (b), 3 (c); there is no total separation of HOMO and LUMO electron clouds

It has been discovered that the HOMO energies of 1, 2, and 3 were 5.84 eV, -6.04 eV, and -6.06 eV, while the LUMO energies were -1.76 eV, -1.53 eV, and -1.53 eV, respectively. Due to the fact that the oxygen atom in phenoxazine (PO) amplifies the pull-push electron effect of 1, the HOMO and LUMO levels of compound 1 are deeper than those of any of the other compounds that were investigated. Using the oxidation onset (E_{onset}) in cyclic voltammetry (CV) curves in relation to the Ag/Ag^+ reference electrode, the ionization potentials (IP) were calculated and determined. The IP values for 1, 2, and 3 were determined to be 5.31 eV, -5.38 eV, and 5.36 eV, respectively. By using photoelectron spectroscopy, it was possible to determine that the IP values of the films 1, 2, and 3 were 6.01, 6.05, and 6.08 eV. Considering the charge transport in the solid state, the ionization potentials estimated by the photoelectron spectroscopy have to be used.

As it can be seen in Fig. 2.4, the photophysical properties of the compounds were investigated by measuring the UV-vis absorption and photoluminescence (PL) spectra of their toluene solutions at room temperature. Absorption peaks with a high energy that are observed below 350 nm can be attributed to the n–π*/π–π* transitions that are coming from the donors. The absorption ranging from 350 nm to 500 nm, which can be referred to as CT absorption peaks, can occur between the donor units and the acceptor units. Natural transition orbital analysis based on time-dependent

density functional theory for ^{1}CT and ^{3}CT states reveals that the HOMO and LUMO transition strongly dominates the lowest transition with a contribution of more than 0.98 for each of the three molecules. All of the transition energies, along with the respective oscillatory strengths that are calculated by TD-TDF, are shifted by 0.6 eV that they would align with the peak of absorption.

The charge transfer transitions from HOMO to LUMO at 2.8 eV, from HOMO-1 to LUMO at 3.0 eV, from HOMO to LUMO+1 at 3.5 eV, and from HOMO-1 to LUMO+1 at 3.6 eV dominate the absorption that occurs between 2.6 and 3.8 eV for compound 1, as shown in Fig. 2.4 b. When calculating the simulated absorption curve, each oscillatory transition is given a Gaussian line shape that has a standard deviation of 0.1 eV. As only the four transition states with the lowest energy are taken into account, the higher energy is significantly deviated. Quantum molecular dynamics simulations have shown that the reason why the CT absorption curve of 2 is different from those of 3 and 1 is because there is a larger energy separation among the 4 lowest CT transitions.

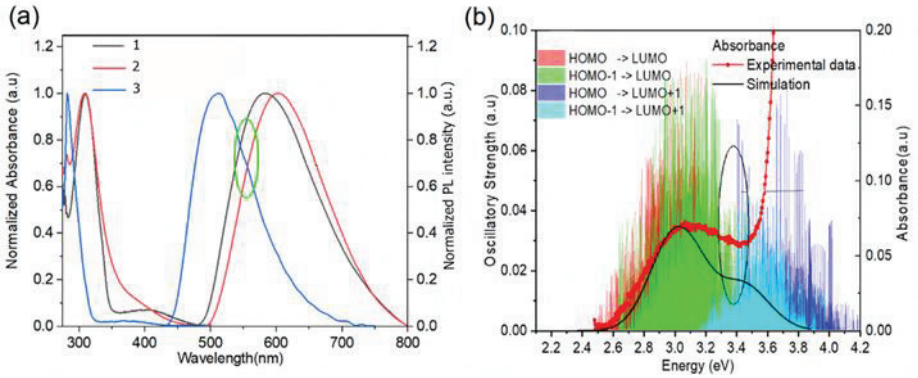

Fig. 2.4. (a) UV−VIS absorption and photoluminescence spectra of solutions of the compounds in toluene and (b) the quantum molecular dynamics simulations of vertical excitation of the 4 lowest excited states for 1 along with their oscillatory strengths and simulated absorption curve by applying Gaussian broadening

Fig. 2.5 displays the PL spectra of the molecular dispersions of the compounds in Zeonex (concentration of 1%) recorded at different temperatures. It was not possible to estimate the ^{3}CT energy by using the optical spectroscopy measurements when the phosphorescence spectra were differentiated from the fluorescence spectra by applying a delay time of 1, 5, or 9 ms at 77 K. The onsets of the phosphorescence spectra that were recorded at 77 K and at the various gate delays of the molecular dispersions of 1, 2, and 3 in Zeonex and MeTHF are related to the triplet LE states that they have in nature. These triplet LE states can be attributed to the triplet LE states (^{3}LE$_{D}$) of the corresponding donor moieties (10-phenyl-10H-phenoxazine (PO–Ph), 10-phenyl-10H- phenothiazine (PS–Ph), or 9,9-dimethyl-10-pheny-9,10-dihydroacridine (AC–Ph)) due to the similarities of the onsets of phosphorescence spectra of 1, 2, and 3 and PO–Ph, PS–Ph, and AC–Ph. The onset of phosphorescence

of the acceptor moiety is observed at a higher energy (^3LE_A = 3.65 eV) than that of the donor units PO–Ph, PS–Ph, and AC–Ph. As a result, the first singlet energy of 1, 2, and 3 was only estimated based on the onset of the PL spectra that were recorded at 300 K. Most of the emission was fluorescence (Fig. 2.5). The PL spectrum that was recorded at room temperature expressed a redshift in comparison to the PL spectrum that was recorded at 77 K with increasing emission intensity at lower energy levels, except for 3. This observation can be explained by the decreased conformational heterogeneity that was found[89,90]. The ^{1}CT energy was only taken as it is shown in Fig. 2.7. It was hypothesized that the energy gaps between the ^{3}CT and the ^{1}CT would be of 0.04 eV, 0.03 eV, and 0.04 eV in the case of 1, 2, and 3, respectively. The compounds showed the values of ΔE_{ST} that were relatively close to one another. Since TADF is a dynamical process, it is necessary to take into consideration both spin–orbit couplings and vibronic couplings at the same time. Since the spin–orbit coupling matrix elements of all organic TADF molecules are incredibly small, the vibronic coupling that exists between the low-lying electronic states is extremely significant.

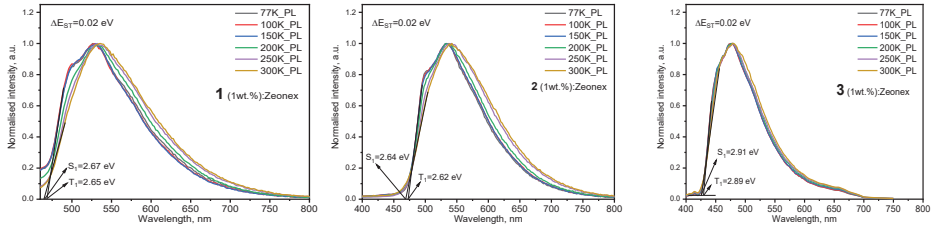

a) b) c)

Fig. 2.5. The low-temperature and room-temperature PL spectra of the molecular dispersions of compounds 1 (a), 2 (b), and 3 (c) in Zeonex and the corresponding onsets of emission at 300 K

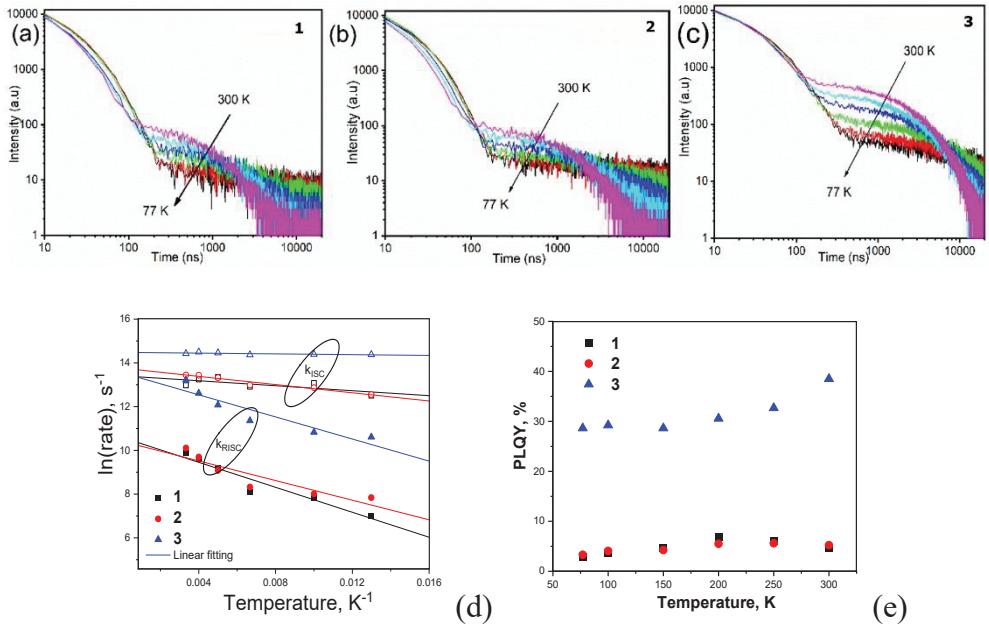

Fig. 2.6. Fluorescence decay curves of the molecular dispersions of 1 (a), 2 (b), and 3 (c) doped 1 wt.% in Zeonex as a function of temperature as well as their k_{ISC}/k_{RISC} (d) and PLQY (e) temperature dependences

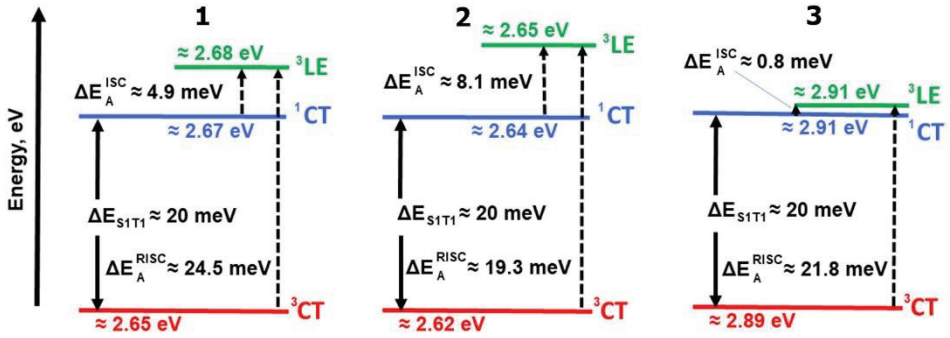

Fig. 2.7. Energy levels of compounds 1 (a), 2 (b), and 3 (c)

The PL decay curves of the molecular dispersions of the compounds in Zeonex were recorded at a variety of temperatures (Fig. 2.6 a–c). The standard TADF decay curves were observed. They demonstrated prompt fluorescence decay (PF) component in the nanosecond range as well as delayed fluorescence (DF) component in the microsecond range. The fact that the DF was observed for all three compounds in response to a decrease in temperature is the evidence that the DF had been thermally activated (Fig. 2.7), PF and DF were found to have lifetimes of 21.5 ns and 18.2 ns, 35.4 ns and 0.93 ms, and 1.41 ms and 2.56 ms for 1, 2, and 3 (Table 2.2).

It is possible to estimate that the rate constants of reverse intersystem crossing (k_{RISC}) are of ca. 1.92 x 104 s^{-1}, 2.46 x 104 s^{-1}, and 5.45 x 105 s^{-1} for compounds 1, 2, and 3, respectively[89].

The smaller gap of $E_{3CT–3LE}$ of compound 3 appears to cause significantly higher k_{RISC} values of 3 when compared to those of 1 and 2. In order to provide evidence in support of this hypothesis, the rates of intersystem crossing (k_{ISC}) and k_{RISC} were calculated at a range of temperatures with the lifetimes of PF and DF derived from a single exponential fit to TADF decays. Fig. 2.6 d shows a plot that illustrates how the rate constants k_{ISC} and k_{RISC} change as a function of temperature. The activation energies of ISC and RISC activation energies (E_A^{ISC} and E_A^{RISC}) were calculated by linearly fitting the plots, which led to the results given in Table 2.2. Arrhenius's dependence was taken into account when performing the fitting:

$$k = A \times exp\left(\frac{-E_a}{k_B t}\right); \quad (1)$$

where E_a is the activation energy, k_B is the Boltzmann constant, and A is the frequency factor that involves the spin–orbit coupling constant[90]. It has been found that 1, 2, and 3 each have their own unique activation energies for intersystem crossing E_A^{ISC} and reverse intersystem crossing E_A^{RISC}. These activation energies were utilized in the construction of the energy diagram that is displayed in Fig. 2.7 in accordance with what was initially proposed (Table 2.2)[91]. Due to the fact that it had the lowest $E_{3LE–3CT}$, 3 was able to produce the best mixing between ^{3}LE and the excited state wave function of ^{3}CT. This finding is in agreement with the highest k_{RISC} value of 5.45 x 105 s^{-1} and the k_{RISC}/k_{ISC} ratio of 0.296, which indicates that the TADF of 3 is the most effective (Table 2.2). It was impossible to determine the ^{3}CT energy state using optical spectroscopy (Fig. 2.5). Despite this, it is possible to calculate the energies of triplet CT states by using the activation energies for the RISC and ISC processes (Fig. 2.7). As a result, the ^{1}CT–^{3}CT energy gaps of 20 meV for 1, of 11 meV for 2, and 21 meV for 3 were obtained (Fig. 2.7, Table 2.2). The trend of the ΔE_{ST} values of 1, 2, and 3 did not agree with the trend of their TADF efficiency. The trend of the TADF efficiency was the same as that of their $E_{3LE–1CT}$ values (Fig. 2.7).

Table 2.2. Photophysical parameters of 1wt.% molecular dispersions of compounds 1, 2, and 3 in Zeonex

Compound	**1**	**2**	**3**
λ_{PL}^{ICT}, nm	535	537	477
PLQY, %	4.6	5.2	38.5
ΔE_{ST}, eV	0.19	0.02	0.02
τ_{PF}, ns (ratio, %)	21.5 (72.3%)	18.2 (28.2%)	35.4 (21.6%)
τ_{DF}, μs (%)	0.93 (27.7%)	1.41 (71.8%)	2.56 (78.4%)
k_{ISC}, s^{-1}	4.33×10^5	6.91×10^5	1.84×10^6
k_{RISC}, s^{-1}	1.92×10^4	2.46×10^4	5.45×10^5
k_{RISC}/k_{ISC}	0.044	0.036	0.296
ΔE_A^{ISC}, meV	4.9	8.1	0.8
ΔE_A^{RISC}, meV	24.5	19.3	21.8
k_{nr}^T	4.78×10^4	3.53×10^4	9.25×10^4
k_{RISC}/k_{nr}^T	0.4	0.7	5.9

The relatively high $E_{3LE–3CT}$ was apparently responsible for the fact that the PLQYs of 1 and 2 reached their maximums at around 200 K (Fig. 2.6 e). The PLQY values decrease as the temperature continues to rise, most likely as a result of an increase in the non-radiative rates of the triplet states (k^T_{nr}). In contrast, the PLQYs of 3 increased by up to 38.5% with the increase of temperature from 77 to 300 K because of the efficient TADF process. The ratio of k_{RISC}/k^T_{nr} for 3 was 5.9, which was the highest observed value. In order to have efficient TADF emitters, this k_{RISC}/k^T_{nr} ratio needs to be higher than unity (as in the case of 3)[92,93].

It is important to point out that the ^{3}LE values of PO–Ph, PS–Ph, and AC–Ph were respectively measured to be 2.83 eV, 2.65 eV, and 3.22 eV through the experimental research. In the cases of 1 and 2, the triplet LE states of PO–Ph and PS–Ph that were calculated using the activation energies for the ISC process that were in relatively good agreement with the experimental ones. An estimated value of 3.19 eV was found for the ^3LE_D of the compound 3. It is a significantly greater than the one that was calculated (2.911 eV). It is possible that this is due to the fact that other donating fragments ought to be used for the experimental determination of ^{3}LE values, as was discussed elsewhere[94]. However, following a more in-depth investigation into the phosphorescence spectra of both 3 and AC–Ph, the presence of two bands was established. According to the PL decay measurements, high (3.19 eV) and low (ca. 2.92 eV) bands can be attributed to phosphorescence rather than delay fluorescence. The phosphorescence was recorded with a delay of 9 ms, while the delay fluorescence was recorded over a time range of up to ca. 0.5 ms. This observation demonstrates that the compound 3 is distinguished by two different ^3LE_D states, which appear to

have the same ππ* and nπ* character that was reported for 10-phenyl-10H, 100H-spiro[acridine9,90-anthracen]-100-one[95,96]. It was possible to obtain a ππ* ^3LE_D value of approximately 3.19 eV and a nπ* ^3LE_D value of approximately 2.92 eV for 3. The triplet LE value and the value of nπ* ^3LE_D are in excellent accord (Fig. 2.7). The energy diagram shown in Fig. 2.7 can appropriately explain the most efficient TADF properties of compound 3.

The PL spectra of the films with various concentrations of 3 were discovered to have similar shapes and wavelengths of maxima. The EL spectra of devices based on 3 are in good agreement with this observation. The film made from the molecular mixture of 10 wt% emitter 3 and SimCP2 was chosen for the study of TADF characteristics. The molecular dispersion of 3 in SimCP2 had PL spectra and PL decays that were extremely similar to those of the molecular dispersion of 3 in Zeonex (Fig. 2.5, Fig. 2.6 c). The laser energy dependence of the delayed emission intensity was recorded for the emitting layer of the molecular dispersion of 3 (10 wt%) in SimCP2. Further evidence for the TADF origin of emission of 3 is provided by the slope of the plot of 0.95[97].

The combination of properties needed for the OLED applications was best demonstrated by the compound 3. It was chosen for the electroluminescence investigation as a TADF emitter. The structure of the device was ITO/MoO_3[0.5 nm]/NPB[40 nm]/TCTA[4 nm]/mCBP[4 nm]/light-emitting layer [24 nm]/ TSPO1[4 nm]/TPBi[40 nm]/LiF[0.5 nm] : Al[88 nm], in which the layers of 3 [5 wt%] : SimCP2, 3 [10 wt%] : SimCP2 and 3 [15 wt%] : SimCP2 were utilized as the corresponding light-emitting layers for devices A, B, and C. The reference device D contained the TADF emitter PFBP-2a with a fluorine-containing acceptor. Light-emitting layer of 20 wt% molecular dispersion of PFBP-2a in SimCP2 was prepared[98]. In order to achieve balanced hole-electron recombination and exciton formation within the light-emitting layers, the materials with typical roles, such as MoO_3 as hole-injecting, NPB and TCTA as hole-transporting, mCBP as electron/exciton-blocking, SimCP2 as the host, TSPO1 as hole/exciton-blocking, TPBi as electron-transporting, and LiF as electron-injecting material, were used (Fig. 2.8 a). When SimCP2 is doped with PFBP-2a or 3, the holes are transferred effortlessly while the emitters have no trouble capturing the electrons. The zone of recombination is located near the interface SMPCP2/TPSO1. The EL spectra (peaking at 485 nm and FWHM of 85 nm) of the devices A–C were very similar to the PL spectra of the corresponding light-emitting layers of 3 doped in SimCP2. They are peaking at 487 nm with a FWHM of 87 nm (Fig. 2.8 b). This discovery suggests that the emission of 3 caused the EL. Small differences between the PL and EL spectra are caused by the different optical and electrical excitation sources that were used. Due to the identical charge-injecting characteristics of 3 and PFBP-2a, turn-on voltages of approximately 4.4 V were obtained for devices A–D (Fig. 2.8 d). Higher operational current densities were reported for devices A–C than for device D at voltages greater than ca. 7V, presumably due to the superior charge-transporting characteristics of 3 in comparison to those of PFBP-2a.

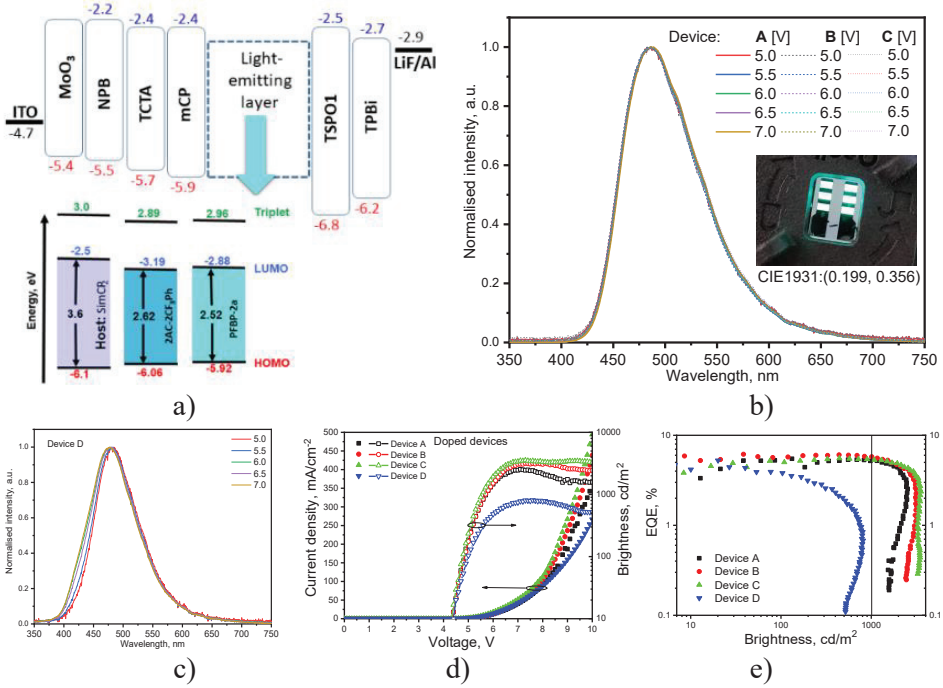

Fig. 2.8. Equilibrium energy diagram (a), EL spectra recorded at different voltages (b, c), current density and brightness as the function of the applied voltages (d) and EQE versus current density plots (e) for the devices A–D; the inset displays a picture of devices A at 6 V along with their CIE1931 color coordinates

At various voltages, the EL spectra of the devices A–C displayed nearly identical shapes and maxima wavelengths. Additionally, even though the emitter 3 was utilized at slightly varying concentrations, the EL spectra for the various devices A–C were identical. As shown in Fig. 2.2 e, this observation can be attributed to the creation of non-covalent intramolecular bonds by 3 in solid state. In contrast, the reference D–A electronic system (9,9-dimethyl-9-10-dihydroacridine-perfluorobiphenyl) demonstrated unstable EL spectra in device D at different external voltages (Fig. 2.8 c). This result effectively illustrates the benefits of the newly developed electron-accepting 1,4-bis(trifluoromethyl)benzene moiety.

In terms of its EL spectra as well as device efficiency roll-offs, the advantages of the device based on the compound containing 1,4-bis(trifluoromethyl)phenyl were noted (Fig. 2.8 e). EQE values at the practical brightness of 1,000 cd m^{-2} were comparable to the maximum EQE values of the devices A–C (Table 2.3). The EQE roll-off of device D was dramatic, and its maximum brightness even did not reach 1,000 cd m^{-2} (Fig. 2.8 d). Devices A–C showed the "stable" EQE at comparatively low operational current densities (lower than 40 mA cm^{-2}). Then, EQEs dramatically decreased. With higher operational current densities (higher than 40 mA cm^{-2}), the

bonds with the lowest cleavage energy may first be broken as a result of exciton-polaron annihilation processes according to the previous discussions[99,100].

Table 2.3. Electroluminescence parameters of host-free (A1–A6) and host containing (B1–B6) OLEDs

Device name	**EML**	λ_{EL}, nm	V_{ON}, V	L_{MAX}, cd/m^2	CE_{MAX}, cd/A	PE_{MAX}, lm/W	EQE_{MAX} /EQE_{1000}, %
Device Structure is ITO/MoO_3/NPB/TCTA/mCBP/light-emitting layer (EML)/TSPO1/TPBi/LiF:Al							
A	**3 [5 wt%]:SimCP2**	487	4.4	2,500	11.7	9.9	4.7/5.18
B	**3 [10 wt%]:SimCP2**	487	4.4	3,000	12.9	10.7	5.9/5.8
C	**3 [15 wt%]:SimCP2**	487	4.4	3,500	12.6	8.97	4.6/5.4
D	**PFBP-2a [20 wt%]:SimCP2**	478	4.4	800	6.2	5.6	4.4/-

λ_{EL} is EL maximum, V_{ON} is the turn-on voltage, L_{MAX} is the maximum brightness, CE_{MAX} is the maximum current efficiency, and PE_{MAX} is the maximum power efficiency. EQE_{MAX} and EQE_{1000} are EQEs at 10 and 1,000 cd/m^2, respectively.

2.2. Investigation of conformational disorder and rigid matrix effects: unveiling the mechanism behind the high oxygen sensitivity and room temperature phosphorescence (Scientific publication No. 2, Q1)

This chapter is based on the paper published in *Sensors and Actuators B: Chemical*, 2023, 380, 133295.

Three compounds were synthesized for optical oxygen sensors using 1,4-difluorobenzene as the acceptor and three different donor moieties (phenothiazine, phenoxazine, and acridine). 10,10'-(2,5-Difluoro-1,4-phenylene)bis(10 H-phenothiazine) (5) exhibits strong room-temperature phosphorescence when molecularly dispersed in rigid Zeonex matrix. Its oxygen detecting capacity is highly sensitive to low oxygen concentrations (<0.1%). Scheme 2.2 illustrates the synthesis of 2,5-disubstituted-1,4-phenylene derivatives. Buchwald–Hartwig coupling reactions of 1,4-dibromo-2,5-difluorobenzene (acceptor) with different donors were carried out for the synthesis of the target compounds in the presence of $Pd_2(dba)_3$ as the metal catalyst and X-Phos as the ligand. Compounds 4, 5, and 6 were obtained with the yields of 68%, 40%, and 27%, respectively. By using ^{1}H, ^{13}C, and ^{19}F NMR spectroscopy and single crystal X-ray analysis, the structures of the produced compounds were determined. With a coupling constant of 7.96 Hz and integration values that corresponded to two protons, the ^{1}H-NMR spectra of compounds 4, 5, and 6 exhibit a triplet peak at 7.45 ppm, 7.53 ppm, and 7.48 ppm, respectively. The H of the benzene ring of the acceptor unit is represented by these peaks. Despite the fact that all three compounds should have thirty carbon atoms in the total, ^{13}C-NMR spectra for all three compounds only reveal nine peaks at the aromatic regions. This demonstrates the symmetry of the molecule. Only one signal, at ca. -119 ppm, is visible in ^{19}F-NMR spectra of all three compounds.

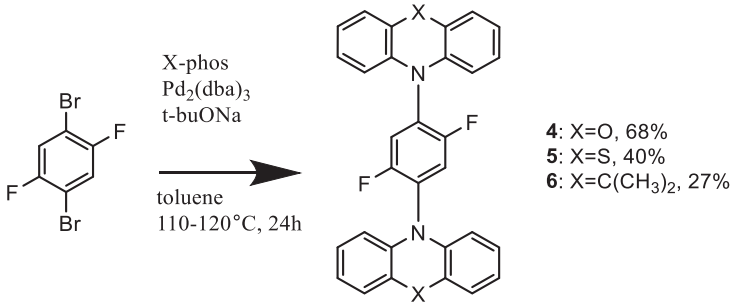

Scheme 2.2. Molecular structure and synthesis of 2,5-disubstituted-1,4-phenylene derivatives 4, 5, and 6

The compounds were examined using differential scanning calorimetry (DSC) and thermogravimetric analysis (TGA). The compounds displayed high temperatures of 5% weight loss. They were between 302 and 333 °C. According to the single-stage entire weight loss of the compound samples, as shown by their TG curves, the temperatures of 5% weight loss are consistent with the beginnings of sublimation but not the thermal degradation Fig. 2.9 a. The study of the DSC curves reveals that the

compounds have a high tendency to crystallize. Molecular glasses are not formed by them (Fig. 2.9 c, d, e).

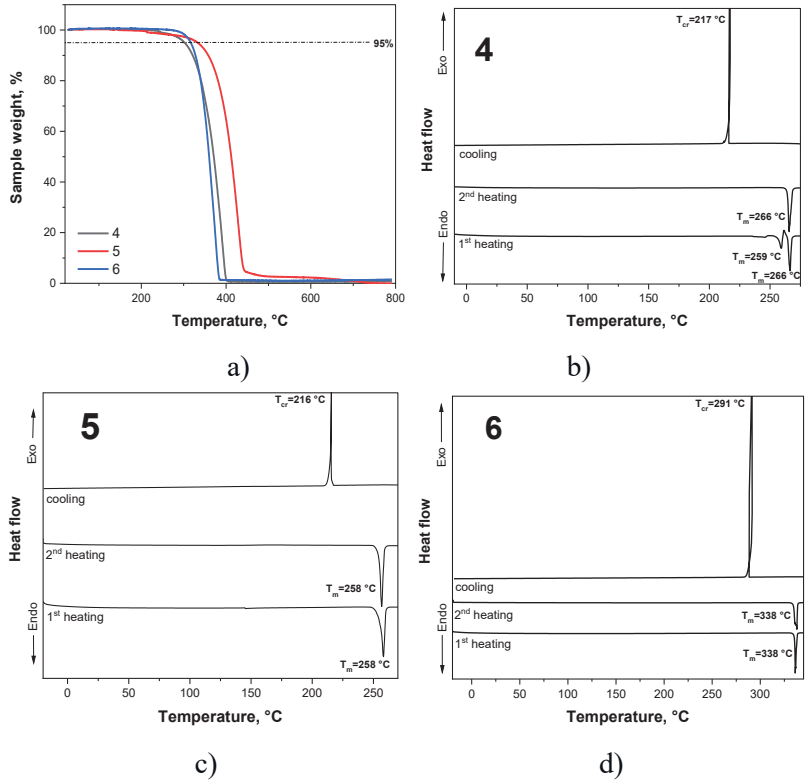

Fig. 2.9. (a) TGA curves of compounds 4, 5, and 6 and DSC curves of 4 (b), 5 (c), and 6 (d)

The electrochemical behavior of D–A–D derivatives of 2,5-didifluoro-1,4-phenylene was investigated in the electrochemical window established for the setup of dichloromethane (DCM) and tetrabutylammonium hexafluorophosphate (TBAHFP). The oxidation onset potential follows the expected donor strength with the lowest observed for the phenoxazine-based compound 4. Furthermore, 4 and 5 showed reversible oxidation, whereas the dimethylacridan substituted compound 6 showed a potential for electropolymerization, as the intensity of voltammograms increased with each subsequent scan. The behavior of polymerized product on the working electrode was investigated by immersing the latter into the DCM electrolyte solution. The oxidation of polymer product was found to be reversible after multiple scans (Fig. 2.10 d) and with the onset potential value lower than that of the monomer indicating a formation of larger conjugated π-electron system.

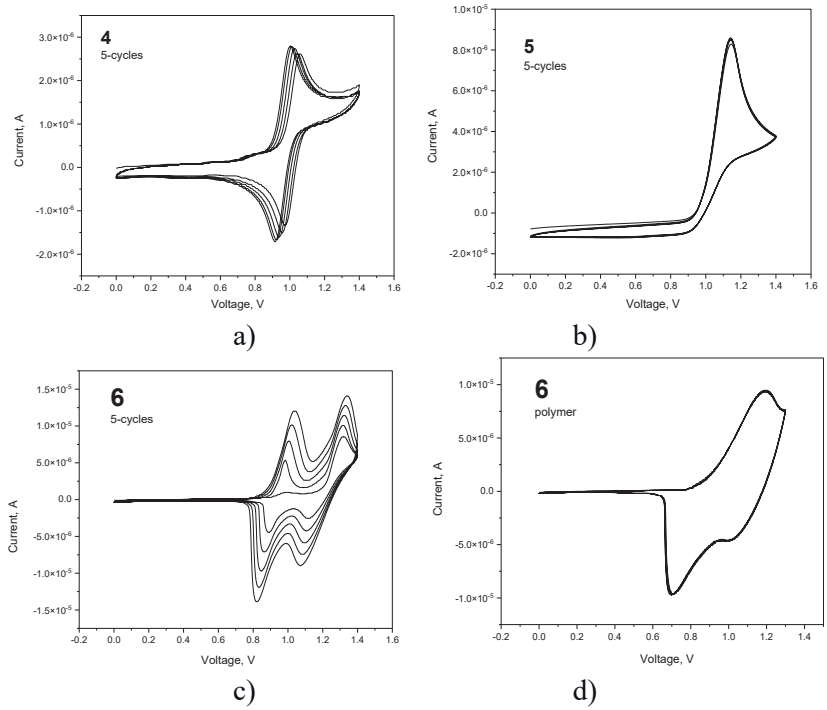

Fig. 2.10. Cyclic voltammograms of 4 (a), 5 (b), 6 (c) and (d) polymerized product of 6

Slow evaporation was used to grow crystals in solvent mixtures as single crystals for XRD examination. Fig. 2.11 displays the projections of 4, 5, and 6 from the Oak Ridge Thermal Ellipsoid Plot (ORTEP). The Van der Waals intermolecular interactions between the neighboring molecules were confirmed by the crystal structures. The small contact distances range from 2.54 to 3.40 Å. All molecules possess weak bonding between the electron-accepting fluorine atoms and hydrogen or carbon atoms shared by the electron-donating moiety: (4) F1···H-C3, (5) F1···H-C8, (6) F1···C5 (Fig. 2.11). The example of 5 as well revealed similar intermolecular interactions between the donor and acceptor moieties (S1···H-C15). Every neighboring molecule in every crystal unit cell is linked by several brief interactions made between the hydrogen and carbon atoms from the acceptors: (4) C4···H-C10, C3···H-C10; (5) C7···H-C3, C6···C9; (6) C3-H···H-C9. As previously reported, the phenothiazine and acridine moieties of 5 and 6 displayed a folded configuration with an angle of 25–28° to the central axis[101]. The phenoxazine moiety 4 was almost planar (~2°). The angles between the two intersecting planes drawn between the acceptor and the donors for 4, 5, and 6 were 68.76°, 83.36°, and 87.08°, respectively. The nitrogen lone-pair electrons of the donor moieties align favorably with the acceptor π-conjugation.

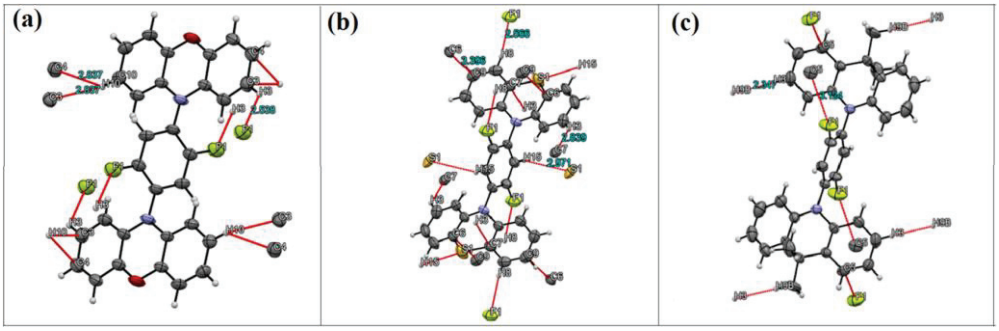

Fig. 2.11. ORTEP structures of 4 (a), 5 (b), and 6 (c); weak forces between the molecules are displayed in red

Fig. 2.12 (a–c) shows the normalized absorption and emission spectra of the solutions of 4, 5, and 6 in three different solvents (toluene, tetrahydrofuran, and acetonitrile). Phenoxazine/phenothiazine and acridine moieties are responsible for the optical transitions at 310 nm and 280 nm, respectively. The onset red-shifted from 3.15 eV to 3.05 eV was observed after the change of the solvent from toluene to acetonitrile in the absorption spectra of 4. Similar to this, the absorption spectra for 6 showed a bathochromic shift for toluene and acetonitrile from 3.40 eV to 3.30 eV. However, in contrast to its PL, the solutions of 5 barely showed any bathochromic shift in absorption after the increase of polarity of the solvent. A distinct redshift with rising solvent polarity was visible in the PL spectra of the three compounds (Fig. 2.12 a–d). The PL spectra revealed the CT characteristics. The energy of singlet charge-transfer state (^{1}CT) for compounds 4, 5, and 6 was found to be 3.05 eV, 3.00 eV, and 3.37 eV, respectively. The solutions of 4 showed the largest shift in emission-onset energy after replacement of toluene with acentronitrile (0.28 eV), followed by the solutions of 5 (0.13 eV) and 6 (0.06 eV). The large red-shift of 4 suggests that its CT state is stabilized with the increase of polarity[102].

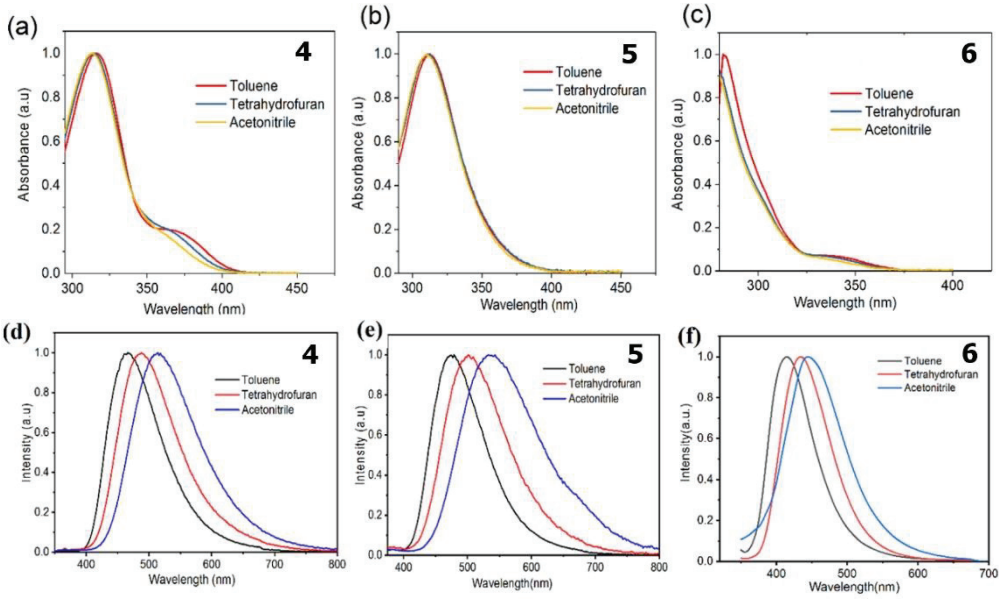

Fig. 2.12. UV absorbance spectra of solutions of 4 (a), 5 (b), 6 (c) and photoluminescence spectra of 4 (d), 5 (e), 6 (f) in toluene, tetrahydrofuran, and acetonitrile

The rise in PL intensity of the solutions in argon-aerated solvents indicates that triplet harvesting was a contributing factor[103]. Deoxygenated and air-equilibrated toluene solutions of 4, 5, and 6 were found to have integrated emission intensity ratios of 1.80, 1.20, and 3.97, respectively. The 1% solid solutions of 4 (Fig. 2.13 a) in Zeonex showed increased PL intensity in vacuum while that of 5 exhibited dual emission (Fig. 2.13 b). After doping in Zeonex, the emission band of the sample of 6 displayed a slight vibronic structure (Fig. 2.13 c), and its PL intensity increased when exposed to intense UV light during excitation.

Time-resolved PL measurements at two distinct wavelengths (400 nm and 504 nm) were carried out to investigate the causes of the dual emission. The PL spectra of 5 molecularly distributed in Zeonex without and with a 9 ms gate delay are shown in Fig. 2.13 d. After applying the gate delay, the emission in the 400–450 nm range disappeared. When measured in air (2.40 ns) and vacuum (2.37 ns), the prompt fluorescence lifetimes were found to be close (Fig. 2.13 e). According to Fig. 2.13 f, the emission at 505 nm had longer radiative decay time of 19.3 ms. This finding supports the existence of phosphorescence at room temperature. The lowest triplet levels for 4, 5, and 6 were determined from the onsets of the corresponding phosphorescence spectra. They were found to be 2.9, 2.7, and 3.28 eV, respectively. The energies of the lowest singlet states of the solutions of 4, 5, and 6 solutions in THF were found to be 2.97, 2.87, and 3.29 eV, respectively (Fig. 2.12 d, e, f). The values of ΔE_{ST} for the solutions of 4, 5, and 6 in 2-methyltetrahydrofuran (me-THF) were found to be 0.07, 0.17, and 0.01 eV, respectively. The close orthogonality of the D and A units (the intersection angle is 83.36°) for 5 did not lead to the small ΔE_{ST}.

The increased PL intensity of the argon-purged solution of deep blue emitting 6 revealed a very small ΔE_{ST} and high triplet harvesting efficiency. Due to the very high triplet energy of 6 (3.28 eV), the presence of ^{1}CT suggests that the presence of a substantial reservoir of long-lived, highly energetic triplet excitons that interact with polarons may cause degradation[104,105].

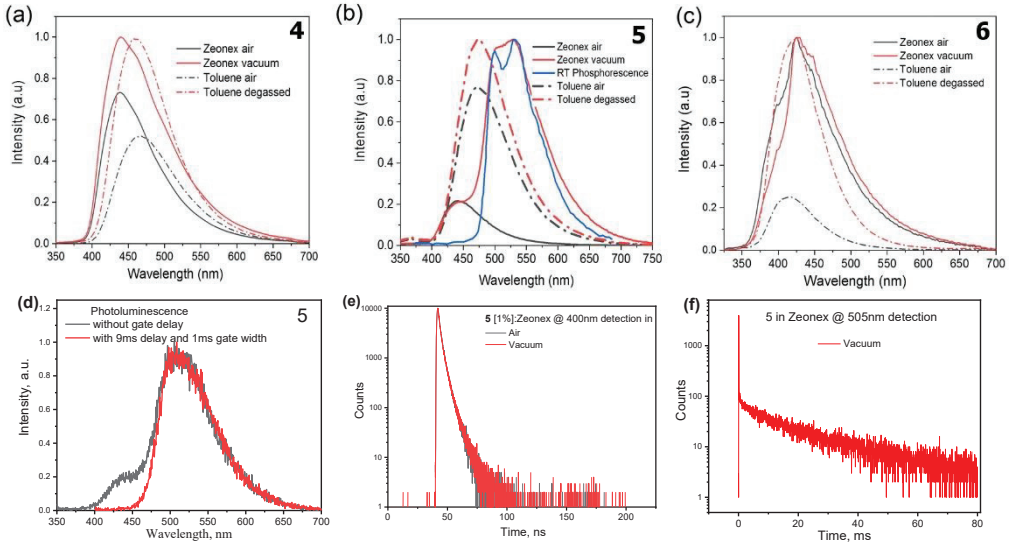

Fig. 2.13. PL spectra of argon-saturated toluene solutions and evacuated and air equilibrated solid solutions in Zeonex of 4 (a), 5 (b) and 6 (c), (d) PL spectra of compound 5 molecularly dispersed in Zeonex without and with gate delay, PL decay curves of 5 doped in Zeonex recorded at 400 nm in air (e) and vacuum (f) recorded at 505 nm

The films of 5 and its solid solution in Zeonex were found to have the lowest photoluminescence quantum yields (PLQY) in the air (Table 2.4). The effective singlet-triplet intersystem crossing (ISC), required for efficient RTP[106], can be partially responsible for the low PLQY values of 5. A relatively high PLQY of RTP was observed for the film of 5 doped in Zeonex (Table 2.4). After deoxygenation, the 6 solution demonstrated 30% increase in the emission lifetime. This finding is compelling evidence of delayed fluorescence. The increase in emission lifetime upon deoxygenation was significantly less for the solution (15%) of 5. When oxygen was removed, the solution of 4 showed a 21% increase in the emission lifetime. The relationship between these values and the ΔE_{ST} values of the compounds is inverse.

Table 2.4. Phophysical parameters of the derivatives

Compounds	**4**	**5**	**6**
	neat/guest-Zeonex films		
$PLQY^{air}$, %	14/5	2/2	10/7
$PLQY^{vacuum}$, %	-/9	-/12.8	-/27.8
* $PLQY^{RTP}$	-	-/10.8	-
$\tau^{fluorescence}$(air/argon), ns	4.70/5.71	3.33/3.83	5.44/7.05
τ^{RTP}, ms	_	-/19.3	_

* Calculated by $PLQY^{RTP}=PLQY^{vac}-PLQY^{air}$, where $PLQY^{vac}=PLQY^{air}\times Area^{vac}/Area^{air}$ as introduced elsewhere[107].

In order to explore the molecular structures, the density functional theory (DFT) computations were made. Fig. 2.14 displays their optimized structures. Large dihedral angles of 79.8°, 99.3°, and 92.6° between the donor and acceptor moieties were present in the molecules of 4, 5, and 6, respectively. They were approximately 10° larger than the results from the single-crystal X-ray measurement. The HOMO to LUMO transition, which had coefficients higher than 0.98, had a considerable dominance over the natural transition orbitals for S_1.

According to the theoretical calculations, the HOMO and LUMO energy levels of a single molecule are 5.97 eV, 6.15 eV, 6.07 eV, 0.65 eV, 0.66 eV, and 0.59 eV for 4, 5, and 6, respectively. The ionization potentials determined from the CV study are 5.50 eV, 5.80 eV, and 5.81 eV (Fig. 2.10). These findings suggest that phenoxazine has a stronger donating strength than phenothiazine and acridine.

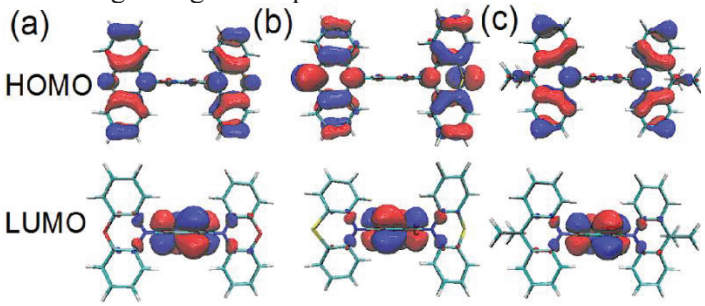

Fig. 2.14. The frontier orbitals of 4 (a), 5 (b), and 6 (c)

The T_1 frontier orbitals were investigated as well. Surprisingly, the natural transition orbitals for T_1 consisted of superposition of multiple CTs and locally excited (LEs) holeparticle excitations, while having well-separated frontier orbitals with the S_1 transition being dominated by the HOMO to LUMO transition (Fig. 2.14 a–c). By comparing the bathochromic shift of the lowest triplet state of 4 with the ^{3}LE of phenoxazine, it was possible to validate the lowest triplet state of 4's hybrid nature. When the solvent's dielectric constant increased, the ^{1}CT state of 4 displayed bathochromic shift, as is common for charge transfer molecules (Fig. 2.15 d). In a solvent with a low dielectric constant, the ^{3}HLCT of 4 increased only slightly (see Fig. 2.15 d, f). By raising the spin-orbit coupling while keeping the EST low, 3HLCT can enhance reverse intersystem crossing (RISC)[108]. For 4, 5, and 6, ΔE_{ST} is

determined to be 0.09 eV, 0.17 eV, and 0.05 eV, respectively. There are about equal amounts of ^{3}LE and ^{3}CT in 4 (Fig. 2.15 a), and ΔE_{ST} is close to 0.1 eV. ΔE_{ST} widens when the ^{3}HLCT becomes more local in excitation, as observed in the example of 5 (Fig. 2.15 b). In Fig. 2.15 c, 6 has the highest triplet harvesting rate and higher ^{3}CT energy for T_1. Between deoxygenated and air-equilibrated solutions, there was a 3.97 integrated emission intensity ratio. The reverse intersystem crossing would provide efficient triplet harvesting if ^{3}HLCT included a well-balanced ratio of ^{3}LE and ^{3}CT characters.

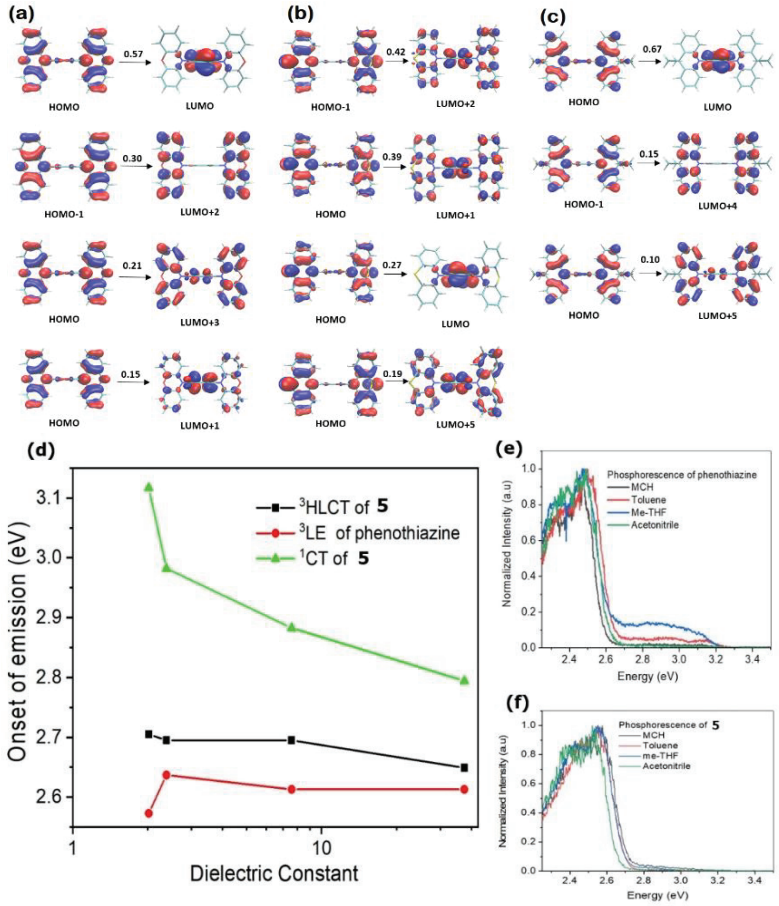

Fig. 2.15. The decomposition of the lowest triplet natural transition orbitals for 4 (a), 5 (b), and 6 (c); the number indicates the coefficient corresponding to the transition; (d) is the comparison of the onset of emission of 3HLCT of compound 5, ^{3}LE of phenothiazine, and 1CT of 5 of different dielectric constant; (e) Phosphorescence spectra (^{3}LE) of phenothiazine in different solvents at 77 K and (f) Phosphorescence spectra of compound 5 in different solvents

A molecular dynamics simulation was conducted for compound 5 doped in Zeonex, and the emitters extracted for time-dependent DFT/LC-PBEh/cc-pVDZ

calculations at optimal ɯ (Fig. 2.16 a) show the probability distribution of ΔE_{ST} with a mean of 0.31 eV, indicating that the conformational heterogeneity imposed by the rigid Zeonex can widen the mean ΔE_{ST}. The molecular structures of the molecules having the smallest and greatest ΔE_{ST} are presented in Fig. 2.16 b and c, respectively. ΔE_{ST} varies from the lowest value of 0.13 eV to the highest value of 0.59 eV. The dihedral angle between the donor and acceptor in Fig. 2.16 b deviated far from the orthogonality with a dihedral angle of 127°, resulting in a large ΔE_{ST} compared with the dihedral angle of 71° shown in Fig. 2.16 c. As it can be seen in Fig. 2.16 c, a constrained environment makes it difficult for the molecule to relax to its equilibrium position, making such a huge distortion possible. As a result, the local transition dominates T_1 for the molecule in Fig. 2.16 b. In contrast to the experimental value of 0.47 eV, the mean ΔE_{ST} in the simulation is 0.31 eV. The higher error is most likely the result of the simulation's usage of fewer Zeonex repeating units and a single ɯ value of 0.063 for the calculation of the excited states of various conformers.

It has been demonstrated that compound 5 doping of Zeonex increases the conformational heterogeneity. In the cases of 4 and 6, the same behavior should take place. It has been investigated how the dihedral angle between the donor and acceptor moieties relates to ΔE_{ST}. The major increase in ΔE_{ST} for 5 began at 70°, but the onsets for 4 and 6 were 40° and 50°, respectively. This difference indicates that these two molecules are less sensitive to the significant change in ΔE_{ST} imposed by the conformational disorder.

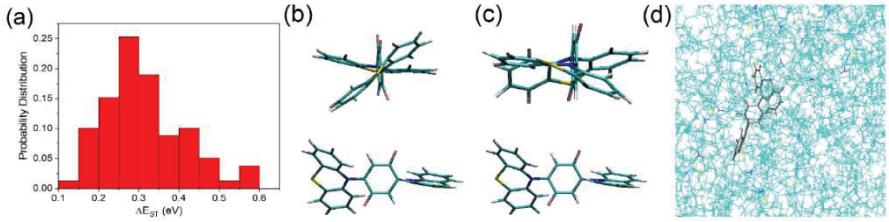

Fig. 2.16. The distribution of ΔE_{ST} of compound 5 in Zeonex (a), structure of 5 with ΔE_{ST} of 0.59 eV (b) and structure of 5 with ΔE_{ST} 0.13 eV (c) and (d) is the molecule in the Zeonex that is embedded in (b)

The time evolution of photoluminescent spectra was carried out as shown in Fig. 2.17 to further support the idea that Zeonex imposed increased heterogeneity of 5. The photoluminescence intensity logarithmic contour map as a function of logarithmic time after excitation and wavelength is shown in Fig. 2.17 a. It has been determined that RTP is responsible for the low-intensity emission at timescales greater than 100 ns. The selected spectra of the contour diagram are represented in Fig. 2.17 b. The ^{1}CT emission cannot be described as typical single Gaussian emission. Three peaks are seen at the wavelengths of 423 nm, 453 nm, and 513 nm. These peaks are apparently not the vibronic peaks from ^{1}LE. Such behavior was seen through space donor–acceptor charge transfer dimers in the solution[109].

During the measurement, the emission peak at 500 nm was batochromically shifted to 550 nm (Fig. 2.17 b). As supported by the simulation spectral shift from

500 nm to 550 nm is the result of heterogeneity leading to large lifetime dispersion of the CT emission. The higher-energy CT states decayed faster than the lower-energy species due to their increased ^{1}LE character, giving an apparent time-dependent spectral shift. Additionally supporting the existence of structural inhomogeneity in a disordered medium was the observation of 5 spectral shift over the time[110]. Since triplet emission is prohibited, the emission at 3.66 ns should correspond to the singlet states, including the emission at 500–550 nm. The emission spectrum at 892 ns looked as a representation of the probability distribution of triplet vertical excitation. As a result, the emission peak at about 525 nm in the steady state photoluminescence spectrum of 5 molecularly dispersed in Zeonex (Fig. 2.13 b) might be interpreted as a combination of fluorescence and phosphorescence spectra. Fig. 2.17 c shows the shift of the peak at around 525 nm. Before it reaches the energy level of equilibrium, the shift exponentially decays. The peak can be attributed to phosphorescence after around 100 ns. Not all TADF compounds containing phenothiazine displayed RTP[101], despite the fact that phenothiazine moieties are known to be phosphorescent at room temperature[111,112,113].

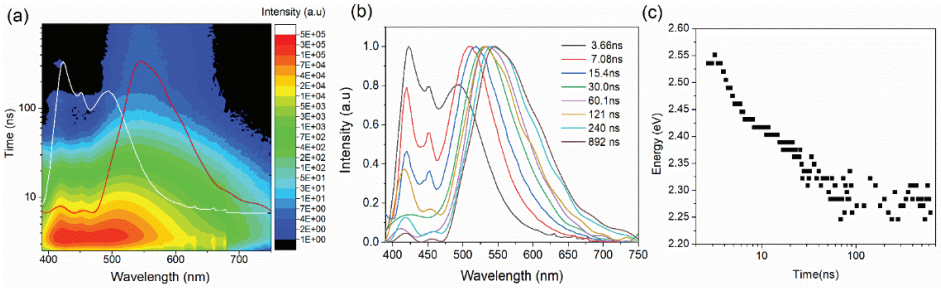

Fig. 2.17. The photoluminescence lifetime evolution of the molecular dispersion of compound 5 in Zeonex (a) two-dimensional intensity map with inserted spectra at 3.66 ns (white) and at 892 ns (red) after excitation, (b) the change of the normalized spectra at the different times, (c) the spectral diffusion of the second dominant peak observed at 500 nm

Phosphorescence quenching by oxygen has been studied since it is the primary emission at room temperature[114]. There was exposed a sample of the solid solution of 5 in Zeonex with the concentration of 1% as in a chamber to various ratios of the concentrations of oxygen and nitrogen to evaluate this effect. Two exact gas flowmeters were used to regulate the ratio of pure oxygen as a quencher and pure nitrogen gas, which served as an inert medium for the gas mixture. RTP intensity changed after every adjustment of the quencher concentration (Fig. 2.18 a). After each change in gas ratio, the sample was left in it for 3 minutes to ensure high accuracy and prevent any spectrum fluctuation caused by the outside influences. The chosen concentration of quencher's final spectrum was then produced by averaging three consecutive spectra during the data analysis.

According to Fig. 2.18 a, it is clear that the intensity of RTP significantly decreases as quencher concentration increases. Under nitrogen and oxygen atmospheres, the considerable difference in emission intensity at 500 nm was noticed.

The intensity of emission at 500 nm was 7.5 times greater under the inert atmosphere than it was in the atmosphere of oxygen.

PL spectra collected at various oxygen concentrations were integrated for the quantitative determination of the sensitivity of RTP of 5 to oxygen quenching. The resulting values of the area under the curves were used for the next analyses. There was applied a Stern–Volmer equation that is modified for these circumstances because the data that had been collected clearly showed a nonlinear relationship between the ratio of RTP intensity to the quencher concentration in ppm (Fig. 2.18 b). When the Stern–Volmer plot is downward curving, it is typically assumed that there are several chromophore species present with one species being available for the quencher and the others not. This combination is considered as multiple species with dynamic quenching[113] .

Equation (2) can be used to express the ratio between intensities observed in the presence and absence of a quencher.

$$\frac{A^0_{RTP}}{A_{RTP}} = \left[\sum_{i=1}^{n} \frac{f(i)}{\{1+K_{SV}(i)[Q]\}}\right]^{-1}; \quad (2)$$

where A^0_{RTP} is the area under the curve measured in the absence of a quencher and A_{RTP} is the area under a curve measured in the presence of a quencher, $K_{SV}(i)$ is the quencher rate coefficient and f(i) is the fractional contribution of the *i*th species of the fluorophore to the steady-state emission of the investigated compound.

The two-component model described in equation (3) provided the best match for the sample of 1% solid solution of compound 5 in Zeonex.

$$\frac{A^0_{RTP}}{A_{RTP}} = \frac{1}{\frac{f_1}{1+K_{SV1}} + \frac{f_2}{1+K_{SV}}} \quad (3)$$

Resulting fit values R^2 of 0.998 demonstrate that the first and dominant fluorophore species contribute to 65.5% of the total photoluminescence while the second species has a fractional contribution f_2 of 34.5%. The obtained values of K_{SV1} of 2.48×10^{-3} ppm^{-1} and of K_{SV2} of 6.23×10^{-6} ppm^{-1} demonstrate significant differences in emission sensitivity of the oxygen. The values of the quenching rate constants are strongly correlated with the Stern–Volmer plot, up to the oxygen concentration of around 2,000 ppm. Overall, these results suggest that the sample of 1% molecular dispersion of compound 5 in Zeonex shows high sensitivity to low concentrations of oxygen (up to 0.2%). At oxygen concentrations above 0.2%, the sensitivity began to decrease. The presence of two sensitivity regions can be attributed to the molecular heterogeneity giving rise to two dominant ^{3}LE states and the ^{3}CT states of 5.

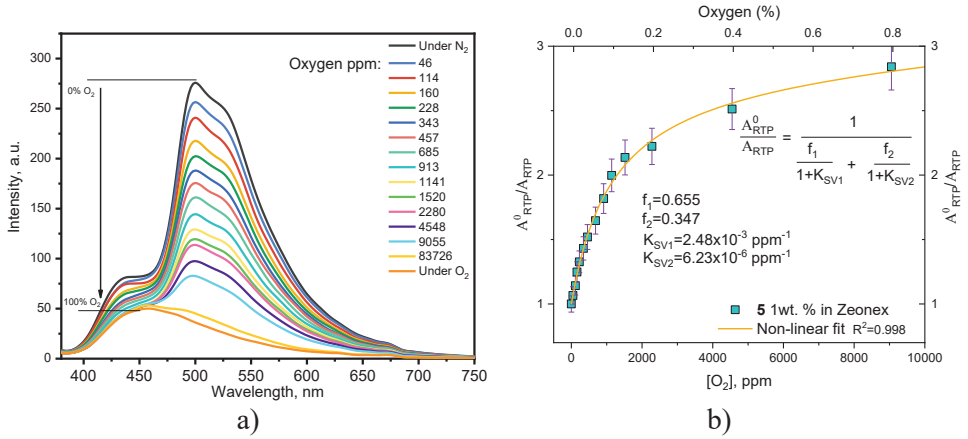

Fig. 2.18. (a) RTP spectra and (b) Stern–Volmer plots for 1% molecular dispersion of 5 in Zeonex recorded at different concentrations of oxygen

2.3. Pyridazine as an acceptor core: synthesis, characterization, and photophysical analysis of compounds containing 9,9-dimethyl-9,10-dihydroacridine and phenoxazine donor moieties (Scientific publication No. 3, Q1)

This chapter is based on the paper published in *Materials*, 2023, 16, 1294. By using the Buchwald–Hartwig cross-coupling reaction, two compounds with pyridazine as the acceptor core and 9,9-dimethyl-9,10-dihydroacridine or phenoxazine as donor moieties were obtained. Scheme 2.3 shows the synthesis of the 2,5-disubstituted-pyridazine derivatives. Compounds 7 and 8 were obtained with yields of 21.8% and 6.4%, respectively.

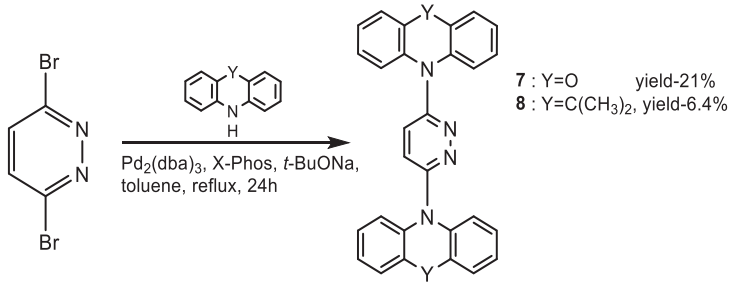

Scheme 2.3. Synthesis of 2,5-disubstituted-pyridazine derivatives

The morphological transitions and thermal stabilities of pyridazine-based compounds were investigated by using DSC and TGA. Table 2.5 summarizes their thermal characteristics. After synthesis and purification, the two target compounds were obtained as crystalline substances. The first heating scans of the DSC measurements showed endothermic melting signals (Fig. 2.19 a, b). The second heating scan of compound 7 revealed crystallization and subsequent melting signals. Glass transition was observed during the second heating scan of compound 8

suggesting that it might transform into the solid amorphous state (molecular glass). Complete weight loss of both compounds was observed during the TGA measurements, which indicates sublimation rather than thermal decomposition of the samples.

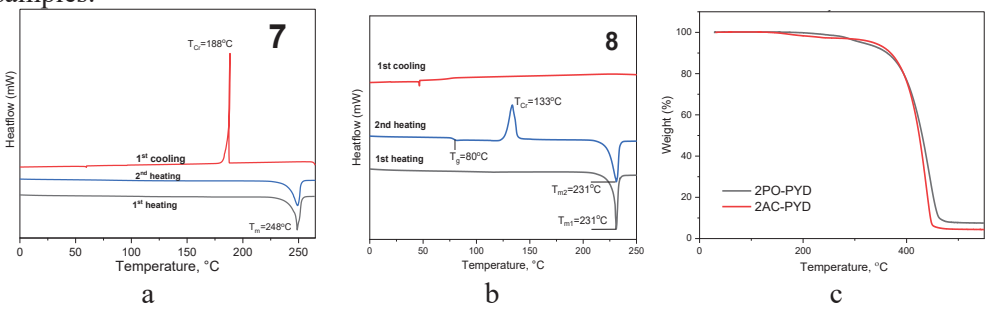

Fig. 2.19. DSC (a, b) and TGA (c) thermograms of compounds 7 and 8

Table 2.5. Thermal characteristics of the compounds

Compound	T_{ID}, °C [1]	T_g, °C	T_{cr}, °C [2]	T_m, °C [3]
7	314	-	188	248
8	336	80	133	231

[1]Temperature of 5% loss of mass determined by TGA, [2]crystallization temperatures determined by DSC, [3]melting points determined by DSC.

The target geometries and electronic structures of the molecules were investigated using DFT computations at the theoretical B3LYP/6-31++G level. In order to evaluate the electronic transitions, the geometries of the pyridazine derivatives 7 and 8 were studied (Fig. 2.20). The D and A fragments are practically perpendicularly oriented in the optimized ground state geometries because their dihedral angle values are close to 90°. Such large dihedral angle values are expected to lead to the minimal conjugation of the D–A fragments. Fig. 2.21 illustrates the calculated HOMOs and LUMOs. Both pyridazine-based compounds have similar electronic structures. According to the calculated HOMO levels, phenoxazine has a slightly better electron-donating ability than the 9,9-dimethyl-9,10-dihydroacridine moiety.

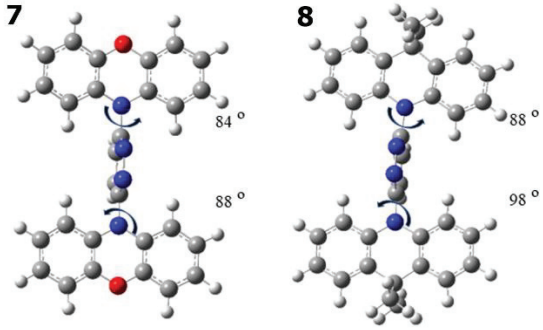

Fig. 2.20. Optimized ground state geometries in vacuum at the B3LYP/6-31++G level of theory of compounds 7 and 8 (gray color – carbon, blue – nitrogen, red – oxygen, white – hydrogen)

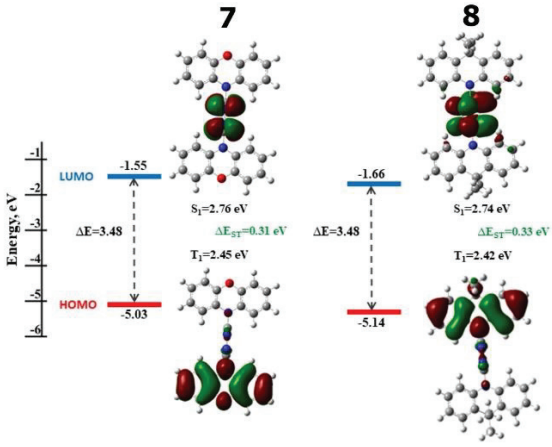

Fig. 2.21. DFT calculated HOMO, LUMO energies as well as HOMO and LUMO topologies (isovalue of 0.02) of compounds 7 and 8

The dihedral angles remain perpendicular in the optimized excited-state geometry. TD-DFT calculations predicted that the dominant S_1 transition is CT in nature (H→L). The calculated ΔE_{ST} values are of ca. 0.3 eV (Fig. 2.21). These pyridazine derivatives are potential TADF emitters due to their small energy gaps.

The electrochemical characteristics of the compounds 7 and 8 were investigated using cyclic voltammetry. The repeated scans of the compound 8 revealed reversible oxidation, whereas the scans of the compound 7 revealed quasi-reversible oxidation. Oxidation onset potentials against ferrocene (Eox onset vs. Fc) were used to determine the ionization potentials using cyclic voltammetry (IP_{CV}). The voltammograms are shown in Fig. 2.22. The strength of the donor moiety was shown to have a small impact on the IP_{CV} values. The phenoxazine containing compound (7) showed slightly higher IP_{CV} than the derivative of 9,9-dimethyl-9,10-dihydroacridine (8).

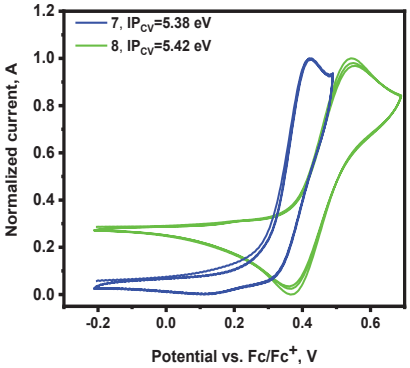

Fig. 2.22. Cyclic voltammograms of compounds 7 and 8

Table 2.6. Photophysical characteristics of 7 and 8

Compound	λ_a, nm[1]	λ_e, nm[2]	Φ[3]	E_{S1}, eV[4]	E_{T1}, eV[4]	ΔE_{ST}[4]
7	308/308	*ca.* 420, 618/398, 639/565	<0.01	2.68	2.59	0.09
8	*ca.* 280/290	353, 535/346, 561/517	<0.01	2.64	2.29	0.35

[1]Wavelengths of the bands of absorption spectra of the solutions of the compounds in toluene/THF, [2]wavelengths of the bands of emission spectra of the toluene/THF solutions and films, [3]PL quantum yield of deoxygenated toluene solutions, [4]derived from spectral data of the films of compounds recorded at 77 K in the absence of oxygen.

In Fig. 2.23 a, b, the absorption and emission spectra of the solutions 7 and 8 are shown. The spectral characteristics are collected in Table 2.6. The absorption spectra for the solutions of 7 and 8 are characterized by a strong bands at 308 nm and 288 nm, respectively. When the non-polar toluene solvent was replaced with the polar THF, the positions of the absorption peaks basically remained unchanged.

In the UV and green spectral regions, two distinct emission bands were visible in the PL spectra of the solutions that were recorded at various excitation wavelengths. The spectral data shown in Table 2.6 give the possibility to follow how the polarity of the medium affects the photophysical properties of the compounds. The locally excited (LE) state emission of the donor is linked with the PL band in the UV region, which ranges from 400 to 450 nm. It is not characterized by the positive solvatochromism caused by the increase in polarity of the solvent. With increasing solvent polarity, the low-energy emission band at about 500–625 nm showed a spectral redshift that indicated intramolecular charge transfer (ICT) state. Different excitation wavelengths barely change the spectral distribution. This finding completely complies with Dr. Michael Kasha's criterion[115] that forbids the possibility of certain optical centers being excited in a way that would impact the analysis of the experimental data. The wavelengths of the ICT peaks in the spectra of the neat films match the peak locations of the ICT band of the corresponding toluene solutions. This

observation shows that polarity, aggregation-related processes, and intermolecular interactions in the solid state have no impact on the ICT of the compounds. As expected, the emission of 9,9-dimethyl-9,10-dihydroacridin-based 8 is blue-shifted in comparison to that of 7 with a stronger donating unit of phenoxazine. The deoxygenated toluene solutions of 7 and 8 did not reach PL quantum yields Φ of 1%.

At the corresponding PL peak wavelengths, the PL decay curves of the deoxygenated toluene solutions of 7 and 8 were recorded (Fig. 2.23 c). The main information regarding PL decays is gathered in Table 2.7. The multiexponential fitting demonstrated a perfect correlation between the lifetime of the LE of 7 and the lifetime of the prompt fluorescent component of the PL decay curve measured at 621 nm. In addition, the ICT bands of the solutions of 7 and 8 exhibited emission lifetimes of 93 and 143 ns, respectively. Such lifetimes are related to what is known as the fast delayed emission or TADF[89].

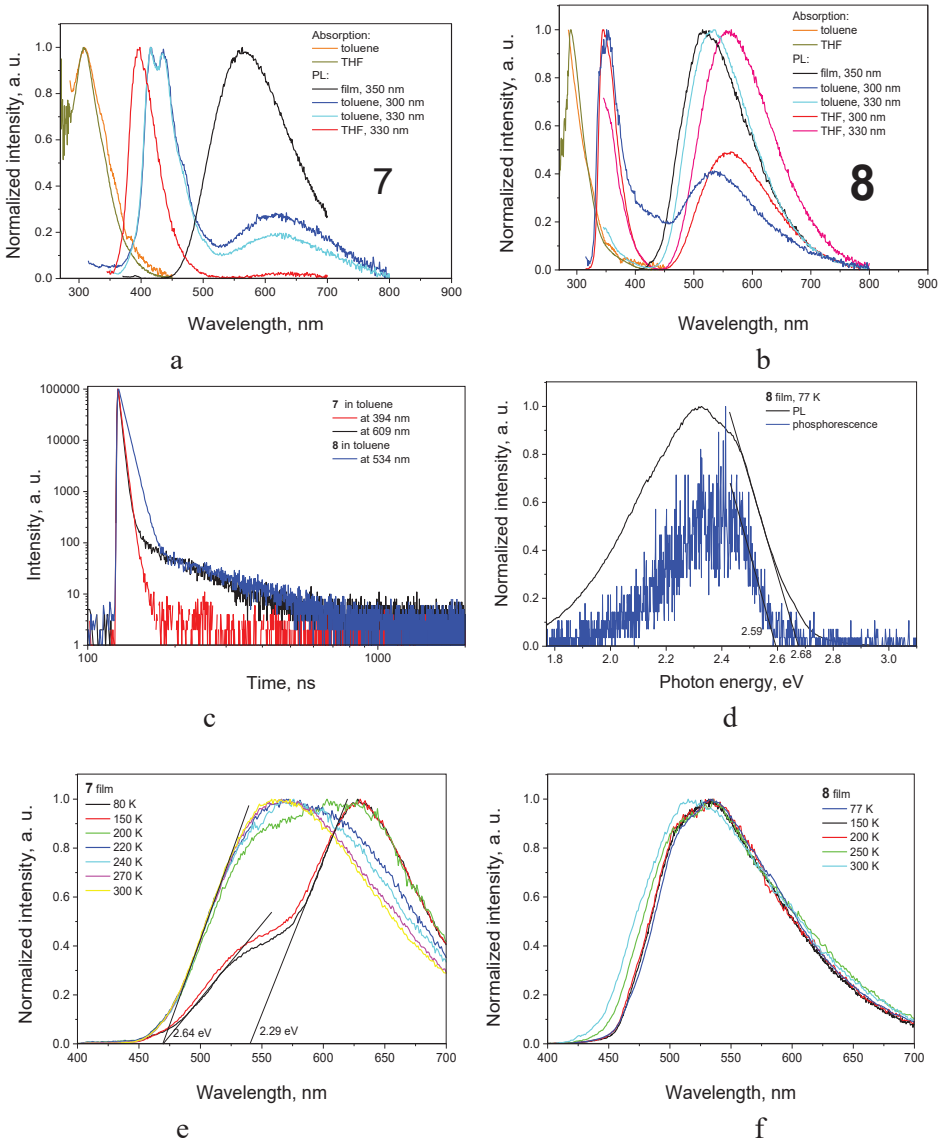

Fig. 2.23. UV and PL spectra of toluene, THF solutions and films of 7 (a) and 8 (b), PL decay curves of deoxygenated toluene solutions (c), PL and phosphorescence spectra of the film of 8 recorded at 77 K (d), PL spectra of the films of 7 (e) and 8 (f) recorded in an inert atmosphere at different temperatures

Table 2.7. Photophysical characteristics of the toluene solutions of 7 and 8

Toluene solution[1]	λ, nm[2]	Lifetime, ns[3]	k_{RISC}, s^{-1}	k_{ISC}, s^{-1}	χ^{2} [4]
7	394	2.85	-	-	1.043
7	609	2.49 (85.44%), 9.75 (6.49%), 92.86 (8.07%)	$9.5 \cdot 10^5$	$2.2 \cdot 10^8$	1.166
8	534	6 (95.52%), 142.96 (4.48%)	$3.3 \cdot 10^5$	$1.6 \cdot 10^8$	1.034

[1]Deoxygenated, [2]wavelength at which the measurement was performed, [3]intensity amplitude in parentheses, [4]weighted sum of fit points square deviations.

In order to unequivocally establish the absence of RTP, PL spectra of the films of 7 and 8 were obtained at various temperatures. The energy levels of the first excited singlet and triplet states were determined from the onsets of the corresponding prompt fluorescent and phosphorescent bands (Fig. 2.23 d, e). During heating, the phosphorescence component disappeared, leaving only the ICT band (Fig. 2.23 e, f). Even if it is expected based on the findings of the theoretical analysis, the TADF phenomenon is not supported by the measured ΔE_{ST} of 0.35 eV (Fig. 2.23 e) of 7 (Fig. 2.21). The RISC in this situation significantly depends on a spin-orbit coupling of energetically close ^{3}CT and ^{3}LE states. The possibility of spin being flipped in the organic material without insertion of heavy atoms into the structure is realized because k_{RISC} is deeply dependent on the triplet excitonic Bohr radius, which enhances k_{RISC} by several orders of magnitude more than the rate constant of ISC (k_{ISC}) (Table 2.7)[116]. Fig. 2.24 e shows that the energy level of ^{3}LE is estimated to be of ca. 2.64 eV, which facilitates TADF. This energy level is near to that of the ^{1}CT state[89,117]. The low PLQY makes it difficult to detect the ^{3}LE experimentally. As expected for 8[118], the first triplet excited state with the energy of 2.59 eV is close to that of ^{1}CT of 2.68 eV, which is beneficial for TADF. The values of k_{RISC} and k_{ISC} were evaluated from the fitting data of the PL decay curves using equations $k_{RISC} = \frac{(\Phi_{PF}+\Phi_{DF})\Phi_{RISC}}{\tau_{DF}\Phi_{PF}}$, $k_{ISC} = \frac{\Phi_{DF}}{\tau_{PF}(\Phi_{PF}+\Phi_{DF})}$, where Φ_{PF}, Φ_{DF}, and Φ_{RISC} are the quantum yields of prompt, delayed fluorescence, and RISC, respectively[119]. Using the formula $\Phi = \Phi_{PF} + \Phi_{DF} = \frac{\Phi_{PF}}{1-\Phi_{ISC}\Phi_{RISC}}$ and knowing that the yield of ISC Φ_{ISC} cannot exceed the electronic excitation energy not utilized in prompt fluorescence, k_{RISC} can be estimated by the formula $k_{RISC} = \frac{\Phi_{DF}}{\tau_{DF}\Phi_{PF}(1-\Phi_{PF})}$[120]. The obtained data are collected in Table 2.7. The k_{RISC} value for 7 reached almost 10^6 s^{-1}, which is only slightly lower than the values of state-of-the-art TADF emitters[119,120,121].

2.4 Flexible organic light-emitting diodes with non-doped TADF emitters utilizing sulfobenzimide moiety: emission colors and performance evaluation (Scientific publication No. 4, Q1)

This chapter is based on the paper published in *Dyes and Pigments*, 2022, 208, 110841. In the current paper, there was provided the synthetic procedure as well as the investigations of the structural and spectroscopic characterization for the novel mechanoluminescent (MCL) TADF D–A molecule, and 2-(3-(9H-carbazol-9-yl)propyl)benzo[d]isothiazol-3(2H)-one 1,1-dioxide (9) were described.

Two steps of the nucleophilic substitution were used to synthesize compound 9 (Scheme 2.4). The first step involved deprotonating carbazole to create a nucleophile, then attacking one of the bromine atoms in 1,3-dibromopropane to obtain 9-(3-bromopropyl)-9H-carbazole[122]. Sulfobenzimide anion replaced the second bromine atom in the alkyl chain to form compound 9 in the second step. The desired compound was purified and obtained as a crystalline substance. The molecular structure of 9 was confirmed by using ^{1}H and ^{13}C NMR, mass spectrometries, and single crystal X-ray investigation.

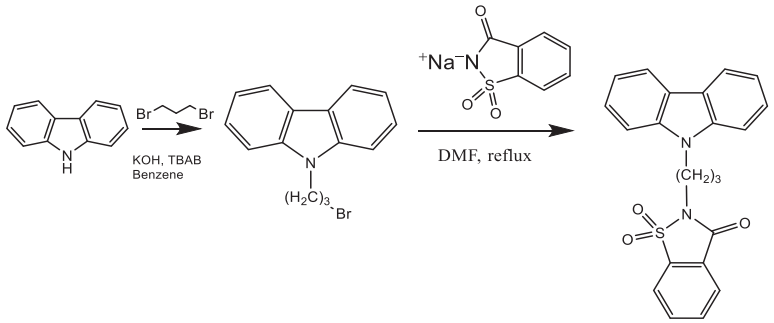

Scheme 2.4. Synthetic route to 9

The nature of the intermolecular interactions stabilizing the crystal structure of 9 was investigated by using Hirshfeld surface analysis. Fig. 2.24 shows Hirshfeld surface of 9. It illustrates the interaction between the electron density of the chosen molecule and the electron density of the surrounding crystal medium. The distance (d) between the surface and the closest external atom, as projected in Fig. 2.24, is called the normalized contact distance (dnorm). Red areas indicate the interactions whose distances (d) are smaller than Van der Waals distances. White regions are in charge of contacts that are exactly equal to Van der Waals distances, whereas blue regions are in charge of interactions that are more than those distances. The long-range, moderate-strength C-H···O hydrogen bonds, which stabilize the crystal structure of 9, are represented by the bright red spots around the oxygen and hydrogen atoms in Fig. 2.25. It reveals the presence of O···H/ H···O interactions with a $d_e + d_i$ distance of ca. 2.64 Å and 21.9% contribution to the total Hirshfeld surface.

The 2D fingerprint plot shows that the main intermolecular interactions in 9 are H···H, C···H, O···H, and C···C. The decomposition of the fingerprint plot shows that

H···H contacts occupy 40.5% of the total Hirshfeld surface area, C···H contacts – 29.8%, O···H contacts – 21.9%, and C···C contacts contribute only 3.7% to the total Hirshfeld surface area.

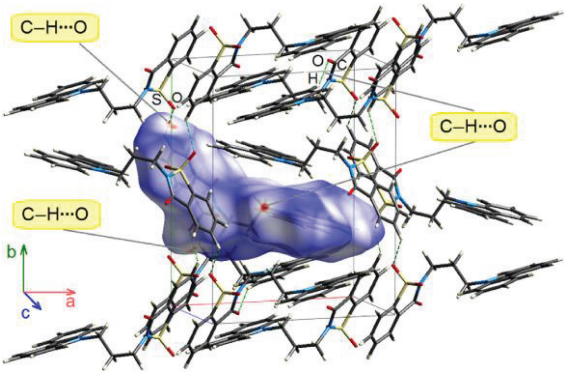

Fig. 2.24. Hirshfeld dnorm surface of the intermolecular interactions plotted in the unit-cell of compound 9; the C–H···O close contacts are denoted as green dashed lines

TGA and DSC were used to perform the thermal characterization of compound 9. TGA showed relatively high 5% weight loss temperature of 314 °C (Fig. 2.25 a). The complete weight loss of the sample during the TGA experiment demonstrates sublimation but not thermal decomposition. Endothermic melting peaks at 175 °C during the first heating scan and 172 °C during the second heating scan were visible on the DSC thermograms of 9. The existence of two meta-stable crystalline forms may be the reason for this difference. Since no crystallization was seen during the cooling scan, the substance consolidated in the amorphous phase. The following heating scan showed glass-transition at 41 °C and exothermic peak signal of crystallization at 132 °C (Fig. 2.25 a).

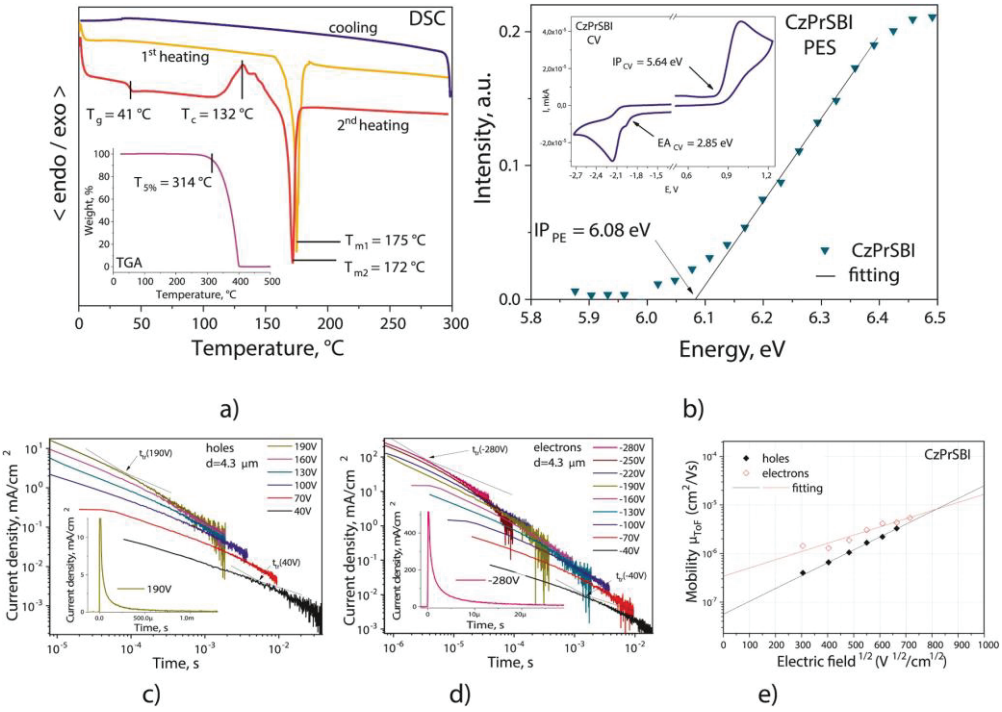

Fig. 2.25. (a) DSC thermograms of compound 9, inset: TGA curve; (b) photoelectron emission spectrum of the solid film of 9, inset: cyclic voltammetry curve of the DMF solution of compound 9; TOF transients for holes (c) and electrons (d) recorded at the different applied voltages and the plots of charge-carrier drift mobilities versus electric field (e) for the layer of 9

The ionization potential (IP) and electron affinity (EA) of 9 were determined by cyclic voltammetry of the solution in DMF (Fig. 2.25 b). The formulas $IP_{CV} = (E_{ox} + 4.8)$ and $EA_{CV} = (E_{red} + 4.8)$ were used to determine the IP_{CV} and EA_{CV}. E_{ox} and E_{red} are the electrochemical oxidation and reduction onset potentials. Ferrocene redox potential was used as a standard. At 0.84 eV and -1.95 eV, compound 9 showed irreversible oxidation and reduction. The irreversibility of the oxidation process was most likely caused by unprotected C-3 and C-6 of carbazole moiety[123]. Electrochemical band gap E_g^{CV} was found to be 2.79 eV, whereas IP_{CV} and EA_{CV} values were determined to be 5.64 eV and 2.85 eV, respectively.

The ionization potential was evaluated by using photoelectron emission spectrometry (Fig. 2.25 b). The IP_{PE} value was found to be of 6.08 eV. In order to calculate electron affinity (EA_{PE}) value, the following equation was used $EA_{PE} = IP_{PE} - E_g^{opt}$. EA_{PE} was estimated to be of 2.65 eV. The optical band gap E_g^{opt} of 3.43 eV, which was taken from the absorption spectrum of the solid film, was used to calculate EA_{PE} value. Stronger intermolecular interactions in the solid state are

believed to be responsible for a relatively large difference between the IP and EA values that were obtained for the solution and solid thin film.

Time-of-flight (ToF) technique was used to study the charge-transporting characteristics of a thin film of 9. The observed hole and electron current transients demonstrated that the charge transport was extremely dispersive (Fig. 2.25 c, d). Compared to the value recorded at low voltages, the lower transit time (t_{tr}) value was obtained at high voltages (Fig. 2.25 c, d). At the electric field of 4.43×10^5 V/cm, the hole mobility value was found to be 3.2×10^{-6} cm^2/V × s, while electron mobility was found to be just slightly higher, i.e., of 4.4×10^{-6} cm^2/V × s (Fig. 2.25 e). Due to fitting the experimental electric field dependences of charge carrier drift mobilities according to the Poole–Frenkel prediction $\mu = \mu_0^{eaE^{1/2}}$[124], very different values of zero-field mobilities (μ_0) of 5.8×10^{-8} and 3.4×10^{-7} cm^2/V × s were obtained for holes and electrons.

The six different types of charge hopping pathways A–F were divided into the X-ray structure (Fig. 2.25) and analyzed using the incoherent hopping model[125,126,127] to understand the charge-transport characteristics of 9 better. This model is appropriate when the intermolecular transfer integrals are much smaller than the charge reorganization energy. The Marcus–Hush equation describes the rates of the charge transfer between nearby molecules (hopping rate W)[128,129,130]:

$$w = \frac{V^2}{\hbar}\sqrt{\left(\frac{\pi}{\lambda k_b T}\right)}\, exp\left(-\frac{\lambda}{4k_b T}\right); \quad (4)$$

where λ is the reorganization energy for holes or electrons, V is the transfer integral, T is the temperature (298.15 K for the calculations), k_b is the Boltzmann constant, $\hbar$ is reduced Planck constant. The strength of the electronic interaction between the two neighboring molecules is described by the transfer integral V. It can be obtained by the so-called direct method in accordance with the following equation:

$$V_{electrone/hole} = \left\langle \varphi_{LUMO/HOMO}^{0,site1} \middle| F^0 \middle| \varphi_{LUMO/HOMO}^{0,site2} \right\rangle; \quad (5)$$

where $\varphi_{LUMO/HOMO}^{0,site1}$ and $\varphi_{LUMO/HOMO}^{0,site2}$ represent the HOMO or LUMO wave functions of the isolated molecules 1 and 2, respectively, F^0 is the Fock operator for the dimer. The suffix zero in equation (5) indicates that the molecular orbitals that appear in the operator are not disturbed. Numerous publications for various molecular crystal types have shown the robustness of this direct method[131,132,133]. Based on the estimated hopping rates (W), the diffusion coefficient D can be expressed as:

$$D = \frac{1}{2n}\sum_i r_i^2 W_i P_i; \quad (6)$$

where n is the spatial dimensionality (n = 3 for the three-dimensional single crystal of compound 1), *i* denotes a particular hopping pathway with hopping distance r_i, and P_i is the hopping probability, which is calculated as follows[134]:

$$P_i = \frac{W_i}{\sum_i W_i}. \quad (7)$$

The drift mobility from charge hopping (μ) is then evaluated from the Einstein relation providing the bulk (isotropic) mobility of holes and electrons for the studied molecule 1 single crystal[134]:

$$\mu = \frac{e}{k_b T} D; \quad (8)$$

where *e* is the electronic charge.

The reorganization energy (λ) has both inner and external contributions. The measure of geometrical distortion of the ionic forms from the neutral molecule is represented by the inner reorganization energy[135,136]. Using the adiabatic potential energy surface method, only the inner reorganization energies for hole (λ_{hole}) and electron ($\lambda_{electron}$) charge carriers were taken into account[137]:

$$\lambda_{hole/electron} = \left(E^*_{cation/anion} - E_{cation/anion}\right) + \left(E^{**}_{cation/anion} - E_{neutral}\right); \quad (9)$$

where $E_{neutral}$ is the optimized ground state energy of the neutral molecule, $E_{cation/anion}$ is the optimized structure energy of the cationic/anionic molecule, $E^{**}_{cation/anion}$ is the energy of the neutral molecule at the cationic/anionic geometry, and $E^{*}_{cation/anion}$ is the energy of the cationic/anionic molecule at the neutral-state geometry. Table 2.8 summarizes the calculated charge transfer characteristics.

Table 2.8. Center-of-mass distances within dimers (r), reorganization energies (λ), transfer integrals (V), charge hopping rates (W), and charge carrier mobility (μ) of 9 calculated at the B3LYP/DZP theory level

Dimer	r(Å)	Reorganization energy (λ, meV)		Transfer integral (V, meV)		Rate of charge hopping (W, s^{-1})		
		Hole	Electron	Hole	Electron	Hole	Electron	
A	4.6	49 [a] (161) [b]	378 [a] (558)[b]	-31.63	0.84	4.74×10^{13}	4.82×10^{8}	
B	7.1			8.49	-0.77	3.42×10^{12}	4.05×10^{8}	
C	9.5			5.24	-0.11	1.30×10^{12}	8.27×10^{6}	
D	10.3			0.01	-20.33	4.74×10^{6}	2.82×10^{11}	
E	11.4			-0.09	-99.73	3.84×10^{8}	6.80×10^{12}	
F	12.6			-0.42	-0.03	6.36×10^{9}	6.15×10^{5}	

Drift mobility from charge hopping, (μ, $cm^2\ V^{-1}\ s^{-1}$) – hole 0.589 [a] (0.108)[b] , electron 0.551 [a] (0.080)[b].

a – the value calculated by taking into account molecular packing.

b – the value obtained without accounting molecular packing.

In the case of hole transfer, the A–C packing modes with the closest intermolecular center-of-mass distances produce the largest transfer integrals (-31.63, 8.49, and 5.24 meV, respectively). The dimers in pathways E and D with face-to-face

π-π stacking interactions are preferable for electron transfer with the corresponding integrals for electron transfer of – 99.73 and – 20.33 meV, respectively (Table 2.8). The dimer E has much larger electron transfer integral and represents the main pathway for electron transfer. This fact can be explained by the presence of strong π-π overlap between the neighboring molecules. The dimers in the other pathways have little molecular orbital overlap for the side-to-face or side-to-side stacks (Fig. 2.26).

As it can be seen from equation (4), the reorganization energy has a significant impact on the carrier hopping rate as well as the final hole/electron mobility. This means that if the molecular packing is included, the estimated charge mobilities may be higher. Molecular donor and acceptor fragments are constrained from rotating due to their molecular packing. However, a free molecule can experience substantial conformational changes that are similar to those possible in the crystal phase. Therefore, the intramolecular reorganization energies of 9 were calculated for both the scenario of an isolated molecule and the solid state. The hole/electron reorganization energies in the first scenario are substantially higher, around 161 and 558 meV (Table 2.8). The conformation changes during the charge transfer process are reduced when the molecule packing is taken into consideration, and the energies for hole/electron reorganization are 49 and 378 eV, respectively (Table 2.8). The molecular packing should be taken into account when calculating the intramolecular reorganization energy to prevent significant discrepancies in mobility estimations.

The hole and electron mobility values for 9, calculated taking into account the molecular packing, were found to be 0.589 and 0.551 $cm^2 V^{-1} s^{-1}$, respectively (Table 2.8). Consequently, compound 9 can be assumed as a promising organic bipolar semiconductor. However, compared to the results of quantum-chemical calculations of the ideal single-crystal phase, the levels of hole and electron mobility that were measured experimentally are significantly smaller. High disorder of the vacuum-deposited thin film of 9 may be the reason for this discrepancy.

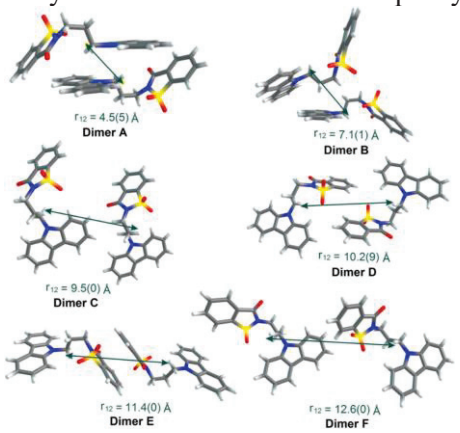

Fig. 2.26. The structure of the pertinent dimer configurations extracted from the single crystal X-ray data of 9; the center-of-mass intermolecular distances (r_{12}) are shown by arrows

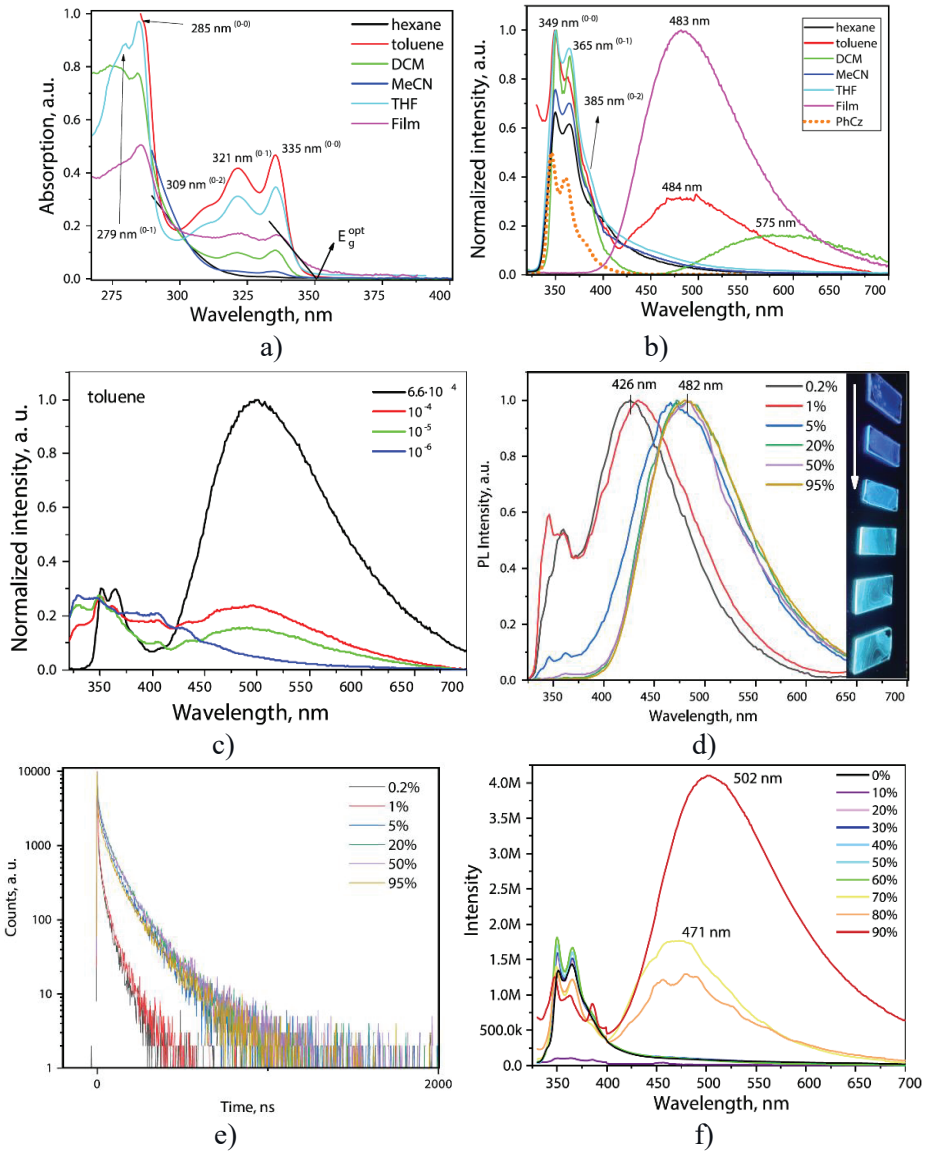

Fig. 2.27. UV (a) and PL (b) spectra of 9, the PL spectrum (b) of PhCz was recorded for its THF solution, PL spectra (c) of toluene solutions of 9 of different concentrations (mol/L), PL spectra (d) and PL decay curves (e) of the molecular dispersion of compound 9 in Zeonex of the different concentrations, the inset shows photo of the samples under UV excitation, PL spectra (f) of the dispersions of compound 9 in the mixtures of THF and water with the different concentrations

Fig. 2.27 a shows the absorption spectra of the solutions (1 x 10^{-5} mol/L) in five solvents with various polarity. Two low-energy absorption bands, which previously were designated as $^1L_b \leftarrow ^1A$ and $^1L_a \leftarrow ^1A$[138], are characterized by considerable vibrational structure (Fig. 2.28 a). As a result, in addition to the most intensive 0-0 transitions at 285 and 335 nm, 0–1 or 0–2 transitions can be seen as well. There are donor and acceptor moieties in the molecular structure of compound 9, but the absorption spectra show no clear indications of the formation of charge-transfer (CT) states. However, quantum-chemical calculations show that the CT states for the various conformations of the molecule 9 are typically visible in the absorption spectrum between 300 and 315 nm.

Carbazole-originated LE emission with the vibrational structure was identified for the solutions of 9 with 0–0 and 0–1 transitions appearing as the maxima at 349 and 365 nm, respectively, and the 0–2 transition appearing as the shoulder (Fig. 2.27 b). As additional proof that the band of the 9 that was described is accurately attributed to the emission of carbazole, the PL spectra of the THF solution of phenylcarbazole (PhCz) is presented in Fig. 2.27 b. The toluene and DCM solutions (1 x 10^{-5} mol/L) of 9 exhibit CT emissions peaking at 484 and 575 nm. Due to the comparatively limited solubility of 9 in the solvents, it is predictable that CT emission of 9 is induced by aggregation. The PL spectra of the toluene solutions with various concentrations of 9 were recorded to confirm this prediction (Fig. 2.28 c). Due to the aggregate formation and strong intermolecular interaction, highly concentrated toluene solution of 9 was distinguished by an intense CT band. As the concentration of toluene solution decreased, the intensity of the CT band decreased as well. The same behavior was observed for the DMC solutions of various concentrations. Due to the formation of various aggregates in various solvents, the position of the CT emission band of 9 was substantially media dependent. The position of dependence on the CT bands was apparently caused by the change in the position of carbazole moiety relative to sulfobenzimide unit. The CT formed between covalently bonded donor and acceptor units in 9 was not usual because of the bridge -$(CH_2)_3$- between the carbazole and sulfobenzimide moieties[139]. It was through-space charge transfer, thus an exciplex-like one[140].

There were recorded PL spectra and PL decay curves of the solid solutions of 9 in ZEONEX at various concentrations to examine the relationship between intramolecular and intermolecular CT states of 9 in the solid state (Fig. 2.27 d, e). When there is no intermolecular interaction at low concentrations (0.2 and 1%), the PL spectra of the solid solutions showed both high and low-energy bands. These PL spectra are remarkably similar to those seen in the spectra of toluene solution (Fig. 2.27 b). When aggregates of compound 9 are formed at the concentrations of the molecular dispersions in ZEONEX higher than 5%, the PL spectra are primarily characterized by low-energy band at 482 nm, which is red-shifted in comparison to the intramolecular CT band of 9 that is observed at low concentrations (Fig. 2.27 d). It is evident that the lifetime of emissions of intramolecular and intermolecular CT states clearly differs (Fig. 2.27 e). Since the emission of 9 occurs from exciplexes, the

PL decay curves of the solid solutions of 9 in ZEONEX at various concentrations have similar shapes. The absorption spectra of 9 and the excitation spectra have a very similar shape (Fig. 2.27 a). When the concentration of 9 increased, bathochromic shifts in the excitation spectra of the films of solid solutions were observed. This finding is explained by the fact that D and A units have stronger CT interactions in 9 aggregates than in individual molecules.

In order to investigate solid-state emission of 9 in further detail, a series of dispersions of the compound in mixtures of THF and water with varying amounts of water but the same concentration of the compound were prepared, and their PL spectra were recorded (Fig. 2.27 f). In mixtures containing more than 70% water, the solid aggregates were formed. The dispersions in the solvent mixtures with THF concentrations of 30% or higher showed emission spectra resembling those of carbazole (Fig. 2.27 b). The higher emission intensity of the solid sample of 9 than that of the solution in the good solvent (THF) indicates aggregation-induced emission enhancement (AIEE). The presence of AIEE is supported by the PLQY values obtained for the dispersions of 9. The solid solution in ZEONEX had a PLQY value of 14.8%, while the dilute solution of 9 in toluene had a lower PLQY value of 1.46%. The wavelengths of maximum emission from the solid aggregates ranged from 471 to 502 nm. This variation in the energy of emission maxima among the various aggregates of 9 is most likely caused by the different distances between the carbazole and sulfobenzimide moieties. Evidently, intermolecular CT states exhibit emission as well as intramolecular CT states. Because of this, the emission spectrum of aggregates is very broad. It extends into the NIR region and almost completely fills the visible spectrum from 400 to 700 nm (Fig. 2.27 f).

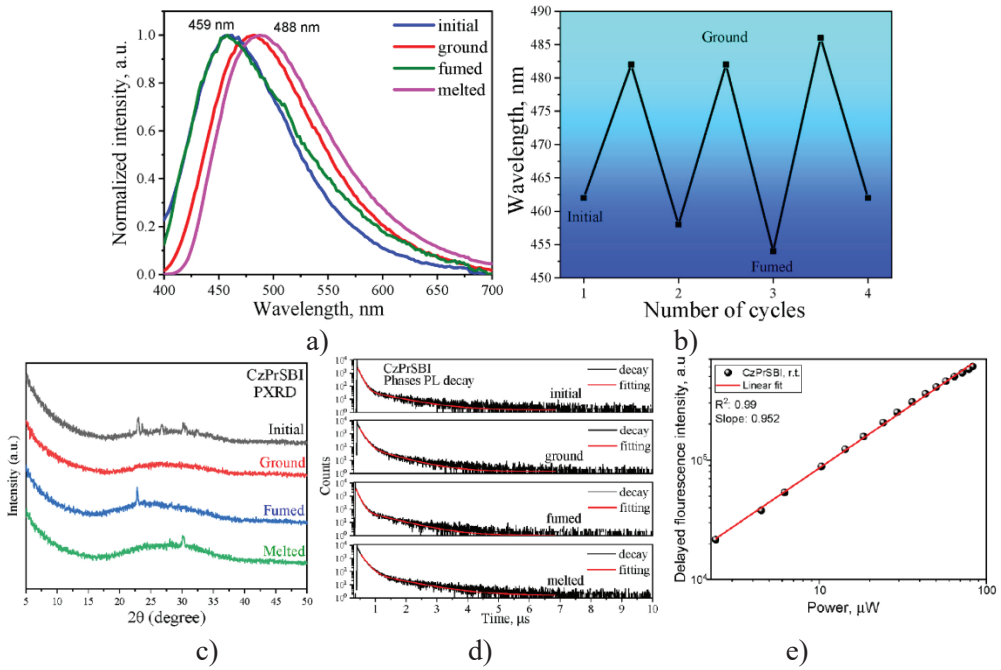

Fig. 2.28. (a) PL spectra of compound 9 after the different external stimuli, (b) PL maxima shifts after four grinding/fuming cycles, (c) powder X-ray diffractograms and (d) photoluminescence decay curves of 9 after various external stimuli, (e) intensity of delayed fluorescence versus excitation power for the film of compound 9

The mechanoluminescent features of 9 can be predicted based on the observation of various emission spectra for various aggregates of the molecule. Indeed, compound 9 demonstrated the capacity to change its photoluminescence wavelength in response to the external stimuli (Fig. 2.28 a). When UV light was used to excite the solid powder of compound 9, as it was obtained after purification, 462 nm emission peaking was visible. Amorphous phase that was created by grinding mechanically, under the same excitation, displayed considerably red-shifted emission peaking at 482 nm. Following a 3-minute treatment with dichloromethane vapors on the amorphous sample, the peak emission intensity was recovered to 484 nm. With a peak at 488 nm, the bathochromic shift of photoluminescence was even stronger after melting the fumed sample (Fig. 2.28 a). By repeating the grinding and fuming procedures, the reversibility of mechanoresponsive emission was investigated. Compound 9 demonstrated reversible emission without degradation after four grinding-fuming cycles (Fig. 2.28 b). The conformational transitions brought on by the mechanical stimuli are one of the potential causes for the spectrum alterations. Quantum-chemical calculations show that conformation I, which predominates in the single-crystal phase, is not a global energy minimum in contrast to conformation III, which should primarily exist in a disordered medium as an amorphous solid or gas phase. Conformation I is stabilized by crystalline phase, while in the absence of

stabilizing effects, it transforms into conformation III sustaining π-tacking interaction between D and A planes. In fact, conformation I exhibits S_1–S_0 emission in the gas phase at 439 nm as a result of calculations, whereas conformation III exhibits red-shifted emission in the gas phase at 454 nm. The S_0–S_1 vertical absorption and S_1–S_0 vertical emission transitions for both conformations I and III in gas phase correspond to one-electron excitation of HOMO–LUMO type. HOMO is localized on carbazole (D) fragment, while LUMO is localized on sulfobenzimide (A) moiety; the S_1 state is assigned to charge-transfer (CT) origin (Fig. 2.29).

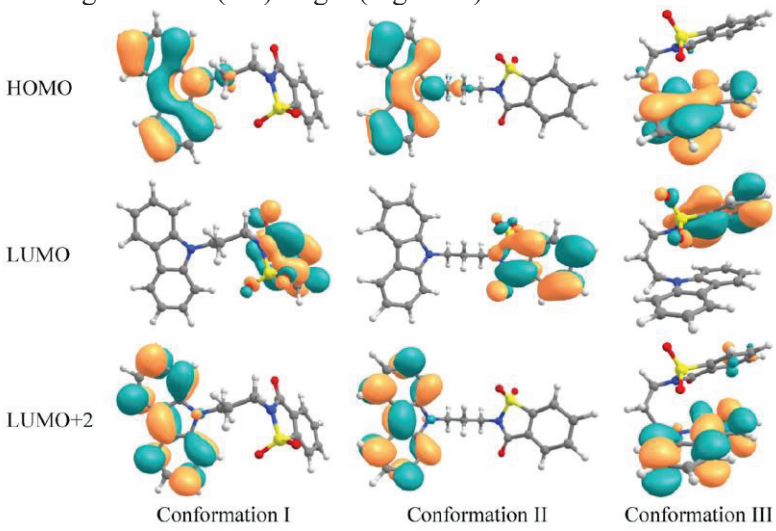

Fig. 2.29. The shape of the selected molecular orbitals of different conformations of 9

Compound 9 conformers formation can be related to the changes of the structure of its powders under different external stimuli. The powder X-ray diffraction investigation clearly demonstrated the phase transitions that take place during the mechanical stimulation (grinding, fuming, and melting) (Fig. 2.28 c). Different diffraction patterns were visible in the crystalline powder that was used initially: the grinded amorphous phase, the fumed crystalline sample, and the melted sample. A complicated series of diffraction peaks were visible in the initial crystalline sample. After grinding, they vanished. In contrast, additional fuming of the amorphous material led to the restoration of a single peak with a 2θ value of 22.9°. The sample then melted, causing the development of the second single peak with a value of 2θ of 30.1°. It appears that the sample's melting and cooling caused recrystallization, which produced second polymorphic form. The data from the DSC, which showed two melting peaks, and these observations are in agreement (Fig. 2.25 a).

Time resolved luminescence spectrometry was used to explore the nature of the emission further. The PL decay curves are shown in Fig. 2.28 d. Similar PL decays could be seen in the samples that had been treated differently. While excited state lifetimes of long-lived components, which were responsible for delayed fluorescence, varied from 679 to 898 ns, short-lived components, which caused prompt

fluorescence, were found to have lifetimes in the range of 87–137 ns (Table 2.9). The slope value of 0.952 on the plot of delayed fluorescence intensity vs. excitation power (Fig. 2.28 e) leads to the conclusion that delayed fluorescence is TADF in nature but is not an emission from triplet-triplet annihilation[141]. The proximity between CT states for the conformations maintaining face-to-face orientation of the donor and acceptor moieties can be used to explain the origin of TADF. It is well known that single molecules and intermolecular molecules (such exciplexes) that have space-separated CT states usually display very small singlet-triplet splitting that causes TADF[142,143]. The singlet-triplet gap estimated for confirmation III in the gas phase approximation is only 0.093 eV, while the intensity of S_1–S_0 is considerable for CT states (f = 0.01, Table 2.9). The ability of 9 to demonstrate TADF is impacted by these two factors.

Table 2.9. Photoluminescence decay characteristics of various forms of 9

Sample	τ_1, ns	τ_2, ns	χ^2	τ_1/ τ_2, %
Initial	88.86	868.67	1.105	84.05/15.95
Ground	113.66	679.73	1.288	80.30/19.70
Fumed	87.22	745.82	1.010	82.59/17.41
Melted	138.24	898.64	1.277	76.38/23.62

The lifetimes of short-lived and long-lived components differed noticeably in the photoluminescence decay parameters of the fumed and melted samples. This observation can be explained by the different conformational compositions of the samples. In order to provide more proof of capacity of compound 9 to harvest triplets via TADF, PL spectrum and PL decay curve of its toluene solution and PL decay curve of the film of its 95 wt% solid solution in ZEONEX were obtained (Fig. 2.30 a–c). Additionally, the PL spectra and PL decay curves of the film of the solid solution in ZEONEX at various temperatures were obtained (Fig. 2.30 d, e). The deoxygenation of the samples increased the intensity of the low-energy band, confirming the role of the triplet states in emission. Due to the TADF effect, an increase in emission intensity of 9 was seen when the temperature rose from 77 to 120 K. Such a result is well supported by the negligibly small ΔE_{ST} of compound 9 (Fig. 2.30 f). Due to the non-emissive losses of the exciplex formed between the D and A units, the emission intensity of 9 continuously decreased at the temperatures higher than 120 K.

The photoluminescence lifetimes of 9 were found to be quite short; however, they were rather long as for prompt fluorescence[80,144].

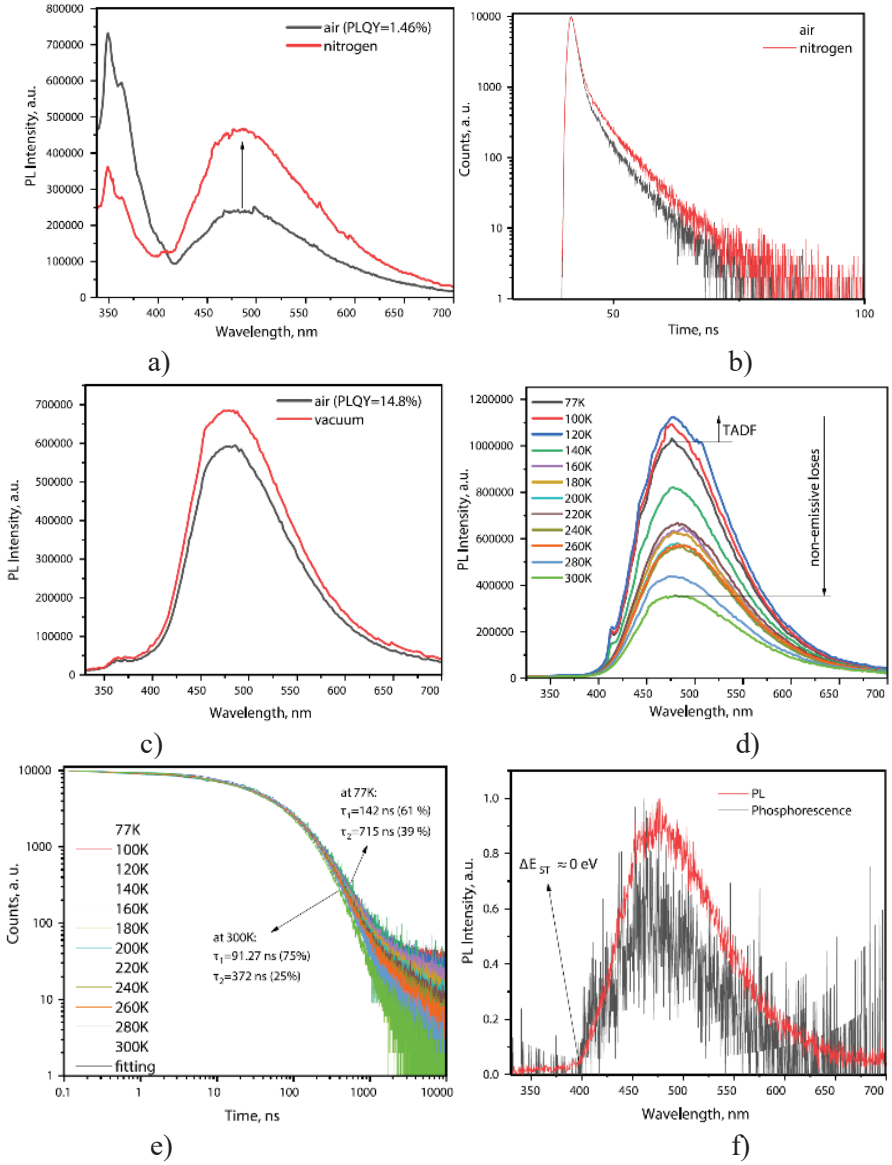

Fig. 2.30. PL spectra (a) and PL decay curves (b) of toluene solution of 9, PL spectra of the film of 95 wt% solid solution of 9 in ZEONEX recorded under air or vacuum (c) and at different temperatures (d) in inert atmosphere, PL decay curves (e) of the film of 95 wt% solid solution of 9 in ZEONEX recorded at different temperatures, PL and phosphorescence spectra (f) of 95 wt% solid solution of 9 in ZEONEX recorded at 77 K, the phosphorescence spectrum was recorded by using the delay of 1 ms after excitation

Using the thermal vacuum evaporation method, OLED with the following structure: CuI/TPD/CzPrSBI/TSPO1/TPBi/Ca/Al was produced in order to investigate the performance of 9 as the TADF emitter. As a hole-injection layer, the layer of CuI was used[145], and as an electron-transporting layer, the layer of 2,2′,2"-(1,3,5-benzinetriyl)-tris(1-phenyl-1-H-benzimidazole) (TPBi)[146] was deposited TPD[147], and TSPO1[148,149] were utilized as well for the deposition of exciton-blocking and hole transporting layers to maintain the balance of charge carriers in the emission layer. Compound 9 was used as the emitter. The cathode was a layer of calcium that was covered by a 200 nm film of aluminum.

The devices displayed structureless EL spectra with intensity peaks in the 490–504 nm region. They were similar to the PL spectra of the neat film of 9 shown in Fig. 2.31 a, c. This finding proves that the source of the EL was the emitter itself. With the increase in the driving bend angle of a flexible OLED, the relative intensity of the shoulder peaking at 630 nm increased (Fig. 2.31 c). This observation is explained by the formation of intermolecular exciplex formation between the donor part of one 9 molecule and acceptor part of another one. The intensity of the peak increased as the angle of the bend in the flexible samples changed. When the angle reached 50°, the intensity reverted to that of OLEDs with the glass substrates. The enforced proximity of the donor and acceptor fragments caused by mechanical impact (bending in examined instance) is responsible for the mechanochromic luminescence of emitter 9 in flexible OLEDs, which enhances the formation of intermolecular exciplexes.

The device based on a glass substrate exhibited the best performance with maximum current efficiency, power efficiency, and external quantum efficiency (EQE) of 11.0 cd A^{-1}, 3.0 lm W^{-1}, and 4.3%, respectively (Table 2.10, Fig. 2.31).

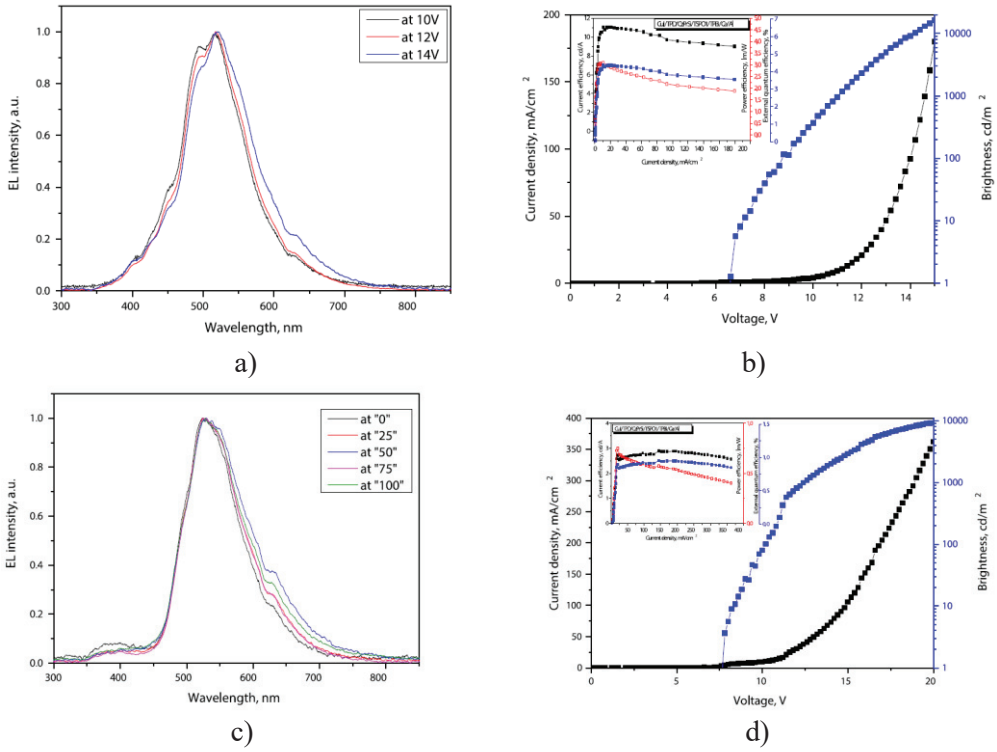

Fig. 2.31. The spectra of electroluminescence of devices recorded at different voltages (a) and different bend angle (c); current density – voltage and luminance voltage, power efficiency – current density, current efficiency – current density and external quantum efficiency – current density plots for the devices (b-glass substrate, d-flexible substrate)

Table 2.10. Characteristics of OLEDs fabricated on the glass and flexible substrates

Device substrate	Von, V	Max. brightness, cd m^{-2}	Current efficiency, cd A^{-1}	Power efficiency, lm W^{-1}	EQE, %
			at 1,000/max. cd m^{-2}		
Glass	6.4	16,000	11.0/9.0	3.0/1.8	4.3/3.5
Flexible	7.4	9,000	2.6/2.5	0.6/0.4	0.8/0.9

3. CONCLUSIONS

1. Using phenoxazine, phenothiazine or 9,9-dimethyl-9-10-dihydroacridine as donor moieties and 1,4-bis(trifluoromethyl)benzene as a new acceptor unit, three new compounds with symmetrical donor–acceptor–donor architectures were designed and synthesized as emitters exhibiting thermally activated delayed fluorescence.

1.1. The derivative of 9,9-dimethyl-9-10-dihydroacridine and 1,4-bis(trifluoromethyl)benzene is a promising blue thermally activated delayed fluorescence emitter with a high energy of singlet charge transfer onset of 2.91 eV.

1.2. Due to the intramolecular interactions, organic light-emitting diode based on the derivative of 9,9-dimethyl-9-10-dihydroacridine shows blue electroluminescence that is "insensitive" to the concentration of the emitter in the light-emitting layer.

1.3. With practically no roll-off up to the brightness of 1,000 cd m^{-2}, the device based on a derivative of 9,9-dimethyl-9-10-dihydroacridine as an emitter shows the external quantum efficiency of 5.9%.

2. Three new compounds were synthesized for optical oxygen sensors, using 1,4-difluorobenzene as the acceptor and three donor compounds: phenothiazine, phenoxazine, and acridine.

2.1. The compounds show high temperatures of 5% weigh loss for compounds with phenothiazine and acridine moieties, i.e., 302 °C and 333 °C, respectively.

2.2. The compounds showed blue and blueish-green emissions. The derivative of phenothiazine exhibits dual emissions in vacuum, one originating from the singlet charge transfer state and the other from the locally excited triplet state phosphorescence.

2.3. Compound with phenothiazine moiety as donor and 1,4-difluorobenzene as an acceptor unit showed high sensitivity at low concentrations <0.1% and low sensitivity at high concentrations of oxygen (>0.2%).

2.4. Van der Waals intermolecular interactions between the nearby molecules were discovered by single-crystal X-ray analysis.

3. Two compounds based on pyridazine as the acceptor and phenoxazine or 9,9-dimethyl-9,10-dihydroacridine as donor moieties were designed and synthesized.

3.1. The compounds exhibit emission from the intramolecular charge transfer state manifested by positive solvatochromism. The emission in the range of 534–609 nm of the toluene solutions of the compounds is thermally activated delayed fluorescence with the lifetimes of 93 and 143 ns for phenoxazine and acridine moieties.

3.2. The compounds are characterized by high thermal stabilities. Their 5% weight loss temperatures are 314 and 336 °C.

3.3. The reverse intersystem crossing rate constant of $9.5 \cdot 105\ s^{-1}$ estimated for phenoxazine derivative is higher than that observed for the derivative of 9,9-dimethyl-9,10-dihydroacridine ($3.3 \cdot 105\ s^{-1}$), primarily due to the fast thermally activated delayed fluorescence.

4. Carbazole-sulfobenzimide derivative was synthesized and characterized.

4.1. The carbazole-σ-sulfobenzimide derivative displays tunable emission in flexible electroluminescent heterostructures, mechanochromic thermally activated delayed fluorescence, and aggregation-induced emission enhancement.

4.2. The donor and acceptor subparts of the carbazole-sulfobenzimide compound are separated by non-conjugated linkers, which give the system conformational flexibility and suppresses the common charge-transfer electronic transitions.

4.3. Carbazole-sulfobenzimide derivative displays sensitivity of the emission to aggregation and mechanical stimuli.

4. SANTRAUKA

Šio darbo tikslas – naujų donoras-akceptorius-donoras ir donoras-akceptorius tipo darinių, kurių akceptorinės dalys yra trifluormetilbenzeno, difluorbenzeno, piridazino ar sulfobenzimido fragmentai, turinčių skirtingus donorinius fragmentus, sintezė ir savybių tyrimas, siekiant juos panaudoti organiniuose šviesos dioduose ir deguonies jutikliuose.

Siekiant darbo tikslo iškelti šie **uždaviniai**:

- Naujų trifluormetilbenzeno darinių, turinčių donoras-akceptorius-donoras struktūras, sintezė.
- Trifluormetilbenzeno darinių terminių, fotofizikinių ir fotoelektrinių savybių tyrimas.
- Naujų simetriškos donoras-akceptorius-donoras struktūros junginių, turinčių piridazino fragmentą ir skirtingus fenoksazino arba 9,9-dimetil-9,10-dihidroakridino donorinius fragmentus, sintezė.
- Piridazino darinių terminių, fotofizikinių, fotoelektrinių ir elektroliuminescencinių savybių tyrimas.
- Karbazolo ir sulfobenzimido darinių sintezė ir tyrimas.
- Karbazolo darinių fotofizikinių savybių (absorbcijos ir emisijos spektrų fluorescencijos kvantinio našumo, fluorescencijos gyvavimo trukmės) tyrimai.

Darbo naujumas:

- Sukurti, susintetinti, charakterizuoti ir pritaikyti termiškai aktyvinama uždelstąja fluorescencija paremtuose (TADF) organiniuose šviesos dioduose (OLED) nauji donoras-akceptorius-donoras tipo 2,5-bis(trifluormetil)-1,4-fenileno dariniai.
- Optiniams deguonies jutikliams sukurti nauji junginiai su skirtingomis donorinėmis grupėmis ir akceptoriniu 1,4-difluorbenzeno fragmentu. Nustatyta, kad fentiazilgrupes turintis darinys pasižymi efektyvia kambario temperatūros fosforescencija (RTP).
- Sukurti, susintetinti ir ištirti nauji junginiai, kurie turi piridazino fragmentą kaip akceptorinį centrą ir skirtingus donorinius fragmentus.
- Susintetintas ir ištirtas naujas junginys, turintis akceptorinį sulfobenzimido fragmentą, kuriam būdinga naujo D-σ-A tipo TADF.
- Sukurti ir susintetinti du nauji junginiai, sudaryti iš akceptorinio trifluormetilfenilo fragmento ir skirtingų donorinių fragmentų. Nustatyta, kad 10,10‘-(2-(2-(trifluormetil)-1,4-fenilen)bis(10*H*-fenotiazinas), kaip efektyvus RTP spinduolis, pasižymi dideliu jautrumu deguoniui.

4.1. 1,4-Bis(trifluormetil)benzeno fragmentus turintys spinduoliai, pasižymintys efektyvia termiškai aktyvinama uždelstąja fluorescencija ir elektroliuminescencija

Šis skyrius parengtas pagal straipsnį, paskelbtą žurnale *Journal of Materials Chemistry C*, 2022, **10**, 4929–4940. Sukurti ir susintetinti nauji simetriškos donoras-akceptorius-donoras struktūros spinduoliai. Dviejų pakopų sintezės keliu gauti trys nauji junginiai – 1,4-bis(trifluormetil)benzeno dariniai su fenoksazino (**1**), fentiazino (**2**) ir akridano (**3**) pakaitais (4.1.1 schema). Susintetintų junginių **1** ir **2** cheminės struktūros patvirtintos naudojant ^{1}H ir ^{13}C BMR spektroskopiją, masių spektrometriją ir rentgeno spindulių kristalografiją. Dėl mažo tirpumo visuose prieinamuose deuterintuose tirpikliuose junginio **3** struktūros nepavyko patvirtinti ^{1}H arba ^{13}C BMR metodais, tačiau monokristalo rentgeno kristalografija leido patvirtinti jo struktūrą.

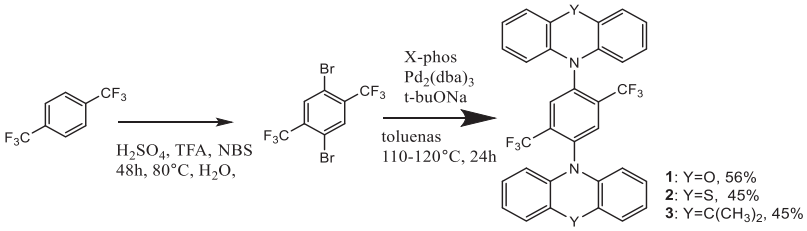

4.1.1 schema. Junginių **1**–**3** molekulinė struktūra ir sintezės eiga

Siekiant ištirti junginių **1**–**3** terminį stabilumą ir jų morfologines savybes, naudoti termogravimetrinės analizės (TGA) ir diferencinės skenuojamosios kalorimetrijos (DSC) metodai. **4.1.1 lentelėje** pateikiama 5 % masės nuostolio (T_{ID}), lydymosi (T_m) ir kristalizacijos (T_{cr}) temperatūrų suvestinė.

4.1.1 lentelė. Junginių **1**–**3** terminės charakteristikos

Junginys	T_{ID}, ℃ [1]	T_{cr}, ℃ [2]	T_m, ℃ [3]
1	290	303	385
2	260	270	321
3	267	296	311

[1] Temperatūra, kurioje buvo prarasta 5 % bandinio masės, nustatyta naudojant TGA; [2] DSC metodu nustatytos junginių kristalizacijos ir [3] lydymosi temperatūros.

4.1.1 pav. pavaizduoti junginių molekulinių dispersijų zeonekse (1 % koncentracijos) fotoliuminescencijos (PL) spektrai, užfiksuoti esant skirtingoms temperatūroms. Visų jų PL ir fosforescencijos spektrai beveik visiškai persidengia, kas yra būdinga TADF reiškiniui, jiems atskirti taikyta 1, 5 arba 9 ms uždelsa esant 77 K. Molekulinių **1**–**3** dispersijų Zeonekse ir MeTHF fosforescencijos spektrų pradžios yra susijusios su tripletinėmis LE būsenomis. Šios tripletinės LE būsenos gali būti priskiriamos atitinkamų donorinių fragmentų (10-fenil-10H-fenoksazino

(PO-Ph), 10-fenil-10H-fenotiazino (PS-Ph) arba 9,9-dimetil-10-fen-9,10-dihidroakridino (AC-Ph)) tripletinėms LE būsenoms (^{3}LED). Akceptorinio fragmento fosforescencijos pradžia matoma esant didesnei energijai (^3LE_A = 3,65 eV) nei donorinių PO-Ph, PS-Ph ir AC-Ph fragmentų. Todėl **1**, **2** ir **3** pirmoji singuletinė energija apskaičiuota tik pagal PL spektrų, užfiksuotų 300 K temperatūroje, pradžią. PL spektras, užfiksuotas kambario temperatūroje, palyginti su PL spektru, užfiksuotu 77 K temperatūroje, yra pasislinkęs raudonos spalvos linkme, o emisijos intensyvumas žemesniuose energijos lygmenyse, išskyrus **3**, didėja. Šį pastebėjimą galima paaiškinti nustatytu sumažėjusiu konformaciniu heterogeniškumu[89,90]. Iškelta hipotezė, kad **1**, **2** ir **3** atveju energijos tarpai tarp ^{3}CT ir ^{1}CT atitinkamai yra 0,04 eV, 0,03 eV ir 0,04 eV. Junginių ΔE_{ST} vertės artimos viena kitai.

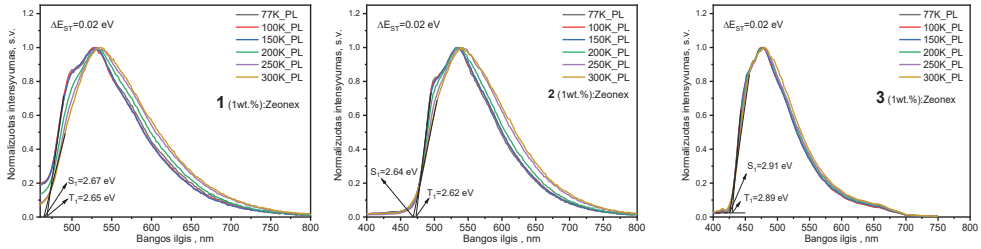

a) b) c)

4.1.1 pav. Junginių **1** (a), **2** (b) ir **3** (c) molekulinių dispersijų Zeonekse žemos ir kambario temperatūros PL spektrai ir atitinkamos emisijos pradžia 300 K temperatūroje

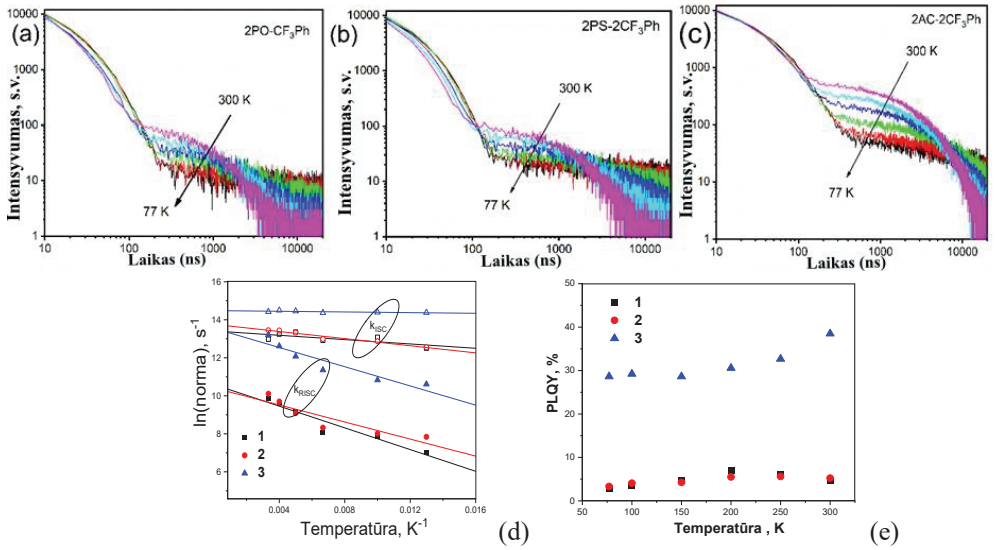

(d) (e)

4.1.2 pav. Junginių **1** (a), **2** (b) ir **3** (c) 1 % molekulinių dispersijų Zeonekse fluorescencijos gesimo kreivės kaip temperatūros funkcija, taip pat jų k_{ISC}/k_{RISC} (d) ir *PLQY* (e) priklausomybės nuo temperatūros

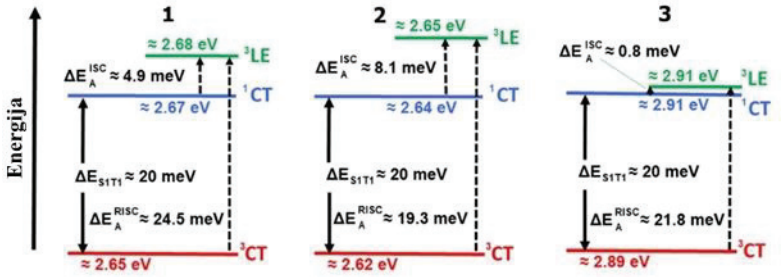

4.1.3 pav. Junginių **1** (a), 2 (b) ir **3** (c) energetiniai lygmenys

Junginių molekulinių dispersijų zeonekse PL gesimo kreivės užregistruotos esant įvairioms temperatūroms (**4.1.2 pav., a–c**), pastebėtos standartinės TADF gesimo kreivės su greitosios fluorescencijos (PF) komponente nanosekundžių intervale ir uždelstosios fluorescencijos (DF) komponente mikrosekundžių intervale. Tai, kad visų trijų junginių DF pastebėti reaguojant į temperatūros sumažėjimą, įrodo, kad DF buvo termiškai aktyvuota (4.1.3 pav., 4.1.2 lentelė).

4.1.2 lentelė. Junginių **1**–**3** molekulinių 1 % dispersijų Zeonekse fotofizikiniai parametrai

Junginys	**1**	**2**	**3**
λ_{PL}^{ICT}, nm	535	537	477
PLQY, %	4,6	5,2	38,5
ΔE_{ST}, eV	0,19	0,02	0,02
τ_{PF}, ns (santykis, %)	21,5 (72,3 %)	18,2 (28,2 %)	35,4 (21,6 %)
τ_{DF}, μs (%)	0,93 (27,7 %)	1,41 (71,8 %)	2,56 (78,4 %)
k_{RISC}/k_{ISC}	0,044	0,036	0,296
ΔE_A^{ISC}, meV	4,9	8,1	0,8
ΔE_A^{RISC}, meV	24,5	19,3	21,8

Santykinai didelis $E_{3LE\text{-}3CT}$, tikėtina, lėmė tai, kad **1** ir **2** PL kvantinis našumas (*PLQY*) pasiekė maksimumą maždaug 200 K temperatūroje (**4.1.2 pav., e**). Keliant temperatūrą *PLQY* vertės mažėja, greičiausiai dėl tripletinių būsenų nespindulinės dezaktyvacijos greičio konstantos (k^T_{nr}) didėjimo. Tačiau dėl efektyvaus TADF proceso **3** *PLQY* padidėjo iki 38,5 %, didinant temperatūrą nuo 77 iki 300 K. Norint turėti veiksmingus TADF spinduolius, k_{RISC}/k^T_{nr} santykis turi būti didesnis už vienetą (kaip junginio **3** atveju)[92,93].

Nustatyta, kad sluoksnių su skirtingomis junginio **3** koncentracijomis PL spektrai yra panašūs. Prietaisų, pagamintų su junginiu **3**, elektroliuminescencijos (EL) spektrai atitinka šį pastebėjimą. TADF charakteristikoms tirti pasirinktas sluoksnis, sudarytas iš 10 % emiterio **3** ir SimCP2 molekulinio mišinio. Junginio **3** molekulinės

dispersijos SimCP2 PL spektrai ir PL gesimas buvo labai panašūs į molekulinės **3** dispersijos zeonekse (**4.1.1** ir **4.1.4 pav**., c).

Geriausią OLED naudojimui reikalingų savybių derinį turėjo junginys **3** ir buvo pasirinktas elektroliuminescencijos tyrimui kaip TADF spinduolis. Prietaisų struktūra buvo tokia: ITO/MoO_3[0,5 nm] / NPB[40 nm] / TCTA[4 nm] / mCBP[4 nm] / šviesą emituojantis sluoksnis [24 nm] / TSPO1[4 nm] / TPBi[40 nm] / LiF[0,5 nm]: Al[88 nm], kurioje junginio **3** [5, 10 arba 15 %] legiruoto SimCP2 sluoksniai panaudoti kaip šviesą emituojantys sluoksniai prietaisuose A, B arba C. Etaloniniame prietaise D šviesą emituojantis sluoksnis buvo 20 % PFBP-2a, turinčio akceptorinį fragmentą su fluoru, molekulinė dispersija[98]. Siekiant užtikrinti subalansuotą skylių ir elektronų rekombinaciją ir eksitonų susidarymą šviesą emituojančiuose sluoksniuose, panaudotos medžiagos: MoO_3 kaip skyles injekuojanti medžiaga, NPB ir TCTA kaip skyles pernešančios medžiagos, mCBP kaip elektronus ir eksitonus blokuojanti medžiaga, SimCP2 kaip matrica, TSPO1 kaip skyles ir eksitonus blokuojanti medžiaga, TPBi kaip elektronus pernešanti medžiaga ir LiF kaip elektronus injekuojanti medžiaga (**4.1.4 pav**., a). Rekombinacijos zona yra netoli SMPCP2/TPSO1 sąsajos. Prietaisų A–C EL spektrai (maksimumas – 485 nm) buvo labai panašūs į atitinkamų šviesą emituojančių sluoksnių, **3** legiruotų SimCP2, PL spektrus (**4.1.4 pav., b**). Nedidelius skirtumus tarp PL ir EL spektrų lemia naudoti skirtingi optinio ir elektrinio sužadinimo šaltiniai. Prietaisų A–D įjungimo įtampa buvo maždaug 4,4 V (**4.1.4 pav**., d) dėl vienodų **3** ir PFBP-2a krūvininkų injekcijos charakteristikų. Esant didesnei nei 7 V įtampai, prietaisuose A–C užfiksuotas didesnis darbinės srovės tankis nei prietaise D, tikriausiai dėl geresnių **3** krūvininkų pernašos charakteristikų, palyginti su PFBP-2a charakteristikomis.

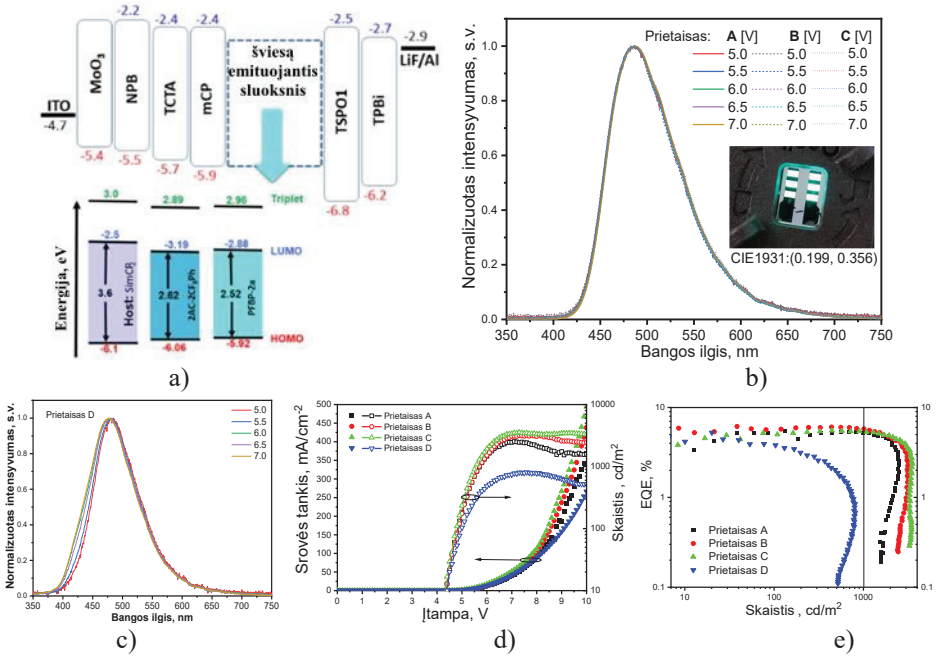

4.1.4 pav. Prietaisų A–D energetinė diagrama (a); EL spektrai esant skirtingoms įtampoms (b, c); srovės tankio ir skaisčio priklausomybė nuo taikomų įtampų (d) ir *EQE* priklausomybės nuo srovės tankio grafikai (e). Intarpe pateikiama prietaiso A, esant 6 V įtampai, nuotrauka bei CIE1931 spalvų koordinatės

Esant skirtingoms įtampoms ir nepaisant naudojamų skirtingų spinduolio **3** koncentracijų, prietaisų A–C EL spektrai buvo beveik vienodi. Tai galima paaiškinti tuo, kad kietosios būsenos **3** sukuria nekovalentinius intramolekulinius ryšius. Priešingai, etaloninis prietaisas D parodė nestabilius EL spektrus esant skirtingoms išorinėms įtampoms (**4.1.4 pav**., c). Šis rezultatas iliustruoja naujai sukurto akceptorinio 1,4-bis(trifluormetil)benzeno fragmento privalumus.

OLED su 1,4-bis(trifluormetil)fenilo turinčiu junginiu veikimo stabilumas būdingas ne tik jo EL spektrui, tačiau ir didžiausias išorinis kvantinis efektyvumas (*EQE*), kuris išlieka nepakitęs net ir esant 1000 cd/m^2 srovės efektyvumui, kai įprastai, OLED pasiekus pakankamai didelę darbinę srovę, jų *EQE* gali sumažėti net ir kelis kartus (**4.1.4 pav**., e, **4.1.3 lentelė**). Remiantis ankstesnėmis diskusijomis[99,100], esant didesniam darbinės srovės tankiui (didesniam nei 40 mA cm^{-2}), dėl eksitono-poliarono anihiliacijos procesų pirmiausia gali nutrūkti mažiausią skilimo energiją turintys ryšiai.

4.1.3 lentelė. OLED charakteristikos

Prietaisas	**EML**	λ_{EL}, nm	V_{ON}, V	L_{MAX}, cd/m^2	CE_{MAX}, cd/A	PE_{MAX}, lm/W	EQE_{MAX}/EQE_{1000}, %
Prietaiso struktūra: ITO/MoO_3/NPB/TCTA/mCBP/šviesą emituojantis sluoksnis (EML)/TSPO1/TPBi/LiF:Al							
A	**3 [5 %]:SimCP2**	487	4,4	2500	11,7	9,9	4,7/5,18
B	**3 [10 %]:SimCP2**	487	4,4	3000	12,9	10,7	5,9/5,8
C	**3 [15 %]:SimCP2**	487	4,4	3500	12,6	8,97	4,6/5,4
D	**PFBP-2a [20 %]:SimCP2**	478	4,4	800	6,2	5,6	4,4/-

λ_{EL} – EL maksimumas; V_{ON} – įjungimo įtampa; L_{MAX} – skaisčio maksimumas; CE_{MAX} – didžiausias srovės efektyvumas ir PE_{MAX} – didžiausias galios efektyvumas. EQE_{MAX} ir EQE_{1000} – tai *EQE*, esant atitinkamai 10 ir 1000 cd/m^2.

Nustatyta, kad 9,9-dimetil-9-10-dihidroakridino ir 1,4-bis(trifluormetil)benzeno darinys (junginys **3**) yra perspektyvus mėlynos spalvos TADF spinduolis, pasižymintis aukšta singuletinio krūvio pernašos pradžia – 2,91 eV. Šis junginys pasižymėjo žydra elektroliuminescencija, kuri dėl vidinių molekulinių sąveikų yra „nejautri“ spinduolio koncentracijai šviesą emituojančiame sluoksnyje. Didžiausias išorinis kvantinis efektyvumas – 5,9 %, su praktiškai nepasireiškiančiu efektyvumo mažėjimu iki 1000 cd m^{-2}, gautas šio spinduolio turinčiame prietaise. Šie rezultatai leidžia daryti išvadą, kad, sumažinus TADF molekulių $\Delta E_{3LE-1CT}$, gali padidėti atvirkštinės interkombinacinės konversijos (RISC) greitis, taigi ir TADF efektyvumas.

4.2. Konformacinės netvarkos ir standžios matricos poveikio tyrimas bei didelio jautrumo deguoniui ir fosforescencijos kambario temperatūroje mechanizmo atskleidimas

Šis skyrius parengtas pagal straipsnį, paskelbtą žurnale *Sensors and Actuators B: Chemical*, 2023, **380**, 133295.

Susintetinti trys junginiai, skirti optiniams deguonies jutikliams, naudojant akceptorinį 1,4-difluorbenzeno fragmentą ir tris skirtingus donorinius fragmentus (fentiaziną, fenoksaziną ir akridiną). 2,5-Dipakeisto 1,4-fenileno darinių sintezė atlikta Buchvaldo ir Hartvigo kopuliavimo metu (**4.2.1 schema**). Gautų junginių **4**, **5** ir **6** išeiga atitinkamai 68 %, 40 % ir 27 %. Naudojant ^{1}H, ^{13}C ir ^{19}F BMR spektroskopiją bei monokristalinę rentgeno analizę, nustatytos gautų junginių struktūros. Molekulių simetriškumą patvirtino visų trijų junginių ^{13}C BMR spektruose pastebimi tik devyni pikai aromatinėse srityse, nors visuose trijuose junginiuose iš viso turėtų būti trisdešimt anglies atomų. Visų trijų junginių ^{19}F BMR spektruose matomas tik vienas signalas, maždaug ties 119 m.d.

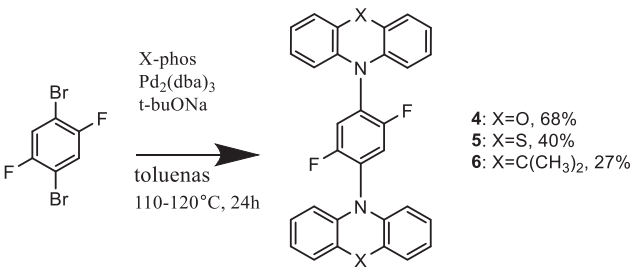

4.2.1 schema. 2,5-Dipakeisto 1,4-fenileno darinių **4**, **5** ir **6** molekulinė struktūra ir sintezė

4.2.1 pav., a–c, pateikti junginių **4**, **5** ir **6** tirpalų trijuose skirtinguose tirpikliuose (toluene, tetrahidrofurane ir acetonitrile) normalizuoti absorbcijos ir emisijos spektrai. Fenoksazino, fentiazino ir akridino fragmentai lemia absorbcijos juostas atitinkamai ties 310 nm ir 280 nm. Junginiui **4** pakeitus tirpiklį iš tolueno į acetonitrilą, absorbcijos kraštas pasislenka raudonos spalvos link nuo 3,15 eV iki 3,05 eV. Panašus absorbcijos krašto batochrominis poslinkis nuo 3,40 eV iki 3,30 eV matomas junginiui **6** pakeitus tolueną acetonitrilu. Tačiau, junginio **5** tirpalų padidinus tirpiklio poliškumą, priešingai nei PL, absorbcija beveik nepakito. Visų trijų junginių PL spektruose (**4.2.1 pav., a–d**) matomas ryškus poslinkis raudonos spalvos link didėjant tirpiklio poliškumui. Junginių PL spektrai atskleidė CT pobūdį. Nustatyta, kad junginių **4**, **5** ir **6** singuletinės krūvio perdavos būsenos (^{1}CT) energija yra atitinkamai 3,05 eV, 3,00 eV ir 3,37 eV. Junginių tirpaluose pakeitus tolueną acentronitrilu, **4** tirpalų emisijos pradžios energija pasikeitė labiausiai (0,28 eV), po to sekė **5** (0,13 eV) ir **6** (0,06 eV) tirpalai. Didelis batochrominis poslinkis junginio **4** spektruose rodo, kad jo CT būsena stabilizuojasi didėjant poliškumui[102].

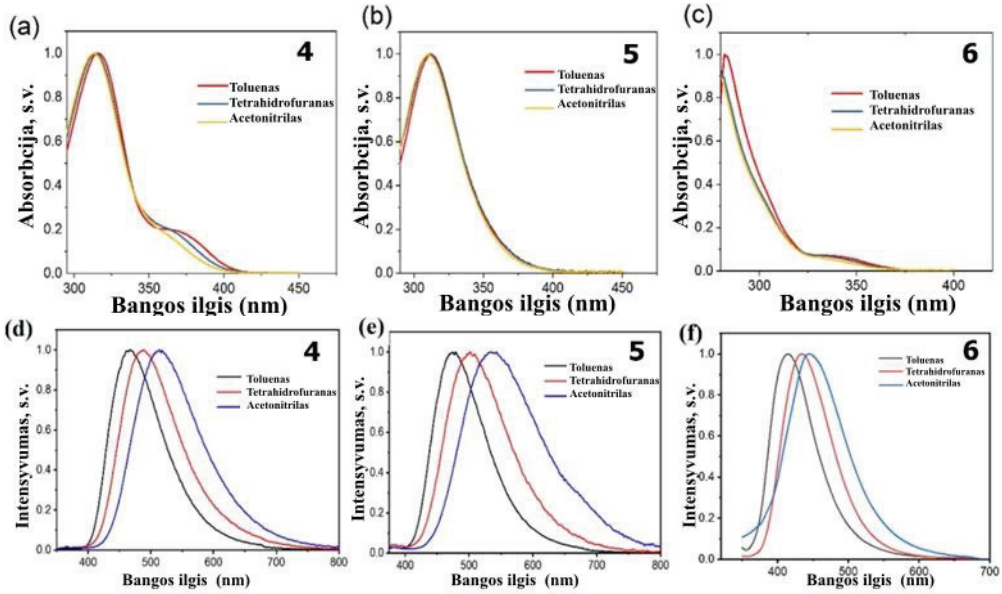

4.2.1 pav. Junginių tirpalų toluene, tetrahidrofurane ir acetonitrile UV spektrai (**4**(a), **5**(b), **6**(c)) ir fotoliuminescencijos spektrai (**4**(d), **5**(e), **6**(f))

Nustatyta, kad junginio **5** ir jo kietojo tirpalo zeonekse sluoksniai ore pasižymėjo mažiausiu *PLQY* (**4.2.1 lentelė**). Efektyvus singuletas-tripletas interkombinacinės konversijos (ISC) greitis, reikalingas efektyviam RTP[106], gali būti iš dalies atsakingas už mažas junginio **5** *PLQY* vertes. Sluoksnyje, kuriame **5** legiruotas zeoneksu, pastebėtas santykinai didelis RTP *PLQY* (**4.2.1 lentelė**). Po dedeguoninimo junginio **6** tirpalas turėjo 30 % ilgesnę emisijos gyvavimo trukmę, tai įrodo uždelstąją fluorescenciją. Emisijos gyvavimo trukmės pailgėjimas po dedeguoninimo buvo gerokai mažesnis **5** tirpale (15 %). Pašalinus deguonį iš junginio **4,** tirpalo emisijos gyvavimo trukmė pailgėjo 21 %. Ryšys tarp šių verčių ir junginio ΔE_{ST} verčių yra atvirkštinis.

4.2.1 lentelė. Darinių **4**–**6** fotofizikiniai parametrai

Junginys	**4**	**5**	**6**
	grynas/molekulinės dispersijos Zeonex‘e sluoksnis		
$PLQY^{ore}$, %	14/5	2/2	10/7
$PLQY^{vakuume}$, %	-/9	-/12,8	-/27,8
* $PLQY^{RTP}$	-	-/10,8	-
τ^{PL}(ore/argono atm.), ns	4,70/5,71	3,33/3,83	5,44/7,05
τ^{RTP}, ms	-	-/19,3	-

* apskaičiuojamas pagal $PLQY^{RTP} = PLQY^{vakuume} - PLQY^{ore}$, kur $PLQY^{vakuume} = PLQY^{ore} \times \text{plotas}^{vakuume}/\text{plotas}^{ore}$ kaip nustatyta literatūroje[107].

Iširtas fosforescencijos gesinimas deguonimi, nes kambario temperatūroje tai yra pagrindinis emisijos gesiklis[114]. Šiam poveikiui įvertinti 1 % koncentracijos **5** kietojo tirpalo zeonekse mėginys veiktas įvairiais deguonies ir azoto koncentracijų santykiais. RTP intensyvumas keitėsi po kiekvieno deguonies koncentracijos koregavimo (**4.2.2 pav**., a).

4.2.2 pav., a, matyti, kad, didėjant deguonies koncentracijai, RTP intensyvumas smarkiai mažėja. Esant azoto ir deguonies atmosferoms, pastebėtas didelis emisijos intensyvumo skirtumas ties 500 nm, inertinėje atmosferoje emisijos intensyvumas buvo 7,5 karto didesnis nei deguonies atmosferoje.

Junginio **5** PL spektrai, gauti esant skirtingoms deguonies koncentracijoms, buvo integruoti siekiant kiekybiškai nustatyti RTP jautrumą deguoniui. Gautos ploto po kreivėmis vertės buvo naudojamos tolesnėms analizėms. Taikėme šioms aplinkybėms modifikuotą Sterno ir Volmerio lygtį, nes surinkti duomenys aiškiai rodė netiesinę priklausomybę tarp RTP intensyvumo ir deguonies koncentracijos santykio (**4.2.2 pav**., b). Kai Sterno ir Volmerio taškai leidžiasi žemyn, paprastai daroma prielaida, kad yra kelios chromoforų rūšys, iš kurių viena yra jautri gesinimui, o kitos – ne. Šis derinys laikomas kelių rūšių su dinaminiu gesinimu[113].

Šie rezultatai rodo, kad 1 % junginio **5** molekulinės dispersijos zeonekse bandinys pasižymi dideliu jautrumu mažoms deguonies koncentracijoms (iki 0,2 %). Esant didesnei nei 0,2 % deguonies koncentracijai, jautrumas pradėjo mažėti. Dviejų jautrumo sričių buvimą galima paaiškinti molekuliniu heterogeniškumu, dėl kurio junginyje **5** susidaro dvi dominuojančios ^{3}LE būsenos ir ^{3}CT būsenos.

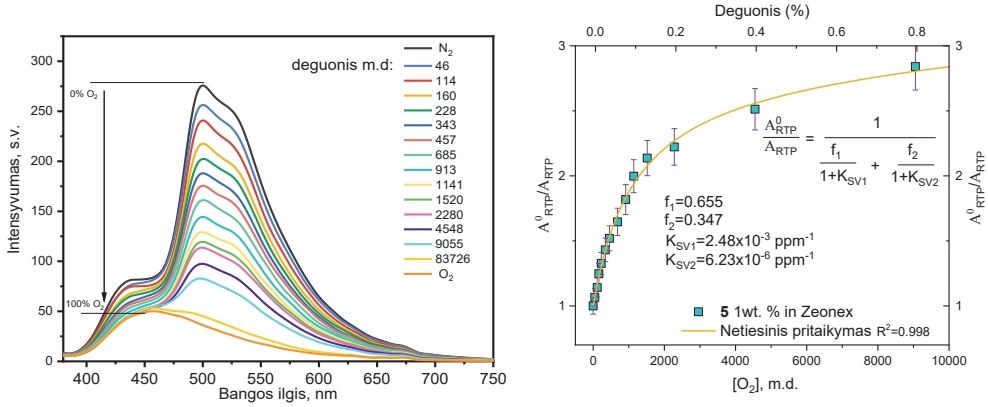

a) b)

4.2.2 pav. Junginio **5** 1 % molekulinės dispersijos Zeonekse RTP spektrai (a) ir Sterno ir Volmerio grafikas(b) esant skirtingoms deguonies koncentracijoms

4.3 Junginių, turinčių akceptorinį piridazino fragmentą ir 9,9-dimetil-9,10-dihidroakridino ir fenoksazino donorinius fragmentus, sintezė, charakterizavimas ir fotofizikinė analizė

Šis skyrius parengtas pagal straipsnį, paskelbtą žurnale *Materials*, 2023, 16, 1294. Taikant Buchvaldo ir Hartvigo kopuliavimo reakciją, susintetinti du junginiai, turintys akceptorinį piridazino fragmentą ir 9,9-dimetil-9,10-dihidroakridino arba fenoksazino donorinį fragmentą (**4.3.1 schema**). Gauti junginiai **7** ir **8**, kurių išeiga atitinkamai 21,8 % ir 6,4 %.

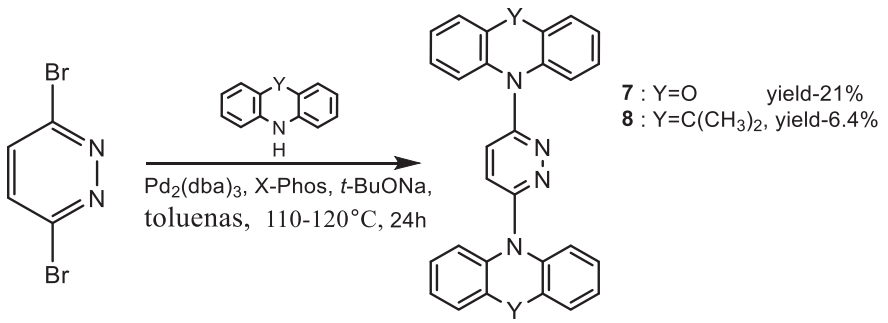

4.3.1 schema. 2,5-Dipakeisto piridazino darinių sintezė

Piridazino darinių terminės savybės ištirtos DSK ir TGA metodais. Jų terminės charakteristikos apibendrintos **4.3.1 lentelėje**. Du tiksliniai junginiai išskirti kristalinės medžiagos. Pirmojo DSK kaitinimo metu matomi endoterminiai lydymosi signalai. Antrojo kaitinimo metu junginio **7** kreivėje matomas kristalizacijos ir vėliau lydymosi signalai. Junginys **8** gali būti transformuotas į amorfinę būseną kaitinant atvėsintą lydalą, kaip vyksta antrojo DSK kaitinimo metu. TGA matavimų metu pastebėtas visiškas abiejų junginių masės sumažėjimas, t. y. mėginiai sublimavosi, o ne termiškai suiro.

4.3.1 lentelė. Junginių **7** ir **8** terminės charakteristikos

Junginys	T_{ID}, ℃ [1]	T_g, ℃	T_{cr}, ℃ [2]	T_m, ℃ [3]
7	314	-	188	248
8	336	80	133	231

[1] 5 % masės nuostolių temperatūra, nustatyta TGA metodu; [2] DSC metodu nustatytos kristalizacijos temperatūros; [3] lydymosi temperatūros, nustatytos DSC metodu.

4.3.2 lentelė. Junginių **7** ir **8** fotofizikinės charakteristikos

Junginys	λ_a, nm[1]	λ_e, nm[2]	Φ[3]	E_{S1}, eV[4]	E_{T1}, eV[4]	ΔE_{ST}[4]
7	308/308	*ca.* 420, 618/398, 639/565	<0,01	2,68	2,59	0,09
8	*ca.* 280/290	353, 535/346, 561/517	<0,01	2,64	2,29	0,35

[1] Junginių tirpalų toluene/THF absorbcijos spektrų maksimumai; [2] junginių tirpalų toluene / THF ir sluoksnių emisijos spektrų maksimumai; [3] *PLQY* deguonies neturinčių tolueno tirpalų; [4] gauta iš junginių sluoksnių spektrinių duomenų, užfiksuotų 77 K temperatūroje, kai nėra deguonies.

4.3.1 pav., a, b, pateikti atitinkamai **7** ir **8** tirpalų absorbcijos ir emisijos spektrai. Spektrinės charakteristikos pateiktos **4.3.2 lentelėje**. Junginių 7 ir 8 tirpaluose nepolinį tolueno tirpiklį pakeitus poliniu THF, absorbcijos smailių padėtys iš esmės nepakito.

Junginių tirpalų PL spektruose, užfiksuotuose esant skirtingiems sužadinimo bangos ilgiams, matomos dvi skirtingos emisijos juostos UV ir žalioje spektro srityse. Terpės poliškumas daro įtaką junginių fotofizikinėms savybėms (žr. **4.3.2 lentelę**). Donorinio fragmento lokaliai sužadintos (LE) būsenos emisija yra susijusi su PL juosta UV srityje, kuri išsidėsto nuo 400 iki 450 nm. Jai nebūdingas teigiamas solvatochromizmas, kurį sukelia tirpiklio poliškumo padidėjimas. Didėjant tirpiklio poliškumui, mažos energijos emisijos juosta, esanti maždaug ties 500–625 nm, pasislinko raudonos spalvos link, rodančiu intramolekulinio krūvio pernašos (ICT) būseną. Skirtingi sužadinimo bangos ilgiai beveik nekeičia spektrinio pasiskirstymo. Tai atitinka daktaro Michaelio Kashos kriterijų[115], kuris draudžia tam tikrų optinių centrų sužadinimo galimybę, kuri turėtų įtakos eksperimentinių duomenų analizei. Grynų junginių sluoksnių spektruose ICT smailės maksimumai sutampa su atitinkamų tolueno tirpalų ICT juostos maksimumais. Tai rodo, kad poliškumas, procesai, susiję su agregacija, ir tarpmolekulinė sąveika esant kietai būsenai neturi įtakos junginių ICT. Akridinilpakeisto junginio **8** emisija pasislinkusi mėlynos spalvos link, palyginti su junginio **7**, turinčio stipresnį donorinį fenoksazino fragmentą, emisija. Junginių **7** ir **8** dedeguonintuose tolueno tirpaluose *PLQY* nesiekė 1 %.

Atitinkamuose PL smailės bangos ilgiuose užregistruotos junginių **7** ir **8** dedeguonintų tolueno tirpalų PL gesimo kreivės (**4.3.2 pav., c**). Pagrindinė informacija apie PL gesimus pateikta **4.3.3 lentelėje**. Pademonstruotas puikus ryšys tarp **7** LE gyvavimo trukmės ir PL gesimo kreivės greitosios fluorescencijos komponento gyvavimo trukmės, išmatuotos esant 621 nm. Be to, **7** ir **8** tirpalų ICT juostos pasižymėjo atitinkamai 93 ir 143 ns emisijos gyvavimo trukme. Tokia gyvavimo trukmė susijusi su vadinamąja greita uždelstąja emisija, arba TADF [89].

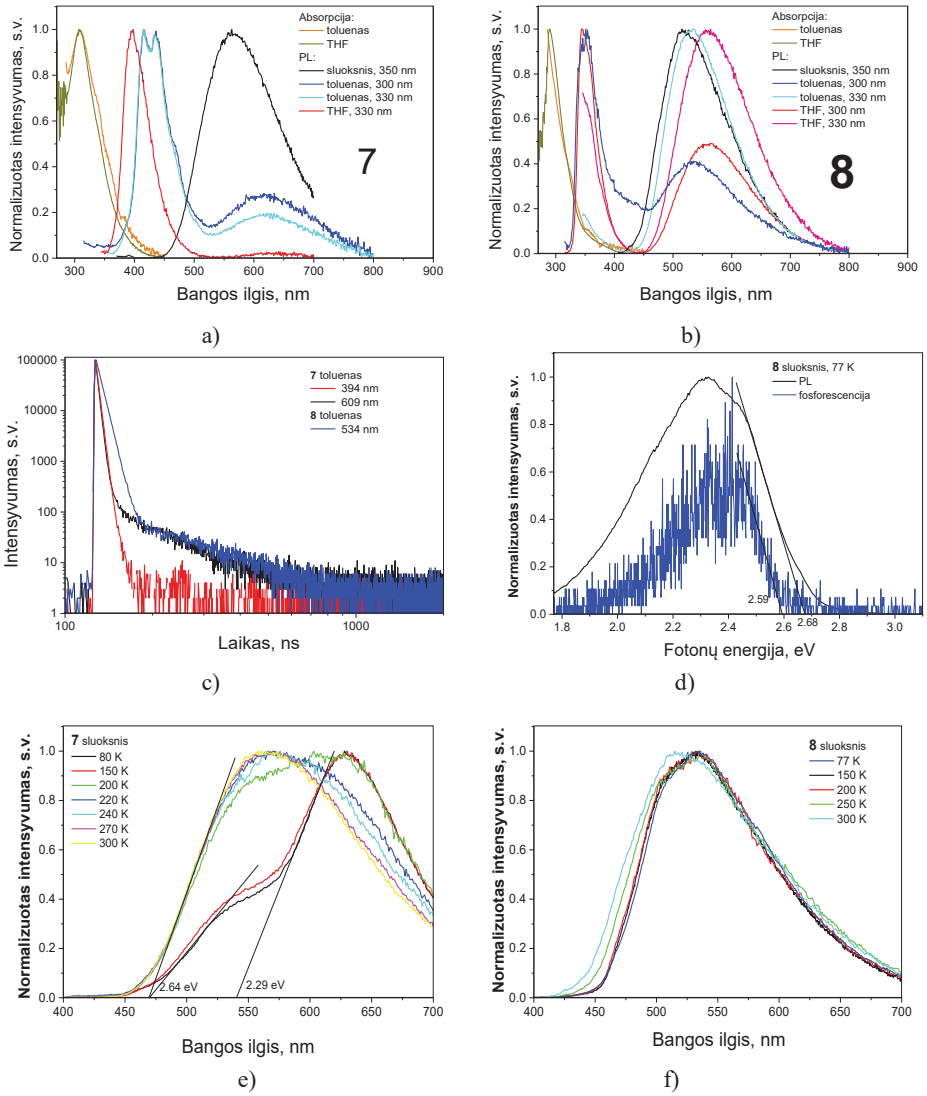

4.3.2 pav. Junginių **7** (a) ir **8** (b) tirpalų toluene, THF ir sluoksnių UV ir PL spektrai; junginių deguonies neturinčių tolueno tirpalų PL gesimo kreivės (c); junginio **8** sluoksnio PL ir fosforescenciniai spektrai, užregistruoti esant 77 K (d); junginių **7** (e) ir **8** (f) sluoksnių PL spektrai, užfiksuoti skirtingose temperatūrose inertinėje aplinkoje

4.3.3 lentelė. Junginių **7** ir **8** tirpalų toluene fotofizikinės charakteristikos

Junginys[1]	λ, **nm**[2]	**Gyvavimo trukmė, ns**[3]	k_{RISC}, s^{-1}	k_{ISC}, s^{-1}			χ^2 [4]
7	394	2,85	-	-			1,043
7	609	2,49 (85,44 %), 9,75 (6,49 %), 92,86 (8,07 %)	$9,5 \cdot 10^5$	$2,2 \cdot 10^8$			1,166
8	534	6 (95,52 %), 142,96 (4,48 %)	$3,3 \cdot 10^5$	$1,6 \cdot 10^8$			1,034

[1] Deguonies neturinčių tolueno tirpalų; [2] bangos ilgis, kuriame atliktas matavimas; [3] intensyvumo amplitudė skliausteliuose; [4] svertinė tinkamumo taškų kvadratinių nuokrypių suma.

Norint vienareikšmiškai nustatyti, kad RTP nėra, gauti **7** ir **8** sluoksnių PL spektrai esant įvairioms temperatūroms. Pagal atitinkamų greitosios fluorescencijos ir fosforescencijos juostų pradžių bangų ilgius nustatyti pirmųjų sužadintų singuletinės ir triletinės būsenų energijos lygiai (**4.3.2 pav**., **d, e**). Kaitinant fosforescencijos komponentas išnyko, liko tik ICT juosta (**4.3.2 pav., e, f**). TADF reiškinio nepatvirtina junginio **7** išmatuotas 0,35 eV ΔE_{ST} (**4.3.2 pav., e**). Šioje situacijoje RISC labai priklauso nuo energiškai artimų ^{3}CT ir ^{3}LE būsenų sukinio-orbitinės sąsajos. Dėl mažo *PLQY* sunku eksperimentiškai aptikti ^{3}LE. Kaip ir tikėtasi, junginio **8**[118] pirmoji tripletinė sužadintoji būsena, kurios energija 2,59 eV, yra artima 1CT energijai, kuri yra 2,68 eV, o tai yra naudinga TADF. k_{RISC} ir k_{ISC} vertės vertintos pagal PL irimo kreivių atitikimo duomenis[119]. Gauti duomenys pateikti **4.3.3 lentelėje**. Junginio **7** k_{RISC} vertė siekė beveik 10^6 s^{-1}, kuri šiek tiek mažesnė už moderniausių TADF emiterių vertes[119,120,121].

4.4 Lanksčių organinių šviesos diodų su nelegiruotais TADF spinduoliais, turinčiais sulfobenzimido fragmentus, emisijos spalvos ir efektyvumo įvertinimas

Šis skyrius parengtas pagal straipsnį, paskelbtą žurnale *Dyes and Pigments*, 2022, **208**, 110841. Dvipakopės sintezės metu gautas junginys **9** (**4.4.1 schema**). Pirmosios pakopos metu gautas 9-(3-brompropil)-9H-karbazolas[122]. Artajame etape alkilgrandinėje esantis bromo atomas pakeistas sulfobenzimido anijonu susidarant junginiui **9**. Išskirtos kristalinės medžiagos molekulinė struktūra patvirtinta ^{1}H ir ^{13}C BMR, masių spektrometrija ir monokristalo rentgeno tyrimu.

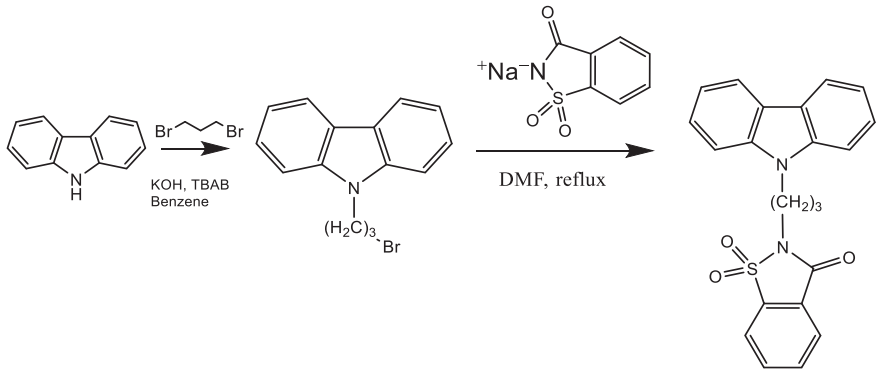

4.4.1 schema. Junginio **9** sintezės eiga

Junginio **9** terminės savybės tirtos DSK ir TGA metodais. TGA parodė santykinai aukštą 5 % masės nuostolių temperatūrą – 314 °C (**4.4.1 pav**., **a**). Visiškas bandinio masės netekimas TGA eksperimento metu rodo sublimavimą, bet ne terminį skilimą. Junginio **9** DSK termogramose matomos endoterminė lydymosi smailė 175 °C temperatūroje pirmojo kaitinimo metu, o antrojo kaitinimo metu ties 172 °C. Šį skirtumą gali lemti tai, kad egzistuoja dvi metastabilios kristalinės formos. Kadangi šaldymo metu kristalizacijos nepastebėta, medžiaga konsoliduota amorfinėje fazėje. Antrojo kaitinimo metu 41 °C temperatūroje matomas stiklėjimas, o 132 °C temperatūroje – egzoterminis kristalizacijos smailės signalas (**4.4.1 pav**., a).

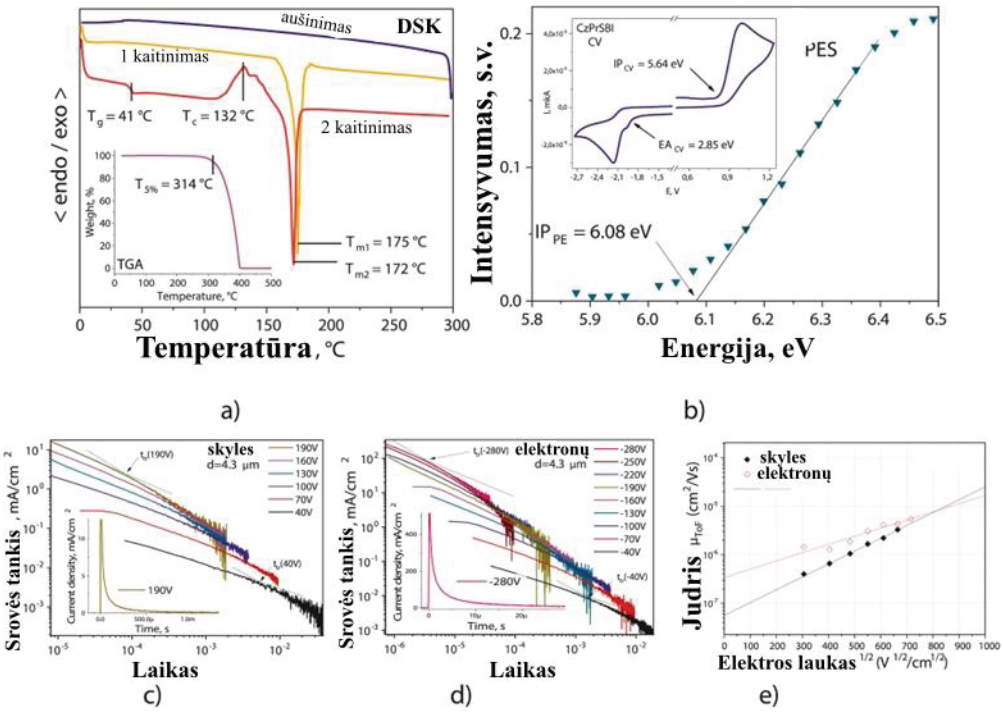

4.4.1 pav. (a) Junginio **9** DSK termogramos. Intarpas: TGA kreivė. (b) Junginio **9** kietojo sluoksnio elektronų fotoemisijos spektras. Intarpas: junginio tirpalo DMF ciklinės voltamperometrijos kreivė. Junginio **9** sluoksnio TOF kreivės skylėms (c) ir elektronams (d), užregistruotos esant skirtingoms taikomoms įtampoms, ir krūvininkų dreifinio judrio priklausomybė nuo elektros lauko stiprio (e)

Junginio **9** tirpalo DMF jonizacijos potencialas (IP) ir gimiringumas elektronui (EA) nustatyti ciklinės voltampertometrijos metodu (**4.4.1 pav., b**). $IP_{CV} = (E_{ox} + 4.8)$ ir $EA_{CV} = (E_{red} + 4{,}8)$ formulės naudotos IP_{CV} ir EA_{CV} apskaičiuoti. E_{ox} ir E_{red} yra atitinkamai elektrocheminės oksidacijos ir redukcijos pradžios potencialai. Ferocenas redokso potencialas naudotas kaip standartas. Esant atitinkamai 0,84 eV ir –1,95 eV, junginys **9** pasižymėjo negrįžtama oksidacija ir redukcija. Oksidacijos proceso negrįžtamumą greičiausiai lėmė neapsaugotos C-3 ir C-6 padėtys karbazolo fragmente[123]. Nustatyta, kad elektrocheminis juostos tarpas E_g^{CV} yra 2,79 eV, o IP_{CV} ir EA_{CV} vertės yra atitinkamai 5,64 eV ir 2,85 eV.

Naudojant elektronų fotoemisijos spektrometriją nustatytas junginio **9** sluoksnio jonizacijos potencialas (IP_{PE}) – 6,08 eV (**4.4.1 pav**., b). Pasinaudojant lygtimi $EA_{PE} = IP_{PE} - E_g^{opt}$ apskaičiuotas junginio gimiringumas elektronui (EA_{PE}) yra 2,65 eV. Optinis juostos tarpas E_g^{opt} (3,43 eV) nustatytas iš kietojo sluoksnio absorbcijos spektro krašto. Manoma, kad stipresnės tarpmolekulinės sąveikos esant kietai būsenai

lemia santykinai didelį skirtumą tarp *IP* ir *EA* verčių, gautų junginio tirpalo ir kieto plono sluoksnio atveju.

Lėkio trukmės (ToF) metodu ištirtos junginio **9** plonų sluoksnių krūvininkų pernašos savybės. Stebėti skylių ir elektronų srovės tankio priklausomybės nuo trukmės parodė, kad krūvininkų pernaša buvo labai dispersinė (**4.4.1 pav., c, d**). Palyginti su verte, užfiksuota esant mažoms įtampoms, mažesnė lėkio trukmės (t_{tr}) vertė gauta esant didelėms įtampoms (**4.4.1 pav., c, d**). Junginio sluoksnio skylių judris buvo $3{,}2 \times 10^{-6}$ $cm^2/V \times s$, o elektronų judris šiek tiek didesnis – $4{,}4 \times 10^{-6}$ $cm^2/V \times s$, esant $4{,}43 \times 10^5$ V/cm stiprio elektros laukui (**4.4.1 pav., e**). Pritaikius eksperimentines krūvininkų dreifinio judrio priklausomybes nuo elektros lauko pagal Poole ir Frenkelio prognozę $\mu = \mu_0^{eaE^{1/2}}$ [124], gautos labai skirtingos skylių ir elektronų nulinio lauko judrio (μ_0) vertės – $5{,}8 \times 10^{-8}$ ir $3{,}4 \times 10^{-7}$ $cm^2/V \times s$.

Siekiant ištirti junginio **9** kaip TADF spinduolio veikimą, terminio vakuuminio nusodinimo metodu pagaminti OLED su tokia struktūra CuI/TPD/CzPrSBI/TSPO1/TPBi/Ca/Al. Kaip skylių injekcinis sluoksnis naudotas CuI sluoksnis[145], o kaip elektronus pernešantis sluoksnis – 2,2′,2"-(1,3,5-benzinitril)-tris(1-fenil-1H-benzimidazolas) (TPBi)[146]. TPD [147] ir TSPO1 [148,149] naudoti atitinkamai eksitonus blokuojančiam ir skyles pernešančiam sluoksniams, siekiant išlaikyti krūvininkų nešėjų pusiausvyrą emisiniame sluoksnyje. Junginys **9** naudotas kaip spinduolis. Kaip katodas buvo kalcio sluoksnis, padengtas 200 nm aliuminio sluoksniu.

Prietaisai pasižymėjo nestruktūriniais EL spektrais su maksimumais 490–504 nm srityje ir buvo panašūs į gryno junginio **9** sluoksnio PL spektrus (**4.4.2 pav., a,c**). Didėjant lanksčiojo OLED lenkimo kampui, didėja santykinis peties, kurio maksimumas ties 630 nm, intensyvumas (**4.4.2 pav., c**). Tai paaiškinama tarpmolekulinio eksciplekso susidarymu tarp vienos junginio **9** molekulės donorinio fragmento ir kitos molekulės akceptorinio fragmento. Smailės intensyvumas didėjo keičiantis lenkimo kampui lanksčiuose bandiniuose. Kai lenkimo kampas pasiekė 50°, EL intensyvumas vėl tapo toks pat kaip OLED su stikliniu pagrindu. Mechaninio poveikio (mūsų atveju – lenkimo) sukeltas priverstinis donorinių ir akceptorinių fragmentų artumas lemia mechanochrominę spinduolio **9** liuminescenciją lanksčiuose OLED, kuri sustiprina tarpmolekulinių ekscipleksų susidarymą.

Prietaisas, pagamintas ant stiklinio pagrindo, pasižymėjo geriausiomis eksploatacinėmis savybėmis: didžiausias srovės efektyvumas, galios efektyvumas ir išorinis kvantinis efektyvumas (*EQE*) atitinkamai 11,0 cd A^{-1}, 3,0 lm W^{-1} ir 4,3%, (**4.4.1 lentelė** ir **4.4.2 pav**.).

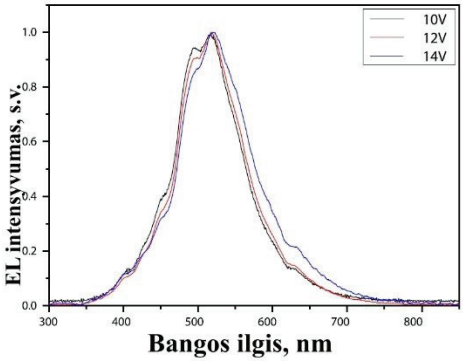

a)

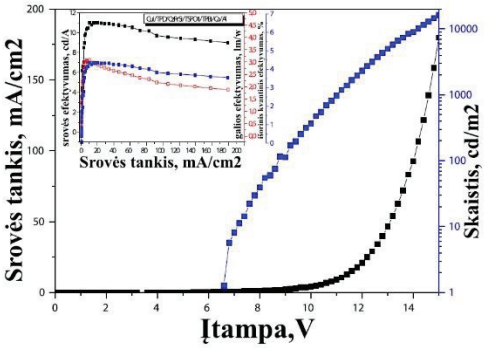

b)

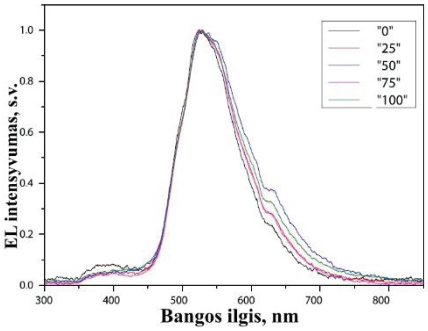

c)

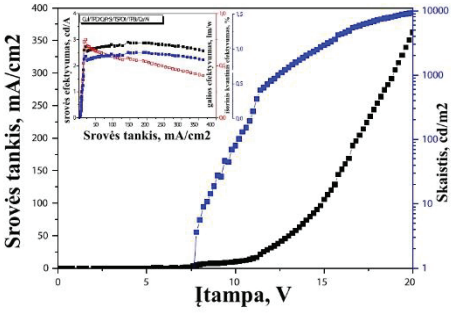

d)

4.4.2 pav. OLED elektroliuminescencijos spektrai, užregistruoti esant skirtingoms įtampoms (a) ir skirtingam lenkimo kampui (c). Prietaisų (b – stiklo substratas, d – lankstus substratas) srovės tankis-įtampa ir skaistis-įtampa, galios efektyvumas – srovės tankis, srovės efektyvumas – srovės tankis ir išorinis kvantinis efektyvumas – prietaisų srovės tankio priklausomybių grafikai

4.4.1 lentelė. OLED, suformuotų ant stiklo ir lanksčių substratų, charakteristikos

Prietaiso substratas	V_{on}, **V**	**Maks. skaistis, cd m^{-2}**	**Srovės efektyvumas, cd A^{-1}**	**Galios efektyvumas, lm W^{-1}**	***EQE*, %**
			esant 1000/maks. cd m^{-2}		
Stiklas	6,4	16000	11,0/9,0	3,0/1,8	4,3/3,5
Lankstus	7,4	9000	2,6/2,5	0,6/0,4	0,8/0,9

5. LIST OF REFERENCES

1 Zhou, X. *et al.* Dewetting-Assisted Patterning of Organic Semiconductors for Micro-OLED Arrays with a Pixel Size of 1 μm. *Small Methods* [interactive]. 2022, vol. 6 (4), 2101509. Access via the Internet: <https://doi.org/10.1021/10.1002/smtd.202101509>.

2 Song, J. *et al.* Organic Light-Emitting Diodes: Pushing Toward the Limits and Beyond. *Advanced Materials* [interactive]. 2020, vol. 32 (35), 1907539. Access via the Internet: <https://doi.org/10.1021/10.1002/adma.201907539>.

3 Pode, R. Organic light emitting diode devices: An energy efficient solid state lighting for applications. *Renewable and Sustainable Energy Reviews* [interactive]. 2020, vol. 133, 110043. Access via the Internet: <https://doi.org/10.1021/10.1016/j.rser.2020.110043>.

4 Hong, Q. The working principle, application and comparative analysis of OLED and OPV. *Highlights in Science, Engineering and Technology* [interactive]. 2022, vol. 23, 34–37. Access via the Internet: <https://doi.org/10.1021/10.54097/hset.v23i.3124>.

5 Chen, J.J. Realizing Thin-Film Encapsulation's Benefits for Large-Scale OLED Panels. *Information Display* [interactive]. 2021, vol. 37 (2), 6–9. Access via the Internet: <https://doi.org/10.1021/10.1002/msid.1193>.

6 Burgués-Ceballos, I. *et al.* Transparent organic photovoltaics: A strategic niche to advance commercialization. *Joule* [interactive]. 2021, vol. 5 (9), 2261–2272. Access via the Internet: <https://doi.org/10.1021/10.1016/j.joule.2021.07.004>.

7 Meng, D. *et al.* Near-Infrared Materials: The Turning Point of Organic Photovoltaics. *Advanced Materials* [interactive]. 2022, vol. 34 (10). Access via the Internet: <https://doi.org/10.1021/10.1002/adma.202107330>.

8 Bernardo, G. *et al.* Progress in Upscaling Organic Photovoltaic Devices. *Advanced Energy Materials* [interactive]. 2021, vol. 11 (23), 2100342. Access via the Internet: <https://doi.org/10.1021/10.1002/aenm.202100342>.

9 Chen, Y. *et al.* High Performance Photovoltaic Applications Using Solution-Processed Small Molecules. *Accounts of Chemical Research* [interactive]. 2013, vol. 46 (11), 2645–2655. Access via the Internet: <https://doi.org/10.1021/10.1021/ar400088c>.

10 Małachowski, M. *et al.* Organic field-effect transistors. *Opto-Electronics Review* [interactive]. 2010, vol. 18 (2). Access via the Internet: <https://doi.org/10.1021/10.2478/s11772-010-0008-9>.
11 Yamashita, Y. Organic semiconductors for organic field-effect transistors. *Science and Technology of Advanced Materials* [interactive]. 2009, vol. 10 (2), 024313. Access via the Internet: <https://doi.org/10.1021/10.1088/1468-6996/10/2/024313>.
12 Wang, D. *et al.* Electrolytic Gated Organic Field-Effect Transistors for Application in Biosensors—A Review. *Electronics* [interactive]. 2016, vol. 5 (1), 9. Access via the Internet: <https://doi.org/10.1021/10.3390/electronics5010009>.
13 Zhang, Z. *et al.* Phase segregation controlled semiconductor crystallization for organic thin film transistors. *Journal of Science: Advanced Materials and Devices* [interactive]. 2020, vol. 5 (2), 151–163. Access via the Internet: <https://doi.org/10.1021/10.1016/j.jsamd.2020.05.004>.
14 Cavallari, M.R. *et al.* Organic Thin-Film Transistors as Gas Sensors: A Review. *Materials* [interactive]. 2020, vol. 14 (1), 3. Access via the Internet: <https://doi.org/10.1021/10.3390/ma14010003>.
15 Lin, P. *et al.* Organic Thin-Film Transistors for Chemical and Biological Sensing. *Advanced Materials* [interactive]. 2012, vol. 24 (1), 34–51. Access via the Internet: <https://doi.org/10.1021/10.1002/adma.201103334>.
16 Prime, D. *et al.* Overview of organic memory devices. *Philosophical Transactions of the Royal Society A: Mathematical, Physical and Engineering Sciences* [interactive]. 2009, vol. 367 (1905), 4141–4157. Access via the Internet: <https://doi.org/10.1021/10.1098/rsta.2009.0165>.
17 Petty, M.C. Organic electronic memory devices. In: *Handbook of Organic Materials for Electronic and Photonic Devices*. Elsevier, 2019, 843–874. Access via the Internet: <https://doi.org/10.1021/10.1016/B978-0-08-102284-9.00026-7>.
18 Heremans, P. *et al.* Polymer and Organic Nonvolatile Memory Devices. *Chemistry of Materials* [interactive]. 2011, vol. 23 (3), 341–358. Access via the Internet: <https://doi.org/10.1021/10.1021/cm102006v>.
19 He, J. *et al.* Three-terminal organic memory devices. *Journal of Applied Physics* [interactive]. 2005, vol. 97 (6), 064507. Access via the Internet: <https://doi.org/10.1021/10.1063/1.1866496>.
20 Chuang, M.-Y. *et al.* Room-temperature-operated organic-based acetone gas sensor for breath analysis. *Sensors and Actuators B:*

Chemical [interactive]. 2018, vol. 260, 593–600. Access via the Internet: <https://doi.org/10.1021/10.1016/j.snb.2017.12.168>.

21 Huang, W. *et al.* Wearable Organic Nano-sensors. In: *Flexible and Wearable Electronics for Smart Clothing*. Wiley, 2020, 1–27. Access via the Internet: <https://doi.org/10.1021/10.1002/9783527818556.ch1>.

22 Lochner, C.M. *et al.* All-organic optoelectronic sensor for pulse oximetry. *Nature Communications* [interactive]. 2014, vol. 5 (1), 5745. Access via the Internet: <https://doi.org/10.1021/10.1038/ncomms6745>.

23 Lee, Y.H. *et al.* Recent advances in organic sensors for health self-monitoring systems. *Journal of Materials Chemistry C* [interactive]. 2018, vol. 6 (32), 8569–8612. Access via the Internet: <https://doi.org/10.1021/10.1039/C8TC02230E>.

24 Song, H.W. *et al.* Recent Advances in Smart Organic Sensors for Environmental Monitoring Systems. *ACS Applied Electronic Materials* [interactive]. 2023, vol. 5 (1), 77–99. Access via the Internet: <https://doi.org/10.1021/10.1021/acsaelm.2c01315>.

25 Caroleo, F. *et al.* Advances in Optical Sensors for Persistent Organic Pollutant Environmental Monitoring. *Sensors* [interactive]. 2022, vol. 22 (7), 2649. Access via the Internet: <https://doi.org/10.1021/10.3390/s22072649>.

26 Bisri, S.Z. *et al.* The pursuit of electrically-driven organic semiconductor lasers. *Journal of Materials Chemistry C* [interactive]. 2014, vol. 2 (16), 2827. Access via the Internet: <https://doi.org/10.1021/10.1039/c3tc32206h>.

27 Yan, C.-C. *et al.* Organic Lasers Harnessing Excited State Intramolecular Proton Transfer Process. *ACS Photonics* [interactive]. 2020, vol. 7 (6), 1355–1366. Access via the Internet: <https://doi.org/10.1021/10.1021/acsphotonics.0c00407>.

28 Kuehne, A.J.C. *et al.* Organic Lasers: Recent Developments on Materials, Device Geometries, and Fabrication Techniques. *Chemical Reviews* [interactive]. 2016, vol. 116 (21), 12823–12864. Access via the Internet: <https://doi.org/10.1021/10.1021/acs.chemrev.6b00172>.

29 Chénais, S. *et al.* Recent advances in solid-state organic lasers. *Polymer International* [interactive]. 2012, vol. 61 (3), 390–406. Access via the Internet: <https://doi.org/10.1021/10.1002/pi.3173>.

30 Morales-Vidal, M. High performance thin film organic lasers for sensing applications. *Optica Pura y Aplicada* [interactive]. 2019, vol.

52 (3), 1–9. Access via the Internet: <https://doi.org/10.1021/10.7149/OPA.52.3.51023>.
31 Álvarez-Conde, J. *et al.* Organic Semiconductor Micro/Nanocrystals for Laser Applications. *Molecules* [interactive]. 2021, vol. 26 (4), 958. Access via the Internet: <https://doi.org/10.1021/10.3390/molecules26040958>.
32 Zheng, C. *et al.* A Flexible Self-Powered Sensing Element with Integrated Organic Thermoelectric Generator. *Advanced Materials Technologies* [interactive]. 2019, vol. 4 (8), 1900247. Access via the Internet: <https://doi.org/10.1021/10.1002/admt.201900247>.
33 Zhang, Y. *et al.* Flexible Organic Thermoelectric Materials and Devices for Wearable Green Energy Harvesting. *Polymers* [interactive]. 2019, vol. 11 (5), 909. Access via the Internet: <https://doi.org/10.1021/10.3390/polym11050909>.
34 Mukaida, M. *et al.* Stable organic thermoelectric devices for self-powered sensor applications. *Journal of Materials Chemistry A* [interactive]. 2020, vol. 8 (43), 22544–22556. Access via the Internet: <https://doi.org/10.1021/10.1039/D0TA08598G>.
35 Masoumi, S. *et al.* Organic-based flexible thermoelectric generators: From materials to devices. *Nano Energy* [interactive]. 2022, vol. 92, 106774. Access via the Internet: <https://doi.org/10.1021/10.1016/j.nanoen.2021.106774>.
36 Ma, H. *et al.* Room-Temperature Phosphorescence in Metal-Free Organic Materials. *Annalen der Physik* [interactive]. 2019, vol. 531 (7), 1800482. Access via the Internet: <https://doi.org/10.1021/10.1002/andp.201800482>.
37 Thomas, H. *et al.* Aromatic Phosphonates: A Novel Group of Emitters Showing Blue Ultralong Room Temperature Phosphorescence. *Advanced Materials* [interactive]. 2020, vol. 32 (19), 2000880. Access via the Internet: <https://doi.org/10.1021/10.1002/adma.202000880>.
38 Zhang, Z.-Y. *et al.* Ultralong room-temperature phosphorescence of a solid-state supramolecule between phenylmethylpyridinium and cucurbit[6]uril. *Chemical Science* [interactive]. 2019, vol. 10 (33), 7773–7778. Access via the Internet: <https://doi.org/10.1021/10.1016/j.ccr.2019.213107>.
39 She, P. *et al.* Lifetime-tunable organic persistent room-temperature phosphorescent salts for large-area security printing. *Science China Materials* [interactive]. 2021, vol. 64 (6), 1485–1494. Access via the Internet: <https://doi.org/10.1021/10.1007/s40843-020-1544-6>.

40 Sun, Y. *et al.* Ultralong lifetime and efficient room temperature phosphorescent carbon dots through multi-confinement structure design. *Nature Communications* [interactive]. 2020, vol. 11 (1), 5591. Access via the Internet: <https://doi.org/10.1021/10.1038/s41467-020-19422-4>.

41 Guo, R. *et al.* Matrix-Assisted Catalytic Printing for the Fabrication of Multiscale, Flexible, Foldable, and Stretchable Metal Conductors. *Advanced Materials* [interactive]. 2013, vol. 25 (24), 3343–3350. Access via the Internet: <https://doi.org/10.1021/10.1002/adma.201301184>.

42 Tian, Z. *et al.* Multilevel Data Encryption Using Thermal-Treatment Controlled Room Temperature Phosphorescence of Carbon Dot/Polyvinylalcohol Composites. *Advanced Science* [interactive]. 2018, vol. 5 (9), 1800795. Access via the Internet: <https://doi.org/10.1021/10.1002/advs.201800795>.

43 Yin, Y. *et al.* Efficient non-doped phosphorescent orange, blue and white organic light-emitting devices. *Scientific Reports* [interactive]. 2014, vol. 4 (1), 6754. Access via the Internet: <https://doi.org/10.1021/10.1038/srep06754>.

44 Lamansky, S. *et al.* Molecularly doped polymer light emitting diodes utilizing phosphorescent Pt(II) and Ir(III) dopants. *Organic Electronics* [interactive]. 2001, vol. 2 (1), 53–62. Access via the Internet: <https://doi.org/10.1021/10.1016/S1566-1199(01)00007-6>.

45 Wang, X. *et al.* Electrophosphorescence from substituted poly(thiophene) doped with iridium or platinum complex. *Thin Solid Films* [interactive]. 2004, vol. 468 (1–2). Access via the Internet: <https://doi.org/10.1021/10.1016/j.tsf.2004.05.095>.

46 Facendola, J.W. *et al.* Synthesis and characterization of phosphorescent platinum and iridium complexes with cyclometalated corannulene. *Dalton Transactions* [interactive]. 2015, vol. 44 (18), 8456–8466. Access via the Internet: <https://doi.org/10.1021/10.1039/C4DT03541K>.

47 To, W.-P. *et al.* Recent Advances in Metal-TADF Emitters and Their Application in Organic Light-Emitting Diodes. *Frontiers in Chemistry* [interactive]. 2020, vol. 8. Access via the Internet: <https://doi.org/10.1021/10.3389/fchem.2020.00653>.

48 Fang, F. *et al.* Thermally Activated Delayed Fluorescence Material: An Emerging Class of Metal-Free Luminophores for Biomedical Applications. *Advanced Science* [interactive]. 2021, vol. 8 (24),

2102970. Access via the Internet: <https://doi.org/10.1021/10.1002/advs.202102970>.
49 Wada, Y. *et al.* Adamantyl Substitution Strategy for Realizing Solution-Processable Thermally Stable Deep-Blue Thermally Activated Delayed Fluorescence Materials. *Advanced Materials* [interactive]. 2018, vol. 30 (8), 1705641. Access via the Internet: <https://doi.org/10.1021/10.1002/adma.201705641>.
50 Skaisgiris, R. *et al.* Origin of dual emission in σ-bridged donor–acceptor TADF compounds. *Journal of Materials Chemistry C* [interactive]. 2019, vol. 7 (40), 12601–12609. Access via the Internet: <https://doi.org/10.1021/10.1039/C9TC03548F>.
51 Olivier, Y. *et al.* Dynamic nature of excited states of donor–acceptor TADF materials for OLEDs: how theory can reveal structure–property relationships. *Journal of Materials Chemistry C* [interactive]. 2017, vol. 5 (23), 5718–5729. Access via the Internet: <https://doi.org/10.1021/10.1039/C6TC05075A>.
52 Naqvi, B.A. *et al.* What Controls the Orientation of TADF Emitters? *Frontiers in Chemistry* [interactive]. 2020, vol. 8. Access via the Internet: <https://doi.org/10.1021/10.3389/fchem.2020.00750>.
53 Zhao, J. *et al.* Efficient triplet harvesting in fluorescence–TADF hybrid warm-white organic light-emitting diodes with a fully non-doped device configuration. *Journal of Materials Chemistry C* [interactive]. 2018, vol. 6 (15), 4257–4264. Access via the Internet: <https://doi.org/10.1021/10.1039/C8TC01210E>.
54 Sagara, Y. *et al.* Highly Efficient Thermally Activated Delayed Fluorescence Emitters with a Small Singlet–Triplet Energy Gap and Large Oscillator Strength. *Chemistry Letters* [interactive]. 2015, vol. 44 (3), 360–362. Access via the Internet: <https://doi.org/10.1021/10.1246/cl.141054>.
55 Bossanyi, D.G. *et al.* Spin Statistics for Triplet–Triplet Annihilation Upconversion: Exchange Coupling, Intermolecular Orientation, and Reverse Intersystem Crossing. *JACS Au* [interactive]. 2021, vol. 1 (12), 2188–2201. Access via the Internet: <https://doi.org/10.1021/10.1021/jacsau.1c00322>.
56 Noda, H. *et al.* Highly Efficient Thermally Activated Delayed Fluorescence with Slow Reverse Intersystem Crossing. *Chemistry Letters* [interactive]. 2019, vol. 48 (2), 126–129. Access via the Internet: <https://doi.org/10.1021/10.1246/cl.180813>.
57 Shakeel, U. *et al.* Study of processes of reverse intersystem crossing (RISC) and thermally activated delayed fluorescence (TADF) in organic

light emitting diodes (OLEDs). *Organic Electronics* [interactive]. 2018, vol. 59, 121–124. Access via the Internet: <https://doi.org/10.1021/10.1016/j.orgel.2018.04.035>.

58 Han, S.H. *et al.* Ideal blue thermally activated delayed fluorescence emission assisted by a thermally activated delayed fluorescence assistant dopant through a fast reverse intersystem crossing mediated cascade energy transfer process. *Journal of Materials Chemistry C* [interactive]. 2019, vol. 7 (10), 3082–3089. Access via the Internet: <https://doi.org/10.1021/10.1039/C8TC06575F>.

59 Etherington, M.K. *et al.* Persistent Dimer Emission in Thermally Activated Delayed Fluorescence Materials. *The Journal of Physical Chemistry C* [interactive]. 2019, vol. 123 (17), 11109–11117. Access via the Internet: <https://doi.org/10.1021/10.1021/acs.jpcc.9b01458>.

60 Ulukan, P. *et al.* Computational descriptor analysis on excited state behaviours of a series of TADF and non-TADF compounds. *Physical Chemistry Chemical Physics* [interactive]. 2022, vol. 24 (26), 16167–16182. Access via the Internet: <https://doi.org/10.1021/10.1039/D2CP01323A>.

61 Stachelek, P. *et al.* Molecular Design Strategies for Color Tuning of Blue TADF Emitters. *ACS Applied Materials & Interfaces* [interactive]. 2019, vol. 11 (30), 27125–27133. Access via the Internet: <https://doi.org/10.1021/10.1021/acsami.9b06364>.

62 Yin, C. *et al.* A perspective on blue TADF materials based on carbazole-benzonitrile derivatives for efficient and stable OLEDs. *Applied Physics Letters* [interactive]. 2020, vol. 116 (12), 120503. Access via the Internet: <https://doi.org/10.1021/10.1063/1.5143501>.

63 Ledwon, P. Recent advances of donor-acceptor type carbazole-based molecules for light emitting applications. *Organic Electronics* [interactive]. 2019, vol. 75, 105422. Access via the Internet: <https://doi.org/10.1021/10.1016/j.orgel.2019.105422>.

64 Sun, D. *et al.* 1,3,5-Triazine-Functionalized Thermally Activated Delayed Fluorescence Emitters for Organic Light-Emitting Diodes. *Advanced Photonics Research* [interactive]. 2022, vol. 3 (11), 2200203. Access via the Internet: <https://doi.org/10.1021/10.1002/adpr.202200203>.

65 Xiang, Y. *et al.* Asymmetric-triazine-cored triads as thermally activated delayed fluorescence emitters for high-efficiency yellow OLEDs with slow efficiency roll-off. *Journal of Materials Chemistry C* [interactive]. 2016, vol. 4 (42), 9998–10004. Access via the Internet: <https://doi.org/10.1021/10.1039/C6TC02702D>.

66 Chen, T. *et al.* Tuning the emissive characteristics of TADF emitters by fusing heterocycles with acridine as donors: highly efficient orange to red organic light-emitting diodes with EQE over 20%. *Journal of Materials Chemistry C* [interactive]. 2019, vol. 7 (29), 9087–9094. Access via the Internet: <https://doi.org/10.1021/10.1039/C9TC01973A>.

67 Patil, V.V. *et al.* Universal blue emitters for high efficiency thermally activated delayed fluorescence and fluorescent organic light-emitting diodes. *Dyes and Pigments* [interactive]. 2020, vol. 174, 108070. Access via the Internet: <https://doi.org/10.1021/10.1016/j.dyepig.2019.108070>.

68 Joo, C.W. *et al.* Highly efficient solution-processed blue organic light-emitting diodes based on thermally activated delayed fluorescence emitters with spiroacridine donor. *Journal of Industrial and Engineering Chemistry* [interactive]. 2019, vol. 78, 265–270. Access via the Internet: <https://doi.org/10.1021/10.1016/j.jiec.2019.06.003>.

69 Woo, S.-J. *et al.* Phenazasiline/Spiroacridine Donor Combined with Methyl-Substituted Linkers for Efficient Deep Blue Thermally Activated Delayed Fluorescence Emitters. *ACS Applied Materials & Interfaces* [interactive]. 2019, vol. 11 (7), 7199–7207. Access via the Internet: <https://doi.org/10.1021/10.1021/acsami.8b20009>.

70 Wang, W. *et al.* Halogen bonding in room-temperature phosphorescent materials. *Coordination Chemistry Reviews* [interactive]. 2020, vol. 404, 213107. Access via the Internet: <https://doi.org/10.1021/10.1016/j.ccr.2019.213107>.

71 Huang, L. *et al.* Stimuli-Responsive Purely Organic Room-Temperature Phosphorescence Materials. *Chemistry – A European Journal* [interactive]. 2020, vol. 26 (52), 11914–11930. Access via the Internet: <https://doi.org/10.1021/10.1002/chem.202000526>.

72 Xiao, F. *et al.* Guest-host doped strategy for constructing ultralong-lifetime near-infrared organic phosphorescence materials for bioimaging. *Nature Communications* [interactive]. 2022, vol. 13 (1), 186. Access via the Internet: <https://doi.org/10.1021/10.1038/s41467-021-27914-0>.

73 Tonge, C.M. *et al.* Color-Tunable Thermally Activated Delayed Fluorescence in Oxadiazole-Based Acrylic Copolymers: Photophysical Properties and Applications in Ratiometric Oxygen Sensing. *ACS Applied Materials & Interfaces* [interactive]. 2020, vol. 12 (5), 6525–6535. Access via the Internet: <https://doi.org/10.1021/10.1021/acsami.9b22464>.

74 Jiang, K. *et al.* Carbon Dots with Dual-Emissive, Robust, and Aggregation-Induced Room-Temperature Phosphorescence Characteristics. *Angewandte Chemie International Edition* [interactive]. 2020, vol. 59 (3), 1263–1269. Access via the Internet: <https://doi.org/10.1021/10.1002/anie.201911342>.

75 Zhu, T. *et al.* Unraveling the Fate of Host Excitons in Host–Guest Phosphorescent Organic Light-Emitting Diodes. *The Journal of Physical Chemistry C* [interactive]. 2019, vol. 123 (16), 10311–10318. Access via the Internet: <https://doi.org/10.1021/10.1021/acs.jpcc.9b02820>.

76 Zhu, T. *et al.* Charge Recombination in Phosphorescent Organic Light-Emitting Diode Host–Guest Systems through QM/MM Simulations. *The Journal of Physical Chemistry C* [interactive]. 2016, vol. 120 (36), 19987–19994. Access via the Internet: <https://doi.org/10.1021/10.1021/acs.jpcc.6b05559>.

77 Narsaria, A.K. *et al.* Computationally Guided Molecular Design to Minimize the LE/CT Gap in D-π-A Fluorinated Triarylboranes for Efficient TADF via D and π-Bridge Tuning. *Advanced Functional Materials* [interactive]. 2020, vol. 30 (31), 2002064. Access via the Internet: <https://doi.org/10.1021/10.1002/adfm.202002064>.

78 Wagner, J. *et al.* Modular Nitrogen-Doped Concave Polycyclic Aromatic Hydrocarbons for High-Performance Organic Light-Emitting Diodes with Tunable Emission Mechanisms**. *Angewandte Chemie International Edition* [interactive]. 2022, vol. 61 (27). Access via the Internet: <https://doi.org/10.1021/10.1002/anie.202202232>.

79 Liang, X. *et al.* Versatile functionalization of trifluoromethyl based deep blue thermally activated delayed fluorescence materials for organic light emitting diodes. *New Journal of Chemistry* [interactive]. 2018, vol. 42 (6), 4317–4323. Access via the Internet: <https://doi.org/10.1021/10.1039/C7NJ04482H>.

80 Yuan, W. *et al.* The electron inductive effect of CF3 on penta-carbazole containing blue emitters: Trade-off between color purity and luminescent efficiency in TADF OLEDs. *Dyes and Pigments* [interactive]. 2018, vol. 159, 151–157. Access via the Internet: <https://doi.org/10.1021/10.1016/j.dyepig.2018.06.017>.

81 Ward, J.S. *et al.* Exploiting trifluoromethyl substituents for tuning orbital character of singlet and triplet states to increase the rate of thermally activated delayed fluorescence. *Materials Chemistry Frontiers* [interactive]. 2020, vol. 4 (12). Access via the Internet: <https://doi.org/10.1021/10.1039/d0qm00429d>.

82 Wu, S. *et al.* Excited-State Modulation in Donor-Substituted Multiresonant Thermally Activated Delayed Fluorescence Emitters. *ACS Applied Materials & Interfaces* [interactive]. 2022, vol. 14 (19), 22341–22352. Access via the Internet: <https://doi.org/10.1021/10.1021/acsami.2c02756>.
83 Jeon, S.O. *et al.* High-efficiency, long-lifetime deep-blue organic light-emitting diodes. *Nature Photonics* [interactive]. 2021, vol. 15 (3), 208–215. Access via the Internet: <https://doi.org/10.1021/10.1038/s41566-021-00763-5>.
84 Zheng, Y. *et al.* Long-Lived Room Temperature Phosphorescence Crystals with Green Light Excitation. *ACS Applied Materials & Interfaces* [interactive]. 2022, vol. 14 (13), 15706–15715. Access via the Internet: <https://doi.org/10.1021/10.1021/acsami.2c04141>.
85 Keruckiene, R. *et al.* Derivatives of Bis(trifluoromethyl)biphenyl and Various Donor Noieties Exhibiting Dual State Emission. *Journal of Luminescence* [interactive]. 2022, vol. 241, 118502. Access via the Internet: <https://doi.org/10.1021/10.1016/j.jlumin.2021.118502>.
86 Yang, Z. *et al.* Recent advances in organic thermally activated delayed fluorescence materials. *Chemical Society Reviews* [interactive]. 2017, vol. 46 (3), 915–1016. Access via the Internet: <https://doi.org/10.1021/10.1039/c6cs00368k>.
87 Woon, K.L. *et al.* Tuning the singlet-triplet energy splitting by fluorination at 3,6 positions of the 1,4-biscarbazoylbenzene. *Dyes and Pigments* [interactive]. 2016, vol. 132, 1–6. Access via the Internet: <https://doi.org/10.1021/10.1016/j.dyepig.2016.04.030>.
88 Grobe, J. *et al.* The chemistry of fluorine containing phosphaalkenes, arsaalkenes and selenocarbonyls. *Journal of Fluorine Chemistry* [interactive]. 2004, vol. 125 (6), 801–821. Access via the Internet: <https://doi.org/10.1021/10.1016/j.jfluchem.2004.01.022>.
89 Dias, F.B. *et al.* Photophysics of thermally activated delayed fluorescence molecules. *Methods and Applications in Fluorescence* [interactive]. 2017, vol. 5 (1), 012001. Access via the Internet: <https://doi.org/10.1021/10.1088/2050-6120/aa537e>.
90 Nikolaenko, A.E. *et al.* Thermally Activated Delayed Fluorescence in Polymers: A New Route toward Highly Efficient Solution Processable OLEDs. *Advanced Materials* [interactive]. 2015, vol. 27 (44), 7236–7240. Access via the Internet: <https://doi.org/10.1021/10.1002/adma.201501090>.
91 Serevičius, T. *et al.* TADF Parameters in the Solid State: An Easy Way to Draw Wrong Conclusions. *The Journal of Physical Chemistry A*

[interactive]. 2021, vol. 125 (7), 1637–1641. Access via the Internet: <https://doi.org/10.1021/10.1021/acs.jpca.0c10391>.

92 Kim, K.H. *et al.* Boosting Triplet Harvest by Reducing Nonradiative Transition of Exciplex toward Fluorescent Organic Light-Emitting Diodes with 100% Internal Quantum Efficiency. *Chemistry of Materials* [interactive]. 2016, vol. 28 (6), 1936–1941. Access via the Internet: <https://doi.org/10.1021/10.1021/acs.chemmater.6b00478>.

93 Mahmoudi, M. *et al.* Exciplex-forming systems with extremely high RISC rates exceeding 107s-1for oxygen probing and white hybrid OLEDs. *Journal of Materials Research and Technology* [interactive]. 2021, vol. 10, 711–721. Access via the Internet: <https://doi.org/10.1021/10.1016/j.jmrt.2020.12.058>.

94 Noda, H. *et al.* Critical role of intermediate electronic states for spin-flip processes in charge-transfer-type organic molecules with multiple donors and acceptors. *Nature Materials* [interactive]. 2019, vol. 18 (10), 1084–1090. Access via the Internet: <https://doi.org/10.1021/10.1038/s41563-019-0465-6>.

95 Franca, L.G. *et al.* Spiro donor–acceptor TADF emitters: naked TADF free from inhomogeneity caused by donor acceptor bridge bond disorder. Fast rISC and invariant photophysics in solid state hosts. *Journal of Materials Chemistry C* [interactive]. 2022, vol. 10 (4), 1313–1325. Access via the Internet: <https://doi.org/10.1021/10.1039/D1TC04484B>.

96 Lyskov, I. *et al.* Climbing up the Ladder: Intermediate Triplet States Promote the Reverse Intersystem Crossing in the Efficient TADF Emitter ACRSA. *The Journal of Physical Chemistry C* [interactive]. 2017, vol. 121 (39), 21145–21153. Access via the Internet: <https://doi.org/10.1021/10.1021/acs.jpcc.7b06187>.

97 Qiao, X. *et al.* Nonlinear optoelectronic processes in organic optoelectronic devices: Triplet-triplet annihilation and singlet fission. *Materials Science and Engineering: R: Reports* [interactive]. 2020, vol. 139, 100519. Access via the Internet: <https://doi.org/10.1021/10.1016/j.mser.2019.100519>.

98 Hladka, I. *et al.* Polymorphism of derivatives of tert -butyl substituted acridan and perfluorobiphenyl as sky-blue OLED emitters exhibiting aggregation induced thermally activated delayed fluorescence. *Journal of Materials Chemistry C* [interactive]. 2018, vol. 6 (48), 13179–13189. Access via the Internet: <https://doi.org/10.1021/10.1039/c8tc04867c>.

99 Lee, J. *et al.* Hot excited state management for long-lived blue phosphorescent organic light-emitting diodes. *Nature Communications*

[interactive]. 2017, vol. 8 (1), 15566. Access via the Internet: <https://doi.org/10.1021/10.1038/ncomms15566>.

100 Giebink, N.C. *et al.* Intrinsic luminance loss in phosphorescent small-molecule organic light emitting devices due to bimolecular annihilation reactions. *Journal of Applied Physics* [interactive]. 2008, vol. 103 (4), 044509. Access via the Internet: <https://doi.org/10.1021/10.1063/1.2884530>.

101 Skhirtladze, L. *et al.* 1,4-Bis(trifluoromethyl)benzene as a new acceptor for the design and synthesis of emitters exhibiting efficient thermally activated delayed fluorescence and electroluminescence: experimental and computational guidance. *Journal of Materials Chemistry C* [interactive]. 2022, vol. 10 (12), 4929–4940. Access via the Internet: <https://doi.org/10.1021/10.1039/D1TC05420A>.

102 Aydemir, M. *et al.* Synthesis and investigation of intra-molecular charge transfer state properties of novel donor–acceptor–donor pyridine derivatives: the effects of temperature and environment on molecular configurations and the origin of delayed fluorescence. *Physical Chemistry Chemical Physics* [interactive]. 2015, vol. 17 (38), 25572–25582. Access via the Internet: <https://doi.org/10.1021/10.1039/C5CP03937A>.

103 Dias, F.B. *et al.* Triplet Harvesting with 100% Efficiency by Way of Thermally Activated Delayed Fluorescence in Charge Transfer OLED Emitters. *Advanced Materials* [interactive]. 2013, vol. 25 (27), 3707–3714. Access via the Internet: <https://doi.org/10.1021/10.1002/adma.201300753>.

104 Kim, J. *et al.* Quantitative Correlation of Triplet Exciton Management in Host with the Device Lifetime of Blue Phosphorescent Organic Light-Emitting Diodes. *Advanced Optical Materials* [interactive]. 2022, vol. 10 (3), 2101444. Access via the Internet: <https://doi.org/10.1021/10.1002/adom.202101444>.

105 Zee, B. *et al.* Role of Singlet and Triplet Excitons on the Electrical Stability of Polymer Light-Emitting Diodes. *Advanced Electronic Materials* [interactive]. 2020, vol. 6 (8), 2000367. Access via the Internet: <https://doi.org/10.1021/10.1002/aelm.202000367>.

106 Hirata, S. Recent Advances in Materials with Room-Temperature Phosphorescence: Photophysics for Triplet Exciton Stabilization. *Advanced Optical Materials* [interactive]. 2017, vol. 5 (17), 1700116. Access via the Internet: <https://doi.org/10.1021/10.1002/adom.201700116>.

107 Liu, H. *et al.* Dual-Emission of Fluorescence and Room-Temperature Phosphorescence for Ratiometric and Colorimetric Oxygen Sensing and Detection Based on Dispersion of Pure Organic Thianthrene Dimer in Polymer Host. *Advanced Optical Materials* [interactive]. 2022, vol. 10 (12), 2102814. Access via the Internet: <https://doi.org/10.1021/10.1002/adom.202102814>.
108 Fan, J. *et al.* Excited State Properties of a Thermally Activated Delayed Fluorescence Molecule in Solid Phase Studied by Quantum Mechanics/Molecular Mechanics Method. *The Journal of Physical Chemistry C* [interactive]. 2018, vol. 122 (4), 2358–2366. Access via the Internet: <https://doi.org/10.1021/10.1021/acs.jpcc.7b10238>.
109 Woon, K.L. *et al.* Effect of Bulky Functional Groups on Donor and Acceptor Interactions and their Photoluminescence Properties. *ChemPhysChem* [interactive]. 2020, vol. 21 (22), 2620–2626. Access via the Internet: <https://doi.org/10.1021/10.1002/cphc.202000612>.
110 Northey, T. *et al.* The role of solid state solvation on the charge transfer state of a thermally activated delayed fluorescence emitter. *Journal of Materials Chemistry C* [interactive]. 2017, vol. 5 (42), 11001–11009. Access via the Internet: <https://doi.org/10.1021/10.1039/C7TC04099G>.
111 Sarkar, T.K. *et al.* Room Temperature Phosphorescent (RTP) N-Acetylphenothiazines. *ChemPhotoChem* [interactive]. 2020, vol. 4 (4), 282–286. Access via the Internet: <https://doi.org/10.1021/10.1002/cptc.201900296>.
112 Wang, Y. *et al.* New Phenothiazine Derivatives That Exhibit Photoinduced Room-Temperature Phosphorescence. *Advanced Functional Materials* [interactive]. 2021, vol. 31 (40), 2101719. Access via the Internet: <https://doi.org/10.1021/10.1002/adfm.202101719>.
113 Qiu, W. *et al.* Dynamic adjustment of emission from both singlets and triplets: the role of excited state conformation relaxation and charge transfer in phenothiazine derivates. *Journal of Materials Chemistry C* [interactive]. 2021, vol. 9 (4), 1378–1386. Access via the Internet: <https://doi.org/10.1021/10.1039/D0TC05343K>.
114 Zhang, G. *et al.* Multi-Emissive Difluoroboron Dibenzoylmethane Polylactide Exhibiting Intense Fluorescence and Oxygen-Sensitive Room-Temperature Phosphorescence. *Journal of the American Chemical Society* [interactive]. 2007, vol. 129 (29), 8942–8943. Access via the Internet: <https://doi.org/10.1021/10.1021/ja0720255>.

115 Kasha, M. Paths of Molecular Excitation. *Radiation Research Supplement* [interactive]. 1960, vol. 2, 243. Access via the Internet: <https://doi.org/10.1021/10.2307/3583599>.
116 Lin, T.-C. *et al.* Probe exciplex structure of highly efficient thermally activated delayed fluorescence organic light emitting diodes. *Nature Communications* [interactive]. 2018, vol. 9 (1), 3111. Access via the Internet: <https://doi.org/10.1021/10.1038/s41467-018-05527-4>.
117 Dey, S. *et al.* Thermally Activated Delayed Fluorescence and Room-Temperature Phosphorescence in Asymmetric Phenoxazine-Quinoline (D2–A) Conjugates and Dual Electroluminescence. *The Journal of Physical Chemistry C* [interactive]. 2022, vol. 126 (12), 5649–5657. Access via the Internet: <https://doi.org/10.1021/10.1021/acs.jpcc.2c00512>.
118 Kwon, D.Y. *et al.* Theoretical Study on Benzazole Derivatives for Use in Blue Thermally Activated Delayed Fluorescence Emitters. *Journal of Nanoscience and Nanotechnology* [interactive]. 2015, vol. 15 (10), 7819–7822. Access via the Internet: <https://doi.org/10.1021/10.1166/jnn.2015.11174>.
119 Hosokai, T. *et al.* Evidence and mechanism of efficient thermally activated delayed fluorescence promoted by delocalized excited states. *Science Advances* [interactive]. 2017, vol. 3 (5). Access via the Internet: <https://doi.org/10.1021/10.1126/sciadv.1603282>.
120 Jang, J.S. *et al.* Electrostatic potential dispersing pyrimidine-5-carbonitrile acceptor for high efficiency and long lifetime thermally activated delayed fluorescence organic light-emitting diodes. *Journal of Materials Chemistry C* [interactive]. 2019, vol. 7 (40), 12695–12703. Access via the Internet: <https://doi.org/10.1021/10.1039/C9TC04304G>.
121 Traskovskis, K. *et al.* All-organic fast intersystem crossing assisted exciplexes exhibiting sub-microsecond thermally activated delayed fluorescence. *Journal of Materials Chemistry C* [interactive]. 2021, vol. 9 (13), 4532–4543. Access via the Internet: <https://doi.org/10.1021/10.1039/D0TC05099G>.
122 Sun, M. *et al.* Ternary donor–acceptor phosphine oxide hosts with peculiar high energy gap for efficient blue electroluminescence. *Journal of Materials Chemistry C* [interactive]. 2015, vol. 3 (36), 9469–9478. Access via the Internet: <https://doi.org/10.1021/10.1039/C5TC02029H>.

123 Ambrose, J.F. *et al.* Anodic Oxidation Pathways of Carbazoles. *Journal of The Electrochemical Society* [interactive]. 1968, vol. 115 (11), 1159. Access via the Internet: <https://doi.org/10.1021/10.1149/1.2410929>.
124 Ambrose, J.F. *et al.* Anodic Oxidation Pathways of Carbazoles. *Journal of The Electrochemical Society* [interactive]. 1968, vol. 115 (11), 1159. Access via the Internet: <https://doi.org/10.1021/10.1149/1.2410929>.
125 Nelsen, S.F. *et al.* Solvent Effects on Charge Transfer Bands of Nitrogen-Centered Intervalence Compounds. *Journal of the American Chemical Society* [interactive]. 2001, vol. 123 (24), 5684–5694. Access via the Internet: <https://doi.org/10.1021/10.1021/ja003436n>.
126 Malagoli, M. *et al.* Density functional theory study of the geometric structure and energetics of triphenylamine-based hole-transporting molecules. *Chemical Physics Letters* [interactive]. 2000, vol. 327 (1–2), 13–17. Access via the Internet: <https://doi.org/10.1021/10.1016/S0009-2614(00)00757-0>.
127 Sakanoue, K. *et al.* A Molecular Orbital Study on the Hole Transport Property of Organic Amine Compounds. *The Journal of Physical Chemistry A* [interactive]. 1999, vol. 103 (28), 5551–5556. Access via the Internet: <https://doi.org/10.1021/10.1021/jp990206q>.
128 Marcus, R.A. Electron transfer reactions in chemistry. Theory and experiment. *Reviews of Modern Physics* [interactive]. 1993, vol. 65 (3), 599–610. Access via the Internet: <https://doi.org/10.1021/10.1103/RevModPhys.65.599>.
129 Marcus, R.A. On the Theory of Oxidation-Reduction Reactions Involving Electron Transfer. I. *The Journal of Chemical Physics* [interactive]. 1956, vol. 24 (5), 966–978. Access via the Internet: <https://doi.org/10.1021/10.1063/1.1742723>.
130 Hush, N.S. Adiabatic Rate Processes at Electrodes. I. Energy-Charge Relationships. *The Journal of Chemical Physics* [interactive]. 1958, vol. 28 (5), 962–972. Access via the Internet: <https://doi.org/10.1021/10.1063/1.1744305>.
131 Yang, X. *et al.* Theoretical modelling of carrier transports in molecular semiconductors: molecular design of triphenylamine dimer systems. *Nanotechnology* [interactive]. 2007, vol. 18 (42), 424029. Access via the Internet: <https://doi.org/10.1021/10.1088/0957-4484/18/42/424029>.
132 Liu, X. *et al.* Charge transfer mobility of naphthodithiophenediimide derivative: Normal-mode and bond length relaxation analysis. *Chemical Physics Letters* [interactive]. 2016, vol. 645, 92–96. Access via the Internet: <https://doi.org/10.1021/10.1016/j.cplett.2015.12.038>.

133 Karaush-Karmazin, N.N. *et al.* Impact of molecular and packing structure on the charge-transport properties of hetero[8]circulenes. *Journal of Materials Chemistry C* [interactive]. 2021, vol. 9 (4), 1451–1466. Access via the Internet: <https://doi.org/10.1021/10.1039/D0TC03674A>.
134 Wen, S.-H. *et al.* First-Principles Investigation of Anistropic Hole Mobilities in Organic Semiconductors. *The Journal of Physical Chemistry B* [interactive]. 2009, vol. 113 (26), 8813–8819. Access via the Internet: <https://doi.org/10.1021/10.1021/jp900512s>.
135 Brunschwig, B.S. *et al.* A semiclassical treatment of electron-exchange reactions. Application to the hexaaquoiron(II)-hexaaquoiron(III) system. *Journal of the American Chemical Society* [interactive]. 1980, vol. 102 (18), 5798–5809. Access via the Internet: <https://doi.org/10.1021/10.1021/ja00538a017>.
136 Newton, M.D. *et al.* Electron Transfer Reactions in Condensed Phases. *Annual Review of Physical Chemistry* [interactive]. 1984, vol. 35 (1), 437–480. Access via the Internet: <https://doi.org/10.1021/10.1146/annurev.pc.35.100184.002253>.
137 Zhang, M.-X. *et al.* BODIPY derivatives as n-type organic semiconductors: Isomer effect on carrier mobility. *Organic Electronics* [interactive]. 2012, vol. 13 (2), 215–221. Access via the Internet: <https://doi.org/10.1021/10.1016/j.orgel.2011.10.015>.
138 Johnson, G.E. Spectroscopic study of carbazole by photoselection. *The Journal of Physical Chemistry* [interactive]. 1974, vol. 78 (15), 1512–1521. Access via the Internet: <https://doi.org/10.1021/10.1021/j100608a014>.
139 Jankus, V. *et al.* Highly Efficient TADF OLEDs: How the Emitter-Host Interaction Controls Both the Excited State Species and Electrical Properties of the Devices to Achieve Near 100% Triplet Harvesting and High Efficiency. *Advanced Functional Materials* [interactive]. 2014, vol. 24 (39), 6178–6186. Access via the Internet: <https://doi.org/10.1021/10.1002/adfm.201400948>.
140 Tsujimoto, H. *et al.* Thermally Activated Delayed Fluorescence and Aggregation Induced Emission with Through-Space Charge Transfer. *Journal of the American Chemical Society* [interactive]. 2017, vol. 139 (13), 4894–4900. Access via the Internet: <https://doi.org/10.1021/10.1021/jacs.7b00873>.
141 Dias, F.B. Kinetics of thermal-assisted delayed fluorescence in blue organic emitters with large singlet–triplet energy gap. *Philosophical Transactions of the Royal Society A: Mathematical, Physical and*

Engineering Sciences [interactive]. 2015, vol. 373 (2044), 20140447. Access via the Internet: <https://doi.org/10.1021/10.1098/rsta.2014.0447>.

142 Ledwon, P. *et al.* The effect of molecular structure on the properties of quinoxaline-based molecules for OLED applications. *Dyes and Pigments* [interactive]. 2020, vol. 173, 108008. Access via the Internet: <https://doi.org/10.1021/10.1016/j.dyepig.2019.108008>.

143 Sarma, M. *et al.* Exciplex: An Intermolecular Charge-Transfer Approach for TADF. *ACS Applied Materials & Interfaces* [interactive]. 2018, vol. 10 (23), 19279–19304. Access via the Internet: <https://doi.org/10.1021/10.1021/acsami.7b18318>.

144 Berenis, D. *et al.* Different RISC rates in benzoylpyridine-based TADF compounds and their implications for solution-processed OLEDs. *Dyes and Pigments* [interactive]. 2020, vol. 182, 108579. Access via the Internet: <https://doi.org/10.1021/10.1016/j.dyepig.2020.108579>.

145 Lee, J.-H. *et al.* High performance top-emitting organic light-emitting diodes with copper iodide-doped hole injection layer. *Organic Electronics* [interactive]. 2008, vol. 9 (5), 805–808. Access via the Internet: <https://doi.org/10.1021/10.1016/j.orgel.2008.05.011>.

146 Yang, Q. *et al.* Double-emission-layer green phosphorescent OLED based on LiF-doped TPBi as electron transport layer for improving efficiency and operational lifetime. *Synthetic Metals* [interactive]. 2012, vol. 162 (3–4), 398–401. Access via the Internet: <https://doi.org/10.1021/10.1016/j.synthmet.2011.12.027>.

147 Kukhta, N.A. *et al.* Deep-Blue High-Efficiency TTA OLED Using *Para* - and *Meta* -Conjugated Cyanotriphenylbenzene and Carbazole Derivatives as Emitter and Host. *The Journal of Physical Chemistry Letters* [interactive]. 2017, vol. 8 (24), 6199–6205. Access via the Internet: <https://doi.org/10.1021/10.1021/acs.jpclett.7b02867>.

148 Sun, J.W. *et al.* Azasiline-based thermally activated delayed fluorescence emitters for blue organic light emitting diodes. *Journal of Materials Chemistry C* [interactive]. 2017, vol. 5 (5), 1027–1032. Access via the Internet: <https://doi.org/10.1021/10.1039/C6TC04653C>.

149 Yook, K.S. *et al.* Solution processed high efficiency blue and white phosphorescent organic light-emitting diodes using a high triplet energy exciton blocking layer. *Organic Electronics* [interactive]. 2011, vol. 12 (8), 1293–1297. Access via the Internet: <https://doi.org/10.1021/10.1016/j.orgel.2011.04.014>.

6. CURRICULUM VITAE

Name, Surname: Levani Skhirtladze
Date of the birth: 20 August 1994
E-mail: Skhirtladze20@gmail.com

Education

2012–2016 Bachelor's degree studies, Ivane Javakhishvili Tbilisi State University, Department of Chemistry, Georgia.
2016–2018 Master's degree studies, Ivane Javakhishvili Tbilisi State University, Department of Chemistry, Georgia.
2019–2023 PhD studies in Chemical Engineering, Kaunas University of Technology, Lithuania.

Professional experience

2019-01-02 to 2021-12-31 Project Junior Researcher: Controlled thermally activated delayed fluorescence polymer emitters for solution casting organic luminaires, LLT194.
2020-03-08 to 2023-01-09 Project Junior Researcher: Self-organizing donor–acceptor materials for efficient electroluminescent devices, SV3/1445.

Work experience

2016-09–2017-05 Company: Laboratory of the Ministry of Agriculture (Food Research Department). Position: Laboratory Assistant.
2017-09–2017-01 Company: Machine mechanics Institute. Position: Laboratorian.
2017-01–2018-02 Company: Georgian High Technologies National Center. Position: Technologist.
2018-05–2019-10 Company: CCT Chemicals Coating Trading LLC. Position: Chemist.

7. LIST OF PUBLICATIONS AND SCIENTIFIC CONFERENCES

1. **Skhirtladze Levani**; Lietonas Karolis; Bucinskas Audrius; Volyniuk Dmytro; Mahmoudi Malek; Mukbaniani Omar; Woon Kai Lin; Ariffin Azhar; Grazulevicius Juozas Vidas. 1,4-Bis(trifluoromethyl)benzene as a new acceptor for the design and synthesis of emitters exhibiting efficient thermally activated delayed fluorescence and electroluminescence: experimental and computational guidance // Journal of Materials Chemistry C. ISSN 2050-7526 eISSN 2050-7534. 2022, vol. 10, iss. 12, p. 4929-4940. DOI: 10.1039/d1tc05420a. (Web of Science); [IF: 8,067; AIF: 6,018; IF/AIF: 1,340; Q1].
2. **Skhirtladze Levani**; Leitonas Karolis; Bucinskas Audrius; Woon Kai Lin; Volyniuk Dmytro; Keruckiene Rasa; Mahmoudi Malek; Lapkowski Mieczyslaw; Ariffin Azhar; Grazulevicius Juozas Vidas. Turn on of room temperature phosphorescence of donor-acceptor-donor type compounds via transformation of excited states by rigid hosts for oxygen sensing // Sensors and actuators B: Chemical. Lausanne: Elsevier. ISSN 0925- 4005. 2023, vol. 380, art. no. 133295, p. 1-10. DOI: 10.1016/j.snb.2023.133295. (Web of Science); [IF: 9,221; AIF: 5,220; IF/AIF: 1,766; Q1].
3. **Skhirtladze Levani**; Bezvikonnyi Oleksandr; Keruckienė Rasa; Dvylys Lukas; Mahmoudi Malek; Labanauskas Linas; Ariffin Azhar; Grazulevicius Juozas Vidas. Derivatives of pyridazine with phenoxazine and 9,9-dimethyl-9,10-dihydroacridine donor moieties exhibiting thermally activated delayed fluorescence // Materials. Basel: MDPI. ISSN 1996-1944. 2023, vol. 16, iss. 3, art. no. 1294, p. 1-10. DOI: 10.3390/ma16031294. (Web of Science); [IF: 3,748; AIF: 6,225; IF/AIF: 0,602; Q1].
4. Danyliv Yan; Ivaniuk Khrystyna; Danyliv Iryna; Bezvikonnyi Oleksandr; Volyniuk Dmytro; Galyna Sych; Lazauskas Algirdas; **Skhirtladze Levani**; Ågren Hans; Stakhira Pavlo; Karaush-Karmazin Nataliya; Ali Amjad; Baryshnikov Glib; Grazulevicius Juozas Vidas. Carbazole-σ-sulfobenzimide derivative exhibiting mechanochromic thermally activated delayed fluorescence as emitter for flexible OLEDs: theoretical and experimental insights // Dyes and pigments. Oxford: Elsevier. ISSN 0143-7208. eISSN 1873-3743. 2022, vol. 208, art. no. 110841, p. 1-11. DOI: 10.1016/j.dyepig.2022.110841 (Web of Science); Scopus; [IF: 5,122; AIF: 5,458; IF/AIF: 0,938; Q1].

Scientific conferences

1. Skhirtladze, Levani; Grazulevicius, Juozas Vidas; Bin Ariffin, Azhar; Lin, Woon Kai. Synthesis and studies of properties of organic semiconductors containing donor and acceptor moieties // ICEPOM -12 conference abstracts: Electronic processes in organic and inorganic materials, June 1–5, 2020, Kamianets-Podilskyi, Ukraine. Kamianets-Podilskyi: Kamianets-Podilskyi National Ivan Ohiienko University. 2020, p. 330.
2. Skhirtladze, Levani; Grazulevicius, Juozas Vidas; Mahmoudi, Malek; Ariffin, Azhar Bin. Synthesis and studies of properties of organic semiconductors containing donor

and acceptor moieties // Advanced materials and technologies: book of abstracts of 24th international conference-school, 22–26 August 2022, Palanga, Lithuania. Kaunas: Kaunas University of Technology. ISSN 2669-1930. 2022, B-P54, p. 91.

8. COPIES OF PUBLICATIONS

Journal of Materials Chemistry C

ROYAL SOCIETY OF CHEMISTRY

PAPER

View Article Online
View Journal | View Issue

Cite this: J. Mater. Chem. C, 2022, 10, 4929

1,4-Bis(trifluoromethyl)benzene as a new acceptor for the design and synthesis of emitters exhibiting efficient thermally activated delayed fluorescence and electroluminescence: experimental and computational guidance†

Levani Skhirtladze,[a] Karolis Lietonas,[a] Audrius Bucinskas,[a] Dmytro Volyniuk,[a] Malek Mahmoudi,[c] Omar Mukbaniani,[b] Kai Lin Woon,[c]* Azhar Ariffin[c,d]* and Juozas V. Grazulevicius[a]*

1,4-Bis(trifluoromethyl)benzene as a new acceptor with hydrogen bonding sites together with phenoxazine, phenothiazine or 9,9-dimethyl-9-10-dihydroacridine as donor moieties was used for the design and synthesis of compounds with symmetrical donor–acceptor–donor architectures as emitters exhibiting thermally activated delayed fluorescence (TADF). The molecules exhibited large dihedral angles between the donor and acceptor moieties which are close to 80° as was shown by single crystal X-ray analysis and theoretical calculations. The compounds showed very broad charge-transfer-state (^{1}CT) absorption which can be accounted for by multiple ^{1}CTs as indicated by quantum molecular dynamics simulations. The magnitude of oscillatory strength increases with deviation away from the orthogonality of the dihedral angle between the donor and acceptor and the presence of in-plane bending of the two donors where the donors swing back and forth with respect to the acceptor at C–N bonds. The localised triplet excited states (^{3}LEs) were experimentally obtained. Although a very small and similar singlet and triplet splitting of *ca.* 20 meV was observed for the compounds, its reverse intersystem crossing rates were different and ranged from 1.92×10^4 to 5.45×10^5 s^{-1} due to the different energy gap between the ^{1}CT and ^{3}LE. A 9,9-dimethyl-9-10-dihydroacridine based compound was shown to be a promising cyan TADF emitter. The selection of the right donor with the appropriate ^{3}LE that matches the charge transfer states is important to obtain an efficient TADF emitter. The X-Ray study of the packing pattern in the crystals of the compounds revealed that the molecules are held together through many weak van der Waals intramolecular bonds, which are formed between the CF_3 fluorine atoms and hydrogen atoms of methyl groups or the carbon and hydrogen atoms of phenyl rings (C–H···F, C–F···N, C–H···H and C–H···C with distances smaller than 2.85 Å). Because of that, this compound emitted cyan electroluminescence with unusually stable colours at different emitter concentrations and different voltages in devices. The efficiency at a brightness of 1000 cd m^{-2} was practically the same as the maximum one due to the extremely low efficiency roll-off.

Received 10th November 2021,
Accepted 15th February 2022

DOI: 10.1039/d1tc05420a

rsc.li/materials-c

[a] Department of Polymer Chemistry and Technology, Faculty of Chemical Technology, Kaunas University of Technology, Lithuania. E-mail: juozas.grazulevicius@ktu.lt
[b] Department of Chemistry, Faculty of Exact and Natural Sciences, Tbilisi State University, Tbilisi, Georgia
[c] Low Dimensional Material Research Centre, Department of Physics, University Malaya, Kuala Lumpur, Malaysia. E-mail: ph7klw76@um.edu.my
[d] Department of Chemistry, Faculty of Science, University Malaya, Kuala Lumpur, Malaysia. E-mail: azhar70@um.edu.my

† Electronic supplementary information (ESI) available. CCDC 2101143, 2108557 and 2108558. For ESI and crystallographic data in CIF or other electronic format see DOI: 10.1039/d1tc05420a

1. Introduction

The triplet state of a metal-free organic emitter is often characterized as a dark state as the emission is quantum mechanically forbidden. In a typical donor–acceptor TADF, this dark state can be converted into a bright state through spin–orbit coupling *via* the use of heavy metals such as iridium[1] or through reverse intersystem crossing if the energy gap between the triplet (T) and singlet states (S) is less than 0.1 eV.[2] The former is the phosphorescent emitter often referred to as a second-generation emitter while the latter often referred to as

an emitter exhibiting thermally activated delayed fluorescence (TADF) is a third-generation emitter.[3] The energy gap between S and T is related to the exchange interaction energy of the system.[4] To minimize the exchange interaction energy, conformational twisting between the donor (D) and acceptor (A) is used to minimize the overlap between the highest occupied molecular orbital (HOMO) and the lowest unoccupied molecular orbital (LUMO). As a result, different combinations of donors and acceptors have been explored in the design of TADF emitters. Common donors are carbazole,[5–7] phenoxazine,[8–10] phenothiazine,[11,12] and 9,9-dimethyl-9-10-dihydroacridine,[13–15] while common acceptors are triphenyltriazine,[9,16–18] sulfonyl groups,[19,20] and cyano groups.[21,22] Cyano and sulfonyl groups are strong electron-withdrawing moieties. Fluorine is also a strong electron-withdrawing group and it has been used as a substituent for the cyano group.[23,24] Such substitution often results in red shifting of the emission spectra. Because of the close proximity of fluorine atoms, the resonance between the π electrons with the 3 lone pairs of electrons can increase the effective conjugation. It is expected that these lone pairs of electrons can participate in π-conjugation and hence increase the extent of electron delocalization of the acceptor.[25,26] The electron-accepting and red-shifting abilities are beneficial for obtaining a small singlet–triplet splitting and promoting reverse intersystem crossing. Highly efficient TADF was observed for molecules containing acceptors with abilities to form intramolecular C–H···F hydrogen bonds.[27] However, the molecular structures of those TADF emitters were very complicated including two electron-accepting difluorocyanobenzene units and seven electron-donating carbazole moieties linked through a diphenylene bridge. Due to such complexity, the advantages of intramolecular non-covalent interactions were not well understood. Using simpler molecular structures, in this work, we provide experimental and computational guidance for the development of TADF emitters with a large number of intramolecular non-covalent interactions.

Hence, a new acceptor, 1,4-bis(trifluoromethyl)benzene (**2CF$_3$Ph**), containing 6 fluorine atoms is explored, expecting the appearance of intramolecular non-covalent interactions. In many cases, one of the key parameters to obtain high internal quantum efficiency is an efficient reverse intersystem crossing between the triplet charge-transfer states (^{3}CTs) and the singlet charge-transfer states (^{1}CTs). This process is mediated by vibronic coupling between a ^{3}CT and a locally excited triplet state (^{3}LE).[28–30] When the energy gap between all these three states becomes small, reverse intersystem crossing becomes efficient. The **2CF$_3$Ph** moiety has a short conjugated system. The lowest local triplet state of fluorinated benzene is above 3.5 eV.[31,32] The contribution of the triplet locally excited (^{3}LE$_A$) state of the **2CF$_3$Ph** acceptor to the overall ^{3}LE of D–A–D TADF will be minimal. Hence, the ^{3}LE state is expected to be contributed mainly by the donor moiety. Phenoxazine (PO), phenothiazine (PS), and 9,9-dimethyl-9-10-dihydroacridine (AC) were selected as the donors configured with symmetrical D–A–D architectures in which D and A moieties are bridged through C–N bonds as shown in Scheme 1. The near orthogonality between the donor and acceptor moieties as a result of large steric hindrance from the extended bis(trifluoromethyl) group in these symmetrical D–A–D systems ensures strong decoupling of electrons on the D and A in the CT state which helps to reduce the singlet–triplet energy splitting. The best TADF emitter demonstrated cyan electroluminescence with unusually stable colours at different emitter concentrations and different voltages. In addition, the efficiency was practically the same at a brightness of up to 1000 cd m^{-2} due to the extremely low efficiency roll-off. These results can be explained by weak van der Waals intramolecular interactions that exist between the fluorine atoms of the CF3 group and methyl hydrogen atoms or carbon and hydrogen atoms of phenyl rings (C–H···F, C–F···N, C–H···H and C–H···C).[27] Thus, the positive effects of intramolecular non-covalent interactions on the TADF properties are demonstrated.

2. Experimental section

In the ESI,† a detailed description of the general procedure for the synthesis of target derivatives and the experimental and theoretical techniques used for their characterization are presented.

OLEDs ware fabricated using glass substrates with pre-patterned bottom indium tin oxide (ITO) electrodes (from Ossila company). Additional materials such as molybdenum oxide (MoO_3), *N*,*N*′-di(1-

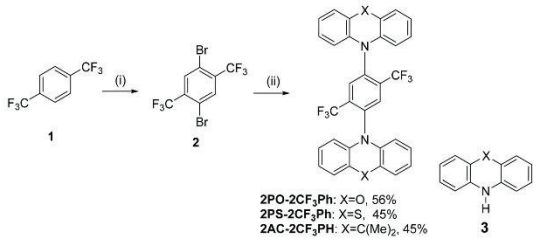

Scheme 1 Synthesis of 2,5-bis(trifluorometyl)-1,4-phenylene derivatives: (i) H_2SO_4, H_2O, TFA, reflux; NBS, r.t. 5 h; 60 °C 48 h (ii) **3**, $Pd_2(dba)_3$, X-Phos, *t*-BuONa, toluene, reflux, 24 h.

naphthyl)-*N*,*N*′-diphenyl-(1,1′-biphenyl)-4,4′-diamine (NPB), tris(4-carbazoyl-9-ylphenyl)amine (TCTA), 3,3′-di(9*H*-carbazol-9-yl)-1,1′-biphenyl (mCBP), 3,5-di(9*H*-carbazol-9-yl)tetraphenylsilane (SimCP2), diphenyl-4-triphenylsilyl-phenylphosphineoxide (TSPO1), 2,2′,2″-(1,3,5-benzinetriyl)-tris(1-phenyl-1-*H*-benzimi-dazole) (TPBi), and lithium fluoride (LiF) were used as received from Ossila, Sigma-Aldrich or Lumtec companies. The reference device was fabricated using 2,7-di-*tert*-butyl-9,9-dimethyl-10-(perfluoro-[1,1′-biphenyl]-4-yl)-9,10-dihydroacridine (**PFBP-2a**) as an emitter which was synthesized according the previously published procedure.[33]

3. Results and discussion

3.1 Synthesis

The synthesis of 2,5-bis(trifluomethyl)-1,4-phenylene derivatives is shown in Scheme 1. Buchwald–Hartwig coupling reactions of 1,4-dibromo-2,5-bis(trifluoromethyl)benzene (2) with phenoxazine, phenothiazine or 9,10-dihydro-9,9-dimethylacridine in the presence of tris(dibenzylideneacetone)dipalladium(0) and X-Phos at 110 °C gave the target D–A–D type compounds. The structures of the synthesized compounds, except that of **2PO-2CF$_3$Ph**, were confirmed by ^{1}H and ^{13}C NMR spectroscopy. It was not possible to confirm the structure of **2PO-2CF$_3$Ph** by ^{1}H and ^{13}C NMR due to solubility problems in all available deuterated solvents. However, we were able to confirm the structure by single crystal X-ray analysis. The single crystal X-ray crystallography data show that the dihedral angle between the donor and acceptor is 85.5° (Fig. 1).

3.2. X-Ray analysis

Additionally, the structures of **2PO-2CF$_3$Ph**, **2PS-2CF$_3$Ph** and **2AC-2CF$_3$Ph** were confirmed using X-ray methodology. Single crystals of each compound were grown from dilute THF solution. **2AC-2CF$_3$Ph** and **2PO-2CF$_3$Ph** compounds crystallize in the *P*21/*c* monoclinic space group while, in the case of **2PO-2CF$_3$Ph**, the monoclinic *C*2/*c* space group was found. The

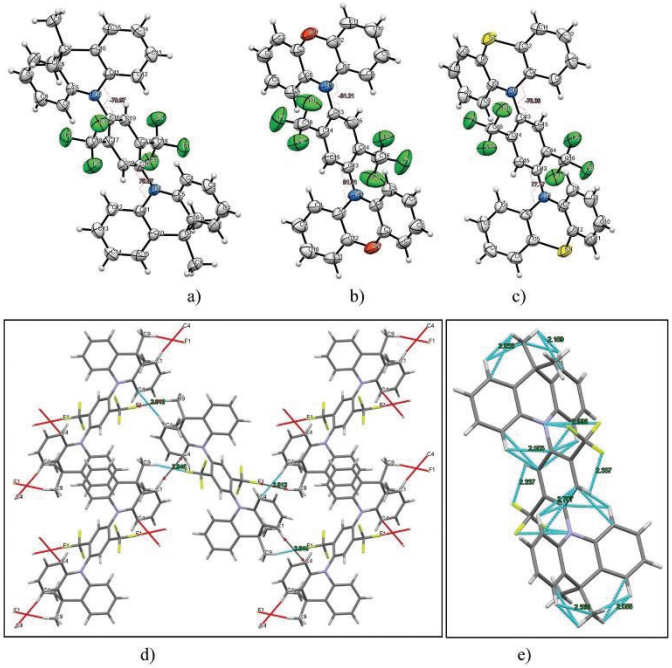

Fig. 1 X-Ray structures of compounds (a) **2PO-2CF$_3$Ph**, (b) **2PS-2CF$_3$Ph** and (c) **2AC-2CF$_3$Ph**. Torsional angles between the donor and acceptor units are shown in purple dashed lines. Packing in the crystal structure of compound **2AC-2CF$_3$Ph** viewed along the *a*-axis (d). Packing in the crystal structure of compound **2AC-2CF$_3$Ph** viewed along the *a*-axis (d) and intramolecular bonding (e).

Oak Ridge Thermal Ellipsoid Plot (ORTEP) projections show (Fig. 1a–c) that all target compounds are symmetrical. In addition, an X-ray study of the packing pattern in the crystal revealed that molecules are held together through weak van der Waals intermolecular bonds, which appear between CF_3 fluorine and methyl hydrogen atoms or carbon and hydrogen atoms of the phenyl ring. For example, in the case of **2AC-2CF$_3$Ph**, C–H···F and C–H···C were found and their distances ranged from 2.61 to 2.85 Å (Fig. 1d). Additionally, the following weak intramolecular bonds (distance $<$ 2.71 Å) are present: C–H···F, C–F···N, C–H···H, and C–H···C. Electron-donating moieties (acridine, phenoxazine and phenothiazine) found in the corresponding compounds (**2PO-2CF$_3$Ph**, **2PS-2CF$_3$Ph** and **2AC-2CF$_3$Ph**) are non-planar, *i.e.* they are twisted by 15°, 30° and 31°, respectively. As for TADF emitters, the significant factor is a large torsional angle between the donor and acceptor fragments.[34] For all three investigated compounds (**2PO-2CF$_3$Ph**, **2PS-2CF$_3$Ph** and **2AC-2CF$_3$Ph**), the torsional angles between 1,4-bis(trifluoromethyl)benzene and phenoxazine phenothiazine, and acridine moieties were found to be 81.2°, 80.0°, and 77.2°, respectively.

3.3. Frontier orbitals

DFT simulations were performed to investigate the molecular structures. Their optimized structures are shown in Fig. 2. The molecules exhibited large dihedral angles of 81.3°, 84.8°, and 82.0° between the donor and acceptor moieties for **2PO-2CF$_3$Ph**, **2PS-2CF$_3$Ph**, and **2AC-2CF$_3$Ph**, respectively. This is in close agreement with the single crystal data. The values of dihedral angles are very close to the experimental X-ray data obtained. The near orthogonal angle between the donor and acceptor is helpful for the efficient separation of frontier molecular orbitals. 9,9-Dimethyl-9-10-dihydroacridine and phenothiazine exhibited a saddle structure with the carbon and sulphur bending away from the planar structure at angles of 29.5° and 30.3°, respectively, while phenoxazine is rather flat. This is confirmed through X-ray data except for phenoxazine which is slightly saddled (~15°) rather than flat. The HOMOs are equally distributed on the two units of donors and the LUMO is concentrated on **2CF$_3$Ph** as seen in Fig. 2. For HOMOs, there is a small overlapping of electron clouds with the LUMOs, which is crucial for increasing the oscillatory strength of the emitters. The nodes at the acceptor at the HOMO level are the antinodes of the LUMO level. The LUMO extends the electron clouds into the trifluoromethyl groups. A closer inspection indicates that the Sigma-bond of C–F is hyperconjugated with the π bonds of the benzene rings while the lone pairs of fluorine atoms interact with the hyperconjugated carbon, resulting in resonance/electron delocalization that extends from the benzene π-electrons to the fluorine lone pair of electrons.[25,26]

The HOMO energies of **2PO-2CF$_3$Ph**, **2PS-2CF$_3$Ph**, and **2AC-2CF$_3$Ph** were found to be 5.84 eV, −6.04 eV, and −6.06 eV, respectively, while the LUMO energies were −1.76 eV, −1.53 eV and −1.53 eV, respectively. The HOMO and LUMO of **2PO-2CF$_3$Ph** are deeper than those of the other compounds studied since the oxygen atom in PO enhances the pull-push electron effect of **2PO-2CF$_3$Ph**. The ionization potentials were determined using the oxidation onset (E_{onset}) in cyclic voltammetry (CV) curves relative to the Ag/Ag^+ reference electrode. The derived values for **2PO-2CF$_3$Ph**, **2PS-2CF$_3$Ph** and **2AC-2CF$_3$Ph** were found to be −5.31 eV, −5.38 eV and −5.36 eV, respectively. These values cannot be directly related to the ionization potentials of **2PO-2CF$_3$Ph**, **2PS-2CF$_3$Ph** and **2AC-2CF$_3$Ph**.[35] According to photoelectron spectroscopy measurements in air, ionization potential values of 6.01, 6.05, and 6.08 eV were obtained for the films of **2PO-2CF$_3$Ph**, **2PS-2CF$_3$Ph** and **2AC-2CF$_3$Ph**, respectively (Fig. S1d, ESI†). Considering the charge transport in the solid state, ionization potentials estimated by photoelectron spectroscopy have to be used. For example, an ionization potential of 6.08 eV for **2AC-2CF$_3$Ph** was used for the selection of OLED structures as will be shown below.

3.4. Molecular dynamics simulation

The photophysical properties of the compounds were analysed by measuring the UV-vis absorption and photoluminescence (PL) spectra of their toluene solutions at room temperature as shown in Fig. 3. High-energy absorption peaks observed below 350 nm can be assigned to the n–π*/π–π* transitions from the

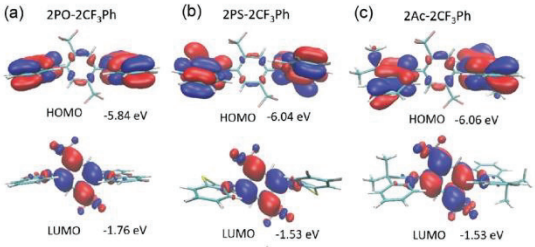

Fig. 2 HOMO and LUMO along with their energy levels for (a) **2PO-2CF$_3$Ph**, (b) **2PS-2CF$_3$Ph** and (c) **2Ac-2CF$_3$Ph**. Note there is no total separation of HOMO and LUMO electron clouds.

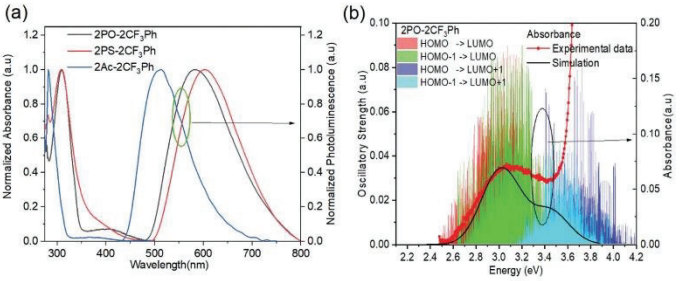

Fig. 3 (a) UV-vis absorption and photoluminescence spectra of the solutions of the compounds in toluene and (b) the quantum molecular dynamics simulations of vertical excitation of the 4 lowest excited states for **2PO-2CF$_3$Ph** along with their oscillatory strengths and simulated absorption curve by applying Gaussian broadening.

donors. Very broad absorption from 350 nm to 500 nm can be designated as CT absorption peaks from the donor to acceptor units. The natural transition orbital analysis based on time-dependent DFT for ^{1}CT and ^{3}CT states indicates that the lowest transition is strongly dominated by HOMO and LUMO transition with a contribution of more than 0.98 for all three molecules. These broad ^{1}CT absorption peaks are clearly seen when there is a wide separation between the ^{3}CT states and ^{1}LE states. Vertical excitation of **2PO-2CF$_3$Ph**, **2PS-2CF$_3$Ph**, and **2AC-2CF$_3$Ph** yields transition energies of 2.37 eV, 2.70 eV and 2.78 eV with an oscillatory strength of less than 0.00005. **2AC-2CF$_3$Ph** yields an oscillatory strength of 0.0002. Such an extremely small oscillatory strength is the result of such near orthogonality between the donor and acceptor. Neglecting the explicit solute–solvent interactions, broadening derived from the spread of vertical excitation energies for different conformations can be computed in its ground state minimum. The disordered nature of molecules can be accounted for by using the ensemble approach. In the ensemble approach, the structures obtained from the molecular dynamics are used for the computation of vertical excitation energies. All the transition energies along with the respective oscillatory strength calculated by TD-TDF are shifted by 0.6 eV so as to align with the peak of absorption. The absorption between 2.6 eV to 3.8 eV for **2PO-2CF$_3$Ph** is dominated by charge transfer transitions from the HOMO to LUMO at ~2.8 eV, from HOMO−1 to the LUMO at ~3.0 eV, from the HOMO to LUMO+1 at ~3.5 eV and from HOMO−1 to LUMO+1 at ~3.6 eV as shown in Fig. 3(b). The simulated absorption curve is calculated by broadening each oscillatory transition by Gaussian line shape with a standard deviation of 0.1 eV. The higher energy deviated significantly because only the 4 lowest transition states are considered. The CT absorption curve of **2PS-2CF$_3$Ph** different from those of **2AC-2CF$_3$Ph** and **2PO-2CF$_3$Ph** as revealed by quantum molecular dynamics simulations is the consequence of a larger energy separation among the 4 lowest CT transitions as shown in (Fig. S2, ESI†).

A plot of the dihedral angle between the donor and acceptor *versus* oscillatory strength of the 1st ^{1}CT state of **2PO-2CF$_3$Ph** shown in Fig. 4(a) indicates that a smaller dihedral angle between the donor and acceptor is not the necessary condition for a larger oscillatory strength. Similar behaviours were also observed for **2PS-2CF$_3$Ph** and **2AC-2CF$_3$Ph** (Fig. S3, ESI†). However, when 100 data points are considered for a narrow range of dihedral angles, the mean oscillatory strengths start to show a parabolic feature with a minimum oscillatory strength at 85° as shown in Fig. 4(b) for **2PS-2CF$_3$Ph** and **2AC-2CF$_3$Ph** with the exception of **2PO-2CF$_3$Ph** where the oscillatory strength shows a spike at around 80°–90°. An extracted molecular structure representing this peculiar region is presented in Fig. 4(c). Fig. 4(c) shows the natural transition orbitals (NTOs) of the selected conformation distortion of **2PO-2CF$_3$Ph** due to the vibration exhibiting an oscillatory strength as high as 0.090 compared with the median oscillatory strength of 0.0044 within the simulated population. The highest occupied transition orbital (HONTO) of this conformer is extended into the acceptor through the C–N bond. The ΔE_{ST} is calculated to be 0.23 eV and the NTO is no longer dominated by the HOMO to LUMO transitions. It is rather a mixture of the HOMO to LUMO (0.83, contribution coefficient) and HOMO−1 to LUMO (−0.50, contribution coefficient). This increases the lowest unoccupied natural transition orbital (LUNTO) and HONTO distorting C–N–C bonds as seen in Fig. 4(b). The molecular distortion is induced by the rocking of the donor–acceptor bond as illustrated in Fig. 4(c) and such rocking has been found to contribute to reverse intersystem crossing.[29] This rocking is the in plane bending of the two donors where the donors swing back and forth with respect to the acceptor. The vibrational frequency of the ground state indicates that the rocking oscillation is the lowest vibrational mode at 7.2 cm^{-1} for **2PO-2FC$_3$Ph** and at 15.2 cm^{-1} and 18.6 cm^{-1} for **2PS-2FC$_3$Ph** and **2AC-2FC$_3$Ph**, respectively. The slow rocking uninterrupted by the jostling of the solvent molecules is captured within the QMD 10 ps simulation window, giving rise to the observed

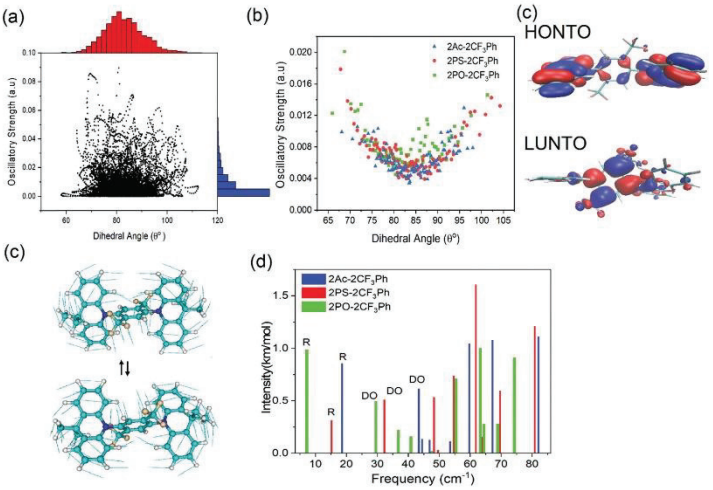

Fig. 4 (a) The dihedral angle between the donor and acceptor and their respective oscillatory strengths with the top histogram corresponding to the distribution of the dihedral angle and the right axis histogram corresponding to the distribution of oscillatory strength. (b) The mean oscillatory strengths *versus* dihedral angle calculated using 100 data points. The mean oscillatory strengths tend to decrease when the dihedral angle approaches 85°. (c) Natural Transition orbitals of **2PO-2CF$_3$Ph** with the top picture corresponding to the highest occupied transition orbital and the bottom picture corresponding to the lowest unoccupied transition orbital. (d) The rocking of the donor–acceptor of **2PO-2CF$_3$Ph**. (e) The vibrational frequencies (<100 cm^{-1}) of the three molecules and their vibrational intensities. The lowest vibrational frequency always corresponding to rocking between the donor and acceptor is indicated as R in the graph while the next higher vibrational frequency corresponding to the dihedral oscillation between the donor and acceptor is indicated as DO in the graph.

'anomaly' seen between 80° and 90° as shown in Fig. 4(b). The lowest D–A torsional oscillation (DO), which is the oscillation around the dihedral angle, occurs at 32.3 cm^{-1}, 32.3 cm^{-1}, and 29.5 cm^{-1} for **2PO-2CF$_3$Ph**, **2PS-2CF$_3$Ph**, and **2AC-2CF$_3$Ph**, respectively, as summarized in Fig. 4(d). The visualization of the lowest four molecular vibrations can be found in Fig. S4 (ESI†). The PL spectra show full-width half maximum (FWHM) values of 0.536 eV, 0.501 eV and 0.488 eV for **2CF$_3$Ph**, **2PS-2CF$_3$Ph**, and **2AC-2CF$_3$Ph**, respectively. The simple phenomenological line shape of flexible molecules can be accounted for through the sampling of molecular conformations.[36] These FWHM values can be related to the conformational disorder of the molecules in the excited state and the ground state. Assuming that the molecular conformations at the excited state and ground state are independent and the change in the molecular conformation is the result of thermal perturbation from the solvent molecules the FWHM of emission (which can be fitted with a Gaussian curve) can be approximated by $\sqrt{2} \times 2.355 \times \sigma^a$, where σ is the standard deviation of the ^{1}CT energy state. The values of σ of the 1st CT state in absorption as calculated from the QMD are 0.135 eV, 0.159 eV and 0.135 eV for **2CF$_3$Ph**, **2PS-2CF$_3$Ph**, and **2AC-2CF$_3$Ph**, respectively. The expected FWHM values for **2CF$_3$Ph**, **2PS-2CF$_3$Ph**, and **2AC-2CF$_3$Ph** are 0.450 eV, 0.503, and 0.450 eV. These values are close to the FWFM of the emission spectra. The σ can be used to infer the FHWM of the TADF emission and design a narrower σ.

3.5. Energy levels and delayed fluorescence

The PL spectra of the matrix of the compounds in Zeonex at 1% concentration recorded at different temperatures are shown in Fig. 5. When the phosphorescence spectra were discriminated from the fluorescence spectra by applying a delay time of 1, 5 or 9 ms at 77 K, it was not possible to estimate the ^{3}CT energy by optical spectroscopy measurements as was noted above (Fig. 5 and Fig. S5, ESI†). The onsets of the phosphorescence spectra recorded at 77K and at the different gate delays of the matrix of **2PO-2CF$_3$Ph**, **2PS-2CF$_3$Ph**, and **2AC-2CF$_3$Ph** in Zeonex and MeTHF are related to their triplet LE states in the nature (Fig. S5a and b, ESI†). These triplet LE states can be attributed to the triplet LE states (^{3}LE$_b$) of the corresponding donor moieties (10-phenyl-10*H*-phenoxazine (PO–Ph), 10-phenyl-10*H*-

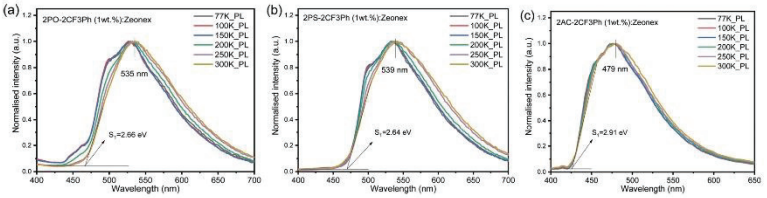

Fig. 5 The low-temperature and room-temperature PL of **2PO-2CF$_3$Ph** (a), **2PS-2CF$_3$Ph** (b) and **2AC-2CF$_3$Ph** (c) in Zeonex and the corresponding onsets of emission at 300 K.

phenothiazine (PS–Ph) or 9,9-dimethyl-10-pheny-9,10-dihydroacridine (AC–Ph)) due to the similarities of the onsets of phosphorescence of **2PO-2CF$_3$Ph**, **2PS-2CF$_3$Ph**, and **2AC-2CF$_3$Ph** and PO–Ph, PS–Ph, and AC–Ph (Fig. S5c, ESI†) In addition, the onset of phosphorescence of the acceptor moiety is observed at a higher energy (^{3}LE$_A$ = 3.65 eV) than that of the donor units PO–Ph, PS–Ph, and AC–Ph (Fig. S5d, ESI†). Therefore, the first singlet energy of **2PO-2CF$_3$Ph**, **2PS-2CF$_3$Ph** and **2AC-2CF$_3$Ph** was only estimated from the onsets of the PL spectra recorded at 300 K. The emission was mostly fluorescence (Fig. 5). The PL spectrum recorded at room temperature was redshifted with respect to the PL spectrum recorded at 77 K with increasing emission intensity at the lower energy levels except for **2AC-2CF$_3$Ph**. This observation can be attributed to the reduced conformational heterogeneity.[37,38] As is discussed below, the ^{1}CT energy was only taken as it is depicted in Fig. 7. Theoretically the energy gaps between the ^{3}CT and ^{1}CT were predicted to be of 0.04 eV, 0.03 eV and 0.04 eV for **2PO-2CF$_3$Ph**, **2PS-2CF$_3$Ph** and **2AC-2CF$_3$Ph**, respectively. The compounds were characterized by close values of ΔE_{ST}. TADF is a dynamical process for which there is a need to consider spin–orbit and vibronic couplings simultaneously. Since the spin–orbit coupling matrix elements of all organic TADF molecules are vanishing small, the vibronic coupling between the low lying electronic states is important. Here, we will consider the coupling with the ^{3}LE state to meditate the RISC.

To examine the TADF behavior of the compounds in detail, their PL decay curves were recorded at different temperatures (Fig. 6a–c). The typical TADF decay curves were observed. They showed prompt decay (PF) in nanosecond range and microsecond delayed decay (DF). As the temperature was decreased, the DF was suppressed for all three compounds indicating that DF was thermally activated (Fig. 7). The fluorescence decays could be fitted by the sum of two exponentials, one describing

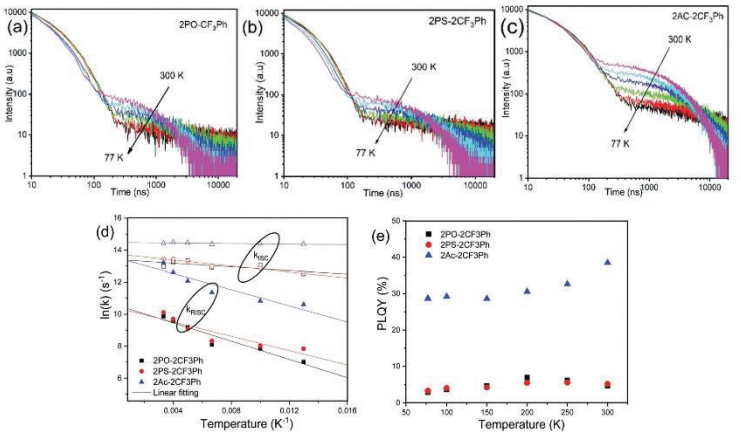

Fig. 6 Fluorescence decay of (a) **2PO-2CF$_3$Ph** (b) **2PS-2CF$_3$Ph** and (c) **2Ac-2CF$_3$Ph** doped 1 wt% in Zeonex as a function of temperature as well as their k_{ISC}/k_{RISC} (d) and PLQY (e) temperature dependences.

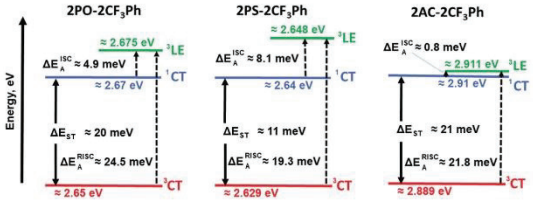

Fig. 7 Energy levels of compounds **2PO-2CF$_3$Ph**, **2PS-2CF$_3$Ph** and **2AC-2CF$_3$Ph**.

the PF and the other DF decays (Fig. S6, ESI†). The lifetimes of PF and DF for **2PO-2CF$_3$Ph**, **2PS-2CF$_3$Ph** and **2AC-2CF$_3$Ph** were found to be 21.5 ns and 18.2 ns, 35.4 ns and 0.93 μs, and 1.41 μs and 2.56 μs, respectively (Table 1).

The rate of reverse intersystem crossing (k_{RISC}) can be approximated to be 1.92×10^4 s^{-1}, 2.46×10^4 s^{-1} and 5.45×10^5 s^{-1} for **2PO-2CF$_3$Ph**, **2PS-2CF$_3$Ph** and **2AC-2CF$_3$Ph**, respectively.[37] The higher k_{RISC} values observed for **2AC-2CF$_3$Ph** compared to those of **2PO-2CF$_3$Ph** and **2PS-2CF$_3$Ph** are apparently due to the lower gap of $\Delta E_{3CT-3LE}$ of **2AC-2CF$_3$Ph**. To prove this prediction, the rates of intersystem crossing (k_{ISC}) and k_{RISC} were calculated at the different temperatures taking lifetimes of PF and DF from the single-exponential fitting of TADF decays recorded at different temperatures (Fig. S6, ESI†). The rates k_{ISC} and k_{RISC} as a function of temperature are plotted in Fig. 6d. By the linear fitting of the plots, the ISC and RISC activation energies (E_A^{ISC} and E_A^{RISC}) were obtained (Table 1). The fitting was performed according to the Arrhenius dependence $k = A \times \exp(-E_a/k_BT)$, where E_a is the activation energy, k_B is the Boltzmann constant and A is the frequency factor involving the spin–orbit coupling constant.[38] The different activation energies of intersystem crossing E_A^{ISC} and reverse intersystem crossing E_A^{RISC} were obtained for **2PO-2CF$_3$Ph**, **2PS-2CF$_3$Ph** and **2AC-2CF$_3$Ph**. Those activation energies were used to construct the energy diagram shown in Fig. 7 as was previously proposed (Table 1).[39] The best mixing of ^{3}LE and the excited state wave function of ^{3}CT was obtained for **2AC-2CF$_3$Ph** due to the lowest $\Delta E_{3LE-3CT}$. This result is coherent with the highest k_{RISC} of 5.45×10^5 s^{-1} and k_{RISC}/k_{ISC} ratio of 0.296, which means the most efficient TADF of **2AC-2CF$_3$Ph** (Table 1). The ^{3}CT energy state was not possible to take from optical spectroscopy measurements as was noted above (Fig. 5 and Fig. S5, ESI†). Nevertheless, the triplet CT states can be calculated using the activation energies for the ISC and RISC processes (Fig. 7). As a result, the ^{1}CT–^{3}CT energy gaps of 20 meV for **2PO-2CF$_3$Ph**, 11 meV for **2PS-2CF$_3$Ph** and 21 meV for **2AC-2CF$_3$Ph** were obtained (Fig. 7 and Table 1). The trend of those ΔE_{ST} values of **2PO-2CF$_3$Ph**, **2PS-2CF$_3$Ph** and **2AC-2CF$_3$Ph** was not in agreement with the trend of their TADF efficiency. However, the trend of the TADF efficiency of studied compounds was the same as that of their $\Delta E_{3LE-1CT}$ values. For example, the best TADF efficiency was observed for **2AC-2CF$_3$Ph** which is characterized by the lowest $\Delta E_{3LE-1CT}$ value of 0.8 meV (Fig. 7).

Apparently due to the relatively high $\Delta E_{3LE-3CT}$, PLQYs of **2PO-2CF$_3$Ph** and **2PS-2CF$_3$Ph** reached their maxima at *ca.* 200 K (Fig. 6e). The further increase of the temperature leads to the decrease of the PLQY values most probably due to the increase of non-radiative rates of the triplet states (k_{nr}^T, Table S1, ESI†). In contrast, **2AC-2CF$_3$Ph** showed an increase of PLQYs up to 38.5% with an increase of the temperature from 77 to 300 K due to the efficient TADF process. The highest ratio k_{RISC}/k_{nr}^T of 5.9 was observed for **2AC-2CF$_3$Ph**. This k_{RISC}/k_{nr}^T ratio has to be higher than unity (the case of **2AC-2CF$_3$Ph**) for efficient TADF emitters.[40,41] As was previously mentioned, the theoretical calculations yielded ^{1}CT values of 2.37 eV, 2.70 eV and 2.78 eV for **2PO-2CF$_3$Ph**, **2PS-2CF$_3$Ph**, and **2AC-2CF$_3$Ph** respectively. We also noted that X-ray data for the phenoxazine moiety in **2PO-2CF$_3$Ph** is slightly saddled (~15°) rather than flat as predicted by geometry optimisation. This resulted in a larger error of ^{1}CT compared with experimental data for **2PO-2CF$_3$Ph**. ^{1}CT values for **2PS-2CF$_3$Ph** and **2AC-2CF$_3$Ph** are close to each other (error less than 0.2 eV). Nevertheless, from the calculations, the oscillatory strengths for all three compounds are virtually zero. From the experiment, the ^{3}LE values of **2PO-2CF$_3$Ph** and **2PS-2CF$_3$Ph** are far higher than that of **2AC-2CF$_3$Ph**, resulting in very low RISC and hence very low

Table 1 Photophysical parameters of 1 wt% molecular dispersions of compounds **2PO-2CF$_3$Ph**, **2PS-2CF$_3$Ph** and **2Ac-2CF$_3$Ph** in Zeonex

Compound	2PO-2CF$_3$Ph	2PS-2CF$_3$Ph	2Ac-2CF$_3$Ph
λ_{PL}^{ICT}, nm	535	537	477
PLQY, %	4.6	5.2	38.5
ΔE_{ST}^a, eV	0.02	0.011	0.021
τ_{PF}, ns (ratio, %)	21.5 (72.3%)	18.2 (28.2%)	35.4 (21.6%)
τ_{DF}, μs (%)	0.93 (27.7%)	1.41 (71.8%)	2.56 (78.4%)
k_{ISC}, s^{-1}	4.33×10^5	6.91×10^5	1.84×10^6
k_{RISC}, s^{-1}	1.92×10^4	2.46×10^4	5.45×10^5
k_{RISC}/k_{ISC}	0.044	0.036	0.296
ΔE_A^{ISC}, meV	4.9	8.1	0.8
ΔE_A^{RISC}, meV	24.5	19.3	21.8
k_{nr}^T	4.78×10^4	3.53×10^4	9.25×10^4
k_{RISC}/k_{nr}^T	0.4	0.7	5.9

[a] The ΔE_{ST} values were calculated using the activation energies of ISC and RISC processes.

PLQY for **2PO-2CF$_3$Ph** and **2PS-2CF$_3$Ph** but not for **2AC-2CF$_3$Ph** (Table 1). This indicates that the $\Delta E_{3LE-3CT}$ gap is critical in increasing RISC which later yields high PLQY.

It should be noted that the ^{3}LE values of PO–Ph, PS–Ph and AC–Ph were experimentally measured to be 2.83 eV, 2.65 eV and 3.22 eV respectively (Fig. S5c, ESI†). In the case of **2PO-2CF$_3$Ph** and **2PS-2CF$_3$Ph**, the triplet LE states of PO–Ph and PS–Ph calculated using the activation energies for the ISC process were in relatively good agreement with the experimental ones. In the case of **2AC-2CF$_3$Ph**, a ^3LE_D of *ca.* 3.19 eV was estimated. It is considerably higher than the calculated one (2.911 eV). It is possibly because other donating fragments should be used for experimental determination of ^{3}LE values as was discussed elsewhere.[42] However, after a more precise analysis of the phosphorescence spectra of **2AC-2CF$_3$Ph** and AC–Ph (Fig. S5b and c, ESI†), two bands were identified. The high (3.19 eV) and low (*ca.* 2.92 eV) bands attributed to phosphorescence but not to delay fluorescence according to the PL decay measurements (Fig. S6, ESI†). The delay fluorescence was recorded in time ranging up to *ca.* 0.5 ms; while the phosphorescence was recorded using a delay of 9 ms (Fig. S5c, ESI†). This observation shows that compound **2AC-2CF$_3$Ph** is characterized by two ^3LE_D states apparently having $\pi\pi^*$ and $n\pi^*$ character as was reported for 10-phenyl-10*H*, 10′*H*-spiro[acridine9,9′-anthracen]-10′-one.[43,44] A $\pi\pi^*$ ^3LE_D value of *ca.* 3.19 eV and an $n\pi^*$ ^3LE_D value of *ca.* 2.92 eV were obtained for **2AC-2CF$_3$Ph** (Fig. S5b, ESI†). The value of $n\pi^*$ ^3LE_D is in very good agreement with the calculated triplet LE value (Fig. 7). Thus, the energy diagram shown in Fig. 7 can appropriately explain the most efficient TADF properties of **2Ac-2CF$_3$Ph**. It is also in good agreement with the experimentally measured ^{3}LE values of **2PO-2CF$_3$Ph**, **2PS-2CF$_3$Ph** and **2Ac-2CF$_3$Ph**.

After selection of SimCP2 as the OLED host, we recorded the PL spectra of the films of molecular mixtures of **2AC-2CF$_3$Ph** and **SimCP2** containing 10, 15, and 20 wt% of **2AC-2CF$_3$Ph** (Fig. S8a, ESI†). The shapes and maxima of the PL spectra of the films with different concentrations of **2AC-2CF$_3$Ph** were found to be very similar. This observation is in good agreement with the EL spectra of **2AC-2CF$_3$Ph**-based devices as is discussed below. The film of the molecular mixture of **2AC-2CF$_3$Ph** and SimCP2 containing 10 wt% of the emitter was selected for the investigation of TADF properties (Fig. S8b–e, ESI†). The PL spectra and PL decays of the molecular dispersion of **2AC-2CF$_3$Ph** in SimCP2 were very similar to those of **2AC-2CF$_3$Ph** in Zeonex (Fig. 5, 6c and Fig. S5, ESI†). The laser energy dependence of the delayed emission intensity was recorded for the emitting layer of **2AC-2CF$_3$Ph** [10 wt%]: SimCP2 (Fig. S7, ESI†). The slope of 0.95 of the dependence additionally supports the TADF origin of emission of **2AC-2CF$_3$Ph**.[45] Taking into account the poor TADF properties of **2PO-2CF$_3$Ph** and **2PS-2CF$_3$Ph**, the photophysical measurements of these compounds in the SimCP2 host were not provided.

3.6. Electroluminescence

Compound **2AC-2CF$_3$Ph** exhibited the best combination of the properties required for OLED applications. It was therefore selected as a TADF emitter for the electroluminescence study. The device structure was ITO/MoO_3[0.5 nm]/NPB[40 nm]/TCTA[4 nm]/mCBP[4 nm]/light-emitting layer [24 nm]/TSPO1[4 nm]/TPBi[40 nm]/LiF[0.5 nm]:Al[88 nm], in which the layers of **2AC-2CF$_3$Ph**[5 wt%]:SimCP2, **2AC-2CF$_3$Ph** [10 wt%]:SimCP2 and **2AC-2CF$_3$Ph**[15 wt%]:SimCP2 were used as the light-emitting layers for device A, B, and C, respectively. The light-emitting layer of 20 wt% molecular dispersion of **PFBP-2a** in SimCP2 was used in the reference device D in which the TADF emitter **PFBP-2a** with a fluorine-containing acceptor (perfluorobiphenyl) was used.[33] As a result, a direct comparison of the electroluminescence performances was possible for the developed D–A electronic systems (9,9-dimethyl-9-10-dihydroacridine-1,4-bis(trifluoromethyl)benzene) with a similar one (9,9-dimethyl-9-10-dihydroacridine-perfluorobiphenyl). The materials with the usual roles, namely MoO_3 as hole-injecting, NPB and TCTA as hole-transporting, mCBP as electron/exciton-blocking, SimCP2 as the host, TSPO1 as hole/exciton-blocking, TPBi as electron-transporting, and LiF as electron-injecting materials, were used in the device structures, aiming to provide balanced hole–electron recombination and exciton formation within the light-emitting layers (Fig. 8a). The selection of the host SimCP2 was caused by the following considerations. SimCP2 has a T_1 of 3.0 eV with a lower polarity than DPEPO and an ambipolar transport property.[46] When **PFBP-2a** or **2AC-2CF$_3$Ph** is doped into SimCP2 (as the HOMO levels of the emitters and the host are almost the same), the holes are easily transported while the electrons can be easily captured by the emitters (since the LUMOs of the emitters are deeper than those of the host). The zone of recombination will be located near the SMPCP2/TPSO1 interface. TPSO1 is an excellent electron-transporting and hole blocking material, which, along with a high triplet energy of over 3.36 eV, can suppress Dexter energy transfer loss into TPS01.[47] The previous studies indicated that a high-triplet-energy ETL is critical for the high efficiency of blue OLEDs at high brightness.[48]

The EL spectra (peaking at 485 nm and with a full-width-at-half-maximum (FWHM) of 85 nm) of the devices A–C were very similar to the PL spectra of the corresponding light-emitting layers of **2Ac-2CF$_3$Ph** doped in SimCP2 peaking at 487 nm with a FWHM of 87 nm (Fig. 8b and Fig. S8, ESI†). According to this observation, the EL is attributed to the emission of **2Ac-2CF3Ph**. Small differences between the PL and EL spectra are caused by the different optical and electrical excitation sources used. The EL spectrum of device D is in agreement with those of the previously studied **PFBP-2a**-based devices.[33] The bands which could be attributed to additional functional materials were not observed. The close values of turn-on voltages of *ca.* 4.4 V were obtained for devices A–D due to the similar charge-injecting properties of **2AC-2CF$_3$Ph** and **PFBP-2a** (Fig. 8d). At voltages higher than *ca.* 7V, higher operating current densities were observed for devices A–C in comparison to that of Device D apparently because of the better charge-transporting properties of **2AC-2CF$_3$Ph** relative to those of **PFBP-2a**.

The EL spectra of devices A–C recorded at different voltages showed practically the same shapes and maxima wavelengths.

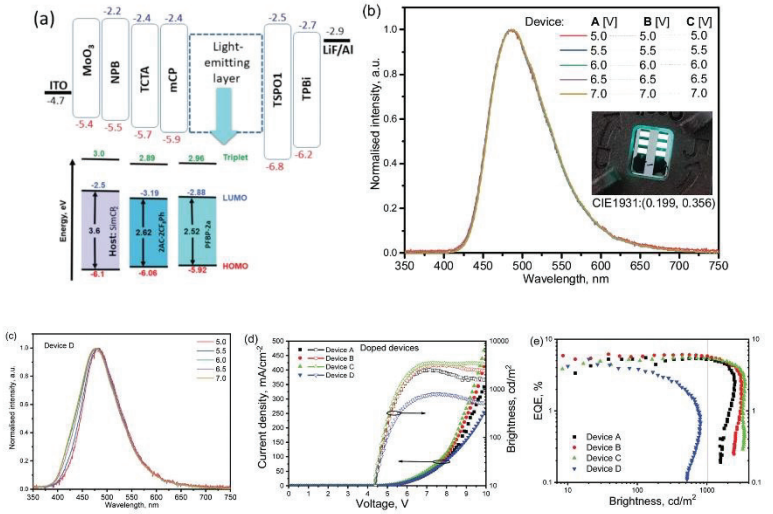

Fig. 8 Equilibrium energy diagram (a), EL spectra recorded at different voltages (b, c), current density and brightness as a function of applied voltages (d) and EQE *versus* current density plots (e) for devices A–D. The inset shows the photo and CIE1931 colour coordinates of devices A at 6V.

In addition, they were very similar for different devices A–C despite the slightly different concentrations of the emitter **2AC-2CF$_3$Ph** used. This observation can be attributed to the formation of non-covalent intramolecular bonds by **2AC-2CF$_3$Ph** in solid-state as is demonstrated in Fig. 1e. In contrast, the reference D–A electronic system (9,9-dimethyl-9-10-dihydroacridine-perfluorobiphenyl) demonstrated unstable EL spectra in device D even at different external voltages (Fig. 8c).[33] This observation well highlights the advantages of the newly designed electron-accepting 1,4-bis(trifluoromethyl)benzene moiety.

In comparison to the OLED based on a perfluorobiphenyl-containing compound, the advantages of the device based on the 1,4-bis(trifluoromethyl)phenyl containing compound were observed not only with respect to its EL spectra but also with respect to device efficiency roll-offs (Fig. 8e). At a valuable brightness of 1000 cd m^{-2}, EQE values were comparable with the maximum EQE values of devices A–C (Table 2). The EQE roll-off of device D was dramatic and its maximum brightness even did not reach 1000 cd m^{-2} (Fig. 8d). The "stable" EQE was observed for devices A–C at relatively low operating current densities (lower than 40 mA cm^{-2}). Then EQEs dramatically decreased. At higher operating current densities (higher than 40 mA cm^{-2}), the bonds with the lowest cleavage energy apparently could be firstly broken due to the exciton-polaron annihilation reactions as discussed elsewhere.[49,50]

Conclusions

Three derivatives of phenoxazine, phenothiazine or 9,9-dimethyl-9-10-dihydroacridine as donors and 1,4-bis(trifluoromethyl)benzene

Table 2 Electroluminescent parameters of non-doped (A1–A6) and doped (B1–B6) OLEDs

Device name	EML	λ_{EL}, nm	V_{ON}, V	L_{MAX}, cd m^{-2}	CE_{MAX}, cd A^{-1}	PE_{MAX}, lm W^{-1}	EQE_{10}/EQE_{1000}, %
Device structure is ITO/MoO_3/NPB/TCTA/mCBP/light-emitting layer (EML)/TSPO1/TPBi/LiF:Al							
A	**2AC-2CF$_3$Ph** [5 wt%]:SimCP2	487	4.4	2500	11.7	9.9	4.7/5.18
B	**2AC-2CF$_3$Ph** [10 wt%]:SimCP2	487	4.4	3000	12.9	10.7	5.9/5.8
C	**2AC-2CF$_3$Ph** [15 wt%]:SimCP2	487	4.4	3500	12.6	8.97	4.6/5.4
D	**PFBP-2a** [20 wt%]:SimCP2	478	4.4	800	6.2	5.6	4.4/–

λ_{EL} is the EL maximum; V_{ON} is the turn-on voltage; L_{MAX} is the maximum brightness; CE_{MAX} is the maximum current efficiency and PE_{MAX} is the maximum power efficiency. EQE_{10} and EQE_{1000} are EQEs at 10 and 1000 cd m^{-2}, respectively.

as an acceptor were synthesized. Despite the high dihedral angle between the donor and acceptor, total separation of frontier orbitals is not observed. The derivative of 9,9-dimethyl-9-10-dihydroacridine and 1,4-bis(trifluoromethyl)benzene was found to be a promising blue TADF emitter with a high singlet charge transfer onset of 2.91 eV. This compound demonstrated cyan electroluminescence which is "insensitive" to the concentration of the emitter in the light-emitting layer due to the intramolecular interactions. The highest external quantum efficiency of 5.9% with practically absent roll-off up to a brightness of 1000 cd m^{-2} was obtained for the device based on this emitter. The result leads to a more important conclusion that a decrease of the $\Delta E_{3LE-1CT}$ of TADF molecules can lead to an increase in the rate of reverse intersystem crossing and hence to an increase of the efficiency of TADF.

Author contributions

Levani Skhirtladze: investigation, conducting synthesis of the organic compounds; Karolis Lietonas: investigation, conducting the photophysics and electroluminescence measurements; Audrius Bucinskas: single crystal X-ray crystallography analysis; Dmytro Volyniuk: analysis of photophysics and electroluminescence data, writing of the manuscript and supervision; Malek Mahmoudi: measurements and analysis of thermal properties; Omar Mukbaniani: supervision; Kai Lin Woon: theoretical calculation, visualisation of the results and wrote the manuscript, Azhar Ariffin: methodology for synthesis, wrote the manuscript, and supervision; Juozas V. Grazulevicius: conceptualization, funding acquisition, and supervision.

Conflicts of interest

There are no conflicts to declare.

Acknowledgements

This project has received funding from European Regional Development Fund (project No 01.2.2-LMT-K-718-03-0019) under the grant agreement with the Research Council of Lithuania (LMTLT). KLW and AA thank for the funding from the European Union's Horizon 2020 research and innovation programme under the Marie Sklodowska-Curie Grant agreement no 823720. The computation is supported by the University Malaya Research University Grant-Faculty Program (GPF086B-2020). Iryna Danyliv is acknowledged for the synthesis of **PFBP-2a**.

References

1 L. Xiao, Z. Chen, B. Qu, J. Luo, S. Kong, Q. Gong and J. Kido, *Adv. Mater.*, 2011, **23**, 926–952.
2 X. K. Chen, D. Kim and J. L. Brédas, *Acc. Chem. Res.*, 2018, **51**, 2215–2224.
3 G. Hong, X. Gan, C. Leonhardt, Z. Zhang, J. Seibert, J. M. Busch and S. Bräse, *Adv. Mater.*, 2021, **33**(2005630), 1–24.
4 X. Liang, Z. L. Tu and Y. X. Zheng, *Chem. – Eur. J.*, 2019, **25**, 5623–5642.
5 Q. Wei, P. Imbrasas, E. Caldera-Cruz, L. Cao, N. Fei, H. Thomas, R. Scholz, S. Lenk, B. Voit, S. Reineke and Z. Ge, *J. Phys. Chem. A*, 2021, **125**, 1345–1354.
6 S. J. Woo, Y. H. Ha, Y. H. Kim and J. J. Kim, *J. Mater. Chem. C*, 2020, **8**, 12075–12084.
7 T. Serevičius, J. Dodonova, R. Skaisgiris, D. Banevičius, K. Kazlauskas, S. Juršėnas and S. Tumkevičius, *J. Mater. Chem. C*, 2020, **8**, 11192–11200.
8 J. Kosai, Y. Masuda, Y. Chikayasu, Y. Takahashi, H. Sasabe, T. Chiba, J. Kido and H. Mori, *ACS Appl. Polym. Mater.*, 2020, **2**, 3310–3318.
9 H. Tanaka, K. Shizu, H. Miyazaki and C. Adachi, *Chem. Commun.*, 2012, **48**, 11392–11394.
10 J. Lu, Y. Zheng and J. Zhang, *Phys. Chem. Chem. Phys.*, 2015, **17**, 20014–20020.
11 S. Xiang, R. Guo, Z. Huang, X. Lv, S. Sun, H. Chen, Q. Zhang and L. Wang, *Dyes Pigm.*, 2019, **170**(107636), 1–8.
12 G. Tang, A. A. Sukhanov, J. Zhao, W. Yang, Z. Wang, Q. Liu, V. K. Voronkova, M. Di Donato, D. Escudero and D. Jacquemin, *J. Phys. Chem. C*, 2019, **123**, 30171–30186.
13 Q. Chen, Y. Xiang, X. Yin, K. Hu, Y. Li, X. Cheng, Y. Liu, G. Xie and C. Yang, *Dyes Pigm.*, 2021, **188**(109157), 1–7.
14 T. Chen, C. H. Lu, Z. Chen, X. Gong, C. C. Wu and C. Yang, *Chem. – Eur. J.*, 2021, **27**, 3151–3158.
15 Q. Zhang, S. Sun, W. J. Chung, S. J. Yoon, Y. Wang, R. Guo, S. Ye, J. Y. Lee and L. Wang, *J. Mater. Chem. C*, 2019, **7**, 12248–12255.
16 H. Tanaka, K. Shizu, H. Nakanotani and C. Adachi, *J. Phys. Chem. C*, 2014, **118**, 15985–15994.
17 L. Su, F. Cao, C. Cheng, T. Tsuboi, Y. Zhu, C. Deng, X. Zheng, D. Wang, Z. Liu and Q. Zhang, *ACS Appl. Mater. Interfaces*, 2020, **12**, 31706–31715.
18 K. L. Woon, C. L. Yi, K. C. Pan, M. K. Etherington, C. C. Wu, K. T. Wong and A. P. Monkman, *J. Phys. Chem. C*, 2019, **123**, 12400–12410.
19 R. Xiao, Y. Xiang, X. Cao, N. Li, T. Huang, C. Zhou, Y. Zou, G. Xie and C. Yang, *J. Mater. Chem. C*, 2020, **8**, 5580–5586.
20 Y. Li, Z. Wang, X. Cai, K. Liu, J. Dong, S. Chang and S. J. Su, *Dyes Pigm.*, 2019, **163**, 249–256.
21 Y. Y. Wang, Y. L. Zhang, K. Tong, L. Ding, J. Fan and L. S. Liao, *J. Mater. Chem. C*, 2019, **7**, 15301–15307.
22 X. Cao, X. Zhang, C. Duan, H. Xu, W. Yuan, Y. Tao and W. Huang, *Org. Electron.*, 2018, **57**, 247–254.
23 Y. Li, J. J. Liang, H. C. Li, L. S. Cui, M. K. Fung, S. Barlow, S. R. Marder, C. Adachi, Z. Q. Jiang and L. S. Liao, *J. Mater. Chem. C*, 2018, **6**, 5536–5541.
24 S. Kothavale, W. J. Chung and J. Y. Lee, *ACS Appl. Mater. Interfaces*, 2020, **12**(16), 18730–18738.
25 K. L. Woon, Z. N. Nadiah, Z. A. Hasan, A. Ariffin and S. A. Chen, *Dyes Pigm.*, 2016, **132**, 1–6.
26 J. Grobe and D. Le Van, *J. Fluorine Chem.*, 2004, **125**, 801–821.
27 W. Yuan, H. Yang, C. Duan, X. Cao, J. Zhang, H. Xu, N. Sun, Y. Tao and W. Huang, *Chem*, 2020, **6**, 1998–2008.

28 M. K. Etherington, J. Gibson, H. F. Higginbotham, T. J. Penfold and A. P. Monkman, *Nat. Commun.*, 2016, 7(13680), 1–7.
29 J. Gibson, A. P. Monkman and T. J. Penfold, *ChemPhysChem*, 2016, **17**(19), 2956–2961.
30 J. Gibson and T. J. Penfold, *Phys. Chem. Chem. Phys.*, 2017, **19**, 8428–8434.
31 R. D. S. Stevens, R. Bonneau and J. Joussot-Dubien, *J. Chem. Phys.*, 1972, **57**, 5340–5342.
32 R. P. Frueholz, W. M. Flicker, O. A. Mosher and A. Kuppermann, *J. Chem. Phys.*, 1979, **70**, 3057–3070.
33 I. Hladka, D. Volyniuk, O. Bezvikonnyi, V. Kinzhybalo, T. J. Bednarchuk, Y. Danyliv, R. Lytvyn, A. Lazauskas and J. V. Grazulevicius, *J. Mater. Chem. C*, 2018, **6**, 13179–13189.
34 Z. Yang, Z. Mao, Z. Xie, Y. Zhang, S. Liu, J. Zhao, J. Xu, Z. Chi and M. P. Aldred, *Chem. Soc. Rev.*, 2017, **46**, 915–1016.
35 J.-L. Bredas, *Mater. Horiz.*, 2014, **1**, 17–19.
36 T. J. Zuehlsdorff and C. M. Isborn, *Int. J. Quantum Chem.*, 2019, **119**(e25719), 1–18.
37 F. B. Dias, T. J. Penfold and A. P. Monkman, *Methods Appl. Fluoresc.*, 2017, **5**(012001), 1–25.
38 A. E. Nikolaenko, M. Cass, F. Bourcet, D. Mohamad and M. Roberts, *Adv. Mater.*, 2015, **27**, 7236–7240.
39 T. Serevičius, R. Skaisgiris, I. Fiodorova, G. Kreiza, D. Banevičius, K. Kazlauskas, S. Tumkevičius and S. Juršėnas, *J. Mater. Chem. C*, 2021, **9**, 836–841.
40 K. H. Kim, S. J. Yoo and J. J. Kim, *Chem. Mater.*, 2016, **28**(6), 1936–1941.
41 M. Mahmoudi, J. Keruckas, K. Leitonas, S. Kutsiy, D. Volyniuk and J. V. Gražulevicius, *J. Mater. Res. Technol.*, 2021, **10**, 711–721.
42 H. Noda, X. K. Chen, H. Nakanotani, T. Hosokai, M. Miyajima, N. Notsuka, Y. Kashima, J. L. Brédas and C. Adachi, *Nat. Mater.*, 2019, **18**, 1084–1090.
43 L. G. Franca, A. Danos and A. Monkman, *J. Mater. Chem. C*, 2022, **10**, 1313–1325.
44 I. Lyskov and C. M. Marian, *J. Phys. Chem. C*, 2017, **121**(39), 21145–21153.
45 X. Qiao and D. Ma, *Mater. Sci. Eng., R*, 2020, **139**(100519), 1–38.
46 J.-H. Jou, W.-B. Wang, S.-Z. Chen, J.-J. Shyue, M.-F. Hsu, C.-W. Lin, S.-M. Shen, C.-J. Wang, C.-P. Liu, C.-T. Chen, M.-F. Wu and S.-W. Liu, *J. Mater. Chem. C*, 2010, **20**, 8411–8416.
47 S. O. Jeon, S. E. Jang, H. S. Son and J. Y. Lee, *Adv. Mater.*, 2011, **23**, 1436–1441.
48 M. A. bin Janai, K. L. Woon and C. S. Chan, *Org. Electr.*, 2018, **63**, 257–266.
49 N. C. Giebink, B. W. D'Andrade, M. S. Weaver, P. B. Mackenzie, J. J. Brown, M. E. Thompson and S. R. Forrest, *J. Appl. Phys.*, 2008, **103**(044509), 1–9.
50 J. Lee, C. Jeong, T. Batagoda, C. Coburn, M. E. Thompson and S. R. Forrest, *Nat. Commun.*, 2017, **8**(15566), 1–9.

Sensors & Actuators: B. Chemical 380 (2023) 133295

Contents lists available at ScienceDirect

Sensors and Actuators: B. Chemical

journal homepage: www.elsevier.com/locate/snb

Turn on of room temperature phosphorescence of donor-acceptor-donor type compounds via transformation of excited states by rigid hosts for oxygen sensing

Levani Skhirtladze [a], Karolis Leitonas [a], Audrius Bucinskas [a], Kai Lin Woon [a,b,*], Dmytro Volyniuk [a], Rasa Keruckienė [a], Malek Mahmoudi [a], Mieczyslaw Lapkowski [d,e], Azhar Ariffin [a,c,*], Juozas V. Grazulevicius [a,**]

[a] Department of Polymer Chemistry and Technology, Kaunas University of Technology, Barsausko 59, Kaunas 51423, Lithuania
[b] Department of Physics, Faculty of Science, Universiti Malaya, 50603 Kuala Lumpur, Malaysia
[c] Department of Chemistry, Faculty of Science, Universiti Malaya, 50603 Kuala Lumpur, Malaysia
[d] Department of Physical Chemistry and Technology of Polymers, Silesian University of Technology, Strzody 9, Gliwice 44-100, Poland
[e] Centre of Polymer and Carbon Materials, Polish Academy of Sciences Zabrze, M. Curie Sklodowskiej 34, 41-819 Zabrze, Poland

ARTICLE INFO

Keywords:
Room temperature phosphorescence
Hybrid local and charge transfer state
Host
Oxygen sensor

ABSTRACT

A series of compounds with the different donor moieties (phenothiazine, phenoxazine and acridine) and 1,4-difluorobenzene unit as the acceptor were developed for optical sensors of oxygen. Among three new compounds, oxygen sensing ability of one compound 10,10'-(2,5-difluoro-1,4-phenylene)bis(10 H-phenothiazine) (**2PS-2FPh**) exhibiting strong room-temperature phosphorescence in rigid matrix Zeonex shows high sensitivity to low concentration of oxygen (<0.1%). To understand the reason of the high oxygen sensitivity of **2PS-2FPh,** the effect of a rigid medium on conformational distortion was studied using a set of experimental and theoretical approaches. Doping **2PS-2FPh** into Zeonex results in strong room-temperature phosphorescence in a vacuum with singlet-triplet splitting (ΔE_{ST}) widened to 0.47 eV as compared to 0.17 eV observed for the solution in 2-methyltetrahydrofuran. Molecular dynamic simulation with **2PS-2FPh** doped in Zeonex indicates the increased molecular heterogeneity. Concomitantly, the hybrid local and charge transfer triplet state (^{3}HLCT) becomes more local allowing the room temperature phosphorescence to be observed from locally excited triplet states. These results showed that conformational disorder and rigidity of the medium can significantly widen ΔE_{ST} of donor-acceptor-donor type molecules transforming ^{3}HLCT into ^{3}LE and thus facilitating the room-temperature phosphorescence and high oxygen sensitivity of **2PS-2FPh.**

1. Introduction

For many decades, organic molecules have been thought to be non-phosphorescent at room temperature because of their weak spin-orbit couplings and large singlet to triplet gaps [1,2]. The recent observations of room-temperature phosphorescence (RTP) in organic aggregates have changed this perception [3–5]. RTP can only be observed in oxygen-free environment as the triplet states are quenched by oxygen[6, 7]. Compounds with the diverse structures have been shown to exhibit RTP[8–10]. Different mechanisms have been proposed to explain the RTP phenomenon [2,11]. Addition of side groups which constrain the dihedral oscillation between the donor and acceptor moieties to the structures of the compounds exhibiting thermally activated delayed fluorescence (TADF) the TADF process can be quenched giving rise to RTP[12]. Rigidification of the TADF molecules can also be achieved by dispersing the molecules in a rigid host [13,14]. Dual emissions (TADF and RTP) depending on the bulkiness of the sterically hindered substituent were also observed for molecules that contained different conformers [15–17]. The compounds exhibiting dual emission are useful for accurate oxygen sensing [18,19]. To enhance spin-orbit coupling (SOC) in TADF molecules, heteroatoms with abundant lone-pair electrons such as oxygen, nitrogen and sulphur can be incorporated. They introduce a

* Corresponding authors at: Department of Polymer Chemistry and Technology, Kaunas University of Technology, Barsausko 59, Kaunas 51423, Lithuania.
** Corresponding author.
E-mail addresses: ph7klw76@um.edu.my (K.L. Woon), azhar70@um.edu.my (A. Ariffin), juozas.grazulevicius@ktu.lt (J.V. Grazulevicius).

https://doi.org/10.1016/j.snb.2023.133295
Received 13 December 2022; Accepted 1 January 2023
Available online 3 January 2023

hybrid mixture of (n,π *) and (π,π *) characteristics into the excited states [20–22]. Other methods such as halogen bonding [23,24], crystal engineering [25,26], formation of H-aggregates [27,28] have been used to induce rigid molecular stacking and consequently to reduce non-radiative loss of triplet states. Functionalization of a rigid core that exhibit intramolecular charge transfer with peripheral moieties can lead to RTP due to the transformation of the lowest triplet state to more local in character [29]. If such transformation is possible when a TADF molecule is dopped into a rigid host remains relatively unexplored.

By the systematic change of the donors and acceptors while maintaining the near orthogonality and by incorporation of the abundant lone-pair of electrons through 1,4-difluorobenzene or 1,4-bis (trifluoromethyl) benzene as acceptors and heteroatoms in the donors such as phenothiazine, phenoxazine and acridine, we show that only the TADF molecule with phenothiazine moiety exhibit significant RTP. Conformational heterogeneity and rigidity imposed by Zeonex transform the hybridized local and charge transfer (^{3}HLCT) states into locally excited state (^{3}LE), widening ΔE_{ST} and facilitating RTP.

1.1. Experimental section

In the ESI, a detailed description of the general procedure of the synthesis of the target derivatives and the experimental and theoretical techniques used for their characterization are presented.

2. Results and discussion

2.1. Synthesis

The synthesis of 2,5-disubstituted-1,4-phenylene derivatives is shown in Scheme 1. In the synthesis of the target compounds, Buchwald-Hartwig coupling reactions of brominated phenylene derivatives **1** (acceptors) with different secondary aromatic amines (donors) were conducted in the presence of tris(dibenzylideneacetone)dipalladium(0) as the metal catalyst and X-Phos as the ligand. This reaction gave donor-acceptor-donor (D-A-D) derivatives of 2,5-disubstituted-1,4-phenylene. Compound **2PO-2FPh**, **2PS-2FPh** and **2AC-2FPh** were isolated in the yields of 68%, 40% and 27% respectively. The structures of the synthesized compounds were confirmed by ^{1}H, ^{13}C, ^{19}F NMR spectroscopies and were further confirmed by single crystal X-ray analysis. Analysis of the spectra is given in SI. All of the newly synthesized molecules were purified by column chromatography followed by vacuum sublimation before characterization.

2.2. Thermal properties and X-ray analysis

The copounds were studied by thermogravimetric analysis (TGA) and differential scanning calorimetry (DSC). The compounds showed high 5% weight loss temperatures. They ranged from 302 to 333 °C. The single-stage full weight loss of the samples of the compounds reflected by their TG curves suggests that 5% weight loss temperatures correspond to the temperatures of the onsets of sublimation but not of the thermal degradation. The analysis of DSC curves shows that the compounds are characterized by strong inclination to crystallization. They do not form molecular glasses. Further results and discussions can be found in the Supporting information (Fig. S1, S2, Table S1).

Single crystals for XRD analysis were grown from the solvent mixtures using a slow evaporation technique. The Oak Ridge Thermal Ellipsoid Plot (ORTEP) projections of **2PO-2FPh**, **2PS-2FPh** and **2AC-2FPh** are shown in Fig. 1. The crystallographic data are listed in Table S2. The crystal structures confirmed the existence of weak Van der Waals intermolecular forces between the adjacent molecules. The short contact distances vary from 2.54 to 3.40 Å. All molecules possess weak bonding between electron-accepting fluorine atoms and hydrogen or carbon atoms shared by the electron-donating moiety: (**2PO-2FPH**) F1•••H-C3, (**2PS-2FPH**) F1•••H-C8, (**2AC-2FPH**) F1•••C5 (Fig. 1). The similar intermolecular interactions between the donor and acceptor moieties were also found in the case of **2PS-2FPh** (S1•••H-C15). In every crystal unit cell, all neighboring molecules are connected by numerous short contacts formed between the carbon and hydrogen atoms from the acceptors: (**2PO-2FPh**) C4•••H-C10, C3•••H-C10; (**2PS-2FPh**) C7•••H-C3, C6•••C9; (**2AC-2FPh**) C3-H•••H-C9. As it was reported previously, the acridine and phenothiazine moieties of **2PS-2FPh** and **2AC-2FPh** exhibited a folded configuration relative to the central axis with an angle of ~25–28° [30]. However, for **2PO-2FPh**, the phenoxazine moiety was nearly planar (~2°). The angles between the two intersecting planes drawn between difluorobenzene and the donors for **2PO-2FPh**, **2PS-2FPh** and **2AC-2FPh** were found to be of 68.76°,83.36° and 87.08° respectively (Fig. S3). The nitrogen lone-pair electrons of the donor moieties align favorably with the acceptor π-conjugation.

2.3. Photophysical properties

Fig. 2**(a-c)** shows the normalized absorption and emission spectra of the solutions of **2PO-2FPh**, **2PS-2FPh**, and **2AC-2FPh** in three different solvents (toluene, tetrahydrofuran, and acetonitrile). The optical transition at 310 nm and 280 nm can be attributed to the PO/PS and AC moieties respectively. The lowest energy band (LEB) of absorption spectra of the solutions of **2PO-2FPh** exhibited a strong positive bathochromic shift from 3.15 eV to 3.05 eV after the change of the solvents from toluene to acetonitrile. Similarly, LEB of absorption spectra of the solutions of **2AC-2FPh** exhibited a bathochromic shift, from 3.40 eV to 3.30 eV after the replacement of toluene by acetonitrile. However, the absorption onsets of the solutions of **2PS-2FPh** barely showed any bathochromic shift after increase of polarity of the solvent. The photoluminescence (PL) spectra of the solutions of the three compounds exhibited clear redshifts with the increase of the solvent polarity (Fig. 2 **(a-d)**). The PL spectra were structureless indicative of CT character. The

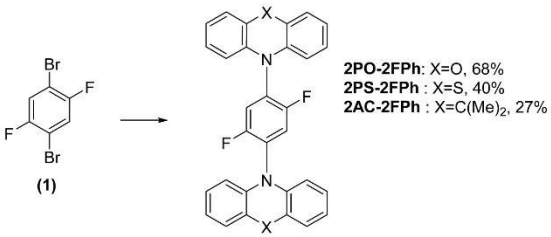

Scheme 1. Synthesis of 2,5-disubstituted-1,4-phenylene derivatives: $Pd_2(dba)_3$, X-Phos, t-BuONa, secondary amines, toluene, reflux, 24 h.

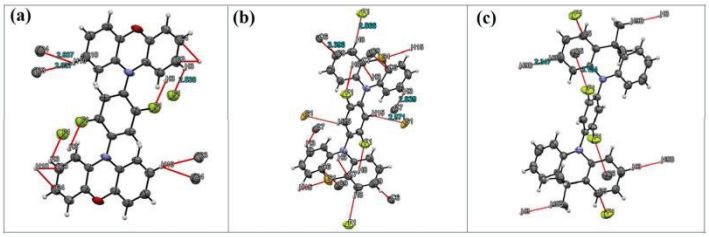

Fig. 1. ORTEP structures of (a) **2PO-2FPh**, (b) **2PS-2FPh** and (c) **2AC-2FPh**.

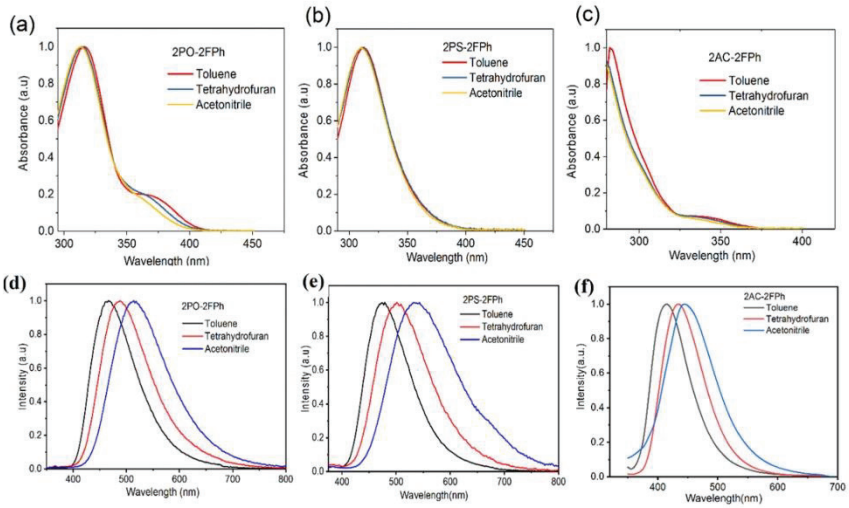

Fig. 2. Absorption and PL spectra of the solutions of **2PO-2FPh** (a,d) **2PS-2FPh** (b,e) **2AC-2FPh** (c,f) in toluene, tetrahydrofuran and acetinitrile.

energies of singlet charge-transfer state (^{1}CT) of the solutions of the **2PO-2FPh**, **2PS-2FPh**, and **2AC-2FPh** in toluene were determined to be of 3.05 eV, 3.00 eV, and 3.37 eV respectively. The largest shift of the emission onset energy observed after the change of the solvent from toluene to acetonitrile was recorded for the solutions of **2PO-2FPh**, (0.28 eV), followed by **2PS-2FPh** (0.13 eV) and **2AC-2FPh** (0.06 eV). The large red-shift of **2PO-2FPh**, indicates stabilization of its CT state with polarity[31].

These three compounds showed blue and blueish-green emissions. The increase in PL intensity of argon-purged solutions indicated a contribution from the triplet harvesting [32]. The integrated emission intensity ratios of deoxygenated and air equilibrated toluene solutions of **2PO-2FPh**, **2PS-2FPh**, and **2AC-2FPh** were found to be of 1.80, 1.20, and 3.97 respectively (Fig. S4). The 1% solid solutions of **2PO-2FPh** (Fig. 3**(a)**) in Zeonex showed increased PL intensity in vacuum while that of **2PS-2FPh** exhibited dual emission (Fig. 3**(b)**). The emission band of sample of **2AC-2FPh** showed slightly vibronic structure after doping in Zeonex (Fig. 3**(c)**) and increased PL intensity after exposure to strong UV light during excitation (Fig. S5).

To investigate the origin of the dual emission, time-resolved PL measurements were performed at two different wavelengths (400 nm and 504 nm). Fig. 3**(d)** shows the PL spectra of **2PS-2FPh** molecularly dispersed in Zeonex without delay and with 9 ms gate delay. The emission in the region between 400 and 450 nm disappeared after applying the gate delay. The prompt fluorescence lifetimes were found to be close when recorded in vacuum (2.37 ns) and air (2.40 ns) (Fig. 3 **(e)**). Meanwhile, the emission at 505 nm exhibited long radiative decay time of 19.3 ms (Fig. 3**(f)**. This observation is indicative of phosphorescence at room temperature which is quenched in the presence of oxygen and solvent. From the onsets of the corresponding phosphorescence spectra, the lowest triplet levels of 2.9, 2.7, and 3.28 eV were obtained for **2PO-2FPh**, **2PS-2FPh**, and **2AC-2FPh**, respectively (Fig. S6). Taking the onsets of PL spectra of THF solutions of **2PO-2FPh**, **2PS-2FPh**, and **2AC-2FPh**, the energies of their lowest singlet states of

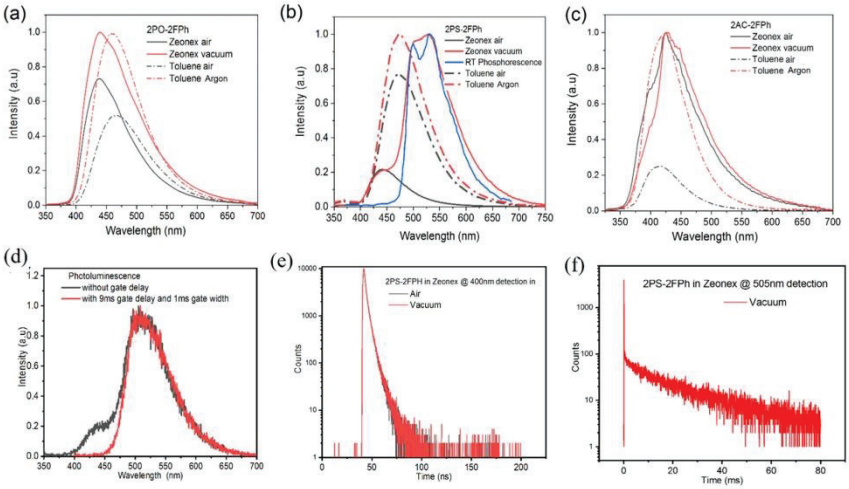

Fig. 3. PL spectra of argon-saturated toluene solutions and of evacuated and air equilibrated solid solutions in Zeonex of (a) **2PO-2FPh** (b) **2PS-2FPh** and (c)**2AC-2FPh**. (d) PL spectra of **2PS-2FPh** molecularly dispersed in Zeonex without and with gate delay. PL decay curves of **2PS-2FPh** doped in Zeonex at (e) recorded at 400 nm in air and vacuum and (f)recorded at 505 nm detected in vacuum.

2.97, 2.87, and 3.29 eV were respectively detected (Fig. 2**(d), (e)** and **(f)**). The singlet-triplet splitting (ΔE_{ST}) values for the solutions of **2PO-2FPh, 2PS-2FPh,** and **2AC-2FPh** in 2-methyltetrahydrofuran (me-THF) were determined to be of 0.07, 0.17, and 0.01 eV respectively. It is important to note that for **2PS-2FPh,** the near orthogonality between the D and A units (the intersection angle obtained by X-ray analysis is of 83.36°) did not result in small ΔE_{ST}. Deep blue emitting **2AC-2FPh** showed very small ΔE_{ST} and high triplet harvesting efficiency indicated by the increased PL intensity of its argon-purged solution. As **2AC-2FPh** has very high triplet energy (3.28 eV), the proximity to ^{1}CT indicates that there is a large reservoir of long-lived highly energetic triplet excitons that interact with polarons which could lead to degradation [33, 34].

In air, the lowest photoluminescence quantum yields (PLQY) were obtained for the neat films of **2PS-2FPh** and of its solid solution in Zeonex (Table 1). The low PLQY values of **2PS-2FPh** can be partly attributed to the efficient singlet-triplet intersystem crossing (ISC) which is required for efficient RTP [35] Indeed, the relatively high PLQY of RTP was obtained for the film of **2PS-2FPh** doped in Zeonex (Table 1). The solution of **2AC-2FPh** showed by 30% increased emission lifetime after deoxygenation by argon. This observation strongly suggests the presence of delayed fluorescence. For the solution of **2PS-2FPh,** the increase of emission lifetime after deoxygenation was considerably lower (15%). The solution of **2PO-2FPh** showed increase of emission lifetime by 21% after removal of oxygen. These values are inversely proportional to the values of ΔE_{ST} of the compounds.

Table 1
The phophysical parameters of the derivatives of difluoro phenylene*.

Compounds	2PO 2FPh	2PS 2FPh	2AC 2FPh
	neat/guest-Zeonex films		
$PLQY^{air}$, %	14/5	2/2	10/7
$PLQY^{vacuum}$, %	-/9	-/12.8	-/27.8
[^] $PLQY^{RTP}$, %	-	-/10.8	-
$\tau^{fluorescence}$(air/argon), ns	4.70/5.71	3.33/3.83	5.44/7.05
τ^{RTP}, ms	-	-/19.3	-

* *The fitting data of PL decay curves can be found in Fig. S7
[^] calculated by $PLQY^{RTP}=PLQY^{vac}-PLQY^{air}$, where $PLQY^{vac}=PLQY^{air}\times(Area^{vac}/Area^{air})$ as introduced elsewhere [36].

2.4. Molecular modelling

Density functional theory (DFT) calculations were performed to investigate the molecular structures. Their optimized structures are shown in Fig. 4. The molecules of **2PO-2FPh, 2PS-2FPh,** and **2AC-2FPh** exhibited large dihedral angles of 79.8°, 99.3°, and 92.6° respectively between the donor and acceptor moieties. They were by ca. 10° larger than those obtained by the single-crystal X-ray analysis. For the highest occupied molecular orbitals (HOMOs), there is a small electron cloud overlapping with the lowest unoccupied molecular orbitals (LUMOs), which is crucial for increasing the oscillator strength of the emitters. The LUMO extends the electron clouds into the N-C bonds of the donors. The

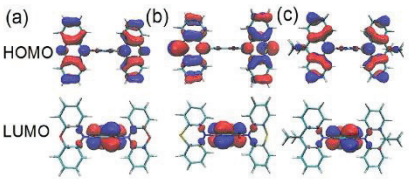

Fig. 4. : The frontier orbitals of (a) **2PO-2FPh,** (b) **2PS-2FPh,** and (c) **2AC-2FPh.**

natural transition orbitals for S_1 were strongly dominated by the HOMO to LUMO transition with coefficients higher than 0.98.

The HOMO and LUMOs energy levels of a single molecule obtained from the theoretical calculations are − 5.97 eV, − 6.15 eV, − 6.07 eV, − 0.65 eV, − 0.66 eV, − 0.59 eV for **2PO-2FPh**, **2PS-2FPh**, and **2AC-2FPh** respectively. The ionization potentials obtained from the CV analysis (Fig. S8) are of 5.50 eV 5.80 eV and 5.81 eV. These data indicate that the donating strength of phenoxazine is stronger than that of phenothiazine and acridine.

We also examined the frontier orbitals of T_1. Surprisingly, despite well-separated frontier orbitals with the S_1 transition dominated by the HOMO to LUMO transition, the natural transition orbitals for T_1 consisted of superposition of various CTs and locally excited (LEs) hole-particle excitations (Fig. 5a-c). Only excitation with coefficients more than 0.1 were drawn. Based on this, the HOMO to LUMO transition only contributed 0.57, 0.27, and 0.67 in terms of coefficients for **2PO-2FPh**, **2PS-2FPh**, and **2AC-2FPh**. It is clear that the lowest T_1 is not a pure ^{3}CT state. It is rather a ^{3}HLCT excited state, a quantum superposition of local and charge transfer. We confirmed the hybrid nature of the lowest triplet state of **2PO-2FPh** by comparing the bathochromic shift of the lowest triplet state of **2PO-2FPh** and ^{3}LE of phenoxazine. The ^{1}CT state of **2PO-2FPh** underwent bathochromic shift with the increasing dielectric constant of the solvent as it is expected for the typical charge transfer molecules (Fig. 5d). Meanwhile the ^{3}LE of phenoxazine as measured at 77 K for the solution in me-THF remained relatively constant since the locally excited state is far less sensitive to the polarity of the medium Fig. 5e.). The ^{3}HLCT of **2PO-2FPh** increased slightly for the solution in low-dielectric-constant solvent and remained relatively constant

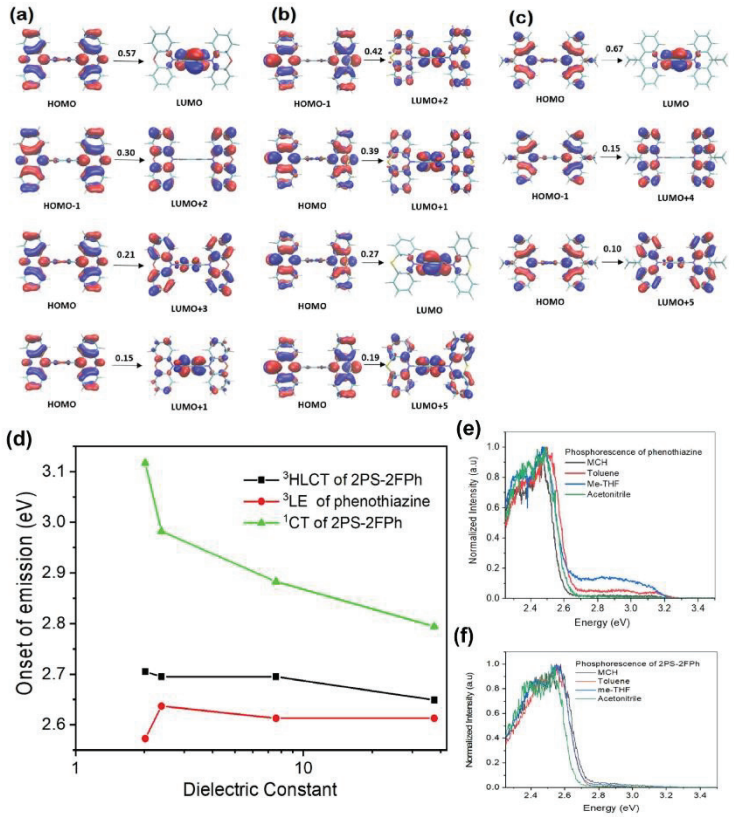

Fig. 5. : The visualizations of the lowest triplet natural transition orbitals for (a) **2PO-2FPh**, (b) **2PS-2FPh**, and (c) **2AC-2FPh.** The number indicates the coefficient corresponding to the transition (d) Comparison of the onset of emission of ^{3}HLCT of **2PS-2FPh**, ^{3}LE of phenothiazine and ^{1}CT of **2PS-2FPh** to different solvent polarity (e) Phosphorescence spectra (^{3}LE) of the solutions of phenothiazine in different solvents at 77 K and (f) Phosphorescence spectra of the solutions of **2PO-2FPh** in different solvents.

thereafter (see Fig. 5d and f). ^{3}HLCT can facilitate reverse intersystem crossing (RISC) by increasing the spin-orbit coupling [37] while keeping the ΔE_{ST} small. ^{3}HLCT facilitate intersystem crossing between ^{1}CT and ^{3}HLCT, as there is no need for ^{3}HLCT to couple to higher ^{3}LE states. ^{1}HLCT has been used to increase the singlet radiative rate as long as efficient RISC occurs at a higher energy level (T_n -> S_1) through a small gap[38,39]. ΔE_{ST} is calculated to be 0.09 eV, 0.17 eV and 0.05 eV for **2PO-2FPh**, **2PS-2FPh**, and **2AC-2FPh** respectively. **2PO-2FPh** (Fig. 5a) has an almost equal amount of ^{3}LE and ^{3}CT and ΔE_{ST} is approaching 0.1 eV. Hence, a smaller contribution from ^{3}LE is required for a smaller ΔE_{ST}. As the ^{3}HLCT becomes more local in excitation, ΔE_{ST} widens as can be seen in case of **2PS-2FPh** (Fig. 5b), where the coefficient for the HOMO to LUMO singlet transition states is only 0.27. **2AC-2FPh** (Fig. 5c) has a higher ^{3}CT energy for T_1 and the highest triplet harvesting rate as shown in Fig. S2. The integrated emission intensity ratio between deoxygenated and air- equilibrated solutions was of 3.97. A balanced mixture of ^{3}LE and ^{3}CT character in ^{3}HLCT would lead to efficient triplet harvesting via the reverse intersystem crossing.

However, in reality, the molecular conformation obtained at 0 K and its characteristics of energy states might be different to that observed at room temperature. We carried out a quantum molecular dynamic simulation of **2PS-2FPh** in solution at 300 K using a polarizable continuum model as a solvent model. The probability distribution of the dominant transition in the T_1 state is categorized into HOMO-> LUMO, HOMO->LUMO+ 1, and HOMO->LUMO+ 2 as shown in Fig. 6a. Only 5% of the dominant transitions are ^{3}LE in character. However, we must keep in mind that T_1 is a quantum superposition of the different transitions of excited states. Some component of the transition has ^{3}CT character and the other has ^{3}LE character with the corresponding coefficient. If the overall transition has a greater ^{3}LE character, the ΔE_{ST} will be larger. ΔE_{ST} of the solid solution of **2PS-2FPh** in Zeonex is of 0.47 eV (Fig. 3b). For the solution, the simulated ΔE_{ST} ranges from near zero eV to a maximum of 0.27 eV as it is seen in Fig. 6(b) with the mean of ΔE_{ST} being of 0.07 eV and a standard deviation of 0.04 eV. The simulated ΔE_{ST} is of 0.17 eV and 0.07 eV at 0 K and 300 K respectively while in the experiment when the emitter was dissolved in me-THF, the ΔE_{ST} was of 0.17 eV at 77 K, and when it was doped in Zeonex, it was of 0.47 eV at 300 K.

It is impossible to measure ΔE_{ST} of a compound molecularly dispersed in a solvent at room temperature. We hypothesized that for **2PS-2FPh** doped in Zeonex, the conformational heterogeneity imposed by the rigid polymer resulted in a distorted molecular conformation which can be shown by the higher energy of the molecule compared to the molecular conformation at 0 K. We can examine the distribution of energy of the molecules in solution to provide a clue to such validity. The molecules with higher energy should have a larger ΔE_{ST} based on this hypothesis. We examined the distribution of the energy at ^{1}CT for molecules in solution with ΔE_{ST} below 0.02 eV and ΔE_{ST} exceeding 0.2 eV (Fig. 6c). The difference in the average energy of each distribution is of 0.11 eV for molecules having ΔE_{ST} exceeding 0.2 eV at higher energy with average ^{1}CT photon energy of 2.40 eV, 0.16 eV higher than photon emitted by molecules with ΔE_{ST} lower than 0.02 eV. The molecule with ΔE_{ST} exceeding 0.2 eV has energy of 0.06 eV higher than molecules with ΔE_{ST} below 0.02 eV at ground state. These results also indicate that for **2PS-2FPh**, a slight change in the molecular geometry can result in a large range of ΔE_{ST}. The molecules with ΔE_{ST} below 0.2 eV exhibit dominant ^{3}LE character in T_1. The large ΔE_{ST} observed for **2PS-2FPh** doped in Zeonex indicates that the molecular conformation is not in thermal equilibrium as in solution. The molecular conformation rather adopts a higher ground state energy than in solution resulting in a significant widening of ΔE_{ST} while the T_1 state becomes more local. To verify this, we carried out a molecular dynamics simulation with **2PS-2FPh** doped into Zeonex (represented by 10 repeated monomers with the molecular structure shown in Fig. S9) and extracted the emitters to be calculated under time-dependent DFT/ LC-ωPBEh//cc-pVDZ at optimal ω. Fig. 7a shows the probability distribution of ΔE_{ST} with a mean of 0.31 eV indicating that the conformational heterogeneity imposed by the rigid Zeonex can widen the mean ΔE_{ST}. ΔE_{ST} ranges from the smallest 0.13 eV to the largest 0.59 eV with the molecular structure for the molecules representing the smallest and the largest ΔE_{ST} as shown in Fig. 7b and c respectively. In Fig. 7b and (c), the top figures represent the side view while the bottom figures represent the front views. The dihedral angle between the donor and acceptor in Fig. 7b deviated far from orthogonality with a dihedral angle of 127° resulting in a large ΔE_{ST} compared with a dihedral angle of 71° shown in Fig. 7(c). Such large distortion was possible in a restricted environment as shown in Fig. 7c where the molecule finds it difficult to relax to its equilibrium position. Consequently, T_1 for the molecule shown in Fig. 7b is dominated by the local transition. It is important to note that we represented the Zeonex polymer as decamer limited by computational resources. In reality, the higher number of repeated units will impose more restricted environment for **2PS-2FPh**. In our simulation, the mean ΔE_{ST} is of 0.31 eV compared with the experimental value which is of 0.47 eV. The larger error most likely originates from the smaller number of repeated units of Zeonex used in this simulation and the single ω of 0.063 used in the calculation of the excited states of the different conformers.

Since we have shown that Zeonex imposed increased conformational heterogeneity when doped with **2PS-2FPh**, such behavior should also occur in case of **2PO-2FPh** and **2AC-2FPh**. We investigated the relationship between ΔE_{ST} and the dihedral angle between the donor and acceptor moieties. As shown in Fig. S10, the ΔE_{ST} remained practically constant at a high dihedral angle before it increased considerably. For **2PS-2FPh**, the onset of considerable increase of ΔE_{ST} occurred at 70° while for **2PO-2FPh** and **2AC-2FPh**, the onsets were 40° and 50° respectively indicating that these two molecules are far less sensitive to the significant change of ΔE_{ST} imposed by the conformational disorder.

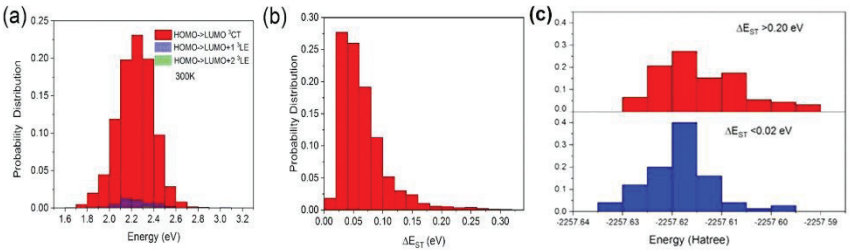

Fig. 6. The probability distribution (a) of dominant T_1 transition (b) ΔE_{ST} at 300 K for the solution in toluene as extracted from quantum molecular dynamic simulations for **2PS-2FPh** (c) The energy distribution of **2PS-2FPh** molecules at their 1st excited state with ΔE_{ST} below 0.02 eV and ΔE_{ST} exceeding 0.20 eV.

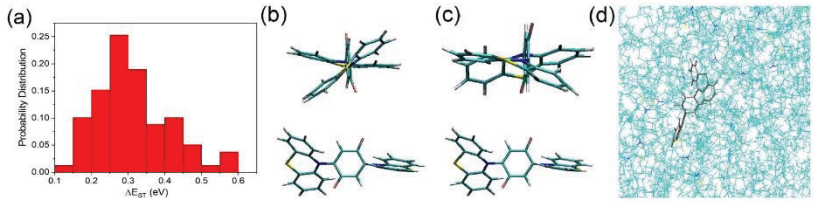

Fig. 7. (a) The distribution of ΔE_{ST} of **2PS-2FPh** in Zeonex, the side (top) and front (bottom) of extracted structure of **2PS-2FPh** with ΔE_{ST} of (b) 0.59 eV and (c) 0.13 eV (d) the embedded molecule (b) in the Zeonex.

We also noted that the stronger the ^{3}CT character in ^{3}HLCT, the smaller the onset.

2.5. Time evolution of Spectra

To support further that Zeonex imposed increased heterogeneity of **2PS-2FPh,** time evolution of photoluminescent spectra was performed as shown in Fig. 8. Fig. 8a shows the logarithmic contour map of the photoluminescence intensity as a function of logarithmic time after excitation and wavelength. The persistence of low-intensity emission at a timescale longer than 100 ns is assigned as RTP. The selected spectra from the contour map are plotted in Fig. 8b. The ^{1}CT emission cannot be described as the usual single Gaussian emission. Three peaks are observed at 423 nm 453 nm and 513 nm. These peaks are apparently not the vibronic peaks from ^{1}LE. They are probably predetermined by the certain conformational disorder of charge transfer molecules. Such behaviour was observed for through space donor-acceptor charge transfer dimers in solution [40]. A plot of the probability distribution of singlet vertical excitation from the simulation performed earlier resembled the emission spectrum observed at 3.66 ns (Fig. S11a) while the molecule maintains the singlet charge transfer characteristics.

The emission peak at 500 nm batochromically shifted towards 550 nm during the measurement (Fig. 8**b**). This spectral shift from 500 nm to 550 nm is the result of heterogeneity leading to large lifetime dispersion of the CT emission as supported by the simulation. The higher-energy CT states decayed faster than the lower-energy species due to their increased ^{1}LE character, giving an apparent time-dependent spectral shift. The observation of the spectral shift over time for **2PS-2FPh** also supported the presence of structural inhomogeneity in a disordered medium[41]. At 3.66 ns the emission should correspond to the singlet states including the emission at 500–550 nm since triplet emission is forbidden. A plot of the probability distribution of triplet vertical excitation resembled the emission spectrum at 892 ns (Fig. S11b), Hence, the emission peak at ca. 525 nm observed in the steady state photoluminescence spectrum of **2PS-2FPh** molecularly dispersed in Zeonex (Fig. 3**b**) can be treated as a combination of fluorescence and phosphorescence spectra. The shift of the peak at ca 525 nm is plotted in Fig. 8**c**. The shift exponentially decays before reaching its equilibrium energy level. After ca. 100 ns, the peak can be assigned solely to phosphorescence. It is important to note that phenothiazine moieties are known to be phosphorescent at room temperature [42–44] but not all TADF compounds containing phenothiazine exhibited RTP[30].

2.6. Oxygen sensing

Since phosphorescence is the predominant emission at ambient temperature, phosphorescence quenching by oxygen was investigated [18,19]. To study this effect, we exposed the sample of the solid solution of **2PS-2FPh** in Zeonex with the concentration of 1% as in a chamber to the different mixtures of oxygen and nitrogen. For the gas mixture, the ratio of pure nitrogen gas as an inert medium and pure oxygen as a quencher was controlled by using two precise gas flowmeters. The gas mixture was directed into the restricted flow-through sample chamber inside the spectrometer. Each change in the concentration of the quencher was followed by a change in RTP intensity (Fig. 9 **a**). In order to avoid any spectral fluctuation influenced by external factors and ensure high accuracy, after each change in gas ratio, the sample was kept in it for 3 min. Then 3 consecutive spectra (Fig. S12) were taken and averaged during data analysis, resulting in one final spectrum for the selected concentration of quencher.

The considerable decrease of the intensity of RTP with an increase in

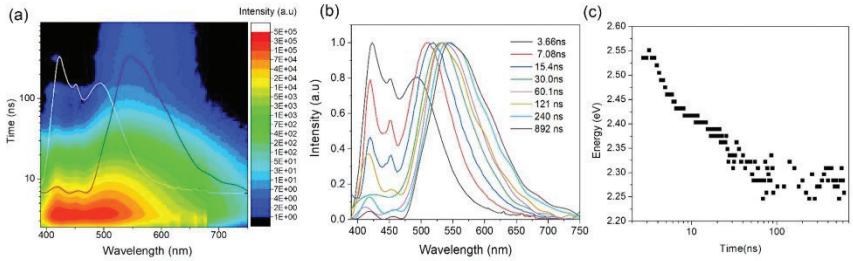

Fig. 8. The photoluminescence lifetime evolution of the molecular dispersion of **2PS-2FPh** in Zeonex **(a)** two dimensional intensity map with inserted spectra at 3.66 ns (white) and at 892 ns (red) after excitation. **(b)** the change of the normalized spectra at the different times. (c) the spectral diffusion of the second dominant peak observed at 500 nm.

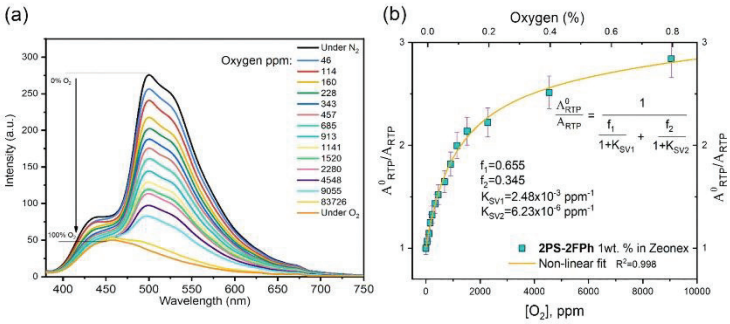

Fig. 9. (a) RTP spectra (b) Stern-Volmer plots for 1% solid solution of **2PS-2FPh** in Zeonex recorded at the different concentrations of oxygen in the atmosphere of the sample.

the concentration of the quencher is obvious from Fig. 9**a**. The significant difference between the emission intensity at 500 nm was observed under the nitrogen and oxygen atmospheres. Under the inert atmosphere, the intensity of emission at 500 nm was by 7.5 times higher compared to that observed in the atmosphere of oxygen.

For the quantitative estimation of the sensitivity to oxygen quenching of RTP of **2PS-2FPh**, PL spectra recorded at the different oxygen concentrations were integrated, and the obtained values of the area under the curves were used for the further calculations. The Stern-Volmer relationship was used for the analysis. Since the collected data demonstrated undoubtedly nonlinear relationship between the ratio of RTP intensity and the quencher concentration in ppm (Fig. 9 **b**)), we used such Stern-Volmer equation, which is adjusted for such conditions. Usually, when the Stern-Volmer plot has a downward curvature, it is assumed that multiple chromophore species exist where one species are available for the quencher, while the other species are not. This combination is considered as multiple species with dynamic quenching [44].

The ratio of intensities observed in the presence and in the absence of a quencher can be given as Eq. (1).

$$\frac{A^0_{RTP}}{A_{RTP}} = \left[\sum_{i=1}^{n} \frac{f(i)}{\{1 + K_{SV}(i)[Q]\}}\right]^{-1} \tag{1}$$

where A^0_{RTP} is area under the curve measured in absence of a quencher and A_{RTP} is the area under curve measured in the presence of a quencher. $K_{SV}(i)$ is quencher rate coefficient and $f(i)$ is the fractional contribution of the ith species of the fluorophore to the steady-state emission of the investigated compound.

For the sample of 1% **2PS-2FPh** solid solution in Zeonex, the best fit was obtained using the two-component model expressed by Eq. (2).

$$\frac{A^0_{RTP}}{A_{RTP}} = \frac{1}{\frac{f_1}{1 + K_{SV1}} + \frac{f_2}{1 + K_{SV2}}} \tag{2}$$

Resulting fit values R^2 of 0.998, demonstrates that the first and dominant fluorophore species contributes to 65.5% of the total photoluminescence while the second species has a fractional contribution f_2 of 34.5%. The obtained values of K_{SV1} of $2.48 \times 10^{-3}\ ppm^{-1}$ and of K_{SV2} of $6.23 \times 10^{-6}\ ppm^{-1}$ demonstrate the significant differences in emission sensitivity for oxygen. The values of the quencher rate coefficients correlate well with Stern-Volmer plot shown in Fig. 9**b**, where the first part of the plot, up to oxygen concentration of ca. 2000 ppm is much steeper and more sensitive to the quencher than the second part, where the plot curves downward. Overall, these results suggest that the sample of 1% solid solution of **2PS-2FPh** in Zeonex shows high sensitivity to low concentrations of oxygen in the atmosphere of the samples (up to 0.2%). The decreasing sensitivity is observed at the concentrations of oxygen above 0.2%. The presence of two sensitivity regions can be attributed to the molecular heterogeneity giving rise to two dominant ^{3}LE states and the ^{3}CT states of **2PS-2FPh**.

3. Conclusions

Derivatives of 1,4-difluorobenzene and the different donors (phenothiazine, phenoxazine and acridine) were obtained. The single-crystal X-ray analysis revealed the existence of weak Van der Waals intermolecular forces between the adjacent molecule. The compounds show high temperatures of 5% weigh loss ranging from 302 to 333 °C. The compounds showed blue and blueish-green emissions. The increase in emission intensity after deoxygenation of the solutions indicate the contribution from the triplet harvesting. The effect of the host on the photophysical properties of the compounds is discussed. The rigidity of the host can impose significant molecular heterogeneity in TADF molecules transforming a hybrid charge transfer and local excited triplet state (^{3}HLCT) into a purely locally excited triplet state. As a result, the singlet and triplet gap (ΔE_{ST}) widened in a rigid host. This is particularly noticeable if the TADF molecule has a larger ΔE_{ST} due to its ^{3}HLCT character. Embedding such molecules in a rigid host can give rise to room temperature phosphorescence. As a result, the derivative of difluoro phenylene and phenothiazine exhibits dual emissions in vacuum, one originating from the singlet charge transfer state and the other from the locally excited triplet state (phosphorescence). The sensitivity of dual emission to oxygen is quantified. Two sensitivities to oxygen regions resulting from two dominant emissive species are observed: high sensitivity at low concentration (below 0.1%) and low sensitivity at high concentration of oxygen (above 0.2%).

Declaration of Competing Interest

The authors declare that they have no known competing financial interests or personal relationships that could have appeared to influence the work reported in this paper.

Data Availability

Data will be made available on request.

Acknowledgements

This project has received funding from European Regional Development Fund (project No 01.2.2-LMT-K-718–03-0019) under grant agreement with the Research Council of Lithuania (LMTLT). KLW and AA thank for the funding from the European Union's Horizon 2020 research and innovation programme under the Marie Sklodowska-Curie Grant agreement no 823720. We want to thank the Ministry of Higher Education Malaysia for the Fundamental Research Grant Scheme (FRGS/1/2019/STG01/UM/01/1). The computation is supported by the University Malaya Research University Grant-Faculty Program (GPF086B-2020).

Appendix A. Supporting information

Supplementary data associated with this article can be found in the online version at doi:10.1016/j.snb.2023.133295.

References

[1] W. Zhao, Z. He, B.Z. Tang, Room-temperature phosphorescence from organic aggregates, Nat. Rev. Mater. 5 (2020) 869–885, https://doi.org/10.1038/s41578020-0223-z.

[2] C. Kenry, B.Liu Chen, Enhancing the performance of pure organic room-temperature phosphorescent luminophores, Nat. Commun. 10 (2019) 2111, https://doi.org/10.1038/s41467-019-10033-2.

[3] L. Yu, Z. Wu, C. Zhong, G. Xie, Z. Zhu, D. Ma, C. Yang, Pure organic emitter with simultaneous thermally activated delayed fluorescence and room-temperature phosphorescence: thermal-controlled triplet recycling channels, Adv. Opt. Mater. 5 (2017) 1700588, https://doi.org/10.1002/adom.201700588.

[4] M. Louis, H. Thomas, M. Gmelch, A. Haft, F. Fries, S. Reineke, Blue-light-absorbing thin films showing ultralong room-temperature phosphorescence, Adv. Mater. 31 (2019) 1807887, https://doi.org/10.1002/adma.201807887.

[5] T. Zhang, X. Wang, Z. An, Z. Fang, Y. Zhang, W.Z. Yuan, Pure organic persistent room temperature phosphorescence at both crystalline and amorphous states, ChemPhysChem 19 (2018) 2389–2396, https://doi.org/10.1002/cphc.201800310.

[6] F. Wilkinson, A.A. Abdel-Shafi, Mechanism of quenching of triplet states by molecular oxygen: biphenyl derivatives in different solvents, J. Phys. Chem. A. 103 (1999) 5425–5435, https://doi.org/10.1021/jp9907995.

[7] C. Grewer, H.-D. Brauer, Mechanism of the triplet-state quenching by molecular oxygen in solution, J. Phys. Chem. 98 (1994) 4230–4235, https://doi.org/10.1021/j100067a006.

[8] X. Wang, Y. Sun, G. Wang, J. Li, X. Li, K. Zhang, TADF-type organic afterglow, Angew. Chem. Int. Ed. 60 (2021) 17138–17147, https://doi.org/10.1002/anie.202105628.

[9] Y. Pan, J. Li, X. Wang, Y. Sun, J. Li, B. Wang, K. Zhang, Highly efficient TADF type organic afterglow of long emission wavelengths, Adv. Funct. Mater. 32 (2022) 2110207, https://doi.org/10.1002/adfm.202110207.

[10] N. Nishimura, Z. Lin, K. Jinnai, R. Kabe, C. Adachi, Many exciplex systems exhibit organic long-persistent luminescence, Adv. Funct. Mater. 30 (2020) 2000795, https://doi.org/10.1002/adfm.202000795.

[11] M. Li, W. Xie, X. Cai, X. Peng, K. Liu, Q. Gu, J. Zhou, W. Qiu, Z. Chen, Y. Gan, S. Su, Molecular engineering of sulfur bridged polycyclic emitters towards tunable TADF and RTP electroluminescence, Angew. Chem. Int. Ed. 61 (2022), https://doi.org/10.1002/anie.202209343.

[12] J.S. Ward, R.S. Nobuyasu, A.S. Batsanov, P. Data, A.P. Monkman, F.B. Dias, M. R. Bryce, The interplay of thermally activated delayed fluorescence (TADF) and room temperature organic phosphorescence in sterically-constrained donor–acceptor charge-transfer molecules, Chem. Commun. 52 (2016) 2612–2615, https://doi.org/10.1039/C5CC09645F.

[13] M. Baroncini, G. Bergamini, P. Ceroni, Rigidification or interaction-induced phosphorescence of organic molecules, Chem. Commun. 53 (2017) 2081–2093, https://doi.org/10.1039/C6CC09288H.

[14] B. Zhou, G. Wang, X. Wang, W. Guo, J. Li, K. Zhang, Highly efficient room-temperature organic afterglow achieved by collaboration of luminescent dimeric TADF dopants and rigid matrices, J. Mater. Chem. C. Mater. 9 (2021) 3939–3947, https://doi.org/10.1039/D0TC05464J.

[15] Y. Takeda, T. Kaihara, M. Okazaki, H. Higginbotham, P. Data, N. Tohnai, S. Minakata, Conformationally-flexible and moderately electron-donating units-installed D–A–D triad enabling multicolor-changing mechanochromic luminescence, TADF and room-temperature phosphorescence, Chem. Commun. 54 (2018) 6847–6850, https://doi.org/10.1039/C8CC02365D.

[16] I. Bhattacharjee, N. Acharya, H. Bhatia, D. Ray, Dual emission through thermally activated delayed fluorescence and room temperature phosphorescence, and their thermal enhancement via solid-state structural change in a carbazole-quinoline conjugate, J. Phys. Chem. Lett. 9 (2018) 2733–2738, https://doi.org/10.1021/acs.jpclett.8b00937.

[17] R. Keruckiene, N. Kusas, L. Dvylys, E. Skuodis, V.E. Matulis, E.G. Ragoyja, D. A. Lyakhov, I. Klymenko, J.V. Grazulevicius, Derivatives of Bis(trifluoromethyl) biphenyl and various donor moieties exhibiting dual state emission, J. Lumin 241 (2022), 118502, https://doi.org/10.1016/j.jlumin.2021.118502.

[18] R. Keruckiene, D. Volyniuk, K. Leitonas, J.V. Grazulevicius, Dual emission fluorescence/room-temperature phosphorescence of phenothiazine and benzotrifluoride derivatives and its application for optical sensing of oxygen, Sens Actuators B Chem. 321 (2020), 128533, https://doi.org/10.1016/j.snb.2020.128533.

[19] G. Zhang, J. Chen, S.J. Payne, S.E. Kooi, J.N. Demas, C.L. Fraser, Multi-emissive difluoroboron dibenzoylmethane polylactide exhibiting intense fluorescence and oxygen-sensitive room-temperature phosphorescence, J. Am. Chem. Soc. 129 (2007) 8942–8943, https://doi.org/10.1021/ja0720255.

[20] Y. Tao, R. Chen, H. Li, J. Yuan, Y. Wan, H. Jiang, C. Chen, Y. Si, C. Zheng, B. Yang, G. Xing, W. Huang, Resonance activated spin-flipping for efficient organic ultralong room temperature phosphorescence, Adv. Mater. 30 (2018) 1803856, https://doi.org/10.1002/adma.201803856.

[21] S. Tian, H. Ma, X. Wang, A. Lv, H. Shi, Y. Geng, J. Li, F. Liang, Z. Su, Z. An, W. Huang, Utilizing d–pπ bonds for ultralong organic phosphorescence, Angew. Chem. Int. Ed. 58 (2019) 6645–6649, https://doi.org/10.1002/anie.201901546.

[22] W. Zhao, Z. He, J.W.Y. Lam, Q. Peng, H. Ma, Z. Shuai, G. Bai, J. Hao, B.Z. Tang, Rational molecular design for achieving persistent and efficient pure organic room-temperature phosphorescence, Chem 1 (2016) 592–602, https://doi.org/10.1016/j.chempr.2016.08.010.

[23] S. Cai, H. Shi, D. Tian, H. Ma, Z. Cheng, Q. Wu, M. Gu, L. Huang, Z. An, Q. Peng, W. Huang, Enhancing ultralong organic phosphorescence by effective π-type halogen bonding, Adv. Funct. Mater. 28 (2018) 1705045, https://doi.org/10.1002/adfm.201705045.

[24] Z. Yang, C. Xu, W. Li, Z. Mao, X. Ge, Q. Huang, H. Deng, J. Zhao, F.L. Gu, Y. Zhang, Z. Chi, Boosting the quantum efficiency of ultralong organic phosphorescence up to 52% via intramolecular Halogen Bonding, Angew. Chem. Int. Ed. 59 (2020) 17451–17455, https://doi.org/10.1002/anie.202007343.

[25] Q. Liao, Q. Gao, J. Wang, Y. Gong, Q. Peng, Y. Tian, Y. Fan, H. Guo, D. Ding, Q. Li, Z. Li, 9,9-dimethylxanthene derivatives with room-temperature phosphorescence: substituent effects and emissive properties, Angew. Chem. Int. Ed. 59 (2020) 9046–9951, https://doi.org/10.1002/anie.201916057.

[26] W. Jia, Q. Wang, H. Shi, Z. An, W. Huang, Manipulating the ultralong organic phosphorescence of small molecular crystals, Chem. – A Eur. J. 26 (2020) 4437–4448, https://doi.org/10.1002/chem.201904500.

[27] Z. An, C. Zheng, Y. Tao, R. Chen, H. Shi, T. Chen, Z. Wang, H. Li, R. Deng, X. Liu, W. Huang, Stabilizing triplet excited states for ultralong organic phosphorescence, Nat. Mater. 14 (2015) 685–690, https://doi.org/10.1038/nmat4259.

[28] E. Lucenti, A. Forni, C. Botta, L. Carlucci, C. Giannini, D. Marinotto, A. Previtali, S. Righetto, E. Cariati, H aggregates granting crystallization-induced emissive behavior and ultralong phosphorescence from a pure organic molecule, J. Phys. Chem. Lett. 8 (2017) 1894–1898, https://doi.org/10.1021/acs.jpclett.7b00503.

[29] Z. Ma, Z. Yang, L. Mu, L. Deng, L. Chen, B. Wang, X. Qiao, D. Hu, B. Yang, D. Ma, J. Peng, Y. Ma, Converting molecular luminescence to ultralong room-temperature phosphorescence via the excited state modulation of sulfone-containing heteroaromatics, Chem. Sci. 12 (2021) 14808–14814, https://doi.org/10.1039/D1SC04118E.

[30] L. Skhirtladze, K. Lietonas, A. Bucinskas, D. Volyniuk, M. Mahmoudi, O. Mukbaniani, K.L. Woon, A. Ariffin, J. v Grazulevicius, 1,4-Bis(trifluoromethyl) benzene as a new acceptor for the design and synthesis of emitters exhibiting efficient thermally activated delayed fluorescence and electroluminescence: experimental and computational guidance, J. Mater. Chem. C Mater. 10 (2022) 4929–4940, https://doi.org/10.1039/D1TC05420A.

[31] M. Aydemir, G. Haykır, F. Türksoy, S. Gümüş, F.B. Dias, A.P. Monkman, Synthesis and investigation of intra-molecular charge transfer state properties of novel donor–acceptor–donor pyridine derivatives: the effects of temperature and environment on molecular configurations and the origin of delayed fluorescence, Phys. Chem. Chem. Phys. 17 (2015) 25572–25582, https://doi.org/10.1039/C5CP03937A.

[32] F.B. Dias, K.N. Bourdakos, V. Jankus, K.C. Moss, K.T. Kamtekar, V. Bhalla, J. Santos, M.R. Bryce, A.P. Monkman, Triplet harvesting with 100% efficiency by way of thermally activated delayed fluorescence in charge transfer OLED emitters, Adv. Mater. 25 (2013) 3707–3714, https://doi.org/10.1002/adma.201300753.

[33] J. Kim, K.H. Lee, J.Y. Lee, Quantitative correlation of triplet exciton management in host with the device lifetime of blue phosphorescent organic light-emitting diodes, Adv. Opt. Mater. 10 (2022) 2101444, https://doi.org/10.1002/adom.202101444.

[34] B. vander Zee, S. Paulus, R.Q. Png, P.K.H. Ho, L.L. Chua, G.J.A.H. Wetzelaer, P.W. M. Blom, Role of singlet and triplet excitons on the electrical stability of polymer light-emitting diodes, Adv. Electron Mater. 6 (2020), https://doi.org/10.1002/aelm.202000367.

[35] S. Hirata, Recent advances in materials with room-temperature phosphorescence: photophysics for triplet exciton stabilization, Adv. Opt. Mater. 5 (2017) 1700116, https://doi.org/10.1002/adom.201700116.

[36] H. Liu, G. Pan, Z. Yang, Y. Wen, X. Zhang, S. Zhang, W. Li, B. Yang, Dual-emission of fluorescence and room-temperature phosphorescence for ratiometric and colorimetric oxygen sensing and detection based on dispersion of pure organic thianthrene dimer in polymer host, Adv. Opt. Mater. 10 (2022) 2102814, https://doi.org/10.1002/adom.202102814.

[37] J. Fan, Y. Zhang, Y. Zhou, L. Liu, C. K. Wang, Excited state properties of a thermally activated delayed fluorescence molecule in solid phase studied by quantum mechanics/molecular mechanics method, J. Phys. Chem. C. 122 (2018) 2358–2366, https://doi.org/10.1021/acs.jpcc.7b10238.

[38] X. Tian, S. T. Zhang, X. Li, S. Xiao, Y. Gao, S. J. Su, B. Yang, Donor π acceptor materials for robust electroluminescence performance based on hybridized local and charge-transfer state, Dyes Pigments 193 (2021), 109495, https://doi.org/10.1016/j.dyepig.2021.109495.
[39] F. Kong, S. Yang, X. Liao, Z. Feng, W. Shen, Z. Jiang, D. Zhou, Y. Zheng, L. Liao, Highly efficient sensitized chiral hybridized local and charge-transfer emitter circularly polarized electroluminescence, Adv. Funct. Mater. 32 (2022) 2201512, https://doi.org/10.1002/adfm.202201512.
[40] K.L. Woon, S.A.S. Mustapa, N.S. Mohd Jamel, V.S. Lee, M.Z. Zakaria, A. Ariffin, Effect of bulky functional groups on donor and acceptor interactions and their photoluminescence properties, ChemPhysChem 21 (2020) 2620–2626, https://doi.org/10.1002/cphc.202000612.
[41] T. Northey, J. Stacey, T.J. Penfold, The role of solid state solvation on the charge transfer state of a thermally activated delayed fluorescence emitter, J. Mater. Chem. C. Mater. 5 (2017) 11001–11009, https://doi.org/10.1039/C7TC04099G.
[42] T.K. Sarkar, S.K. Sarkar, P. Thilagar, Room temperature phosphorescent (RTP) N-acetylphenothiazines, ChemPhotoChem 4 (2020) 282–286, https://doi.org/10.1002/cptc.201900296.
[43] Y. Wang, J. Yang, M. Fang, Y. Gong, J. Ren, L. Tu, B.Z. Tang, Z. Li, New phenothiazine derivatives that exhibit photoinduced room-temperature phosphorescence, Adv. Funct. Mater. 31 (2021) 2101719, https://doi.org/10.1002/adfm.202101719.
[44] W. Qiu, X. Cai, M. Li, L. Wang, Y. He, W. Xie, Z. Chen, M. Liu, S.-J. Su, Dynamic adjustment of emission from both singlets and triplets: the role of excited state conformation relaxation and charge transfer in phenothiazine derivates, J. Mater. Chem. C Mater. 9 (2021) 1378–1386, https://doi.org/10.1039/D0TC05343K.

Levani Skhirtladze graduated from Department of Chemistry, Tbilisi State University, Georgia in 2016, obtained B.Sc. (chemistry) in 2016 and M.Sc. (physical and analytical chemistry) in 2018. From 2018 he is PhD student in Polymer Chemistry, Ivane Javakhishvili Tbilisi State University. From 2019 he joined the scientific research group as PhD student under the supervision of prof. Juozas Vidas Grazulevicius at Kaunas University of Technology. He has experience in the synthesis and investigation of organic compounds for optoelectronics.

Karolis Leitonas Leitonas received his MSc degree in material science from Kaunas University of Technology (KTU) in June 2020. He is currently studying his PhD under the supervision of Dr. Dmytro Volyniuk in materials engineering at the same university. In October 2017, he joined the scientific research group as an intern under the supervision of prof. J.V. Grazulevicius at KTU. Currently, he is a PhD student and junior researcher at the same research group. He works with optical spectroscopy techniques as well as device fabrication and characterization. His research focuses on the characterization of new thermally activated delayed fluorescent, room temperature phosphorescence materials, organic light-emitting diodes, transistors and photodiodes. He is co-author of 17 scientific papers published in the international journals included in "Clarivate Analytics Web of Science".

Dr. Audrius Bucinskas is assocoate professor at KaunasUniversity of Technology. His PhD thesis got a nominee in competition "Best Dissertations in 2015 " organized by Lithuanian Society of Young Researchers. Dr. Audrius Bucinskas has experience in modeling organic compounds by theoretical methods, synthesis, purification, identification (NMR, XRD, MS) of new organic compounds and studying their thermal, optical, electrochemical and photoelectrical properties. During 2011–2022 he has published 25 articles in the international scientific journals journals (H index = 10). From 2011 till now dr. A. Bucinskas has participated in 10 projects: 4 international (EU FP7 CEOser, Horizon 2020 PHEBE, Lithuania-Latvia-Taiwan) and 6 national. He gave presentations at 16 international conferences.

Dr. Kai Lin Woon is associate professor at University of Malaya.Dr. Woon Kai Lin obtained his PhD in University of Hull in photonic liquid crystal. After graduation, he worked as a postdoc in electroluminescent liquid crystalline light emitting display He also spent a year as a Postdoc in Oxford University Later, he returned to Malaysia to work as organic light emitting diode materials and device specialist under OSRAM co-operating with well-known multinational companies such as Mercks, Sumitomo and Philips. Later he joined University Malaya working in the field of organic electronics specializing in organic light emitting diode. The works including leading cost effective synthesis of organic semiconducting materials for lighting application, interfacial physics and fundamental mechanism of high performance OLED, accurate computation of OLED materials by investigating and optimizing critical parameters and mechanism in organic devices using various analytical and processing tools available domestically and internationally including the use of synchrotron facilities.He is also a Rutherford fellow in Durham University under Professor Andy Monkman.

Dr. Dmytro Volyniuk is a research fellow at Kaunas University of Technology (Lithuania). He graduated from Department of Electronic Devices, Lviv Polytechnic National University (Ukraine), defended his doctoral dissertation at Lviv Polytechnic National University in 2008 and habilitation work (Solid State Electronics) in 2013. His research interests are related to investigation of photophysical and photoelectrical properties of organic electroactive compounds using different technics including photoelectron emission spectrometry, time of flight charge transport probing, steady stay and time resolved spectrometry. In addition, his research interests are related to fabrication and characterization of organic solid-state devices including organic light-emitting diodes, solar cells and optical sensors.

Dr. Rasa Keruckiene is a research fellow at Kaunas University of Technology. She graduated from Kaunas University of Technology Faculty of Chemical Technology in 2011, obtained MSc degree in 2013, and defended her doctoral thesis at KTU in 2017. She has spent extended periods at Leuven Catholic University (Belgium), Intelligent Polymer Research Institute (Australia), and Silezian University of Technology (Poland). She has experience in the field of the design, synthesis, characterization of organic electroactive compounds by experimental and theoretical methods including their electrochemical and photophysical properties investigation. She is co-author of 27 scientific papers published in the international journals included in"Clarivate Analytics Web of Science"(h=9).

Malek Mahmoudi received his MSc degree in photonics from Laser and Plasma Research Institute at Shahid Beheshti University, Iran. He is currently PhD student in materials engineering at Kaunas University of Technology. His research activities are mainly related to investigations of organic semiconductors towards their applications in organic light-emitting devices according t. In addition, his research interests are related to thermal analysis of organic compounds using different techniques, such as differential scanning calorimetry and thermogravimetric analysis. He is co-author of 16 scientific papers published in the international journals included in "Clarivate Analytics Web of Science".

Professor Mieczyslaw Lapkowski is professor at Silesian University of Technology since 1991 to date. Currently is director of the Centre of Organic and Nanohybrid Electronics. He was the head of Department of Physical Chemistry of Polymers, Faculty of Chemistry, at the same university from 2008 to 2021. He was director of Institute of Coal Chemistry, Polish Academy of Sciences in 2000 – 2005. Member of Polish Chemical Society 1976 - to date. He is member of Polish Chemical Society since 1976. He is a corresponding member of Polish Academy of Sciences since 2022. He is the author of about 350 articles in the scientific journals and of 3 books

Professor Azhar Ariffin obtained his PhD from University of Nottingham in the field of Asymmetry Organic Synthesis. After graduation in 1999, he returned to Malaysia and joined Chemistry Department, University Malaya working as young lecturer. In 2003 he was promoted to the rank of Associate Professor, then to full Professor in 2016. His research interest focus in the field of organic synthesis, particularly synthesis of bioactive compounds such as derivatives of butylated hydroxyl toluene, oxadiazole, thiadiazole and triazole for application as antioxidant. He also synthesis various derivatives of quinazoline for anticancer application. His current research involve the synthesis of carbazole derivatives for application as OLED materials. Some of the works carried out in the Universiti Malaya involves co-operating with various department and faculty in UM. This include Physics Department, Pharmacy Department from Medical Faculty and Artificial Intelligent Department from Computer Science Faculty. He has been invited as Experience Researcher at Kaunas University of Technology for 12 months under the Mega Horizon 2020 between 2019 and 2023.

Professor Juozas Vidas Grazulevicius is professor at Kaunas University of Technology. He is an expert in the synthesis, investigation, application of organic semiconductors and other organic electroactive materials. He has spent extended periods at Heriot-Watt University (Edinburgh, Great Britain), Bayreuth University (Germany), Lancaster University (Great Britain), Cergy Pontoise University (France) and the National University of Singapore. J.V. Grazulevicius has published more than 470 papers published in the international scientific journals. His H index is of 41 according to Web of Science. He is co-author of 25 international patents and 5 chapters of books published by the international publishers. He was scientific supervisor of 30 defended doctoral theses. He is a member of Lithuanian Academy of Sciences, a winner of Lithuanian National Science Prizes in 1997 and 2008 and of Baltic Assembly prize in 2014.

materials

MDPI

Article

Derivatives of Pyridazine with Phenoxazine and 9,9-Dimethyl-9,10-dihydroacridine Donor Moieties Exhibiting Thermally Activated Delayed Fluorescence

Levani Skhirtladze [1], Oleksandr Bezvikonnyi [1,2], Rasa Keruckienė [1], Lukas Dvylys [1], Malek Mahmoudi [1], Linas Labanauskas [3], Azhar Ariffin [4] and Juozas V. Grazulevicius [1,*]

[1] Department of Polymer Chemistry and Technology, Faculty of Chemical Technology, Kaunas University of Technology, LT-51423 Kaunas, Lithuania
[2] Department of Physics, Faculty of Mathematics and Natural Science, Kaunas University of Technology, LT-51369 Kaunas, Lithuania
[3] Center for Physical Sciences & Technology, Department of Organic Chemistry, LT-10257 Vilnius, Lithuania
[4] Department of Chemistry, Faculty of Science, Universiti Malaya, Kuala Lumpur 50603, Malaysia
* Correspondence: juozas.grazulevicius@ktu.lt

Abstract: Two compounds based on pyridazine as the acceptor core and 9,9-dimethyl-9,10-dihydroacridine or phenoxazine donor moieties were designed and synthesized by Buchwald–Hartwig cross-coupling reaction. The electronic, photophysical, and electrochemical properties of the compounds were studied by ultraviolet-visible spectroscopy (UV-vis), photoluminescence spectrometry, differential scanning calorimetry, thermogravimetric analysis, and cyclic voltammetry. The compounds are characterized by high thermal stabilities. Their 5% weight loss temperatures are 314 and 336 °C. Complete weight loss of both pyridazine-based compounds was detected by TGA, indicating sublimation. The derivative of pyridazine and 9,9-dimethyl-9,10-dihydroacridine is capable of glass formation. Its glass transition temperature is 80 °C. The geometries and electronic characteristics of the compounds were substantiated using density functional theory (DFT). The compounds exhibited emission from the intramolecular charge transfer state manifested by positive solvatochromism. The emission in the range of 534–609 nm of the toluene solutions of the compounds is thermally activated delayed fluorescence with lifetimes of 93 and 143 ns, respectively.

Keywords: pyridazine; 9,9-dimethyl-9,10-dihydroacridine; phenoxazine; delayed fluorescence

Citation: Skhirtladze, L.; Bezvikonnyi, O.; Keruckienė, R.; Dvylys, L.; Mahmoudi, M.; Labanauskas, L.; Ariffin, A.; Grazulevicius, J.V. Derivatives of Pyridazine with Phenoxazine and 9,9-Dimethyl-9,10-dihydroacridine Donor Moieties Exhibiting Thermally Activated Delayed Fluorescence. *Materials* **2023**, *16*, 1294. https://doi.org/10.3390/ma16031294

Academic Editors: Haichang Zhang and Maning Liu

Received: 30 December 2022
Revised: 18 January 2023
Accepted: 26 January 2023
Published: 2 February 2023

1. Introduction

Thermally activated delayed fluorescence (TADF) has emerged as a promising photophysical mechanism useful in the development of efficient organic light emitting diodes (OLEDs) [1–4]. TADF is a phenomenon that relies on the upconversion of triplet excitons to singlet excited states by means of reverse intersystem crossing (RISC) due to the thermal motion of atoms [5–7] (Figure 1).

OLEDs based on TADF are an alternative type of OLED to phosphorescent OLEDs (PhOLEDs) [8]. The radiative utilization of triplet electronic excitation energy in the case of PhOLEDs is due to the exciton-spin-orbit-photon interaction relying on the largest atomic number of atoms incorporated in the structure [8]. Therefore, the phosphorescent emitters of OLEDs commonly have noble metal atoms such as Ir or Pt attached to the organic moieties. TADF is of great interest in this regard, as it allows the utilization of triplet energy without the use of expensive materials. Efficient RISC can be reached by combining electron-accepting and electron-donating moieties in a single molecule and constraining their dihedral angles in such a way that it minimizes the overlap of HOMO and LUMO [9–11]. Electron-withdrawing moieties containing cyano groups or azoheterocycles have been used most extensively for the design of TADF emitters [8–16]. The use of

9-[4-(4-(4,6-diphenyl-1,3,5-triazin-2-yl) phenyl]-N, N, N0, N0-tetraphenyl-9H-carbazole-3,6-diamine (DACT-II), which has a triazine electron-acceptor (A) moiety, allowed the design of OLEDs with internal quantum efficiency of 100% [17]. 1,2,3,5-Tetrakis(carbazol-9-yl)-4,6-dicyanobenzene (4CzIPN), with dicyanobenzene as the electron acceptor, has shown excellent redox window, good stability, and excellent TADF characteristics [18].

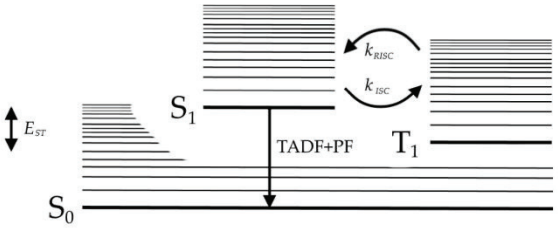

Figure 1. Simplified Jablonski diagram for TADF emitters.

Aromatic azaheterocycles are among the most electron-deficient aromatic heterocycles [19,20]. Triazine, pyridine, and naphthyridine contain strongly electronegative nitrogen atoms in their molecular skeletons. Therefore, they display an intrinsic electron-deficient character, enabling them to be used in the design of compounds for a wide range of applications, such as pH sensing, optoelectronics, nonlinear optical materials, and pharmaceuticals [21–24]. Reports on the synthesis of the studied pyridazine derivatives for optoelectronic and related applications are still scarce. They were reported as host materials for OLEDs and liquid-crystalline materials, and as phosphorescent iridium complexes [25–28]. A series of pyridazine-based TADF emitters have been described, where the combination of the pyridazine moiety with phenoxazine resulted in an emitter with a photoluminescence quantum efficiency of 10.9% with an estimated high RISC rate k_{RISC} of 3.9×10^6 s^{-1} and a small singlet–triplet splitting value of 86 meV [29]. The OLED based on this emitter demonstrated external quantum efficiency of over 5.8%, confirming triplet utilization in the device via TADF [29]. Pyridazine is not only more electron-accepting, but also more polar than pyridine, which is beneficial for its use as an electron acceptor in the design of D-A-type materials [28]. In this work, the synthesis and properties of two derivatives of pyridazine bearing phenoxazine and 9,9-dimethyl-9,10-dihydroacridine electron-donating moieties are reported. The interesting structure–properties relationship was disclosed by studies of thermal, photophysical, and electrochemical properties, as well as by quantum chemistry studies. Investigation of the photophysical properties of the toluene solutions and films of the compounds confirmed that TADF showed lifetimes of 93 and 143 ns, corresponding to the toluene solutions of the compounds having phenoxazine and 9,9-dimethyl-9,10-dihydroacridine, respectively.

2. Results and Discussion

2.1. Synthesis and Thermal Properties

The synthesis of the derivatives of 2,5-disubstituted-pyridazine is shown in Scheme 1. For the synthesis of the target compounds, Buchwald–Hartwig coupling reactions of brominated pyridazine with phenoxazine or 9,9-dimethyl-9,10-dihydroacridine were carried out in the presence of tris(dibenzylideneacetone)dipalladium(0) as the metal catalyst and X-Phos as the ligand. The reactions produced donor–acceptor–donor (D-A-D) derivatives 2PO-PYD and 2AC-PYD in yields of 21.8% and 6.4%, respectively. The target compounds were purified by column chromatography. The structures of the synthesized compounds were confirmed by ^{1}H, ^{13}C NMR, and FT-IR spectroscopies, as well as mass spectrometry. They were found to be soluble in common organic solvents. Characteristics of the compounds 2PO-PYD and 2AC-PYD can be found in the Supplementary Materials File.

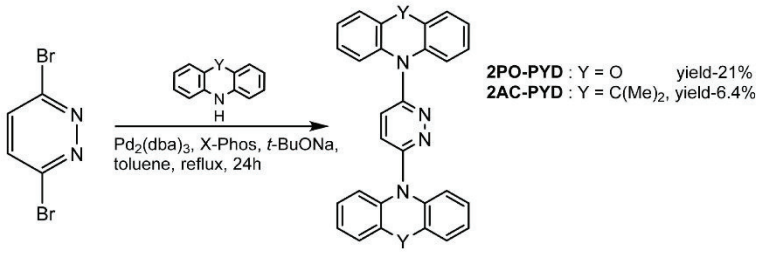

Scheme 1. Synthesis of 2,5-disubstituted pyridazine derivatives.

Morphological transitions and thermal stabilities of pyridazine-based compounds (2PO-PYD and 2AC-PYD) were investigated by differential scanning calorimetry (DSC) and thermogravimetric analysis (TGA) (Figure S5). Their thermal characteristics are shown in Table 1.

Table 1. Thermal characteristics of the compounds.

Compound	T_{ID}, °C [1]	T_g, °C	T_{cr}, °C [2]	T_m, °C [3]
2PO-PYD	314	-	188	248
2AC-PYD	336	80	133	231

[1] Temperature of 5% loss of mass determined by TGA. [2] Crystallization temperatures determined by DSC from the first cooling scan. [3] Melting points determined by DSC from the second heating scan.

Both target compounds were obtained after the synthesis and purification as crystalline substances. Endothermic melting signals were observed in the first heating scans of the DSC measurements (Figure S5a,b). Crystallization and subsequent melting signals were observed during the cooling and second heating scans. The glass transition of compound 2AC-PYD was detected during the second heating scan, indicating the possibility of transformation into a solid amorphous state (molecular glass). During the TGA measurements, complete weight loss of both pyridazine-based compounds was detected, indicating sublimation rather than thermal degradation of the samples.

2.2. *Theoretical Calculations and Electrochemical Properties*

The geometries and electronic structures of the target molecules were analyzed using DFT calculations at the B3LYP/6-31++G theoretical level. The ground-state geometries were optimized by using the B3LYP (Becke three parameters hybrid functional with Lee-Yang-Perdew correlation) [30] functional at 6-31G (d, p) level in vacuum with the Gaussian program [31]. To evaluate the electronic transitions, the geometries of the pyridazine derivatives **2PO-PYD** and **2AC-PYD** were evaluated (Figure 2). As the acceptor and donor moieties are directly linked, the values of the dihedral angles are crucial for intramolecular charge transfer (ICT). In the optimized ground-state geometries, the D and A fragments are almost perpendicularly orientated, as their dihedral angle values are close to 90°. Such large dihedral angle values are expected to lead to minimal conjugation of the D-A fragments.

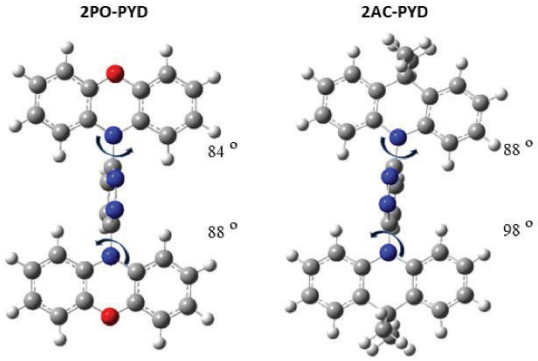

Figure 2. Optimized ground-state geometries in vacuum at the B3LYP/6-31++G level of theory of pyridazine derivatives **2PO-PYD** and **2AC-PYD** (grey color: carbon; blue: nitrogen; red: oxygen; white: hydrogen).

The calculated HOMOs and LUMOs are presented in Figure 3. The electronic structures of both pyridazine-based compounds are similar. The HOMOs are situated on the electron-donating fragments of phenoxazine and 9,9-dimethyl-9,10-dihydroacridine, with a small electron density residing on the pyridazine fragment, whereas the LUMO is situated solely on the acceptor fragment. The calculated HOMO levels confirm the slightly stronger electron-donating strength of phenoxazine compared to that of the 9,9-dimethyl-9,10-dihydroacridine moiety. The levels of LUMO are in good agreement with the LUMO values of previously reported pyridazine-based host compounds [29].

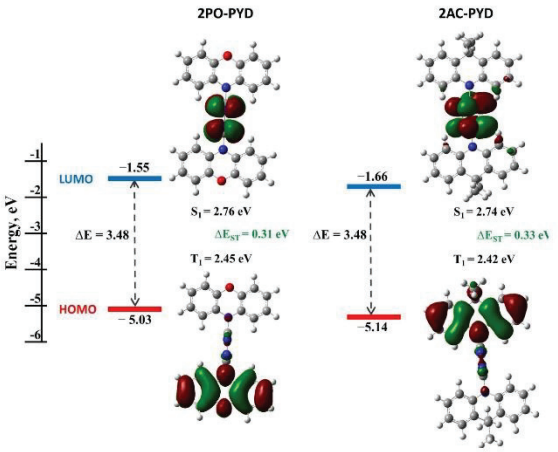

Figure 3. DFT calculated HOMO and LUMO energies, as well as HOMO and LUMO topologies (isovalue of 0.02), of compounds **2PO-PYD** and **2AC-PYD**.

In the optimized excited-state geometry, the dihedral angles remain perpendicular. TD-DFT calculations predicted that the dominant S1 transition is CT in nature (H→L). The calculated values of the energy gaps between the singlet and triplet states (ΔE_{ST}) are ca. 0.3 eV (Figure 3), and are in line with the slightly stronger electron-donating nature of the phenoxazine moiety. Such small energy gaps make these pyridazine derivatives promising as TADF emitters.

Cyclic voltammetry was used to investigate the electrochemical properties of pyridazine-based compounds **2PO-PYD** and **2AC-PYD**. **2AC-PYD** showed reversible oxidation during repeated scans, whereas the pyridazine-based compound **2PO-PYD** showed quasi-reversible oxidation. Ionization potentials estimated by the cyclic voltammetry (IP_{CV}) values were estimated from oxidation onset potentials against ferrocene (Eox onset vs. Fc). The voltammograms are shown in Figure 4.

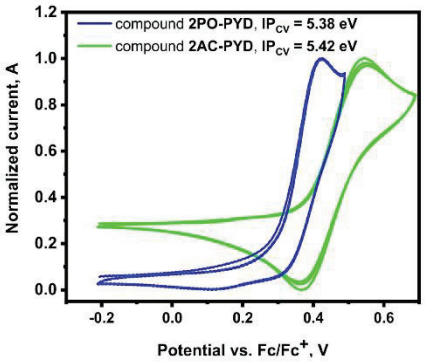

Figure 4. Cyclic voltammograms of compounds **2PO-PYD** and **2AC-PYD**.

The IP_{CV} values were found to be only slightly dependent on the strength of the donor moieties attached. The phenoxazine-containing compound (**2PO-PYD**) showed slightly higher IP_{CV} than the derivative of 9,9-dimethyl-9,10-dihydroacridine (**2AC-PYD**). Despite the small differences, overall, the experimentally determined characteristics correlate well with the theoretically calculated ones.

2.3. Photophysical Properties

The absorption and emission spectra of the solutions of **2PO-PYD** and **2AC-PYD** are presented in Figure 5a,b, respectively, and in Table 2.

Table 2. Photophysical characteristics of **2PO-PYD** and **2AC-PYD**.

Compound	λ_a, nm [1]	λ_e, nm [2]	Φ [3]	E_{S1}, eV [4]	E_{T1}, eV [4]	ΔE_{ST} [4]
2PO-PYD	308/308	ca. 420, 618/398, 639/565	<0.01	2.68	2.59	0.09
2AC-PYD	ca. 280/290	353, 535/346, 561/517	<0.01	2.64	2.29	0.35

[1] Wavelengths of the bands of absorption spectra of the solutions of the compounds in toluene/THF. [2] Wavelengths of the bands of emission spectra of the compounds of the toluene/THF solutions and films. [3] PL quantum yield of deoxygenated toluene solutions. [4] Derived from spectral data of the films of compounds recorded at 77 K in the absence of oxygen.

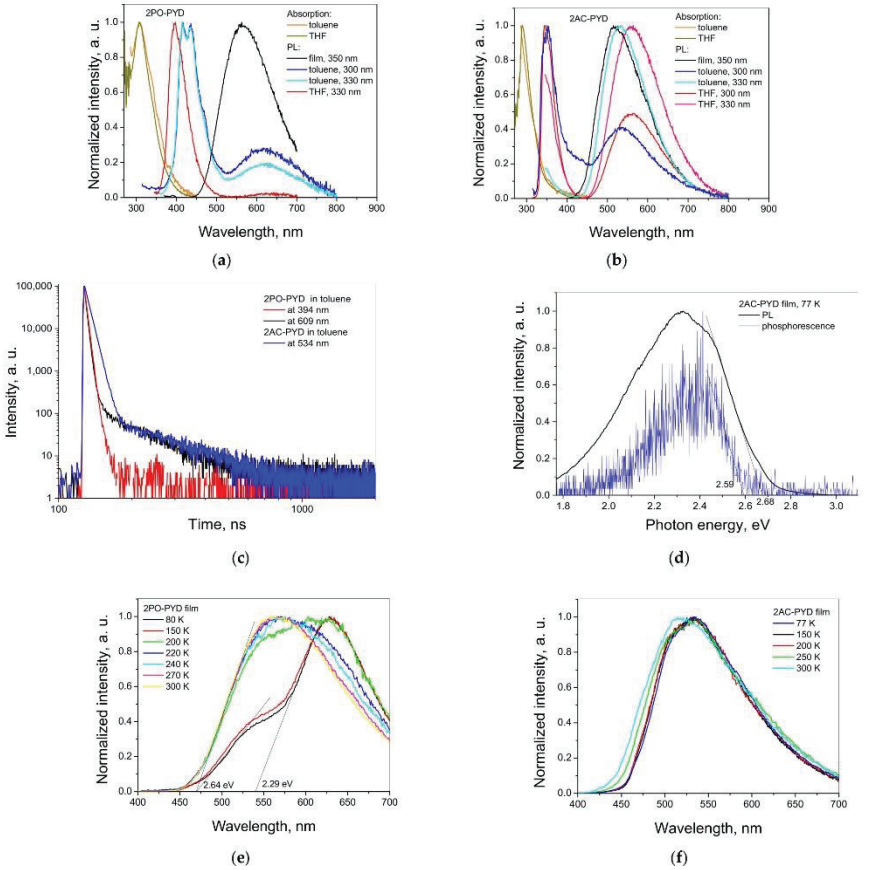

Figure 5. Absorption and PL spectra of toluene, THF solutions, and films of **2PO-PYD** (**a**) and **2AC-PYD** (**b**). PL decay curves of deoxygenated toluene solutions (**c**). PL and phosphorescence spectra of the film of **2AC-PYD** recorded at liquid nitrogen temperature (**d**). PL spectra of the films of **2PO-PYD** (**e**) and **2AC-PYD** (**f**) recorded in inert atmosphere at different temperatures.

The absorption spectra are characterized by the prominent band at 308 nm for the solutions of **2PO-PYD** and 288 nm for those of **2AC-PYD**. The positions of the absorption peaks almost did not change when changing the non-polar toluene solvent with the polar THF. DFT predicts that this band originates from the locally excited (LE) state of donor fragments (Figure S6). The very low oscillator strength of 0.002 of the transition of the ICT state ($S_0 \rightarrow S_1$) is apparently the reason for the lack of this absorption band in the experimental UV spectra.

The different photoluminescence (PL) spectra of the solutions recorded at the different excitation wavelengths showed the presence of two distinguished emission bands in the UV and green spectral regions. The spectral data presented in Table 2 provide an opportunity to track the influence of polarity of the medium on photophysical characteristics of the compounds. Toluene is a non-polar solvent, while THF is a moderately polar one. The investigated compounds are designed to have a donor–acceptor–donor structure; thus, the dipole moment must be affected by the polarity of the solvents, exhibiting solvatochromism. The PL band in the UV region covering the range of ca. 400–450 nm is related to the local excited (LE) state emission of the donor. It is not characterized by the positive solvatochromism caused by the increase in polarity of the solvent. The low-energy emission band at ca. 500–625 nm exhibited a spectral redshift with the increase of the solvent polarity, pointing to the intramolecular charge transfer (ICT) state. Different excitation wavelengths alter the spectral distribution insignificantly. This observation is in full accordance with Dr. Michael Kasha's rule excluding the possibility of excitation of specific optical centers affecting the analysis of the experimental data. The ICT peak wavelengths of the spectra of neat films of the compounds correspond to the peak positions of the ICT band of respective toluene solutions. This demonstrates the absence of the effect of intermolecular interactions in solid state, polarity, or aggregation-related phenomena on the ICT of the compounds. The emission of 9,9-dimethyl-9,10-dihydroacridin-based **2AC-PYD** is expectedly blue-shifted with respect to that of **2PO-PYD** with a stronger donating unit of phenoxazine. The PL quantum yields of the deoxygenated toluene solutions Φ of both **2PO-PYD** and **2AC-PYD** did not reach 1%. The deoxygenation of the solutions and of the solid films of the compounds did not lead to the change of the photoluminescence spectra, highlighting the ICT nature of the respective band at ca. 500–625 nm and the absence/weakness of the room-temperature phosphorescence.

The PL decay curves of the deoxygenated toluene solutions of **2PO-PYD** and **2AC-PYD** were recorded at the corresponding PL peak wavelengths (Figure 5c). The major data of PL decays are collected in Table 3 and Figure S7. The multiexponential fitting exhibited that the lifetime of the **2PO-PYD** LE band totally correlates with the lifetime of the prompt fluorescent component of the PL decay curve recorded at 621 nm. At the same time, the ICT bands of the solutions of **2PO-PYD** and **2AC-PYD** exhibited emission lifetimes of 93 and 143 ns, respectively. Such lifetimes are associated with the so-called fast delayed emission, i.e., TADF [32].

Table 3. Photophysical characteristics of the toluene solutions of **2PO-PYD** and **2AC-PYD**.

Toluene Solution [1]	λ, nm [2]	Lifetime, ns [3]	k_{RISC}, s^{-1}	k_{ISC}, s^{-1}	χ [2,4]
2PO-PYD	394	2.85	-	-	1.043
2PO-PYD	609	2.49 (85.44%), 9.75 (6.49%), 92.86 (8.07%)	9.5×10^5	2.2×10^8	1.166
2AC-PYD	534	6 (95.52%), 142.96 (4.48%)	3.3×10^5	1.6×10^8	1.034

[1] Deoxygenated. [2] Wavelength at which the measurement was performed. [3] Intensity amplitude in parentheses. [4] Weighted sum of fit points square deviations.

PL spectra of the films of **2PO-PYD** and **2AC-PYD** were taken at different temperatures to decisively confirm the absence of room-temperature phosphorescence. The energy levels of the first excited singlet and triplet states were estimated from the onsets of the respective prompt fluorescent and phosphorescent bands (Figure 5d,e). The phosphorescence component of the emission disappeared while heating, leaving only the ICT band (Figure 5e,f). The presumption about the TADF phenomenon is inconsistent with the obtained ΔE_{ST} of 0.35 eV (Figure 5e) between the first singlet and triplet excited states of **2PO-PYD**, even though it is predicted based on the results of the theoretical analysis (Figure 3). In this case, the RISC relies heavily on a spin–orbit coupling of energetically close ^{3}CT and ^{3}LE states. The possibility of spin being flipped in the organic material without insertion of heavy atoms into the structure is realized because k_{RISC} is deeply dependent on the triplet excitonic Bohr radius, which enhances k_{RISC} by several orders

of magnitude more than the rate constant of ISC (k_{ISC}) (Table 3) [11]. The energy level of 2.29 eV is attributed to ^{3}CT of **2PO-PYD**, similar to previously reported phenoxazine-based TADF compounds [28,29,31]. The presence of ^{3}LE is anticipated with an energy level close to that of ^{1}CT state, i.e., of ca. 2.64 eV (Figure 5e), facilitating TADF [32,33]. The low Φ makes it difficult to detect the ^{3}LE experimentally. As expected for **2AC-PYD** containing the 9,9-dimethyl-9,10-dihydroacridine donor moiety [28,29,32,34,35], the first triplet excited state with the energy of 2.59 eV is close to that of ^{1}CT of 2.68 eV, which is beneficial for TADF. The values of k_{RISC} and k_{ISC} were evaluated from the fitting data of the PL decay curves using equations $k_{RISC} = \frac{(\Phi_{PF}+\Phi_{DF})\Phi_{RISC}}{\tau_{DF}\Phi_{PF}}$, $k_{ISC} = \frac{\Phi_{DF}}{\tau_{PF}(\Phi_{PF}+\Phi_{DF})}$, where Φ_{PF}, Φ_{DF}, and Φ_{RISC} are the quantum yields of prompt, delayed fluorescence, and RISC, respectively [36]. Using the formula $\Phi = \Phi_{PF} + \Phi_{DF} = \frac{\Phi_{PF}}{1-\Phi_{ISC}\Phi_{RISC}}$ and knowing that the yield of ISC Φ_{ISC} cannot exceed the electronic excitation energy not utilized in prompt fluorescence, k_{RISC} can be estimated by the formula $k_{RISC} = \frac{\Phi_{DF}}{\tau_{DF}\Phi_{PF}(1-\Phi_{PF})}$ [37]. The data obtained are collected in Table 3. The k_{RISC} value for 2PO-PYD reached almost 10^6 s^{-1}, which is only slightly lower than the values of state-of-the-art TADF emitters [29,36–38].

3. Conclusions

The derivatives of pyridazine and 9,9-dimethyl-9,10-dihydroacridine or phenoxazine were obtained by single-step synthesis employing Buchwald–Hartwig cross-coupling reactions. The compounds are characterized by high thermal stabilities. Their 5% weight loss temperatures are 314 and 336 °C. During the TGA measurements, complete weight loss of both pyridazine-based compounds was detected, indicating sublimation rather than thermal degradation of the samples. The derivative of pyridazine and 9,9-dimethyl-9,10-dihydroacridine is capable of glass formation. Its glass transition temperature is 80 °C. The ionization potential values, determined by cyclic voltammetry, are only slightly dependent on the strength of the donor moieties. They are 5.38 and 5.42 eV. The theoretical study revealed that $S_0 \rightarrow S_1$ excitation is characterized by intramolecular charge transfer that is the result of large dihedral angles between the pyridazine moieties and donor fragments in both molecules. The long-living components of the photoluminescence decay curves were detected for the deoxygenated toluene solutions of the compounds, additional to the prompt fluorescence components. The appearance of thermally activated delayed fluorescence (TADF) is presumed from the theoretical analysis of distribution of the highest occupied and lowest unoccupied molecular orbitals and based on the experimental data of time-resolved photoluminescence spectroscopy measurements conducted at different temperatures. The reverse intersystem crossing rate constant of 9.5×10^5 s^{-1} estimated for phenoxazinyl disubstituted pyridazine is higher than that observed for the derivative of 9,9-dimethyl-9,10-dihydroacridine and pyridazine (3.3×10^5 s^{-1}), primarily due to the fast TADF.

Supplementary Materials: The following supporting information can be downloaded at: https://www.mdpi.com/article/10.3390/ma16031294/s1, Figure S1: ^{1}H spectrum of 2PO-PYD; Figure S2. ^{13}C NMR spectrum of **2PO-PYD**; Figure S3. ^{1}H spectrum of **2AC-PYD**; Figure S4. ^{13}C NMR spectrum of **2AC-PYD**; Figure S5. DSC (a,b) and TGA (c) thermograms of compounds **2PO-PYD**, and **2AC-PYD**; Figure S6. Theoretical UV spectra (in toluene) obtained from TD-DFT calculations of the pyridazine-based compounds **2PO-PYD** (a) and **2AC-PYD** (b); Figure S7. PL decay curves of deoxygenated toluene solutions of **2PO-PYD** (a,b), **2AC-PYD** (c). Refs. [30,31] are cited in the Supporting Information.

Author Contributions: Conceptualization and methodology, A.A., L.L. and L.S.; investigation and data curation, O.B., M.M., R.K. and L.D.; writing—original draft preparation, L.S.; writing—review and editing, R.K. and O.B.; supervision, A.A. and J.V.G.; funding acquisition, J.V.G. All authors have read and agreed to the published version of the manuscript.

Funding: The research was funded by the European Union's Horizon 2020 Research and Innovation Programme under the Marie Skłodowska-Curie grant agreement No. 823720.

Institutional Review Board Statement: Not applicable.

Informed Consent Statement: Not applicable.

Data Availability Statement: The data presented in this study are available on request from the corresponding author.

Conflicts of Interest: The authors declare no conflict of interest.

References

1. Schleper, A.L.; Goushi, K.; Bannwarth, C.; Haehnle, B.; Welscher, P.J.; Adachi, C.; Kuehne, A.J.C. Hot Exciplexes in U-Shaped TADF Molecules with Emission from Locally Excited States. *Nat. Commun.* **2021**, *12*, 6179. [CrossRef] [PubMed]
2. Wu, C.; Zhang, Y.; Ma, D.; Wang, Q. Phthalonitrile-Based Bipolar Host for Efficient Green to Red Phosphorescent and TADF OLEDs. *Dye. Pigment.* **2020**, *173*, 107895. [CrossRef]
3. Wang, Q.; Zhang, Y.-X.; Yuan, Y.; Hu, Y.; Tian, Q.-S.; Jiang, Z.-Q.; Liao, L.-S. Alleviating Efficiency Roll-Off of Hybrid Single-Emitting Layer WOLED Utilizing Bipolar TADF Material as Host and Emitter. *ACS Appl. Mater. Interfaces* **2019**, *11*, 2197–2204. [CrossRef] [PubMed]
4. Haase, N.; Danos, A.; Pflumm, C.; Stachelek, P.; Brütting, W.; Monkman, A.P. Are the Rates of Dexter Transfer in TADF Hyperfluorescence Systems Optically Accessible? *Mater. Horiz.* **2021**, *8*, 1805–1815. [CrossRef]
5. Chen, X.-K.; Bakr, B.W.; Auffray, M.; Tsuchiya, Y.; Sherrill, C.D.; Adachi, C.; Bredas, J.-L. Intramolecular Noncovalent Interactions Facilitate Thermally Activated Delayed Fluorescence (TADF). *J. Phys. Chem. Lett.* **2019**, *10*, 3260–3268. [CrossRef] [PubMed]
6. Fu, C.; Luo, S.; Li, Z.; Ai, X.; Pang, Z.; Li, C.; Chen, K.; Zhou, L.; Li, F.; Huang, Y.; et al. Highly Efficient Deep-Blue OLEDs Based on Hybridized Local and Charge-Transfer Emitters Bearing Pyrene as the Structural Unit. *Chem. Commun.* **2019**, *55*, 6317–6320. [CrossRef]
7. Gao, F.; Du, R.; Han, C.; Zhang, J.; Wei, Y.; Lu, G.; Xu, H. High-Efficiency Blue Thermally Activated Delayed Fluorescence from Donor–Acceptor–Donor Systems *via* the through-Space Conjugation Effect. *Chem. Sci.* **2019**, *10*, 5556–5567. [CrossRef]
8. Colella, M.; Danos, A.; Monkman, A.P. Identifying the Factors That Lead to PLQY Enhancement in Diluted TADF Exciplexes Based on Carbazole Donors. *J. Phys. Chem. C* **2019**, *123*, 17318–17324. [CrossRef]
9. Rajamalli, P.; Senthilkumar, N.; Gandeepan, P.; Huang, P.-Y.; Huang, M.-J.; Ren-Wu, C.-Z.; Yang, C.-Y.; Chiu, M.-J.; Chu, L.-K.; Lin, H.-W.; et al. A New Molecular Design Based on Thermally Activated Delayed Fluorescence for Highly Efficient Organic Light Emitting Diodes. *J. Am. Chem. Soc.* **2016**, *138*, 628–634. [CrossRef]
10. Han, C.; Zhang, J.; Ma, P.; Yang, W.; Xu, H. Host Engineering Based on Multiple Phosphorylation for Efficient Blue and White TADF Organic Light-Emitting Diodes. *Chem. Eng. J.* **2021**, *405*, 126986. [CrossRef]
11. Lin, T.-C.; Sarma, M.; Chen, Y.-T.; Liu, S.-H.; Lin, K.-T.; Chiang, P.-Y.; Chuang, W.-T.; Liu, Y.-C.; Hsu, H.-F.; Hung, W.-Y.; et al. Probe Exciplex Structure of Highly Efficient Thermally Activated Delayed Fluorescence Organic Light Emitting Diodes. *Nat. Commun* **2018**, *9*, 3111. [CrossRef]
12. Chen, D.; Zysman-Colman, E. Exploring the Possibility of Using Fluorine-Involved Non-Conjugated Electron-Withdrawing Groups for Thermally Activated Delayed Fluorescence Emitters by TD-DFT Calculation. *Beilstein. J. Org. Chem.* **2021**, *17*, 210–223. [CrossRef]
13. Pereira, J.A.; Pessoa, A.M.; Cordeiro, M.N.D.S.; Fernandes, R.; Prudêncio, C.; Noronha, J.P.; Vieira, M. Quinoxaline, Its Derivatives and Applications: A State of the Art Review. *Eur. J. Med. Chem.* **2015**, *97*, 664–672. [CrossRef]
14. Tao, Y.; Yuan, K.; Chen, T.; Xu, P.; Li, H.; Chen, R.; Zheng, C.; Zhang, L.; Huang, W. Thermally Activated Delayed Fluorescence Materials Towards the Breakthrough of Organoelectronics. *Adv. Mater.* **2014**, *26*, 7931–7958. [CrossRef]
15. Wang, K.; Bao, Y.; Zhu, S.; Liu, R.; Zhu, H. Novel 1,5-Naphthyridine-Chromophores with D-A-D Architecture: Synthesis, Synthesis, Luminescence and Electrochemical Properties. *Dye. Pigment.* **2020**, *181*, 108596. [CrossRef]
16. Zhou, X.; Yang, H.; Chen, Z.; Gong, S.; Lu, Z.-H.; Yang, C. Naphthyridine-Based Emitters Simultaneously Exhibiting Thermally Activated Delayed Fluorescence and Aggregation-Induced Emission for Highly Efficient Non-Doped Fluorescent OLEDs. *J. Mater. Chem. C Mater.* **2019**, *7*, 6607–6615. [CrossRef]
17. Kaji, H.; Suzuki, H.; Fukushima, T.; Shizu, K.; Suzuki, K.; Kubo, S.; Komino, T.; Oiwa, H.; Suzuki, F.; Wakamiya, A.; et al. Purely Organic Electroluminescent Material Realizing 100% Conversion from Electricity to Light. *Nat. Commun.* **2015**, *6*, 8476. [CrossRef]
18. Shang, T.-Y.; Lu, L.-H.; Cao, Z.; Liu, Y.; He, W.-M.; Yu, B. Recent Advances of 1,2,3,5-Tetrakis(Carbazol-9-Yl)-4,6-Dicyanobenzene (4CzIPN) in Photocatalytic Transformations. *Chem. Commun.* **2019**, *55*, 5408–5419. [CrossRef] [PubMed]
19. He, Z.-X.; Gong, Y.-P.; Zhang, X.; Ma, L.-Y.; Zhao, W. Pyridazine as a Privileged Structure: An Updated Review on Anticancer Activity of Pyridazine Containing Bioactive Molecules. *Eur. J. Med. Chem.* **2021**, *209*, 112946. [CrossRef]
20. Achelle, S.; Hodée, M.; Massue, J.; Fihey, A.; Katan, C. Diazine-Based Thermally Activated Delayed Fluorescence Chromophores. *Dye. Pigment.* **2022**, *200*, 110157. [CrossRef]
21. Yuan, W.; Hu, D.; Zhu, M.; Shi, W.; Shi, C.; Sun, N.; Tao, Y. Simple Peripheral Modification for Color Tuning of Thermally Activated Delayed Fluorescence Emitters in OLEDs. *Dye. Pigment.* **2021**, *191*, 109395. [CrossRef]
22. Gauthier, S.; Fréchet, J.M.J. Phase-Transfer Catalysis in the Ullmann Synthesis of Substituted Triphenylamines. *Synthesis* **1987**, *1987*, 383–385. [CrossRef]

23. Qu, Y.; Pander, P.; Vybornyi, O.; Vasylieva, M.; Guillot, R.; Miomandre, F.; Dias, F.B.; Skabara, P.; Data, P.; Clavier, G.; et al. Donor–Acceptor 1,2,4,5-Tetrazines Prepared by the Buchwald–Hartwig Cross-Coupling Reaction and Their Photoluminescence Turn-On Property by Inverse Electron Demand Diels–Alder Reaction. *J. Org. Chem.* **2020**, *85*, 3407–3416. [CrossRef]
24. Franz, A.W.; Popa, L.N.; Rominger, F.; Müller, T.J.J. First Synthesis and Electronic Properties of Diphenothiazine Dumbbells Bridged by Heterocycles. *Org. Biomol. Chem.* **2009**, *7*, 469–475. [CrossRef] [PubMed]
25. Tang, R.; Wang, X.; Zhang, W.; Zhuang, X.; Bi, S.; Zhang, W.; Zhang, F. Aromatic Azaheterocycle-Cored Luminogens with Tunable Physical Properties via Nitrogen Atoms for Sensing Strong Acids. *J. Mater. Chem. C Mater.* **2016**, *4*, 7640–7648. [CrossRef]
26. Plé, N.; Achelle, S.; Kreher, D.; Mathevet, F.; Turck, A. Oligomers Containing Ethynylpyridazine Moieties: Synthesis, Fluorescence and Liquid Crystalline Properties. Diazines 50. *Heterocycles* **2008**, *75*, 357. [CrossRef]
27. Zhang, X.L.; Liu, S.J.; Guo, L.Y.; Wang, C.J.; Tong, Y.; Mi, B.X.; Cao, D.P.; Song, J.; Gao, Z.Q. Design of C^N=N Type Iridium(III) Complexes towards Short-Wavelength Emission for High Efficiency Organic Light-Emitting Diodes. *RSC Adv.* **2016**, *6*, 81869–81876. [CrossRef]
28. Liu, S.; Zhang, X.; Ou, C.; Wang, S.; Yang, X.; Zhou, X.; Mi, B.; Cao, D.; Gao, Z. Structure–Property Study on Two New D–A Type Materials Comprising Pyridazine Moiety and the OLED Application as Host. *ACS Appl. Mater. Interfaces* **2017**, *9*, 26242–26251. [CrossRef]
29. Krotkus, S.; Matulaitis, T.; Diesing, S.; Copley, G.; Archer, E.; Keum, C.; Cordes, D.B.; Slawin, A.M.Z.; Gather, M.C.; Zysman-Colman, E.; et al. Fast Delayed Emission in New Pyridazine-Based Compounds. *Front. Chem.* **2021**, *8*, 572862. [CrossRef]
30. Becke, A.D. Density-functional exchange-energy approximation with correct asymptotic behavior. *Phys. Rev. A* **1988**, *38*, 3098–3100. [CrossRef]
31. Frisch, M.J.; Trucks, G.W.; Schlegel, H.B.; Scuseria, G.E.; Robb, M.A.; Cheeseman, J.R.; Scalmani, G.; Barone, V.; Petersson, G.A.; Nakatsuji, H.; et al. *Gaussian 09, Revision A.02*; Gaussian, Inc.: Wallingford, UK, 2016.
32. Dias, F.B.; Penfold, T.J.; Monkman, A.P. Photophysics of Thermally Activated Delayed Fluorescence Molecules. *Methods Appl. Fluoresc.* **2017**, *5*, 012001. [CrossRef] [PubMed]
33. Dey, S.; Hasan, M.; Shukla, A.; Acharya, N.; Upadhyay, M.; Lo, S.-C.; Namdas, E.B.; Ray, D. Thermally Activated Delayed Fluorescence and Room-Temperature Phosphorescence in Asymmetric Phenoxazine-Quinoline (D2–A) Conjugates and Dual Electroluminescence. *J. Phys. Chem. C* **2022**, *126*, 5649–5657. [CrossRef]
34. Kwon, D.Y.; Lee, G.H.; Kim, Y.S. Theoretical Study on Benzazole Derivatives for Use in Blue Thermally Activated Delayed Fluorescence Emitters. *J. Nanosci. Nanotechnol.* **2015**, *15*, 7819–7822. [CrossRef] [PubMed]
35. Santos, P.L.; Ward, J.S.; Data, P.; Batsanov, A.S.; Bryce, M.R.; Dias, F.B.; Monkman, A.P. Engineering the Singlet–Triplet Energy Splitting in a TADF Molecule. *J. Mater. Chem. C Mater.* **2016**, *4*, 3815–3824. [CrossRef]
36. Hosokai, T.; Matsuzaki, H.; Nakanotani, H.; Tokumaru, K.; Tsutsui, T.; Furube, A.; Nasu, K.; Nomura, H.; Yahiro, M.; Adachi, C. Evidence and Mechanism of Efficient Thermally Activated Delayed Fluorescence Promoted by Delocalized Excited States. *Sci. Adv.* **2017**, *3*, e1603282. [CrossRef]
37. Jang, J.S.; Lee, H.L.; Lee, K.H.; Lee, J.Y. Electrostatic Potential Dispersing Pyrimidine-5-Carbonitrile Acceptor for High Efficiency and Long Lifetime Thermally Activated Delayed Fluorescence Organic Light-Emitting Diodes. *J. Mater. Chem. C Mater.* **2019**, *7*, 12695–12703. [CrossRef]
38. Traskovskis, K.; Sebris, A.; Novosjolova, I.; Turks, M.; Guzauskas, M.; Volyniuk, D.; Bezvikonnyi, O.; Grazulevicius, J.V.; Mishnev, A.; Grzibovskis, R.; et al. All-Organic Fast Intersystem Crossing Assisted Exciplexes Exhibiting Sub-Microsecond Thermally Activated Delayed Fluorescence. *J. Mater. Chem. C Mater.* **2021**, *9*, 4532–4543. [CrossRef]

Dyes and Pigments 208 (2022) 110841

Contents lists available at ScienceDirect

Dyes and Pigments

journal homepage: www.elsevier.com/locate/dyepig

Carbazole-σ-sulfobenzimide derivative exhibiting mechanochromic thermally activated delayed fluorescence as emitter for flexible OLEDs: Theoretical and experimental insights

Yan Danyliv [a], Khrystyna Ivaniuk [a], Iryna Danyliv [a], Oleksandr Bezvikonnyi [b], Dmytro Volyniuk [b], Sych Galyna [c], Algirdas Lazauskas [d], Levani Skhirtladze [b], Hans Ågren [e], Pavlo Stakhira [a], Nataliya Karaush-Karmazin [f], Amjad Ali [g], Glib Baryshnikov [f,g,**], Juozas V. Grazulevicius [b,*]

[a] Lviv Polytechnic National University, Stepan Bandera 12, 79013, Lviv, Ukraine
[b] Department of Polymer Chemistry and Technology, Kaunas University of Technology, Radvilenu pl. 19, LT-50254, Kaunas, Lithuania
[c] Univ. Grenoble Alpes, Univ. Savoie Mont Blanc, CNRS, Grenoble INP, LEPMI, 38000, Grenoble, France
[d] Institute of Materials Science Kaunas University of Technology, K Baršausko St. 59, LT51423, Kaunas, Lithuania
[e] Department of Physics and Astronomy, Uppsala University, Box 516, Uppsala, SE-751 20, Sweden
[f] Department of Chemistry and Nanomaterials Science, Bohdan Khmelnytsky National University, Cherkasy, 18031, Ukraine
[g] Linköping University, Department of Science and Technology, Laboratory of Organic Electronics, Norrköping, SE-60174, Sweden

ABSTRACT

For the first time exploiting sulfobenzimide moiety as an acceptor unit, the new type of donor-σ-acceptor emitter exhibiting thermally activated delayed fluorescence (TADF) is demonstrated. In different solutions, the synthesized compound emits light resulting from either locally excited carbazole moiety or trough-space charge transfer (exciplex-like) between carbazole and sulfobenzimide units. In the solid state, this emitter demonstrates aggregation-induced emission enhancement and different emission colours due to its different conformations. The mechanoluminescence of the donor-σ-acceptor compound was observed and studied in detail by experimental and theoretical approaches including single-crystal and powder X-ray analyses. Electroluminescence of the different colours was observed when the compound was utilized as non-doped TADF emitter in rigid and flexible organic light-emitting diodes fabricated on glass or poly(ethylene terephthalate) substrates. The device fabricated on the rigid substrate exhibited the best performance with maximum current efficiency, power efficiency, and external quantum efficiency of 11.0 cd A^{-1}, 3.0 lm W^{-1}, and 4.3%, respectively.

1. Introduction

Significant competitive potential of organic light emitting diodes (OLED) and a number of unique design and technological features, created the preconditions for widespread commercialization of OLEDs as a basic elements in display technologies (projection and transparent displays), automotive engineering, biomedicine and modern dynamic lighting systems [1,2]. Flexible displays for smartphones and TV screens, coloured light sources are the examples of devices with wide application of OLEDs [1–4]. Therefore, research interest in the development of new organic electroactive compounds, suitable for application in OLEDs, is still high. Despite of the unique characteristics of OLED displays, such as flexibility, high contrast, low thickness and efficient energy consumption etc., there are still some disadvantages (relatively fast device degradation, especially of blue OLEDs), and as the result short service time of the consumer product. The development of new donor-acceptor organic compounds, exhibiting thermally activated delayed fluorescence (TADF) [5,6], aggregation-induced emission enhancement (AIEE) [7] and mechanoluminescent (MCL) properties [8,9] or the combination of these properties is an opportunity to increase the device efficiency and multifunctionality. MCL materials have great potential for the application in security inks, data storage, sensors, memory devices [10,11]. They demonstrate spectral response not only to mechanical stimuli but also to fuming of solvents, temperature gradient, electric field impact, etc. [12–15].

In the current report we present the synthetic protocol, together with the results of the structural and spectroscopic characterization for the novel MCL TADF D-A compound (D is carbazole, A is sulfobenzimide) i.

* Corresponding author.
** Corresponding author. Department of Chemistry and Nanomaterials Science, Bohdan Khmelnytsky National University, Cherkasy, 18031, Ukraine.
E-mail addresses: glib.baryshgnikov@liu.se (G. Baryshnikov), juozas.grazulevicius@ktu.lt (J.V. Grazulevicius).

https://doi.org/10.1016/j.dyepig.2022.110841
Received 6 June 2022; Received in revised form 30 September 2022; Accepted 6 October 2022
Available online 11 October 2022
0143-7208/

e., 2-(3-(9H-carbazol-9-yl)propyl)benzo[d]isothiazol-3(2H)-one 1,1-dioxide (**CzPrSBI**). Using this material, OLEDs on flexible substrate were fabricated and characterized, including the analysis of dependence of electroluminescence on the curvature of the OLED active area. The computational analysis of the different conformations of **CzPrSBI** explains the spectral changes of the fabricated diodes upon mechanical bending. Our report provides a new insight into application of conformationally flexible donor-acceptor molecules with non-conjugated D and A counterparts in color tunable flexible OLEDs that creates a background for the further development of flexible OLEDs based on alkyl linked donor-acceptor compounds.

2. Results and discussion

2.1. Synthesis and structural characterization

The synthesis of 2-(3-(9H-carbazol-9-yl)propyl)benzo[d]isothiazol-3(2H)-one 1,1-dioxide (**CzPrSBI**) was performed via two steps utilizing nucleophilic substitution mechanism S_N2 (Scheme 1). In the first step, carbazole was deprotonated to form nucleophile (carbazolyl anion) followed by the attack one of the bromine atoms in 1,3-dibromopropane to form 9-(3-bromopropyl)-9H-carbazole [16]. In the second step, sulfobenzimide anion replaced second bromine atom in alkyl chain to form **CzPrSBI**.

After purification, the target compound was obtained as crystalline substance. The chemical structure of **CzPrSBI** was confirmed by ^{1}H and ^{13}C NMR, mass spectrometries and single crystal X-ray analysis (CCDC number is 2165228). The details of experimental measurements and characterizations are presented in Supplementary Materials. **CzPrSBI** demonstrated moderate solubility in common organic solvents, such as chloroform, dichloromethane, dimethylformamide (DMF), acetonitrile, acetone while solubility in toluene and hexane was found to be significantly lower.

Hirshfeld surface analysis was performed in order to understand the nature of the intermolecular contacts stabilizing the crystal structure of **CzPrSBI** (the methodology of computations is presented in Supplementary Materials). A Hirshfeld surface of **CzPrSBI** is shown in Fig. 1. It represents the interaction of the electron density of the selected molecule with that of the surrounding crystal medium. The property projected in Fig. 1 is the normalized contact distance (d_{norm}) from the surface to the nearest external atom, where red regions indicate interactions, the distances (d) of which are less than van der Waals distances (the hydrogen bond interactions). Blue regions d exceed the van der Waals distances, and white regions are responsible for the contacts exactly equal to the van der Waals distances. As it is shown in Fig. 1, the intense red spots around the oxygen and hydrogen atoms correspond the long-range, moderate-strength C–H···O hydrogen bonds which stabilize the crystal structure of **CzPrSBI**. The two-dimensional fingerprint plot of

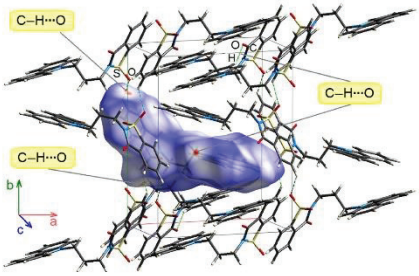

Fig. 1. Hirshfeld d_{norm} surface of the intermolecular interactions plotted in the unit-cell of compound **CzPrSBI**. The C–H···O close contacts are denoted as green dashed lines.

CzPrSBI is shown in ESI Fig. S1. It reveals the presence of the O···H/H···O interactions with a $d_e + d_i$ distance of ca. 2.64 Å, and 21.9% contribution to the total Hirshfeld surface.

The two-dimensional (2D) fingerprint plot of compound **CzPrSBI** (Fig. S1, top) illustrates the contributions from the different interaction types that overlap in the full fingerprint and then separate into partial contributions (Fig. S1, bottom). The 2D fingerprint plot reveals that the main intermolecular interactions in **CzPrSBI** are H···H, C···H, O···H and C···C. The decomposition of the fingerprint plot shows that H···H contacts occupy 40.5% of the total Hirshfeld surface area, C···H contacts of 29.8%, O···H contacts of 21.9%, and C···C contacts contribute only 3.7% to the total Hirshfeld surface area.

2.2. Thermal, electrochemical, photoelectrical and charge-transporting properties

Thermal characterization of **CzPrSBI** was performed using thermogravimetric analysis (TGA) and differential scanning calorimetry (DSC). TGA revealed relatively high 5% weight loss temperature of 314 °C (Fig. 2a). Full weight loss of the sample in TGA experiment shows that the recorded process was sublimation but not thermal decomposition. DSC thermogram of **CzPrSBI** revealed endothermic melting peaks at 175 °C during the 1st heating scan and 172 °C during the 2nd heating scan. This difference apparently could be related to the presence of two meta-stable crystalline forms. In the cooling scan there was no crystallization was observed, therefore, the material solidified in the amorphous phase. The following heating scan showed specific transition at

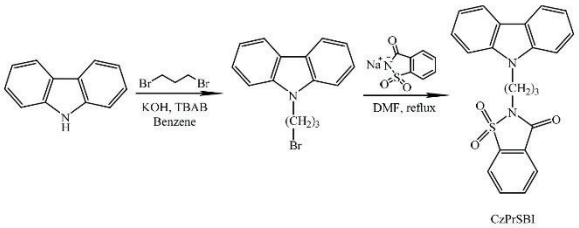

Scheme 1. Synthetic route to **CzPrSBI**.

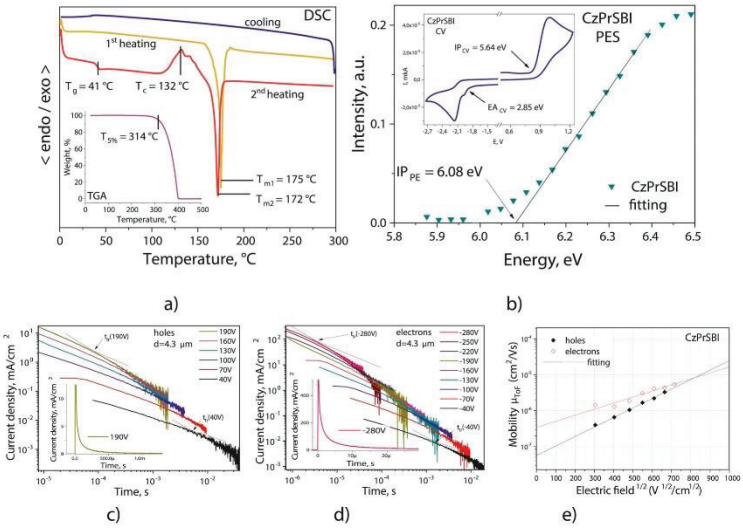

Fig. 2. DSC thermograms (a) **of CzPrSBI**. Inset: TGA curve of **CzPrSBI**. Photoelectron emission spectrum (b) of the solid film of **CzPrSBI**. Inset: Cyclic voltammetry curve of the DMF solution of **CzPrSBI**. TOF transients for holes (c) and electrons (d) recorded at the different applied voltages and the plots of charge-carrier drift mobilities versus electric field (e) for the layer of **CzPrSBI**.

41 °C which can be characterized as glass-transition and exothermic peak at 132 °C which can be recognized as crystallization signal (Fig. 2a).

Ionization potential (IP) and electron affinity (EA) of **CzPrSBI** were estimated by cyclic voltammetry of the solution in DMF (Fig. 2b, inset). To calculate IP_{CV} and EA_{CV} of the compound, the equations $IP_{CV} = (E_{ox} + 4.8)$ and $EA_{CV} = (E_{red} + 4.8)$ were used, where E_{ox} and E_{red} are electrochemical oxidation and reduction onset potentials, respectively. Ferrocene/ferrocenium redox potential was used as a standard. **CzPrSBI** demonstrated irreversible oxidation and reduction at 0.84 eV and −1.95 eV, respectively. Unprotected C-3 and C-6 positions of carbazole moiety most likely were responsible for irreversibility of the oxidation process [17]. IP_{CV} and EA_{CV} values were estimated to be 5.64 eV and 2.85 eV, respectively, while electrochemical band gap E_g^{CV} was found to be of 2.79 eV.

Ionization potential of the solid thin film (IP_{PE}) was estimated by photoelectron emission spectrometry (Fig. 2b). The solid-state IP_{PE} value was found to be of 6.08 eV. The equation $EA_{PE} = IP_{PE} - E_g^{opt}$ was used for the calculation of electron affinity (EA_{PE}) value. It was estimated to be of 2.65 eV. This EA_{PE} value was calculated using the optical band gap E_g^{opt} of 3.43 eV taken from the absorption spectrum of the solid film. Relatively high difference between the values of IP and EA measured for the solution and for the solid thin film is apparently related to the stronger intermolecular interactions in the solid state.

Charge-transporting properties of vacuum deposited thin film of **CzPrSBI** were examined by time-of-flight (ToF) technique. The obtained current transients for holes and electrons showed that the charge transport was very dispersive (Fig. 2c and d inset). Nevertheless, the transit times (t_{tr}) at the different applied voltages (positive for holes and negative for electrons) were clearly observed in log-log scales (Fig. 2 c, d). The lower t_{tr} value was obtained at high voltages in comparison to that recorded at low voltages (Fig. 2 c,d). At the electric field of 4.43×10^5 V/cm, the hole mobility value was found to be of 3.2×10^{-6} $cm^2/V \times s$, while electron mobility was found to be just slightly higher, i.e. of 4.4×10^{-6} $cm^2/V \times s$ (Fig. 2e). By fitting of the experimental electric field dependences of charge carrier drift mobilities according to the Poole–Frenkel prediction $\mu = \mu_0 e^{\alpha E^{1/2}}$ [18], very different values of zero-field mobilities (μ_0) of 5.8×10^{-8} and 3.4×10^{-7} $cm^2/V \times s$ were obtained for holes and electrons, respectively. Such big differences are because of the different field dependence parameters (α) of 6.1×10^{-3} and 3.9×10^{-3} $(cm/V)^{1/2}$ obtained for holes and electrons, respectively. It should be noted that bipolar compounds preferably transporting electrons are much rarer in the literature than bipolar compounds preferably transporting holes. Such compounds are required especially for guest-host organic systems [19]. However, at very high electric fields the hole mobility values of **CzPrSBI** exceeding those of electron mobility are expected according the Poole–Frenkel fitting.

To study charge-transport properties of **CzPrSBI** in more detail, the six various types of charge hopping pathways A–F were separated within the X-ray structure (Fig. 1) and then analysed using the incoherent hopping model proposed in Refs. [20–25] This model is appropriate when the intermolecular transfer integrals are much smaller than the charge reorganization energy. The rates of charge transfer between neighbouring molecules (hopping rate W) are described by the Marcus-Hush equation [26–30]:

$$W = \frac{V^2}{\hbar}\sqrt{\left(\frac{\pi}{\lambda k_b T}\right)}\exp\left(-\frac{\lambda}{4k_b T}\right) \quad (1)$$

where λ is the reorganization energy for holes or electrons, V is the transfer integral, T is temperature (298.15 K for our calculations), k_b is

the Boltzmann constant, $\hbar$ is a reduced Planck constant. The transfer integral V characterizes the strength of electronic coupling between the two adjacent molecules. It can be obtained by so-called direct method [31] in accordance with the following equation:

$$V_{electron/hole} = \langle \varphi^{0,site1}_{LUMO/HOMO} \left| F^0 \right| \varphi^{0,site2}_{LUMO/HOMO} \rangle \quad (2)$$

where $\varphi^{0,site1}_{LUMO/HOMO}$ and $\varphi^{0,site2}_{LUMO/HOMO}$ represent the HOMO or LUMO wave functions of the isolated molecules 1 and 2, respectively, F^0 is the Fock operator for the dimer. In Eq. (2) the suffix zero means that the molecular orbitals appearing in the operator are unperturbed. The robustness of this direct approach was demonstrated by numerous reports for different kinds of molecular crystals [32–35]. Based on the estimated hopping rates (W) the diffusion coefficient D can be expressed as

$$D = \frac{1}{2n} \sum_i r_i^2 W_i P_i \quad (3)$$

where n is the spatial dimensionality ($n = 3$ for the three-dimensional single crystal of compound **1**), i denotes a particular hopping pathway with hopping distance r_i (the intermolecular center-to-center distance in particular dimer), and P_i is the hopping probability, which is calculated as [36].

$$P_i = \frac{W_i}{\sum_i W_i}, \quad (4)$$

ikiThe drift mobility from charge hopping (μ) is then evaluated from the Einstein relation providing the bulk (isotropic) mobility of holes and electrons for the studied molecule **1** single crystal [36]:

$$\mu = \frac{e}{k_b T} D, \quad (5)$$

where e is the electronic charge.

The reorganization energy (λ) has both inner and the external contributions. The inner reorganization energy represents a measure of geometrical distortion of the ionic forms from the neutral molecule [37, 38]. We only considered the inner reorganization energies for hole (λ_{hole}) and electron ($\lambda_{electron}$) charge carriers employing the adiabatic potential energy surface approach [39]:

$$\lambda_{hole\ /electron} = \left(E^*_{cation\ /anion} - E_{cation\ /anion} \right) + \left(E^{**}_{cation\ /anion} - E_{neutral} \right) \quad (6)$$

where $E_{neutral}$ is the optimized ground state energy of the neutral molecule, $E_{cation\ /\ anion}$ is the optimized structure energy of the cationic/anionic molecule, $E^{**}_{cation\ /anion}$ is the energy of the neutral molecule at the cationic/anionic geometry and $E^{*}_{cation\ /anion}$ is the energy of the cationic/anionic molecule at the neutral-state geometry. The calculated charge-transport characteristics are summarized in Table 1.

According to the Marcus–Hush theory (Eq. (1)) the charge transfer mobility is dependent on the three factors including the reorganization energy ($\lambda_{hole}/\lambda_{electron}$), the electronic coupling (V) and the intermolecular center-of-mass distance (r). The A–C packing modes with the shortest intermolecular center-of-mass distances yield the largest transfer integrals in the case of hole transfer (−31.63, 8.49 and 5.24 meV, respectively). The dimers in pathways E and D with face-to-face π-π stacking interactions are preferable for electron transfer with the corresponding integrals for electron transfer of −99.73 and −20.33 meV, respectively (Table 1). The dimer E has much larger electron transfer integral and represents the main pathway for electron transfer. This fact can be explained by the presence of strong π-π overlap between neighbouring molecules. The dimers in other pathways have little molecular orbital overlap for the side-to-face or side-to-side stacks (Fig. 3).

As one can see from Eq. (1), the reorganization energy strongly affects the carrier hopping rate and plays an important role in determination of the final hole/electron mobility. This means that the estimated charge mobilities can be higher if the molecular packing is taken into account. Being in a molecular packing, molecular donor and acceptor fragments cannot rotate freely. Meanwhile a free molecule can undergo significant conformational changes similar to those possible in the crystal phase. Therefore, the intramolecular reorganization energies of **CzPrSBI** were calculated both for the case of isolated molecule (free rotation of D and A fragments) and for the solid state (rotation of D and A fragments is frozen). In the first case the hole/electron reorganization energies have much larger values of 161 and 558 meV, respectively (Table 1). When the molecular packing is taken into account, the conformation changes are smaller during the charge transfer process and hole/electron reorganization energies are of 49 and 378 eV, respectively (Table 1). The degree of decrease of reorganization energy is associated with the decrease in conformational changes. The main structural changes of free molecule of **CzPrSBI** and its charged ions, observed during optimization process, are presented in ESI (Fig. S2–S5). To avoid large deviations in mobility estimations the molecular packing should be taken into consideration in calculations of the intramolecular reorganization energy.

The hole and electron mobility values for **CzPrSBI** calculated taking into account molecular packing were found to be of 0.589 and 0.551 $cm^2\ V^{-1}\ s^{-1}$, respectively (Table 1). Thus, compound **CzPrSBI** can be considered as a promising organic bipolar semiconductor. Experimentally measured hole and electron mobility values are however much smaller than those obtained by quantum-chemical simulations of idealistic single-crystal phase. This discrepancy might be explained by high disorder of vacuum deposited thin film of CzPrSBI.

2.3. Common photophysical properties, aggregation-induced emission enhancement and mechanoluminescence

Absorption spectra of the solutions (1×10^{-5} mol/L) in five solvents with the different polarities are depicted in Fig. 4a. In general, absorption spectra have distinctive motif for carbazolyl-containing organic molecules [40]. Two low-energy absorption bands, which previously were designated as $^1L_b \leftarrow {}^1A$ and $^1L_a \leftarrow {}^1A$ [41], are characterized by

Table 1
Center-of-mass distances within dimers (r), reorganization energies (λ), transfer integrals (V), charge hopping rates (W) and charge carrier mobility (μ) of **CzPrSBI** calculated at the B3LYP/DZP theory level.

Dimer	r (Å)	Reorganization energy (λ, meV)		Transfer integral (V, meV)		Rate of charge hopping (W, s^{-1})		Drift mobility from charge hopping, (μ, $cm^2\ V^{-1}\ s^{-1}$)	
		Hole	Electron	Hole	Electron	Hole	Electron	Hole	Electron
A	4.6	49 [a] (161) [b]	378 [a] (558) [b]	−31.63	0.84	4.74×10^{13}	4.82×10^{8}	0.589 [a] (0.108) [b]	0.551 [a] (0.080) [b]
B	7.1			8.49	−0.77	3.42×10^{12}	4.05×10^{8}		
C	9.5			5.24	−0.11	1.30×10^{12}	8.27×10^{6}		
D	10.3			0.01	−20.33	4.74×10^{6}	2.82×10^{11}		
E	11.4			−0.09	−99.73	3.84×10^{8}	6.80×10^{12}		
F	12.6			−0.42	−0.03	6.36×10^{9}	6.15×10^{5}		

[a] – the value calculated with taking into account molecular packing.
[b] – the value obtained without accounting molecular packing.

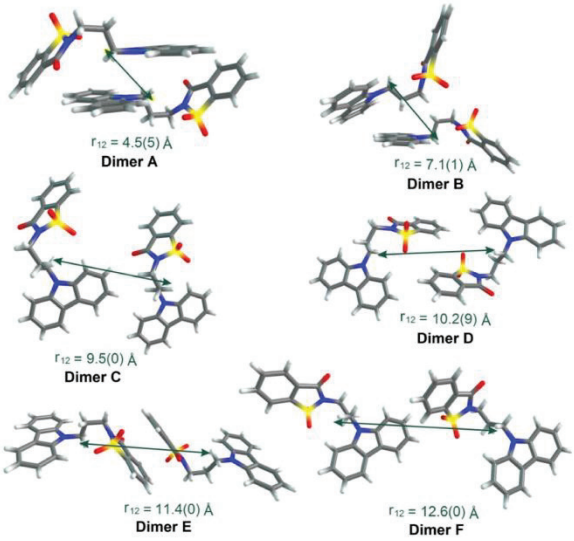

Fig. 3. The structure of the pertinent dimer configurations extracted from the single crystal X-ray data of CzPrSBI. The center-of-mass intermolecular distances (r_{12}) are shown by green arrows.

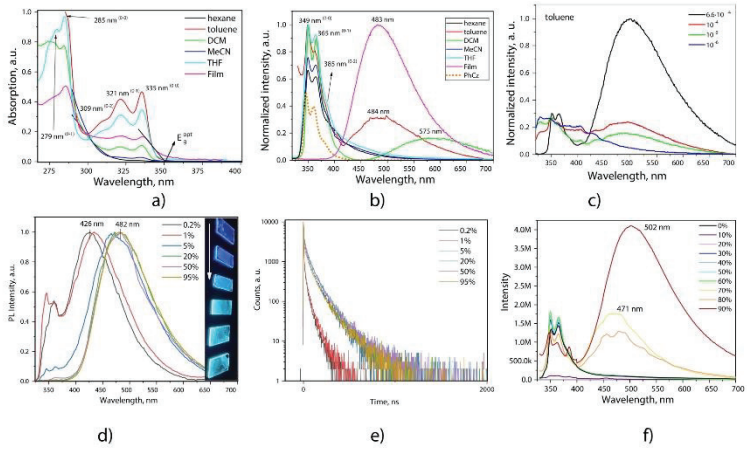

Fig. 4. Absorption (a) and PL (b) spectra of **CzPrSBI** in different media. The PL spectrum (b) of PhCz was recorded for its THF solution. PL spectra (c) of toluene solutions of **CzPrSBI** of the different concentrations (mol/L). PL spectra (d) PL decay curves (e) of the solid solutions of **CzPrSBI** in ZEONEX of the different concentrations. The inset shows a photo of the samples under UV excitation. PL spectra (f) of the dispersions of **CzPrSBI** in the mixtures of THF and water with the different fractions of water.

considerable vibrational structure (Fig. 4a). As a result, not only the most intensive 0-0 transitions at 285 and 335 nm can be recognized but also 0–1 or 0–2 transitions are observed. Despite compound **CzPrSBI** contains donor and acceptor moieties in its molecular structure, there are no well-recognized signs of formation of charge-transfer (CT) states in the absorption spectra. The similar observation was reported for exciplex-forming systems for which intermolecular CT formation in ground state could not be observed by simple absorption measurements [42]. However, as it follows from our quantum-chemical calculations the CT states for the different conformations of **CzPrSBI** molecule are generally observed in the range 300–315 nm of absorption spectrum (Table 2). Meanwhile, the distinct carbazole absorption is predicted (LE states) at higher energies i.e., at ca. 285 nm. We assume that range-separated cam-B3LYP functional used in this work overestimates the energy of carbazole $^1L_b \leftarrow ^1A$ band (theor: 283–288 for different conformations, exp: 335), while more correctly predicts the energy of CT states (theor: 300–315 nm). However, the intensity of CT transitions in absorption spectrum is much lower than for $^1L_b \leftarrow ^1A$ band. Thus, CT transitions are overlapped by the main $^1L_b \leftarrow ^1A$ band and are not observed by experimental measurements.

Carbazole-originated LE emission with the vibrational structure, where 0-0 and 0–1 transitions appeared as the maxima at respectively 349 and 365 nm, the 0–2 transition appeared as the shoulder, were detected for the solutions of **CzPrSBI** (Fig. 4b). The PL spectrum of THF solution of phenylcarbazole (PhCz) is plotted in Fig. 4b as additional evidence that the mentioned band of **CzPrSBI** is correctly ascribed to the emission of carbazole. Additionally, CT emissions peaked at 484 and 575 nm were well recognized for the toluene and DCM solutions (1×10^{-5} mol/L) of **CzPrSBI**. Predictively, CT emission of **CzPrSBI** is caused by aggregation due to the relatively low solubility of **CzPrSBI** in the solvents. To check this prediction, PL spectra of the toluene solutions of the different concentrations of **CzPrSBI** were recorded (Fig. 4c, S6a). The highly concentrated toluene solution of **CzPrSBI** was characterized by the intensive CT band due to the aggregate formation leading to strong intermolecular interaction. The intensity of the CT band decreased with the decreasing concentration of toluene solution. The similar behaviour was observed was for the DMC solutions of the different concentrations (Fig. S6a). The position of the CT emission band of **CzPrSBI** were strongly media dependent because of the formation of different aggregates in the different solvents. The position of CT band dependence was apparently caused by the change of position of carbazole relatively to sulfobenzimide. Because of the bridge $-(CN_2)_3-$ between carbazole and sulfobenzimide moieties, CT of **CzPrSBI** was not a typical one formed between covalently bonded donor and acceptor units [43]. It was through-space CT (TSCT), thus exciplex-like one [44]. It was previously demonstrated that the shift of emission spectra of exciplexes is mainly related to the distance/position between donor and acceptor units [45,46].

It should be specified that the red-shifted and aggregation-dependent emission band of **CzPrSBI** mainly resulted from the emissive relaxation of the intramolecular CT (exciplex-like) states formed between D and A fragments in solutions as it is noted above. However, exciplex formation (intermolecular CT states) between the neighbouring molecules of **CzPrSBI** can be additionally expected in the solid state. To investigate the relation between intramolecular and intermolecular CT states of **CzPrSBI** in the solid state, we recorded PL spectra and PL decay curves of the solid solutions of **CzPrSBI** in ZEONEX of the different concentrations (Fig. 4d and e). At the low concentrations (0.2 and 1%) when there is no intermolecular interaction, the solid solutions were characterized by PL spectra with high-energy (LE emission) and low-energy (intramolecular CT emission at 426 nm) bands. These PL spectra are very similar to those detected for the toluene solutions of **CzPrSBI** (Fig. 4b). At the concentrations of **CzPrSBI** in ZEONEX higher than 5% when the aggregates are formed, the PL spectra are mainly characterized with the low-energy (intermolecular CT emission) band at 482 nm which is red-shifted in comparison to the intramolecular CT band of **CzPrSBI** observed at the low concentrations (Fig. 4d). The clear difference between the lifetimes of emissions of intramolecular and intermolecular CT states is also detected (Fig. 4e). The shapes of PL decay curves of the solid solutions of **CzPrSBI** in ZEONEX of the different concentrations are similar since the emission of **CzPrSBI** originates from the exciplexes (either from intramolecular or/and intermolecular ones). The contribution of intramolecular and intermolecular exciplex formation of **CzPrSBI** is also confirmed by the excitation spectra of the films of the solid solution of **CzPrSBI** in ZEONEX (Fig. S6b). The shape of the excitation spectra is very similar to that of the absorption spectra of **CzPrSBI** (Fig. 4a). However, the bathochromic shifts were detected in the excitation spectra of the films of the solid solutions with the increase of the concentration of **CzPrSBI**. This observation can apparently be attributed to the stronger CT interactions of D and A units in **CzPrSBI** aggregates than in the separate molecules.

To study solid-state emission of **CzPrSBI** in more detail, the series of dispersions of the compound in the mixtures of THF and water with the different fraction of water but with the same concentration of **CzPrSBI** were prepared and their photoluminescence spectra were recorded (Fig. 4f). **CzPrSBI** formed solid aggregates with the increase of amount of water in the mixtures. The dispersions in the mixtures of the slovents with the concentration of THF of 30% or more exhibited emission spectra similar to that carbazole (Fig. 4b). The solid aggregates were formed in the mixtures with water fraction higher than 70%. The higher emission intensity of the solid sample of **CzPrSBI** than that of the solution in the good solvent (THF) indicates aggregation-induced emission enhancement (AIEE). Photoluminescence quantum yield (PLQY) values recorded for the dispersions of **CzPrSBI** support the presence of AIEE. The lower PLQY value of 1.46% was recorded for the dilute solution of **CzPrSBI** in toluene in comparison to PLQY value of 14.8% observed for the solid solution in ZEONEX. The solid aggregates showed wide and intensive emission with the maxima in the range from 471 to 502 nm. Such difference between emission maxima of the different aggregates of CzPrSBI are most probably due to the different distances between carbazole and sulfobenzimide moieties. Apparently, not only intramolecular CT states demonstrate emission, but also intermolecular CT states (exciplex emission). This makes emission spectrum of aggregates extremely broad. It covers almost the whole visible region from 400 to 700 nm and extends to NIR region (Fig. 4f).

Observation of the different emission spectra for the different aggregates of **CzPrSBI** suggests prediction of mechanoluminescent properties of the compound. Indeed, **CzPrSBI** showed ability to respond to external stimuli (such as grinding, solvent treatment and melting) by changing its photoluminescence wavelength (Fig. 5a). As-prepared solid

Table 2
Vertical absorption (λ_{abs}, nm) and vertical emission (λ_{fl}, nm) characteristics of the different molecular conformations of **CzPrSBI** calculated by TDA/TDDFT/cam-B3LYP/6-31G(d,p). Oscillator strength values are presented in parentheses. Relative energies of molecular conformations (E_{rel}, kcal mole^{-1}) are also included.

	Conf I				Conf II				Conf III			
	λ_{abs} (f)	λ_{fl} (f)	Nature	E_{rel}	λ_{abs} (f)	λ_{fl} (f)	Nature	E_{rel}	λ_{abs} (f)	λ_{fl} (f)	Nature	E_{rel}
GasPhase	298 (<0.01)	439 (<0.01)	CT [H L]	+1.1	280 (0.05)	288 (0.08)	LE [H L−2]	+4.2	315 (0.01)	454 (0.01)	CT [H L]	0
Hexane	285 (<0.01)	398 (<0.01)	CT [H-L]	+1.0	281 (0.06)	290 (0.08)	LE [H-L−2]	+3.8	311 (0.02)	439 (0.02)	CT [H L]	0
THF	283 (0.07)	301 (0.11)	LE [H-L+2]	+1.1	282 (0.06)	291 (0.10)	LE [H-L−2]	+3.5	307 (0.02)	425 (0.02)	CT [H-L]	0
DCM	282 (0to07)	303 (0.11)	LE [H-L+2]	+1.3	282 (0.06)	302	LE [H-L−2]	+4.1	306	426 (0.02)	CT [H-L]	0

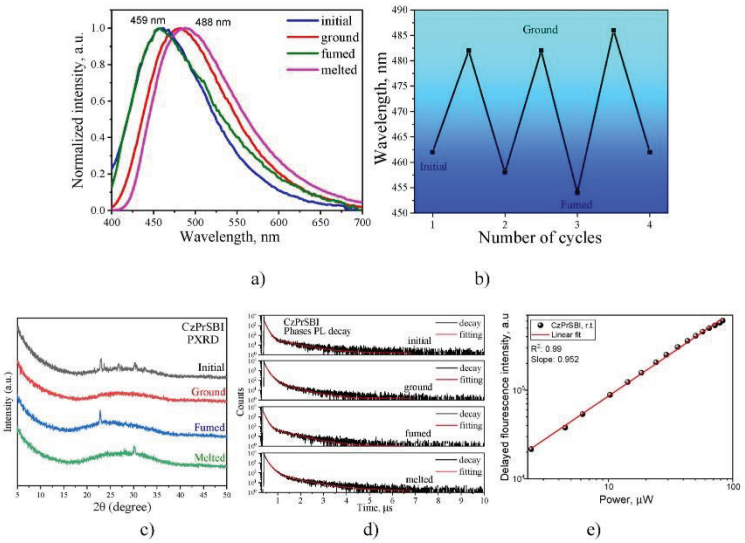

Fig. 5. PL spectra (a) of **CzPrSBI** after the different external stimuli; PL maxima shifts (b) after four grinding/fuming cycles; powder X-Ray diffractograms (c) and photoluminescence decay curves (d) of **CzPrSBI** after various external stimuli. Intensity of delayed fluorescence versus excitation power (e) **for** the film of **CzPrSBI**.

powder (obtained after the synthesis and purification) exhibited emission peaking at 462 nm under UV excitation. Mechanically obtained (by grinding) amorphous phase under the same excitation exhibited noticeably red-shifted emission peaking at 482 nm. The following treatment of the amorphous sample by dichloromethane vapour for 3 min (fuming), recovered peak of emission intensity back to the 484 nm. Melting of the fumed sample resulted in even stronger bathochromic shift of photoluminescence with a peak at 488 nm (Fig. 6a). The reversibility of mechanoresponsive emission was tested by the consequent repetition of grinding and fuming processes. Four grinding-fuming cycles of the sample of **CzPrSBI** showed that emission was reversible without degradation (Fig. 5b). One of the possible

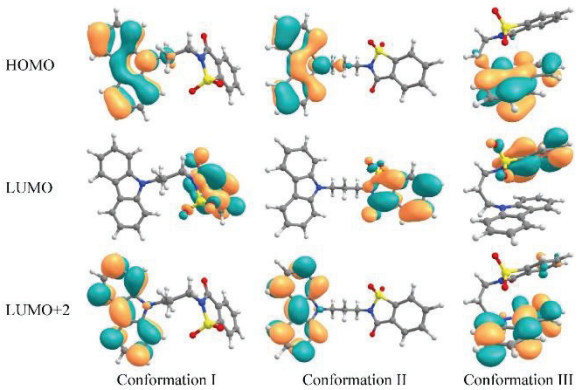

Fig. 6. The shape of selected molecular orbitals of the different conformations of **CzPrSBI**.

explanations for the above described spectral changes of **CzPrSBI** is conformational transitions induced by mechanical stimuli. As it follows from the results of quantum-chemical calculations, the conformation I that dominates in the single-crystal phase is not a global energy minimum compared to conformation III which should mainly exist in a disordered medium such as amorphous solid or gas phase (compare E_{rel} in Table 2). Conformation I is stabilized by crystalline phase, while in the absence of stabilizing effects it transforms into conformation III sustaining π-tacking interaction between D and A planes. Indeed, as it follows from our computations, conformation I demonstrates S_1–S_0 emission at 439 nm in gas phase, while conformation III demonstrates red-shifted emission at 454 nm. These results are in excellent agreement with the experimental data (462 nm and 484 nm for single crystal and amorphous phase, respectively). For both conformations I and III in gas phase the S_0–S_1 vertical absorption and S_1–S_0 vertical emission transitions correspond to one-electron excitation of HOMO-LUMO type. Taking into account, that HOMO is localized on carbazole (D) fragment, while LUMO is localized on sulfobenzimide (A) moiety, the S_1 state is assigned to charge-transfer (CT) origin (Fig. 6).

The formation of conformers of **CzPrSBI** is apparently related to the changes of the structure of its powders under the different external stimuli. The phase transitions which occur during mechanical stimulation (grinding, fuming, melting) were distinctly shown by the powder X-ray diffraction analysis (Fig. 5c). The initial crystalline powder, grinded amorphous phase, fumed crystalline sample and the melted sample demonstrated the different diffraction patterns. The initial crystalline sample showed complex set of diffraction peaks. They disappeared after grinding. However, the further fuming of the amorphous sample resulted in the restoration of single peak with the value of 2θ of 22.9°. The following melting of the sample resulted in appearance of the other single peak with the value of 2θ of 30.1°. Apparently, melting and cooling of the sample led to the recrystallization and formation of the second polymorphic form. These observations are in a very good agreement with the information obtained by DSC, which revealed two melting peaks (Fig. 2a).

The nature of emission was also examined by time resolved luminescence spectrometry. The PL decay curves are shown in Fig. 5d. The differently treated samples demonstrated the similar PL decays. The lifetimes of short-lived components, which were responsible for the prompt fluorescence, were found to be in the range of 87–137 ns, while excited state lifetimes of the long-lived components, which were responsible for delayed fluorescence, ranged from 679 to 898 ns (Table 3). Taking into account the slope value of 0.952 of the plot of the intensity of delayed fluorescence versus excitation power (Fig. 5e) [47], we conclude that delayed fluorescence is TADF in nature but not the emission resulted from triplet-triplet annihilation. The origin of TADF can be explained in terms of proximity between CT states for the conformations sustaining face-to-face orientation of donor and acceptor moieties. It is well known that space-separated CT states in single molecules and in intermolecular moieties (such as exciplexes) usually demonstrate very small singlet-triplet splitting that results in TADF [48,49]. Indeed, the singlet-triplet gap estimated for confirmation III in gas phase approximation is only 0.093 eV, while the intensity of S_1–S_0 is considerable as for CT states (f = 0.01, Table 2). These two factors affect the possibility of **CzPrSBI** to demonstrate TADF.

The photoluminescence decay parameters of the fumed and melted samples, which represent two polymorphic forms, showed remarkable difference of the lifetimes of short-lived and long-lived components. This observation can be explained by the different conformational compositions of the samples.

Table 3
Photoluminescence decay characteristics of various forms of CzPrSBI.

Sample	τ_1, ns	τ_2, ns	χ^2	τ_1/τ_2, %
Initial	88.86	868.67	1.105	84.05/15.95
Ground	113.66	679.73	1.288	80.30/19.70
Fumed	87.22	745.82	1.010	82.59/17.41
Melted	138.24	898.64	1.277	76.38/23.62

To provide additional evidence of the triplet harvesting ability of **CzPrSBI** via TADF, PL spectra and PL decay curves of its toluene solution and of the film of 95 wt% solid solution in ZEONEX were recorded (Fig. 7a–c). In addition, PL spectra and PL decay curves of the film of the solid solution in ZEONEX were recorded at the different temperatures (Fig. 7d and e). Deoxygenation of the samples lead to the increase of intensity of the low-energy band of **CzPrSBI** confirming the contribution of the triplet states in emission. With the increase of the temperature from 77 to 120 K, the increase of emission intensity of **CzPrSBI** was observed due to the TADF effect. Such a conclusion is in good agreement with the negligibly small ΔE_{ST} of **CzPrSBI** (Fig. 7f). At temperatures higher than 120 K, the emission intensity of **CzPrSBI** continually decreased due to the non-emissive losses of exciplex formed between the D and A units.

The photoluminescence lifetimes of **CzPrSBI** were found to be rather long as for prompt fluorescence, but they were very short in comparison to PL lifetimes of compounds exhibiting conventional TADF [50,51]. The similar exciplex-based TADF emission was previously observed for 6-cyano-9-phenylpurine and for the compounds containing benzoyl-1H-1,2,3-triazole acceptor and carbazole-based donor moieties [52,53]. These TADF exciplex systems were characterized by the lifetimes attributed only to delayed fluorescence because of the fast intersystem system crossing (FISC). The conventional exciplexes are characterized by prompt and delayed fluorescence with the lifetimes in the ranges of nanoseconds and of tens or hundreds of microseconds respectively. In contrast, FISC-assisted TADF exciplex systems are mostly characterized by delayed fluorescence with lifetimes in the ranges of tens or hundreds of nanoseconds [52,53]. Taking into account the similarity of PL decay curves of **CzPrSBI** to the corresponding PL decay curves of the previously published FISC-assisted TADF exciplex systems, it can be concluded that emitter **CzPrSBI** is one more example of FISC-assisted TADF exciplex systems.

2.4. Electroluminescence

To explore the performance of **CzPrSBI** as the TADF emitter, OLED with the structure CuI/TPD/CzPrSBI/TSPO1/TPBi/Ca/Al was fabricated utilizing the thermal vacuum evaporation technique. The layer of CuI was used as hole-injection layer [54,55] and that of 2,2′,2″-(1,3,5-benzinetriyl)-tris(1-phenyl-1-H-benzimidazole) (TPBi) [56] was employed as an electron-transporting layer. Additionally, the TPD [57] and TSPO1 [58,59] were used for hole transporting and exciton–blocking layers, which ensured the balance of charge carriers in the emission layer. **CzPrSBI** was used as the emitter. The layer of calcium topped with a 200 nm layer of aluminium was used as the cathode.

Similarly to the PL profiles of the neat film of **CzPrSBI**, shown in Fig. 8 a,c, the devices exhibited the structureless electroluminescence (EL) spectra (Fig. 8 a,c) with the intensity peaks in the range of 490–504 nm. This observation demonstrates that EL resulted from the emitter itself. The relative intensity of the shoulder peaking at 630 nm increased with the increase of driving bend angle of flexible OLED (Fig. 8 c). We assign this observation to intermolecular exciplex formation between the donor part of one **CzPrSBI** molecule and acceptor part of another one. When the flexible samples changed the angle of the bend, the intensity of the peak grew. When the angle reached 50° the intensity reverted to that of OLEDs with the glass substrates. The mechanochromic luminescence of **CzPrSBI** in flexible OLED is attributed to the enforced approach of donor and acceptor fragments due to mechanical impact (bending in our case) that results in the enhancement of the formation of intermolecular exciplexes.

The device based on a glass substrate exhibited the best performance with maximum current efficiency, power efficiency, and external quantum efficiency (EQE) of 11.0 cd A^{-1}, 3.0 lm W^{-1}, and 4.3%,

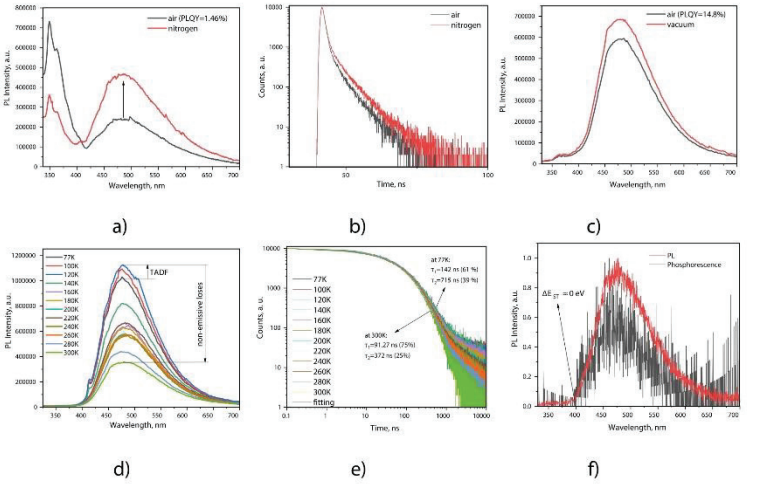

Fig. 7. PL spectra (a) and PL decay curves (b) of toluene solution of **CzPrSBI** as prepared and deoxygenated by nitrogen purging during 5 min. PL spectra of the film of 95 wt% solid solution of **CzPrSBI** in ZEONEX recorded under air or vacuum (c) and at the different temperatures (d) in inert atmosphere. PL decay curves (e) of the film of 95 wt% solid solution of **CzPrSBI** in ZEONEX recorded at the different temperatures. PL and phosphorescence spectra (f) of 95 wt% solid solution of **CzPrSBI** in ZEONEX recorded at 77K. The phosphorescence spectrum was recorded using the delay of 1 ms after excitation.

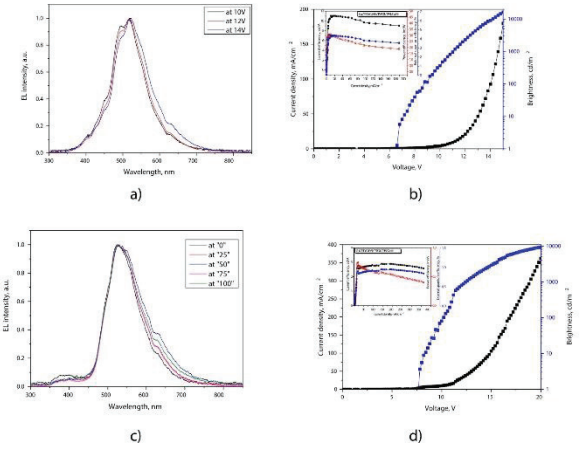

Fig. 8. The spectra of electroluminescence of devices recorded at the different voltages (a) and different bend angle(c); Current density-voltage and luminance-voltage, power efficiency – current density, current efficiency - current density and external quantum efficiency – current density plots for the devices (b-glass substrate, d-flexible substrate).

Table 4
Characteristics of OLEDs fabricated on the glass and flexible substrates.

Device substrate	V_{on}, V	Max. brightness,cd m^{-2}	Current efficiency,cd A^{-1}	Power efficiency,lm W^{-1}	EQE, %
			at 1000/max. cd m^{-2}		
glass	6.4	16000	11.0/9.0	3.0/1.8	4.3/3.5
flexible	7.4	9000	2.6/2.5	0.6/0.4	0.8/0.9

respectively (Fig. 8, Table 4).

3. Conclusions

We synthesized and characterized the new carbazole-σ-sulfobenzimide derivative, where σ is $(CH_2)_3$. It showed mechanochromic thermally activated delayed fluorescence and aggregation-induced emission shift as well as tunable emission in flexible electroluminescent heterostructures. The unique property of the compound is that it consists of donor and acceptor subparts separated by non-conjugated linker that makes the system conformationally variable and supresses the common charge-transfer electronic transitions mediated by π-conjugated linkers. The only space-separated inter- and intramolecular charge-transfer excited states are thus possible. This possibility well explains the sensitivity of emission properties of the compound to aggregation and mechanical stimuli as well as sheds light on the origin of thermally activated delayed fluorescence and on bending-dependent electroluminescence of flexible light-emitting diodes. Although the efficiency of the best flexible OLED was not high, we demonstrated the approach for the design of color-tunable flexible OLEDs which can be extended onto broader variety of mechanochromic TADF emitters.

Author contribution statement

Yan Danyliv: ***Conceptualization, Writing – original draft, Investigation***, Khrystyna Ivaniuk: ***Data curation, Investigation, Writing – review & editing, Visualization***, Iryna Danyliv: ***Investigation***; Dmytro Volyniuk: ***Conceptualization, Writing – original draft, Investigation, Validation, Visualization;*** Galyna Sych: ***Investigation***; Algirdas Lazauskas: ***Data curation, Methodology, Investigation;*** Levani Skhirtladze: ***Investigation***; Hans Ågren: ***Supervision, Formal analysis***; Pavlo Stakhira: ***Supervision, Formal analysis***; Nataliya Karaush-Karmazin: ***Investigation***; Glib Baryshnikov: ***Investigation***, Funding ***acquisition, Validation, Writing – review & editing, Supervision***; Juozas V. Grazulevicius: Funding ***acquisition, Validation, Writing – review & editing, Supervision.***

Declaration of competing interest

The authors declare the following financial interests/personal relationships which may be considered as potential competing interests:

Data availability

Research data are presented in Supplementary information file.

Acknowledgements

This research was funded by the European Social Fund under the No 09.3.3-LMT-K-712 "Development of Competences of Scientists, other Researchers and Students through Practical Research Activities" measure (Project No 09.3.3-LMT-K-712-19-0136). This work was also supported by the Ministry of Education and Science of Ukraine (project no. 0121U107533 and 0121U109506). The financial support of the Marie Curie International Research Staff Exchange Scheme within FP7- Peoples EU project No. PIRSES-GA-2013-612670 is gratefully acknowledged. A.A. and G.B. thanks for support from Carl Tryggers Stiftelse (Sweden), project number CTS 21:1430. I.D., P.S. and D.V. thanks for support from funds within the project of scientific cooperation program between Lithuania and Ukraine "Development of highly efficient white light-emitting diodes utilizing organic emitters with exciplex and thermally-assisted fluorescence for lighting applications (LUW)" (grant No. S-LU-20-9) under grant agreement with the Research Council of Lithuania (LMTLT). The quantum-chemical calculations were performed with computational resources provided by the Swedish National Infrastructure for Computing (SNIC 2022/5–103) at the National Supercomputer Centre at Linköping University (NSC) partially funded by the Swedish Research Council through Grant Agreement No. 2018–05973.

Appendix A. Supplementary data

Supplementary data to this article can be found online at https://doi.org/10.1016/j.dyepig.2022.110841.

References

[1] Zou S-J, Shen Y, Xie F-M, Chen J-D, Li Y Q, Tang J X. Recent advances in organic light emitting diodes: toward smart lighting and displays. Mater Chem Front 2020;4:788–820.
[2] Zhao C, Duan L. Review on photo- and electrical aging mechanisms for neutral excitons and ions in organic light emitting diodes. J Mater Chem C 2020;8:803–20.
[3] Berggren M, Nilsson D, Robinson ND. Organic materials for printed electronics. Nat Mater 2007;6:3–5.
[4] Ostroverkhova O. Organic optoelectronic materials: mechanisms and applications. Chem Rev 2016;116(22):13279–412.
[5] Uoyama H, Goushi K, Shizu K, Nomura H, Adachi C. Highly efficient organic light-emitting diodes from delayed fluorescence. Nature 2012;492(7428):234–8.
[6] Yang Z, Mao Z, Xie Z, Zhang Y, Liu S, Zhao J, Xu J, Chi Z, Aldred MP. Recent advances in organic thermally activated delayed fluorescence materials. Chem Soc Rev 2017;46:915–1016.
[7] Mei J, Leung NLC, Kwok RTK, Lam JWY, Tang BZ. Aggregation induced emission: together we shine, united we soar. Chem Rev 2015;115(21):11718–940.
[8] Li Z, Wang Y, Baryshnikov G, Shen S, Zhang M, Zou Q, Ågren H, Zhu L. Lighting up solid states using a rubber. Nat Commun 2021;12:908.
[9] Xie Y, Li Z. The development of mechanoluminescence from organic compounds: breakthrough and deep insight. Mater Chem Front 2020;4:317–31.
[10] Sagara Y, Kato T. Mechanically induced luminescence changes in molecular assemblies. Nat Chem 2009;1:605–10.
[11] Lee JE, Ahn G, Shim J, Lee YS, Ryu S. Optical separation of mechanical strain from charge doping in graphene. Nat Commun 2012;3:1–8.
[12] Data P, Takeda Y. Recent Advancements in and the future of organic emitters: TADF- and RTP-active multifunctional organic materials. Chem Asian J 2019;14:1613–36.
[13] Chi Z, Zhang X, Xu B, Zhou X, Ma C, Zhang Y, Liu S, Xu J. Recent advances in organic mechanofluorochromic materials. Chem Soc Rev 2012;41:3878–96.
[14] Yagai S, Seki T, Aonuma H, Kawaguchi K, Karatsu T, Okura T, Sakon A, Uekusa H, Ito H. Mechanochromic luminescence based on crystal to crystal transformation mediated by a transient amorphous state. Chem Mater 2016;28:234–41.
[15] Xue P, Ding J, Wang P, Lu R. Recent progress in the mechanochromism of phosphorescent organic molecules and metal complexes. J Mater Chem C 2016;4:6688–706.
[16] Sun M, Zhu L, Kan W, Wei Y, Ma D, Fan X, Huang W, Xu H. Ternary donor–acceptor phosphine oxide hosts with peculiar high energy gap for efficient blue electroluminescence. J Mater Chem C 2015;3:9469–78.
[17] Ambrose JF, Nelson RF. Anodic oxidation pathways of carbazoles: I. Carbazole and N-substituted derivatives. J Electrochem Soc 1968;115:1159–64.
[18] Bässler H. Charge transport in disordered organic photoconductors a Monte Carlo simulation study. Phys Status Solidi 1993;175:15–56.
[19] Lee J H, Chen C H, Liu B Y, Lee Y H, Huang Y M, Chen N J, Huang J J, Volyniuk D, Keruckiene R, Grazulevicius JV, Wu Y-R, Leung M-K, Chiu T-L. Bistriazoles with a biphenyl core derivative as an electron favorable bipolar host of efficient blue phosphorescent organic light-emitting diodes. ACS Appl Mater Interfaces 2020;12(44):49895–904.
[20] Nelsen SF, Blomgren F. Estimation of electron transfer parameters from AM1 calculations. J Org Chem 2001;66(20):6551–9.
[21] Nelsen SF, Trieber Ii DA, Ismagilov RF, Teki Y. Solvent effects on charge transfer bands of nitrogen-centered intervalence compounds. J Am Chem Soc 2001;123(24):5684–94.
[22] Malagoli M, Bredas JL. Density functional theory study of the geometric structure and energetics of triphenylamine-based hole-transporting molecules. Chem Phys Lett 2000;327:13–7.

[23] Sakanoue K, Motoda M, Sugimoto M, Sakaki S. A molecular orbital study on the hole transport property of organic amine compounds. J Phys Chem A 1999;103(28):5551–6.
[24] Li XY, Tong J, He FC. Ab initio calculation for inner reorganization energy of gas phase electron transfer in organic molecule–ion systems. Chem Phys 2000;260:283–94.
[25] Marcus RA, Sutin N. Electron transfers in chemistry and biology. Biochim Biophys Acta 1985;811:265–322.
[26] Marcus RA. Electron transfer reactions in chemistry. Theory and experiment. Rev Mod Phys 1993;65:599–610.
[27] Marcus RA. On the theory of oxidation reduction reactions involving electron transfer. I. J Chem Phys 1956;24:966–78.
[28] Hush NS. Adiabatic rate processes at electrodes. I. Energy Charge relationships. J Chem Phys 1958;28:962–72.
[29] Hush NS. Adiabatic theory of outer sphere electron-transfer reactions in solution. Trans Faraday Soc 1961;57:577–80.
[30] Berlin YA, Hutchinson GR, Rampla P, Ratner MA, Michl J. Charge hopping in molecular wires as a sequence of electron transfer reactions. J Phys Chem A 2003;107:3970–80.
[31] Yin S, Yi Y, Li Q, Yu G, Liu Y, Shuai Z. Balanced carrier transports of electrons and holes in silole-based compounds – a theoretical study. J Phys Chem A 2006;110:7138–43.
[32] Yang X, Li Q, Shuai Z. Theoretical modelling of carrier transports in molecular semiconductors: molecular design of triphenylamine dimer systems. Nanotechnology 2007;18:424029–35.
[33] Liu X, Liu Y, Zheng Y. Charge transfer mobility of naphthodithiophenediimide derivative: normal mode and bond length relaxation analysis. Chem Phys Lett 2016;645:92–6.
[34] Ma H, Liu N, Huang J-D. A DFT study on the electronic structures and conducting properties of rubrene and its derivatives in organic field-effect transistors. Sci Rep 2017;7:331.
[35] Karaush-Karmazin NN, Baryshnikov G, Kuklin A, Saykova D, Ågren H, Minaev B. Impact of molecular and packing structure on the charge-transport properties of hetero[8]circulenes. J Mater Chem C 2021;9:1451–66.
[36] Wen S H, Li A, Song J, Deng W Q, Han K L, Goddard III WA. First principles investigation of anistropic hole mobilities in organic semiconductors. J Phys Chem B 2009;113:8813–9.
[37] Brunschwig BS, Logan J, Newton MD, Sutin N. A semiclassical treatment of electron exchange reactions. Application to the hexaaquoiron(II) hexaaquoiron (III) system. J Am Chem Soc 1980;102(18):5798–809.
[38] Newton MD, Sutin N. Electron transfer reactions in condensed phases. Annu Rev Phys Chem 1984;35:437–80.
[39] Zhang MX, Chai S, Zhao G-J. BODIPY derivatives as n-type organic semiconductors: isomer effect on carrier mobility. Org Electron 2012;13:215–21.
[40] Wong K-T, Chen Y-M, Lin Y-T, Su H-C, Wu C-C. Nonconjugated hybrid of carbazole and fluorene: a novel host material for highly efficient green and red phosphorescent OLEDs. Org Lett 2005;7(24):5361–4.
[41] Johnson GE. Spectroscopic study of carbazole by photoselection. J Phys Chem 1974;78(15):1512–21.
[42] Kim H-B, Kim J-J. A simple method to measure intermolecular charge-transfer absorption of organic films. Org Electron 2018;62:511–5.
[43] Jankus V, Data P, Graves D, McGuinness C, Santos J, Bryce MR, Dias FB, Monkman AP. Highly efficient TADF OLEDs: how the emitter-host interaction controls both the excited state species and electrical properties of the devices to achieve near 100% triplet harvesting and high efficiency. Adv Funct Mater 2014;24(39):6178–86.
[44] Tsujimoto H, Ha D G, Markopoulos G, Chae HS, Baldo MA, Swager TM. Thermally activated delayed fluorescence and aggregation induced emission with through-space charge transfer. J Am Chem Soc 2017;139(13):4894–900.
[45] Moon C-K, Huh J-S, Kim J-M, Kim J-J. Electronic structure and emission process of excited charge transfer states in solids. Chem Mater 2018;30(16):5648–54.
[46] Li X, Baryshnikov G, Deng C, Bao X, Wu B, Zhou Y, Ågren H, Zhu L. A three-dimensional ratiometric sensing strategy on unimolecular fluorescence–thermally activated delayed fluorescence dual emission. Nat Commun 2019;10:731.
[47] Dias FB. Kinetics of thermal-assisted delayed fluorescence in blue organic emitters with large singlet–triplet energy gap. Phil Trans R Soc A 2015;373:20140447.
[48] Ledwon P, Motyka R, Ivaniuk K, Pidluzhna A, Martyniuk N, Stakhira P, Baryshnikov G, Minaev BF, Ågren H. The effect of molecular structure on the properties of quinoxaline-based molecules for OLED applications Dyes. Pigm 2020;173:108008.
[49] Sarma M, Wong K-T. Exciplex: an intermolecular charge-transfer approach for TADF. ACS Appl Mater Interfaces 2018;10(23):19279–304.
[50] Berenis D, Kreiza G, Jursenas S, Kamarauskas E, Ruibys V, Bobrovas O, Adomenas P, Kazlauskas K. Different RISC rates in benzoylpyridine-based TADF compounds and their implications for solution-processed OLEDs. Dyes Pigments 2020;182:108579.
[51] Yuan W, Zhang M, Zhang X, Cao X, Sun N, Wan S, Tao Y. The electron inductive effect of CF_3 on penta carbazole containing blue emitters: trade off between color purity and luminescent efficiency in TADF OLEDs. Dyes Pigments 2018;159:151–7.
[52] Traskovskis K, Sebris A, Novosjolova I, Turks M, Guzauskas M, Volyniuk D, Bezvikonnyi O, Grazulevicius JV, Mishnev A, Grzibovskis R, Vembris A. All organic fast intersystem crossing assisted exciplexes exhibiting sub-microsecond thermally activated delayed fluorescence. J Mater Chem C 2021;9:4532–43.
[53] Stanitska M, Mahmoudi M, Pokhodylo N, Lytvyn R, Volyniuk D, Tomkeviciene A, Keruckiene R, Obushak M, Grazulevicius JV. J Org Chem 2022;87(6):4040–50.
[54] Lee J-H, Leem D-S, Kim J-J. High performance top-emitting organic light-emitting diodes with copper iodide-doped hole injection layer. Org Electron 2008;9(5):805–8.
[55] Hotra Z, Stakhira P, Cherpak V, Volynyuk D, Voznyak L, Gorbulyk V, Tsizh B. Effect of thickness of CuI hole injection layer on properties of organic light emitting diodes. Phot Lett Pol 2012;4(1):35–7.
[56] Yang Q, Hao Y, Wang Z, Li Y, Wang H, Xu B. Double emission layer green phosphorescent OLED based on LiF-doped TPBi as electron transport layer for improving efficiency and operational lifetime. Synth Met 2012;162(3–4):398–401.
[57] Kuklita NA, Matulaitis T, Volyniuk D, Ivaniuk K, Turyk P, Stakhira P, Grazulevicius JV, Monkman AP. Deep-blue high-efficiency TTA OLED using para- and meta-conjugated cyanotriphenylbenzene and carbazole derivatives as emitter and host. J Phys Chem Lett 2017;8(24):6199–205.
[58] Sun JW, Baek JY, Kim K-H, Huh J-S, Kwon S-K, Kim Y-H, Kim J-J. Azasiline-based thermally activated delayed fluorescence emitters for blue organic light emitting diodes. J Mater Chem C 2017;5:1027–32.
[59] Yook KS, Lee JY. Solution processed high efficiency blue and white phosphorescent organic light-emitting diodes using a high triplet energy exciton blocking layer. Org Electron 2011;12(8):1293–7.

9. ACKNOWLEDGEMENTS

Prof. Dr. Hab. Juozas Vidas Gražulevičius (Department of Polymer Chemistry and Technology, Kaunas University of Technology) is sincerely thanked for the supervision of my PhD research, consultations, valuable advices, and great support.

Prof. Dr. Azhar Bin Ariffin (Department of Chemistry, University of Malaya) is sincerely thanked for teaching, consultations, support, and useful advices during my PhD research.

Dr. Dmytro Volyniuk (Department of Polymer Chemistry and Technology, Kaunas University of Technology) is greatly acknowledged for measurements of charge-transporting and photoelectron emission properties and help interpreting the photophysical results.

Dr. Oleksandr Bezvikonnyi and PhD student Karolis Leitonas (Department of Polymer Chemistry and Technology, Kaunas University of Technology) are thanked for the measurements, device fabrication, and help interpreting the photophysical results.

Assoc. Prof. Dr. Kai Lin Woon (Department of Physics, University of Malaya) is greatly thanked for the theoretical calculations, describing photophysical, and theoretical calculations results.

Dr. Rasa Keruckienė (Department of Polymer Chemistry and Technology, Kaunas University of Technology) is greatly thanked for support, sharing of knowledge in theoretical calculations, and invaluable ideas, advices, and interpreting the results of theoretical calculations.

Dr. Eigirdas Skuodis (Department of Polymer Chemistry and Technology, Kaunas University of Technology) is thanked for the measurements of thermal properties and mass spectra.

PhD student Malek Mahmoudi Sharabiani (Department of Polymer Chemistry and Technology, Kaunas University of Technology) is thanked for the measurements of thermal properties.

Dr. Audrius Bučinskas (Department of Polymer Chemistry and Technology, Kaunas University of Technology) is thanked for the singe crystal X-ray measurements and interpreting the results.

All the colleagues of the research group are thanked for their help and friendly working atmosphere.

UDK [539.216 + 661.844] (043.3)

SL344. 2024-02-26, 18,5 leidyb. apsk. l. Tiražas 14 egz. Užsakymas 26.
Išleido Kauno technologijos universitetas, K. Donelaičio g. 73, 44249 Kaunas
Spausdino leidyklos „Technologija“ spaustuvė, Studentų g. 54, 51424 Kaunas